

Iowa Research Online

Target-mediated drug disposition (TMDD) in pharmacokinetics and pharmacodynamics (PK/PD) of large-molecule and small-molecule compounds

Wu, Nan

<https://iro.uiowa.edu/esploro/outputs/doctoral/Target-mediated-drug-disposition-TMDD-in-pharmacokinetics/9984546750602771/filesAndLinks?index=0>

Wu, N. (2023). Target-mediated drug disposition (TMDD) in pharmacokinetics and pharmacodynamics (PK/PD) of large-molecule and small-molecule compounds [University of Iowa].
<https://doi.org/10.25820/etd.006981>

Target-Mediated Drug Disposition (TMDD) in Pharmacokinetics and Pharmacodynamics
(PK/PD) of Large-Molecule and Small-Molecule Compounds

by

Nan Wu

A thesis submitted in partial fulfillment
of the requirements for the Doctor of Philosophy
degree in Pharmacy (Pharmaceutics) in the
Graduate College of
The University of Iowa

December 2023

Thesis Committee: Guohua An, Thesis Supervisor
 Maureen Donovan
 Robert Kerns
 Gary Milavetz

ACKNOWLEDGMENTS

This dissertation owes its existence to the unwavering guidance and support of numerous individuals who contributed their invaluable assistance and feedback. Foremost, my profound gratitude extends to my advisor, Dr. Guohua An, who entrusted me with the opportunity to embark on this project. Throughout my journey in graduate studies, Dr. An served as a dedicated mentor, nurturing my growth as a research scientist in the field of pharmacometrics. No words can adequately convey my heartfelt thanks for her steadfast guidance, boundless support, unwavering patience, and constant encouragement throughout the course of this study.

Furthermore, I wish to express my appreciation to my esteemed committee members: Dr. Maureen Donovan, Dr. Robert Kerns, and Dr. Gary Milavetz. Their contributions enriched the content of this thesis with valuable insights.

I would like to express my deepest gratitude to the individuals and organizations who have generously contributed to the completion of this work. Their invaluable support and collaboration have been instrumental in the development of this thesis. First and foremost, I extend my sincere thanks to Dr. David Katz of Sparrow Pharmaceuticals, Inc. for graciously sharing the SPI-62 Phase I clinical pharmacokinetics (PK) and pharmacodynamic (PD) data featured in Chapter 2. I am also deeply grateful to Dr. Bruce D. Hammock of the University of California, Davis, and Dr. Kin Sing Stephen Lee of Michigan State University for their kind assistance in providing the preclinical PK data for TPPU and TCPU, which will be presented in Chapter 3. Additionally, I would like to express my appreciation to Dr. Peter Veng-Pedersen, an emeritus professor within our department, and Dr. John A. Widness from the Department of Pediatrics, College of Medicine, University of Iowa, for their generous sharing of Epo clinical PK data in patients undergoing hematopoietic

transplantation, as featured in Chapter 6. Without their invaluable data, the development of the models and findings within this thesis would not have been possible.

I extend my gratitude to all the past and present members of Dr. Guohua An's laboratory, including Demet Nalbant, Huynh-Yen-Thanh Bach, Joshua Reeder, Peizhi Li, Min Xu, and Xuanzhen Yuan, for their support and shared experiences.

I am deeply appreciative of the Department of Pharmaceutics at the University of Iowa for their consistent and generous financial support that has been instrumental in sustaining my educational journey.

Lastly, but by no means of lesser significance, I extend my sincere and heartfelt gratitude to my parents, whose unwavering support and sacrifices have been my constant motivation and source of strength. Their belief in me has been unwavering, and I owe them immeasurable gratitude. I also want to express my appreciation to all my friends who have stood by me, offering encouragement, understanding, and companionship throughout this challenging and rewarding endeavor. Your collective support has been an invaluable part of my academic and personal growth.

ABSTRACT

Target-mediated drug disposition (TMDD) represents a pivotal phenomenon in pharmacology, where the interaction between a potent drug and its pharmacological target yields significant implications for pharmacokinetics (PK). Large-molecule compounds like erythropoietin are well-recognized to exhibit TMDD, due to the specific binding to high-affinity receptors and minimal non-specific binding. However, the TMDD of small-molecule compounds is often obscured by non-specific bindings with plasma protein such as albumin, which have greater binding capacity. The emergence of more potent small-molecule drugs and sensitive bioanalytical methods has unveiled strong TMDD in various small-molecule compounds, including 11 β -hydroxysteroid dehydrogenase type I inhibitor (HSD-1) inhibitors (e.g., SPI-62, ABT-384), soluble epoxide hydrolase inhibitors (sEH) (e.g., TPPU and TCPU), and dipeptidyl peptidase 4 (DPP-4) inhibitors (e.g., linagliptin) etc. Both large and small molecule compounds that exhibit TMDD often display nonlinear PK, adding complexity to the task of elucidating the connections between dose, drug exposure, and response. Interestingly, the localization of pharmacological targets contributes to the distinctive non-linear PK patterns observed in small molecules with TMDD, further complicating our comprehension of the dose-exposure-response relationship in this context. To tackle this challenge, the application of advanced pharmacometrics models, drawn from both preclinical and clinical data, becomes essential. These models facilitate more efficient and well-informed decision-making, ultimately enhancing the selection of appropriate dosages for both large and small-molecule compounds exhibiting TMDD throughout the drug development process.

My thesis objectives were utilizing pharmacometrics modeling approaches to investigate TMDD's role in the PK of (1) small molecules with pharmacological targets in tissues, and (2)

small molecules with pharmacological targets located in plasma, and (3) a large molecule, recombinant human erythropoietin (rhEpo).

For the first objective, my initial research (Chapter 2) focused on SPI-62, a potent HSD-1 inhibitor undergoing Phase II clinical trials. A TMDD model was developed to elucidate the nonlinear PK/pharmacodynamics (PD) relationship observed in Phase I clinical trials with healthy adults, providing a foundation for dose selection in current and future clinical studies. The second project (Chapter 3) delved into the preclinical stage, where two sEH inhibitors with pharmacological targets located in tissues exhibited pronounced TMDD characteristics. An interactive TMDD model was established to concurrently characterize TPPU and TCPU PK and the model was applied to predict the target occupancy.

Shifting to the second objective, the third project (Chapter 4) highlighted Linagliptin, an FDA-approved DPP-4 inhibitor with pronounced TMDD affecting both tissue and plasma PK. To facilitate dose selection for linagliptin, a comprehensive Whole-Body Physiologically-Based Pharmacokinetic (WB-PBPK) model was built in rats and then was scaled up to human. In the fourth project (Chapter 5), a Quantitative Systems Pharmacology (QSP) model was built to quantify Linagliptin's impact on two incretins, GLP-1 and GIP, alongside influential factors (e.g., glucose, glucagon and insulin) in glycemic control.

For the third objective (Chapter 6), our focus is on recombinant human erythropoietin (rhEpo), a crucial therapy for anemia. Extensive investigation was conducted on rhEpo, and it has been reported to exhibit target-mediated drug disposition (TMDD) in both animals and humans. However, a significant knowledge gap exists in comprehending erythropoietin's PK in patients with varying bone marrow conditions, posing a substantial obstacle in dose selection for this unique population. This project developed a comprehensive TMDD model to quantitatively

characterize rhEpo PK data in patients undergoing varying stages of bone marrow ablation following hematopoietic transplantation.

My work in pharmacometrics models encompasses both large-molecule and small-molecule compounds, highlighting key distinctions as they exhibit TMDD. These models provide a quantitative framework for characterizing the nonlinear PK and PD of several small molecules, including SPI-62, Linagliptin, TPPU/TCPU, and the large molecule erythropoietin. This quantitative understanding serves as a guiding compass throughout the drug development journey, from preclinical phases through clinical trials to post-clinical stages, embodying the essence of Model-informed Drug Development (MIDD).

PUBLIC ABSTRACT

Target-mediated drug disposition (TMDD) represents a pivotal phenomenon in pharmacology, where the interaction between a potent drug and its pharmacological target yields significant effect on pharmacokinetics (PK). Large-molecule compounds like erythropoietin are well-known for exhibiting TMDD due to specific binding to high-affinity receptors. In contrast, small-molecule compounds often experience TMDD less visibly. Recent advancements in small-molecule drugs and sensitive bioanalytical methods have unveiled strong TMDD in several small molecules.

Both large and small molecule compounds with TMDD frequently show nonlinear PK, making it challenging to understand the relationships between dose, drug exposure, and response. To address this challenge and facilitate dose selection in drug development, my thesis objectives were to use pharmacometrics to study TMDD in (1) small molecules with pharmacological targets in tissues, (2) small molecules with pharmacological targets in plasma, and (3) a large molecule, recombinant human erythropoietin (rhEpo).

In the first objective, research on SPI-62, a potent HSD-1 inhibitor, characterized the nonlinear PK/PD relationship in Phase I clinical trials, guiding dose selection. The second project examined two sEH inhibitors, establishing an interactive TMDD model. For the second objective, the third project focused on Linagliptin, developing a comprehensive Whole-Body Physiologically-Based Pharmacokinetic (WB-PBPK) model for dose selection. The fourth project used a Quantitative Systems Pharmacology (QSP) model to assess Linagliptin's effects on incretins and glycemic control. In the third objective, a comprehensive TMDD model was developed to

capture rhEpo PK in patients undergoing bone marrow ablation after hematopoietic transplantation.

TABLE OF CONTENTS

LIST OF TABLES	xiii
LIST OF FIGURES	xiv
CHAPTER 1: INTRODUCTION	1
1.1. Background	2
1.2. Experiments verifying if the compound's nonlinear PK is mediated by its pharmacological targets	3
1.2.1. PK experiments conducted in knock-out or target-deficient animals	3
1.2.2. In vivo displacement experiment	4
1.3. TMDD in small molecules	4
1.3.1. Pharmacological targets located in tissues	5
1.3.2. Pharmacological targets located in plasma	11
1.4. TMDD in large molecules	12
1.4.1. Erythropoietin (Epo)	13
1.5. Pharmacometrics modeling	15
1.5.1. First general TMDD model	15
1.5.2. Population pharmacokinetic (popPK) model	16
1.5.3. Pharmacodynamics (PD) model	17
1.5.4. Physiologically based pharmacokinetic (PBPK) model	17
1.5.5. Quantitative system pharmacology (QSP) model	18
1.6. Significance & Novelty	19
1.6.1. Significance of recognizing TMDD for dose selection in drug development	19
1.6.2. Significance of Model-Informed Drug Development (MIDD)	20
1.6.3. Novelty of development of TMDD models for small molecules	21
1.7. Objectives	21

1.8. Outline of the thesis	21
CHAPTER 2: POPULATION TARGET-MEDIATED PHARMACOKINETICS/PHARMACODYNAMICS MODELING TO EVALUATE SPI-62 EXPOSURE AND HEPATIC 11β-HYDROXYSTEROID DEHYDROGENASE TYPE 1 (HSD-1) INHIBITION IN HEALTHY ADULTS.....	
2.1. Abstract	33
2.2. Introduction.....	34
2.3. Methods.....	36
2.3.1. Data source.....	36
2.3.2. Pharmacokinetics (PK) and pharmacodynamics (PD) modeling.....	38
2.4. Results.....	43
2.4.1. Observed data.....	43
2.4.2. Final model structure	43
2.4.3. Parameter estimates	44
2.4.4. Model evaluation	44
2.4.5. Simulation profiles.....	45
2.5. Discussion.....	46
2.6. Conclusions.....	49
CHAPTER 3: SIMULTANEOUS TARGET-MEDIATED DRUG DISPOSITION MODEL FOR TWO SMALL-MOLECULES COMPOUNDS COMPETING FOR THEIR PHARMACOLOGICAL TARGET: SOLUBLE EPOXIDE HYDROLASE	
3.1. Abstract	64
3.2. Introduction.....	65
3.3. Methods.....	67
3.3.1. Data source.....	67
3.3.2. Population pharmacokinetics modeling.....	68
3.3.3. Target occupancy simulation	73

3.4. Results.....	74
3.5. Discussion.....	77
3.6. Conclusions.....	81
CHAPTER 4: INCORPORATING PHARMACOLOGICAL TARGET-MEIDATED DRUG DISPOSITION IN A PHYSIOLOGICALLY BASED PHARMACOKINETIC MODEL OF LINAGLITIN IN RAT AND SCALE-UP TO HUMAN	98
4.1. Abstract.....	99
4.2. Introduction.....	100
4.3. Methods.....	103
4.3.1. Data source.....	103
4.3.2. Whole-body PBPK- TMDD model development in rats	104
4.3.3. PBPK-TMDD model scaling up to human	110
4.4. Results.....	113
4.4.1. Whole-body PBPK- TMDD model development in rats.....	113
4.4.2. PBPK-TMDD model scale-up to human	115
4.5. Discussion.....	117
4.6. Conclusions.....	122
CHAPTER 5: A QUANTITATIVE SYSTEM PHARMACOLOGY MODEL OF THE INCRETIN HORMONES GIP AND GLP-1, GLUCAGON, GLUCOSE, INSULIN AND THE SMALL MOLECULE DPP-4 INHIBITOR, LINAGLITIN	136
5.1. Abstract.....	137
5.2. Introduction.....	138
5.3. Methods.....	140
5.3.1. Data source.....	140
5.3.2. Model description	141
5.3.3. Model implementation.....	152
5.3.4. Model evaluation	152

5.4. Results.....	152
5.4.1. Final model structure	152
5.4.2. Goodness of model fitting.....	153
5.4.3. Parameter estimation.....	155
5.5. Discussion.....	157
5.6. Conclusions.....	161
CHAPTER 6: A FULL TARGET-MEDIATED DRUG DISPOSITION MODEL TO EXPLAIN THE CHANGES IN RECOMBINANT HUMAN ERYTHROPOIETIN (rhEpo) PHARMACOKINETICS IN PATIENTS WITH DIFFERENT BONE MARROW INTERTY FOLLOWING HEMATOPOIETIC TRANSPLANTATION	176
6.1. Abstract	177
6.2. Introduction.....	177
6.3. Methods.....	179
6.3.1. Data source.....	179
6.3.2. Population pharmacokinetics modeling	181
6.4. Results.....	186
6.4.1. Parameter estimation.....	186
6.4.2. Model fitting results	187
6.4.3. Dynamics of free receptors, drug-receptor complex and total receptors	188
6.4.4. Clearance vs. time profiles.....	188
6.5. Discussion.....	189
6.6. Conclusions.....	192
CHAPTER 7: SUMMARY AND CONCLUSIONS	208
REFERENCES	212

LIST OF TABLES

Table 2-1. Overview of SPI-62 PK and hepatic HSD-1 activity data included in the population PK-PD analysis.....	50
Table 2-2. Model development history for PD model.....	51
Table 2-3. Parameter estimation from the final PK-PD model.....	52
Table 3-1. Model development history.....	82
Table 3-2. Estimated parameters from the final TMDD model.....	84
Table 3-3. Parameters comparison between observed and predicted values.....	85
Table 4-1. Data source used for linagliptin whole-body PBPK-TMDD model development and model scale-up.....	123
Table 4-2. Physiological and kinetic parameters for modeling linagliptin pharmacokinetics and tissue distribution in rat.....	125
Table 4-3. Physiological and kinetic parameters for linagliptin PBPK simulations in human...	126
Table 4-4. Estimated parameters from the final whole-body PBPK-TMDD model of linagliptin.....	127
Table 4-5. DPP-4 expression level prediction in different rat tissues.....	128
Table 4-6. Comparison of model predicted vs literature reported pharmacokinetics parameters of linagliptin in human.	129
Table 5-1. The data source used for linagliptin QSP model integrating GIP, GLP-1, glucagon, glucose and insulin.....	163
Table 5-2. Model development history.....	165
Table 5-3. Final parameter estimations for the proposed QSP model of the incretin hormones GIP and GLP-1, glucagon, glucose, insulin and small-molecule DPP-4 inhibitor, linagliptin. .	166
Table 6-1. Summary of demographics of study participants.	194
Table 6-2. Model development history.....	195
Table 6-3. Estimated parameters from the final TMDD model for rhEpo.	197

LIST OF FIGURES

Figure 1-1. Comparison between linear and nonlinear PK.....	23
Figure 1-2. Dose-normalized linagliptin mean plasma concentration-time profiles after single intravenous bolus administration of linagliptin to (A) wild-type rats and (B) DPP-4-deficient rats.....	24
Figure 1-3. In vivo displacement assay of potent sEH inhibitors TPPU and TCPU conducted in mice.....	25
Figure 1-4. Effects of time and dose on V_{ss} , f_u , and CL for small molecule compounds with (A-C) saturable and specific binding in tissues and (D-F) saturable and specific binding in plasma, following single and multiple escalating IV bolus doses.....	26
Figure 1-5. Dose-normalized mean plasma concentration-time course of SPI-62 following single oral doses of SPI-62.	27
Figure 1-6. In a multiple ascending dose study of SPI-62 conducted in healthy adults, both dose-normalized (right panel) and original (left panel) mean plasma concentration-time profiles were examined following the initial and last dose.....	28
Figure 1-7. Urine 11β -hydroxysteroid dehydrogenase type 1 (11β -HSD1) activity from first morning void in healthy adults following 0.7 or 2 mg multiple doses. HSD1 activity, ratio of 5α tetrahydrocortisol + 5β tetrahydrocortisol to tetrahydrocortisone.	29
Figure 1-8. Representative plasma ^{125}I -rhEPO concentration-time profiles in a sheep before and after busulfan administration.....	30
Figure 1-9. Representative plasma ^{125}I -rhEPO concentration-time profiles in a sheep during 3 study phases (i.e., before phlebotomy, day 1 post-phlebotomy, and day 7 post-phlebotomy)....	31
Figure 2-1. Chemical structure of SPI-62, a potent and highly selective HSD-1 inhibitor.	53
Figure 2-2. Time courses of mean \pm SD observed hepatic HSD-1 inhibition and mean \pm SD of individual model- predicted SPI-62 plasma concentrations following 0.2, 0.4, 0.7, and 2 mg oral multiple doses of SPI-62.....	54
Figure 2-3. Log-scale scatter plot of the relationship between time-matched SPI-62 plasma concentrations predicted using the established TMDD model and the percentage of the observed baseline-corrected hepatic HSD-1 activity.....	55
Figure 2-4. Final TMDD model describing the pharmacokinetics and pharmacodynamics of SPI-62.	56

Figure 2-5. Time courses of mean observed (symbols) and population model-predicted (lines) SPI-62 plasma concentrations following 1, 3, 6, and 10 mg single oral doses of SPI-62; as well as 0.2, 0.4, 0.7, and 2 mg oral once-daily doses of SPI-62.....	57
Figure 2-6. Time courses of mean observed (symbols) and population model-predicted (lines) SPI-62 plasma concentrations and hepatic HSD-1 activity following 0.2, 0.4, 0.7, and 2 mg oral once-daily doses of SPI-62.....	58
Figure 2-7. Goodness-of-fit plots for the final model of SPI-62.....	59
Figure 2-8. Prediction-corrected visual predicted check (pcVPC) of SPI-62 PK and PD.....	60
Figure 2-9. The time course of median, 5 th and 95 th percentage of the simulated SPI-62 plasma concentration and hepatic HSD-1 activity in 1000 virtual subjects receiving 0.4, 1, 2, 3, 6, or 10 mg SPI-62 once-daily on Days 1-14.....	61
Figure 2-10. The time course of median, 5 th and 95 th percentage of the simulated SPI-62 plasma concentration and hepatic HSD-1 activity in 1000 virtual subjects receiving 3 mg loading dose on Day 1 followed by 0.4 mg or 1 mg SPI-62 once-daily on Days 2-14.....	62
Figure 3-1. Chemical structure of TPPU and TCPUs, two potent sEH inhibitors.....	86
Figure 3-2. Schematic flow diagram of animal study protocol in experiment 1 and experiment 2.....	87
Figure 3-3. Model structures in model development history.....	88
Figure 3-4. Final TMDD model describing the pharmacokinetics of TPPU and TCPUs.....	89
Figure 3-5. Time courses of mean observed (symbols) and model-predicted (lines) TPPU blood concentrations following 0.3 mg/kg TPPU at time 0 in (a) sEH knock-out mice without TCPUs displacement, (b) wild-type mice without TCPUs displacement, and (c) wild-type mice with 3 mg/kg TCPUs displacement at 168 hours.....	90
Figure 3-6. Time courses of the mean observed TPPU and TCPUs blood concentrations in wild-type mice following 0.3 mg/kg TPPU at time 0 and 0.3 mg/kg TCPUs at time 168 hours... ..	91
Figure 3-7. Time courses of mean observed TCPUs plasma concentrations following 0.3 mg/kg TPPU at time 0 in wild-type mice with 1,3, 10 mg/kg TCPUs displacement at 168 hours.....	92
Figure 3-8. Goodness fit plots for the final population pharmacokinetics modeling.....	93
Figure 3-9. Time courses of mean observed (symbols) and model-predicted (lines) TPPU blood concentrations following 0.3 mg/kg TPPU at time 0.	94

Figure 3-10. Time courses of mean observed (symbols) and model-predicted (lines) TPPU blood concentrations when wild-type mice received 0.3 mg/kg TPPU at time 0 and different doses of TCPU (1 or 10 mg/kg) at 168 hours (n = 6 per group).....	95
Figure 3-11. Time courses of mean observed (symbols) and model-predicted (lines) TCPU blood concentrations when wild-type mice received 0.3 mg/kg TPPU at time 0 and different doses of TCPU (1, 3, or 10 mg/kg) at 168 hours (n = 6 per group).....	96
Figure 3-12. Simulated time course of fraction of sEH occupied by TPPU when wild-type mice receive 0.3 mg/kg TPPU at time 0 and different doses of TCPU (1, 3, or 10 mg/kg) at 168 hours.....	97
Figure 4-1. Chemical structure of linagliptin, an approved DPP-4 inhibitor for the treatment of T2DM.	130
Figure 4-2. Schematic representation of the whole-body PBPK-TMDD model for linagliptin in rats.....	131
Figure 4-3. Goodness of fit plots for the final whole-body PBPK-TMDD model for linagliptin observed versus model-predicted concentrations in 14 different tissues in both wildtype and DPP4-deficient rat after a single 2 mg/kg intravenous dose.	132
Figure 4-4. Goodness of fit plots for the final whole-body PBPK-TMDD model for linagliptin observed versus model-predicted concentrations in 14 different tissues in wildtype rat after 2 mg/kg oral dose once daily for 14 days.....	133
Figure 4-5. Goodness of fit plots for the final whole-body PBPK-TMDD model for linagliptin observed versus model-predicted plasma concentrations in both wild type and DPP4-defficient rats.....	134
Figure 4-6. Observed (symbols) vs simulated (solid lines) linagliptin plasma-time concentration profiles in human adults.....	135
Figure 5-1. Model structure of base model.	168
Figure 5-2. Model structure of the final QSP model.	170
Figure 5-3. Time course of model predicted (lines) vs observed mean (symbols) linagliptin plasma concentrations in both healthy and T2DM patients.	172
Figure 5-4. Time course of model predicted (lines) vs observed mean (symbols) plasma DPP-4 inhibition (%) in both healthy and T2DM patients.	173
Figure 5-5.Goodness-of-fit plots for the final QSP model built for GLP-1, GIP, glucose, glucagon insulin and linagliptin. (A) Observed versus model-predicted linagliptin plasma concentrations. (B) Observed versus population-predicted plasma DPP-4 inhibition. (C) Observed versus population-predicted concentrations of GLP-1 (triangle), GIP (square), glucagon (diamond), and glucose (circle). Solid black lines represent lines of identity.	174

Figure 5-6. Time courses of mean observed (symbols) and population model-predicted (lines) concentrations of (A) glucose (B) GLP-1 (C) GIP and (D) GIP for T2DM patients after MTT test receiving 5 mg linagliptin (brown) and placebo (blue).	175
Figure 6-1. Structure of human erythropoietin, a 30.4 kDa glycoprotein hormone (PDB ID: 1BUY).....	198
Figure 6-2.Schematic flow diagram of clinical study 1 and study 2.	199
Figure 6-3.Final TMDD model structure describing the pharmacokinetics of rhEpo.	200
Figure 6-4. Exploratory test for covariates.	201
Figure 6-5.Time courses of mean ± SD observed (symbols) and model predicted (lines) rhEpo plasma concentrations following 10, 100 and 500 IU/kg doses in healthy subjects.	202
Figure 6-6.Time courses of mean ± SD observed (symbols) and model predicted (lines) rhEpo plasma concentrations following 10, 100 and 1000 IU/kg doses in patients undergoing four periods of hematopoietic transplantation.	203
Figure 6-7. Goodness fit plots for the final population pharmacokinetics modeling.	204
Figure 6-8. Prediction corrected visual predicted check (pcVPC) of plasma rhEpo data.	205
Figure 6-9. Graphs of simulated concentrations of free receptor (left), drug-receptor complex (middle) and total receptor (right) vs. time profiles.....	206
Figure 6-10.Graphs of simulated time course of receptor-mediated clearance and the ratio of receptor-mediated clearance to the total clearance in subjects.	207

CHAPTER 1: INTRODUCTION

1.1. Background

Nonlinear pharmacokinetics (PK) is time and/or dose-dependent PKs, which may arise from saturation in drug absorption, distribution, metabolism, and excretion (ADME) processes. As shown in **Figure 1-1**, when a drug exhibits nonlinear PK, non-superimposable drug plasma concentration-time profiles are observed when normalized to the dose. Drug plasma concentration at a given time and area under the curve (AUC) are no longer directly proportional to the dose administered.

Among the various sources of PK nonlinearity, target-mediated drug disposition (TMDD) is a unique one. TMDD concept was introduced by Dr. Levy in 1994 [1]. In most typical cases, TMDD occurs when a significant portion of a potent drug, relative to the administered dose, specifically binds to high-affinity, low-capacity pharmacological targets, leading to observable nonlinear PK profiles at corresponding dose levels. After administration, compounds rapidly and specifically bind to their high-affinity, low-capacity pharmacological targets. At low doses, a significant portion of the drug is sequestered by these targets in tissues, resulting in only a small fraction of the drug being observed in the systemic circulation. As the dose increases, the fraction of drug molecules binding to the targets relative to the total dose gradually decreases. The lower the dose, the greater the fraction of the drug relative to the total dose that is trapped by the tissues. This results in a higher degree of nonlinearity, and the resulting nonlinear pharmacokinetic (PK) profiles at corresponding dose levels reflect this phenomenon. If the dose is high enough to saturate all the pharmacological targets, the portion of the drug binding to the targets becomes negligible relative to the total dose. Consequently, linear PK characteristics are observed.

Starting in the early 2000s, the development and market introduction of protein-based drugs have experienced significant growth. The concept of TMDD has been widely applied to

comprehend the nonlinear PK exhibited by large molecules due to the specific binding of large molecules to their pharmacological targets [2-11].

However, it's important to note that TMDD isn't limited to large molecules alone. Small molecules can also exhibit TMDD, although it often goes undetected. In the context of small molecules, the saturable specific binding can be masked by nonspecific binding with various plasma proteins with higher binding capacities than the pharmacological targets. Consequently, the recognition of TMDD in small molecules has been limited and largely overlooked for several decades. Nevertheless, due to advancements in sensitive bioanalytical techniques and the development of more potent drugs, an increasing number of small molecules have been reported to exhibit TMDD [12-18]. Consequently, it becomes imperative to conduct research on TMDD's impact on the nonlinear PK of small molecules. Such investigations are essential for understanding the intricate relationship among dose, exposure, and response in compounds exhibiting nonlinear PK due to TMDD. Ultimately, this knowledge can greatly facilitate the dose selection in drug development process.

1.2. Experiments verifying if the compound's nonlinear PK is mediated by its pharmacological targets

To determine if the compound's nonlinear PK is mediated by its pharmacological target, the following are experiments that can be conducted.

1.2.1. PK experiments conducted in knock-out or target-deficient animals

A direct and effective method to ascertain if the nonlinear PK is a consequence of target binding is to evaluate and compare the PK of the compound in both wild-type and knock-out or target-deficient animals. In the absence of gene expression for the corresponding pharmacological

targets in the knock-out or target-deficient animals, the PK of the compound is expected to be linear. This expectation means that all dose-normalized concentration-time profiles should overlap in knock-out animals.

This approach has been successfully applied to compounds such as linagliptin (a small molecule DPP-4 inhibitor) [14]. As shown in **Figure 1-2**, in the case of linagliptin, linear PK was observed in DPP-4 deficient rats, contrasting the nonlinearity observed in wild-type rats [14].

1.2.2. In vivo displacement experiment

An additional method to confirm the impact of target binding on a drug's pharmacokinetics (PK) involves administering a displacer after the initial administration of the compound. The displacer is a potent compound with high affinity for the same pharmacological target as the first compound. When the first compound binds tightly to its target, the competitive displacer can displace the drug molecules from the target, leading to a second peak of the first compound in the PK profile.

An excellent example demonstrating the application of this method is the study of two potent soluble epoxide hydrolase (sEH) inhibitors, TCPU and TPPU [19]. As shown in **Figure 1-3**, after administering a 0.3 mg/kg dose of TPPU, a clear second peak is observed following the administration of 3 mg/kg TCPU at 168 hours in wild-type mice [19].

1.3. TMDD in small molecules

While compounds may possess all the necessary prerequisites for demonstrating TMDD, it's crucial to differentiate the underlying mechanisms between small-molecule and large-molecule compounds. In this section, we will specifically delve into TMDD in small molecules. Small

molecules can display unique pharmacokinetic (PK) characteristics, which are often influenced by the location of their pharmacological targets [20].

1.3.1. Pharmacological targets located in tissues

Many classes of small molecules have exhibited complex PK behaviors, primarily due to TMDD. This phenomenon arises from saturable binding with the drug's target, primarily located in tissues. Examples of such drugs encompass a wide range of compounds, including vitamin K epoxide reductase inhibitors (e.g., warfarin) [21], aldose reductase inhibitors (e.g., imirestat) [22], angiotensin-converting enzyme (ACE) inhibitors (e.g., enalaprilat) [23], small-molecule heat shock protein (HSP90) inhibitors [16], monoamine oxidase (MAO) inhibitors (e.g., selegiline) [24], endothelin-receptor antagonists (e.g., bosentan) [25], 11 β -hydroxysteroid dehydrogenase type I inhibitor (HSD-1) inhibitors (e.g., SPI-62, ABT-384) [15, 26], soluble epoxide hydrolase inhibitors (sEH) (e.g., TPPU and TCPU) [19], etc. **Figure 1-4** summarizes the common PK behaviors and the TMDD impact on key PK parameters observed in small molecules exhibiting TMDD with pharmacological targets in tissues.

In my pursuit of investigating the impact of target-mediated drug disposition (TMDD) on the pharmacokinetics (PK) of small molecules with pharmacological targets located in tissues, I have been involved in two research projects. The first project centers around a potent HSD-1 inhibitor called SPI-62, and the second project focuses on two sEH inhibitors, TPPU and TCPU.

In the first project, SPI-62 is currently advancing through our collaborative drug development efforts with Sparrow Pharmaceuticals, Inc. This compound is currently in Phase II clinical trials and has exhibited substantial and complicated nonlinear PK profiles in two Phase I clinical trials, primarily due to TMDD. This PK nonlinearity presents a considerable challenge in

understanding the intricate relationship between dosage, exposure, and response. To address this challenge, we have developed a quantitative TMDD model to guide dose selection.

My second research project centers around the two sEH inhibitors, TPPU and TCPU, which have pharmacological targets located in tissues. Through collaboration with scientists from Michigan State University and the University of California, Davis, we have identified distinctive PK patterns in several sEH inhibitors, with a particular focus on TPPU and TCPU. These compounds have demonstrated noteworthy TMDD characteristics. Our collaborators have successfully developed a range of potent sEH inhibitors, actively progressing them toward clinical trials. To facilitate the selection of appropriate doses for these sEH inhibitors, my second research project utilizes quantitative pharmacometrics modeling techniques to characterize the PK data for TPPU and TCPU in mice. This comprehensive analysis aims to provide valuable insights and support the dose selection process throughout the development of sEH inhibitors.

Next, details will be provided on how HSD-1 inhibitors and sEH inhibitors exhibit TMDD.

1.3.1.1. HSD-1 inhibitors

HSD-1 inhibitors have gained interest in drug development due to their ability to inhibit the enzyme HSD-1, responsible for converting inactive cortisone to active cortisol. HSD-1, is highly expressed in various tissues, including adipose, liver, and brain. HSD-1 inhibition can be utilized in the treatment of various unwanted symptoms caused by excess cortisol, such as Cushing's syndrome and autonomous cortisol secretion (ACS). Several small molecules that have reached clinical phases have been reported to exhibit TMDD due to specific binding with HSD-1, including MK-0916, BMS-823778, ABT-384, and SPI-62 [15, 26-28].

Nonlinear PK of SPI-62 (formally known as ASP3662) due to TMDD

SPI-62, also formally known as ASP3662, stands as a potent and highly selective inhibitor of HSD-1 with a molecular weight of 424.8 g/mol. It undergoes metabolism, primarily leading to the formation of its inactive metabolite, AS2570469, via a non-CYP enzyme. Additionally, it demonstrates high affinity to its pharmacological target (HSD-1). The binding affinity of SPI-62 to HSD-1 is reflected in its k_i value of 5.3 nM.

As shown in **Figure 1-5**, during the single ascending dose (SAD) study, where SPI-62 was administered in doses ranging from 1 to 10 mg to healthy subjects, concentrations at the 1 mg dose remained below the lower limit of quantification (LLOQ), rendering them undetectable in the systemic circulation. This observation aligns with the concept that a substantial portion of the dose promptly binds tightly to its target, resulting in minimal systemic exposure. Consequently, a low C_{max} becomes apparent. Nevertheless, with the escalation of SPI-62 dosage, the fraction of drug binding to its target decreased. This resulted in pharmacokinetics that displayed greater-than-dose-proportional characteristics (**Figure 1-5**), characterized by elevated C_{max} and AUC in comparison to the dose increment. Nonetheless, when doses of SPI-62 exceeded 6 mg in the SAD study, the PK became linear (**Figure 1-5**), likely due to target saturation, where only a negligible portion of the drug binds to the targets compared to the total dose.

As depicted in **Figure 1-6**, in the MAD study, the SPI-62 concentration following the initial low dose falls below the LLOQ. However, as illustrated in **Figure 1-7**, there is significant hepatic HSD-1 inhibition observed for doses of 0.7 and 2 mg on day 1. This provides direct evidence that a substantial portion of the administered molecules, relative to the dose, binds to the pharmacological target, namely, HSD-1, within the liver. On the other hand, even with low doses ranging from 0.4 to 2 mg, SPI-62 PK became linear after multiple doses, further supporting the

role of target saturation in generating linear pharmacokinetic behavior during a steady state **Figure 1-6**. With repeated doses, the drug from previous administrations may remain sequestered in tissues due to high-affinity binding with its pharmacological targets. Typically, the pharmacological targets involved in this process have a limited capacity for binding, which means they can only bind a limited number of drug molecules. Consequently, the fraction of subsequent repeated doses available for binding progressively decreased. With continuous drug administration, these targets eventually become saturated, reaching a point where further binding is constrained. At this juncture, the drug's pharmacokinetics shift from nonlinear to linear as the formation of drug-target complexes reaches its maximum capacity. This shift from nonlinear to linear drug PK with repeated dosing exemplifies a hallmark feature of TMDD.

TMDD is the class effect of HSD-1 inhibitors

Similar to SPI-62, ABT-384, MK-0916, and BMS-823778 exhibited comparable PK behaviors, including high accumulation ratios at low doses, more-than-dose proportional nonlinear PK at low single doses, and a transition to linear PK when the single dose exceeded specific levels for each compound (e.g., 8 mg, 6 mg, and 12 mg for ABT-384, MK-0916, and BMS-823778, respectively) in their respective SAD studies [15, 27, 28]. Additionally, HSD-1 inhibition by ABT-384 was significant (~90%) at the 1 mg dose level, indicating substantial trapping of ABT-384 in target sites in the tissues. However, after repeated doses, the PK of the last dose of ABT-384, MK-0916, and BMS-823778 was minimally affected by target binding due to target saturation caused by binding from the previous doses, leading to linear PK behavior.

Due to complicated nonlinear PK observed in HSD-1 inhibitors, the relationship among dose, exposure, and response is no longer intuitive and a mathematical modeling approach is required to facilitate dose selection.

1.3.1.2. sEH inhibitors

sEH is a promising pharmacological target with widespread expression in various tissues, including the liver, kidney, heart, lung, intestine, brain, and vasculature of mammals. Inhibition of sEH is of great interest as it prevents the conversion of epoxyeicosatrienoic acids (EETs) into less active dihydroxyeicosatrienoic acids (DHETs), thereby stabilizing EETs. EETs play crucial roles in diverse physiological processes, such as blood pressure regulation, pain and inflammation modulation, and heart function regulation [29].

Several highly potent and effective sEH inhibitors have been developed with promising preclinical drug efficacy profiles [30, 31]. These inhibitors hold immense potential in therapeutic applications for various medical conditions.

TPPU/TCPU complicated PK in human

The accidental discovery of TMDD characteristics in a pilot clinical trial conducted by Dr. Bruce D. Hammock revealed fascinating insights into the behavior of a series of sEH inhibitors in humans [32]. Among them, TPPU is a potent and highly selective sEH inhibitor and was reported to be mainly metabolized by CYP enzymes [33]. In this trial, TPPU was administered orally at a dose of 0.1 mg/kg once daily for nine days. Subsequently, two other sEH inhibitors, Syn 29 and Syn 1, were given at the same dose on days 25 and 31, respectively.

Surprisingly, the administration of Syn 29 resulted in the appearance of a second peak of TPPU, and similarly, a second peak of Syn 29 occurred after the administration of Syn 1. This observation strongly suggested that Syn 29 and TPPU compete for binding to their common pharmacological target, sEH. When Syn 29 was administered, it displaced TPPU that was previously bound to the target, causing TPPU to be released back into the systematic circulation and detected as a second peak. The same mechanism was observed with Syn 1.

TPPU/TCPU complicated PK in animals

After the pilot clinical trial, in vivo displacement studies were conducted in both wildtype mice and sEH knockout mice [19]. In these studies, 0.3 mg/kg TPPU was given to both groups of mice. The long terminal half-life of TPPU was only observed in wildtype mice, indicating tight binding of TPPU with sEH and a slow dissociation process of the TPPU-sEH complex in tissues. In another experiment, both types of mice received 0.3 mg/kg TPPU at the beginning of the study, followed by 3 mg/kg TCPU at 168 hours. The second peak of TPPU observed shortly after the TCPU dose occurred only in the wildtype mice (**Figure 1-3**) but not in the sEH knockout mice. This provided strong evidence that TPPU tightly binds with sEH before TCPU administration, and TCPU competes with TPPU to bind with sEH, leading to the release of bound TPPU back into the plasma.

TMDD is a class effect for sEH inhibitors

Indeed, the slow and tight binding affecting the pharmacokinetics of TPPU is not unique to TPPU alone but rather a class effect observed in sEH inhibitors. To further investigate this phenomenon, similar in vivo displacement experiments were conducted with other sEH inhibitors, including TUPS, TPAU, and APAU [19]. In these experiments, TCPU was administered as the displacer at 168 hours after the initial dosing of each sEH inhibitor in wildtype mice.

Consistent with the observations in the TPPU study, second peaks of TUPS, TPAU, and APAU were also observed after the administration of TCPU, indicating that these compounds, like TPPU, also bind tightly to the sEH target. The occurrence of the second peaks in all these sEH inhibitors further supports the notion that slow and tight binding is a class effect among sEH inhibitors, leading to the accumulation of drug molecules bound to the target over time.

Overall, the findings from these in vivo displacement experiments shed light on the complex behavior of sEH inhibitors and their interactions with the sEH target.

1.3.2. Pharmacological targets located in plasma

Figure 1-4 summarizes the common PK behaviors and the TMDD impact on key PK parameters observed in these drugs exhibiting TMDD with pharmacological targets in plasma.

Dipeptidyl peptidase-4 (DPP-4) is an enzyme that exists in both a membrane-bound form in tissues and a soluble form in plasma. Linagliptin is an approved DPP-4 inhibitor for the treatment of T2DM. The absolute bioavailability of linagliptin in humans is 30% [34]. It displays concentration-dependent protein binding in human [35]. The majority of linagliptin is excreted unchanged with minimal metabolism, primarily through biliary excretion [36].

Linagliptin exhibits TMDD characteristics, making it an ideal model compound for investigating TMDD in small molecules with targets in plasma. As demonstrated in Chapters 4 and 5, the wealth of available data, owing to linagliptin's approved status, offers an excellent opportunity to develop a comprehensive model for characterizing the pharmacokinetic (PK) and pharmacodynamic (PD) data of linagliptin. This includes examining the time course of concentrations of key biomarkers involved in glycemic control.

Linagliptin's PK is complex and nonlinear due to TMDD, while other DPP-4 inhibitors show limited nonlinearity, with vildagliptin demonstrating slight nonlinearity [37]. Linagliptin's high potency, reflected in its low k_i value (1 nM), sets it apart from other inhibitors [38]. Linagliptin exhibits concentration-dependent plasma protein binding, characterized by higher binding at low concentrations (approximately 90%) and reduced binding as concentrations increase (around 70-80%) [35]. At lower doses, a significant portion of linagliptin molecules binds to the pharmacological target located in plasma, resulting in a low fraction of unbound linagliptin

(f_u). As the dose escalates, the relative fraction of linagliptin molecules binding to the target decreases, causing an increase in the f_u of linagliptin in plasma. This behavior is observed in wildtype rats, mice, and humans but not in DPP-4 deficiency rats and mice, where binding remains constant [35].

The concentration-dependent protein binding of linagliptin in wildtype rats leads to less-than-dose proportional nonlinear plasma PK (**Figure 1-2**). The elimination of linagliptin primarily depend on the concentration of the free, unbound drug in plasma. At low doses, when only a small amount of linagliptin is present in the plasma in its unbound form, the apparent clearance is expected to be low. This is because only the free drug can undergo metabolic processes and be eliminated from the body. In contrast, at higher doses, the fraction of unbound linagliptin in plasma increases. This leads to a higher concentration of free drug molecules, resulting in an increase in apparent clearance. With more linagliptin available in its unbound form, the body can eliminate it, leading to a higher apparent clearance. The presence of both free and bound drugs can be observed in plasma, and as the dose increases, the clearance of the drug also increases. Consequently, less-than-dose proportional drug exposure is expected, leading to an increase in the apparent volume of distribution. However, DPP-4 deficiency rats do not exhibit this nonlinearity [14]. These findings are consistent with the observations from first-in-human clinical trials, where linagliptin exhibits less-than-dose proportional nonlinear PK [39].

1.4. TMDD in large molecules

Notably, many large molecules have been reported to demonstrate TMDD, including recombinant G-CSF products (filgrastim and pegfilgrastim) [40-43], erythropoietin (Epo) [44-46], thrombopoietin [7], interferon- β 1a [9, 11], various monoclonal antibodies [5, 6, 47-50], antibody-drug conjugates (ADC) [51-53], bispecific antibodies [4, 54, 55] and others. Among these research

endeavors, erythropoietin has been the focal point of comprehensive investigations led by Dr. Peter Veng-Pedersen's group at the University of Iowa College of Pharmacy. Their pioneering work has encompassed in-depth studies on the elimination mechanism of erythropoietin in animal models, alongside the execution of three clinical studies conducted at the University of Iowa Hospital and Clinics. The first clinical study focus on Epo PK in healthy adults. The second study centered on evaluating Epo PK in premature neonates. Drawing from these datasets, our group developed TMDD models characterizing erythropoietin PK in both healthy adults and premature neonates [56, 57].

In addition to those 2 studies, Dr. Peter Veng-Pedersen's group conducted another interesting clinical study that evaluated sequential PK in patients undergoing pre-bone marrow myeloablation to achieve complete engraftment [45]. One of my research projects is utilizing the data from this clinical trial to investigate Epo PK in these patients.

Next, details will be provided on Epo PK affected by TMDD.

1.4.1. Erythropoietin (Epo)

Epo, a 34-kDa glycoprotein hormone primarily secreted by the kidney, plays a critical role in erythrocyte production and oxygen homeostasis. Recombinant human erythropoietin (rhEpo), structurally similar to endogenous Epo, serves as a major therapeutic agent for treating anemia in patients with chronic renal failure and cancer patients undergoing chemotherapy [58-61]. rEpo is a large molecule with limited extravascular distribution. Upon binding to its receptor located in the bone marrow, it undergoes target-mediated elimination [62-67].

Upon binding to Epo receptors (EpoRs) present on bone marrow erythroid progenitors, both endogenous Epo secreted during hypoxia and exogenous rhEpo undergo internalization, followed by erythropoiesis and the production of red blood cells, vital for oxygen delivery to

tissues. Simultaneously, the internalized drug-target complex is degraded within the endosome. rhEpo elimination occurs primarily via EpoR in the bone marrow rather than the liver, and this has been substantiated through various intriguing mechanistic experiments conducted in animals and clinical trials involving humans [62-67]. For instance, Dr. Peter Veng-Pedersen's group conducted an experiment involving five adult sheep who received busulfan to induce bone marrow ablation, following which they assessed rhEpo PK both before and eight days after busulfan administration [44]. As illustrated in **Figure 1-8**, the mean rhEpo plasma concentration, normalized by the initial plasma concentration before bone marrow ablation, was lower than that on day eight after bone marrow ablation at different time points. Additionally, rhEPO PK revealed reductions in both plasma clearance (CL) and the volume of distribution at steady state (V_{ss}), accompanied by increases in both elimination half-life on day eight after bone marrow ablation in comparison to the pre-dose values.

The same group also conducted an assessment of rhEpo PK before phlebotomy, as well as on day 1 and day 7 post-phlebotomy [46]. As depicted in **Figure 1-9**, rhEpo elimination decreased on day 1 post-phlebotomy due to transient saturation of rhEpo receptors. However, on day 7, rhEpo elimination increased and surpassed the pre-phlebotomy levels. This increase was attributed to the expanded pool of progenitor cells, resulting in an increased number of Epo receptors in response to the need for restoring hemoglobin levels. To validate the existence of an expanded Epo receptor pool after phlebotomy and further confirm that the Epo receptor serves as the elimination pathway for Epo, Nalbant D et al. conducted experiments involving 11 newborn lambs who received rhEpo during phlebotomy-induced anemia [68]. After nine days, the investigators observed a significant increase in EpoR mRNA levels following phlebotomy. In tandem with the rising mRNA levels, rhEpo's clearance also exhibited a substantial increase. However, by day 28 post-phlebotomy, both

EpoR mRNA levels and rhEpo clearance had returned to baseline. These findings provide compelling evidence that the alterations in rhEpo's clearance are indeed attributed to significant changes in the EpoR pool.

Subsequent human studies have provided further substantiation of these findings. In a similar vein, the same research group conducted sequential pharmacokinetic (PK) investigations in patients undergoing pre-bone marrow myeloablation to achieve complete engraftment. These studies revealed notable reductions in rhEpo clearance and concurrent increases in terminal elimination half-life when EpoRs were ablated. This compelling evidence solidifies the existence of TMDD in humans [45].

Nevertheless, a notable knowledge gap persists in quantitatively understanding rhEpo PK in patients with diverse bone marrow conditions, which presents a significant hurdle in determining appropriate dosages for this distinct population. To address this challenge, this research endeavor offers a unique opportunity to conduct a thorough investigation of rhEpo PK in these patients. Additionally, leveraging quantitative modeling approaches, we can enhance our comprehension of the dynamic interplay between free and total Epo receptors and the Epo-Epo receptor complex.

1.5. Pharmacometrics modeling

1.5.1. First general TMDD model

The first general pharmacokinetics model for drugs with TMDD was introduced by Dr. Mager and Dr. Jusko in 2001 [69]. This model accounts for the intricate interactions between drug molecules and their pharmacological targets. Upon absorption from the depot, drug molecules can distribute between the central compartment and peripheral compartment and may undergo linear elimination or bind with the free receptors via a second-order rate constant, k_{on} , forming drug-

target complexes. These complexes can further follow two pathways: internalization and subsequent degradation at a first-order rate constant, k_{int} , or dissociation back into free drug and target with a first-order rate constant k_{off} . Additionally, the turnover of free receptors can be characterized by k_{syn} (synthesis rate constant) and k_{deg} (degradation rate constant).

It is essential to note that the internalization process and k_{int} are specific to large molecules as they can be internalized into cells upon binding to their targets. In the case of small molecules, internalization is not applicable, and the k_{int} term does not play a role in the model.

1.5.2. Population pharmacokinetic (popPK) model

Population pharmacokinetic (popPK) models are indispensable tools for evaluating drug exposure in diverse populations, accounting for both interindividual variability (IIV) and residual variability (RV) [70]. These models comprise three essential components. Firstly, the structural base PK model employs fixed pharmacokinetic parameters to outline the overall drug concentration-time trend within the population, forming the cornerstone for characterizing typical drug disposition. Secondly, the stochastic model, often depicted as a variance-covariance model, encompasses both IIV and RV components. IIV captures variations in drug PK among individuals, reflecting various factors influencing drug ADME within the population, while RV accounts for random variability and data measurement errors. Lastly, the covariate model explores the connection between specific covariates (e.g., body weight, age, gender) and IIVs, identifying factors contributing to variability. This enhances predictive accuracy and enables personalized drug dosing based on patient characteristics. By integrating these components, popPK models provide a comprehensive understanding of drug behavior in diverse patient populations [70]. This knowledge is important in drug development and clinical practice, facilitating the optimization of dosing strategies to accommodate the varying drug's PK observed in patients.

1.5.3. Pharmacodynamics (PD) model

PK/PD models play a critical role in understanding how drug concentrations relate to the observed pharmacological effects over time. When there is an immediate drug effect without any time delay, simple equations like the linear, E_{max} , or sigmoid E_{max} models are commonly used to describe the PK/PD relationship [71]. The linear model assumes a proportional relationship between drug concentration and effect, while the E_{max} model represents a maximum achievable effect at a specific drug concentration and the sigmoid E_{max} model introduces a sigmoidal shape to describe the exposure-response curve. Additionally, there might be a time delay between drug administration and the onset of drug effect, requiring the consideration of more complex models [72]. The indirect PK/PD model accounts for indirect drug effects through intermediary processes, such as feedback mechanisms.

1.5.4. Physiologically based pharmacokinetic (PBPK) model

Physiology-based pharmacokinetic (PBPK) models offer a comprehensive and mechanistic understanding of drug behavior in the body [73]. These models describe the complex processes of drug absorption, distribution, metabolism, and excretion within a compartmental framework, with each compartment representing a specific organ or tissue. These compartments are interconnected through organ blood flows. PBPK models distinguish themselves through their realism and mechanistic nature when compared to traditional one- or two-compartment models. They incorporate critical physiological parameters, such as blood flow and tissue composition, along with drug-specific data.

Another advantage of PBPK models lies in their flexibility to accommodate different physiological conditions across species. By adjusting parameters based on species-specific data, PBPK models enable accurate predictions of drug behavior in various preclinical species, bridging

the gap between animal studies and human pharmacokinetics. PBPK modeling has become an indispensable tool in drug development and regulatory submissions, aiding in dose selection and formulation optimization.

1.5.5. Quantitative system pharmacology (QSP) model

The concept of Quantitative Systems Pharmacology (QSP) modeling emerged from the convergence of pharmacology and systems biology, as defined in a National Institutes of Health (NIH) white paper in 2011 [74]. QSP models represent a paradigm shift from the traditional "one drug-one target-one pathway" approach in pharmacology towards a more holistic and network-centric view of biological systems. These models aim to establish a comprehensive, multiscale, and mechanistic mathematical framework that captures the intricate interactions between drugs, biochemical biomarkers, and pathways.

By integrating data from multiple sources and levels of biological organization, QSP models enable a deeper understanding of the complex dynamics underlying drug action and disease processes. They provide a means to investigate the effects of drugs in a more physiologically relevant context and facilitate clinical predictions to support decision-making in drug development and personalized medicine.

QSP models have the potential to revolutionize drug discovery and development by offering a quantitative and predictive platform for optimizing drug design, dose selection, and target identification. These models help bridge the gap between preclinical and clinical studies, enhancing our ability to translate experimental findings to human patients. As a result, QSP modeling holds great promise in advancing therapeutic strategies and improving patient outcomes across a wide range of therapeutic areas.

1.6. Significance & Novelty

1.6.1. Significance of recognizing TMDD for dose selection in drug development

As mentioned, TMDD occurs more frequently at low dose levels and is generally not a concern for drug safety. However, TMDD represents a unique PK nonlinearity influenced by PD, making a quantitative understanding of TMDD crucial for gaining valuable insights into target engagement.

In the case of SPI-62, as demonstrated in the SAD and MAD studies, significant and long-lasting pharmacodynamic effects (i.e., HSD-1 hepatic inhibition) can be observed even at low doses, such as 0.7 mg once-daily in the MAD study [26]. However, once the SAD dose of SPI-62 exceeds 6 mg, linear PK is evident [26]. Accurate interpretation of the observed low drug exposure and significant pharmacodynamic effect relies on a comprehensive understanding of TMDD. Additionally, target saturation is the underlying reason for the transition from nonlinear PK at low doses to linear PK at high doses. Understanding target occupancy provides critical information for optimizing dose selection to achieve high target engagement.

Furthermore, TMDD significantly impacts dose selection in first-in-human (FIH) clinical trials. During the transition from animal studies to human trials, the human equivalent dose (HED) is determined based on the no-observed-adverse-effect level (NOAEL) in the most sensitive animal species. A safety factor, typically higher than 10, is applied to derive the maximum recommended starting dose (MRSD) for the human trial. Hence, exceptionally low doses may be used in FIH clinical trials, and TMDD could potentially occur at these low dose levels.

At such low initial doses, the majority of the drug may become sequestered in tissues due to TMDD, leading to undetectable levels in plasma. Consequently, the drug's PK profile at these low doses might not be accurately observed. As a result, if a higher next dose, e.g., 2-3-fold, is

administered to increase drug exposure, it might have been perceived as safe under normal circumstances. However, due to the presence of TMDD, the drug exposure may exhibit a more-than-dose proportional increase, leading to unpredictable and potentially adverse responses without a comprehensive understanding of the underlying TMDD mechanism.

Therefore, a detailed understanding of TMDD is crucial during the dose selection process for first-in-human clinical trials to ensure safe and effective dosing regimens and to establish a meaningful relationship between drug exposure and response.

Small molecules demonstrating TMDD typically exhibit a prolonged terminal half-life because of the slow dissociation process of tightly bound drug-target complexes back into free drugs and targets. Consequently, the PK profile after the first dose may differ from that after subsequent doses. To ensure the accuracy and reliability of clinical trials, especially those involving crossover study designs like bioequivalence studies, it is essential to incorporate TMDD to calculate adequate washout periods.

1.6.2. Significance of Model-Informed Drug Development (MIDD)

The dose-exposure-response relationship for small molecules and large molecules exhibiting TMDD is complex and non-intuitive, posing challenges in dose selection during drug development. Model-informed drug development (MIDD) is an innovative approach that utilizes pharmacometrics models derived from preclinical and clinical data to inform decision-making throughout the drug development process. By employing these advanced modeling approaches in MIDD, the drug development process becomes more efficient and informed, leading to better dose selection and increased success rates in clinical trials. The integration of pharmacometrics models allows researchers and clinicians to optimize drug dosing, anticipate drug behavior in different patient populations, and enhance drug efficacy and safety profiles. Ultimately, MIDD empowers

the pharmaceutical industry to make data-driven decisions, accelerating the development of novel therapeutics and improving patient outcomes.

1.6.3. Novelty of development of TMDD models for small molecules

While small molecules are known to exhibit TMDD, the literature on TMDD models for small molecules is limited. This may be attributed to the complexity and challenges in characterizing TMDD in small-molecule PK. However, as research in this area continues to evolve, more comprehensive models and insights into TMDD for small molecules are expected to emerge, offering valuable contributions to drug development and optimization.

1.7. Objectives

The thesis aims to develop pharmacometrics models to characterize the PK-PD of (1) small molecules whose pharmacological targets are located in tissues, (2) small molecules whose pharmacological targets are located in plasma, and (3) large molecules, thereby facilitating drug development.

1.8. Outline of the thesis

In the pursuit of these defined objectives, the thesis follows a structured approach that includes the development of models for several small molecules (namely, TPPU/TCPU, SPI-62, linagliptin) and one large molecule, rhEpo. For the first objective, Chapter 2 focused on SPI-62, a potent HSD-1 inhibitor undergoing Phase II clinical trials. A TMDD model was developed to elucidate the nonlinear PK/pharmacodynamics (PD) relationship observed in Phase I clinical trials with healthy adults, providing a foundation for dose selection in current and future clinical studies. Chapter 3 focuses on two sEH inhibitors, TPPU and TCPU, which exhibit pronounced TMDD

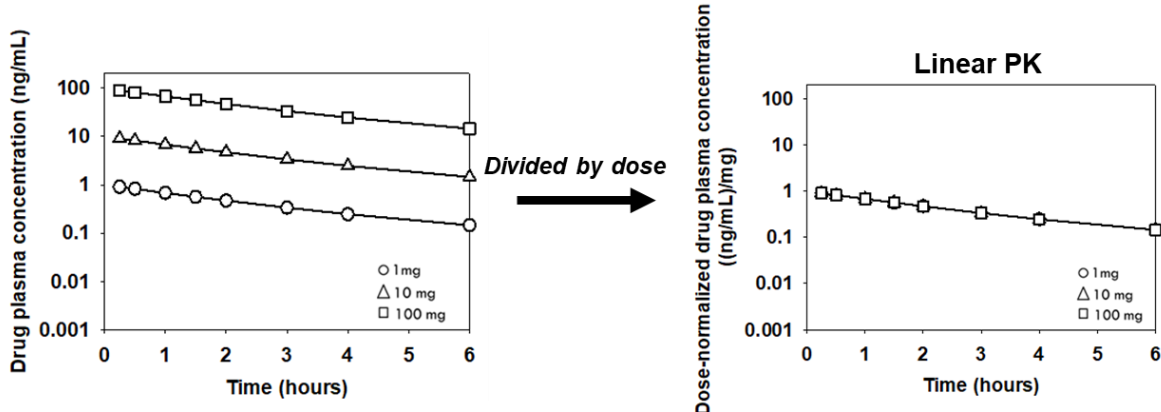
characteristics due to their competitive binding with their pharmacological target in tissues. An interactive TMDD model was established to concurrently characterize TPPU and TCPU PK and perform predictions for target occupancy.

Shifting to the second objective, Chapter 4 highlighted Linagliptin, an FDA-approved DPP-4 inhibitor with pronounced TMDD affecting both tissue and plasma PK. To facilitate dose selection, a comprehensive Whole-Body Physiologically-Based Pharmacokinetic (WB-PBPK) model was built in rats, with human extrapolation aided by Linagliptin as a model compound. In Chapter 5, a Quantitative Systems Pharmacology (QSP) model was built to quantify Linagliptin's impact on two incretins, GLP-1 and GIP, alongside influential factors (e.g., glucose, glucagon and insulin) in glycemic control.

For the third objective, the focus of Chapter 6 is recombinant human erythropoietin (rhEpo), a crucial therapy for anemia, has undergone extensive investigation, uncovering evidence of TMDD in both animal and human studies. However, a significant knowledge gap exists in comprehending erythropoietin's PK in patients with varying bone marrow conditions, posing a substantial obstacle in dose selection for this unique population. This project developed a comprehensive TMDD model to quantitatively characterize rhEpo PK data in patients undergoing varying stages of bone marrow ablation following hematopoietic transplantation.

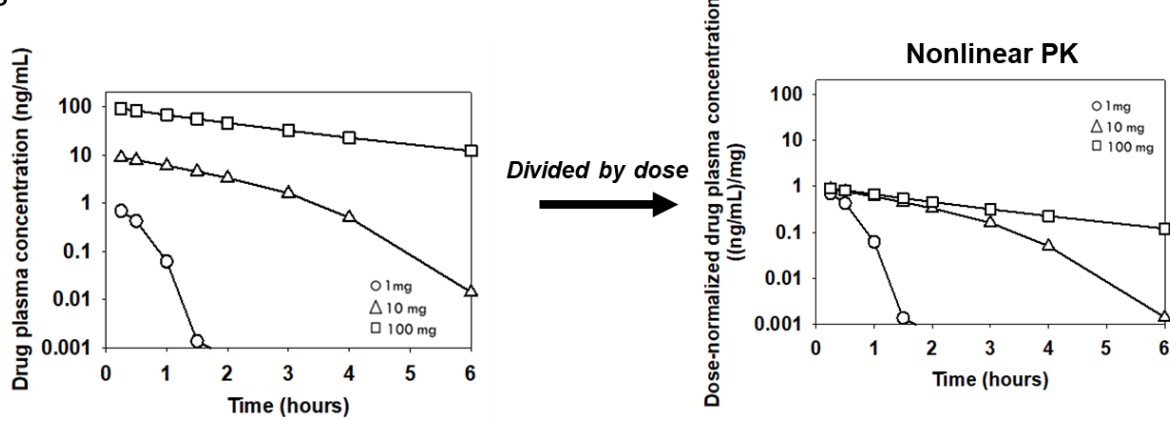
These models provide a quantitative framework for characterizing the nonlinear PK and PD of several small molecules, including SPI-62, Linagliptin, TPPU/TCPU, and the large molecule erythropoietin. This quantitative understanding serves as a guiding compass throughout the drug development journey, from preclinical phases through clinical trials to post-clinical stages, embodying the essence of MIDD.

A



Linear PK

B



Nonlinear PK

Figure 1-1. Comparison between linear and nonlinear PK.

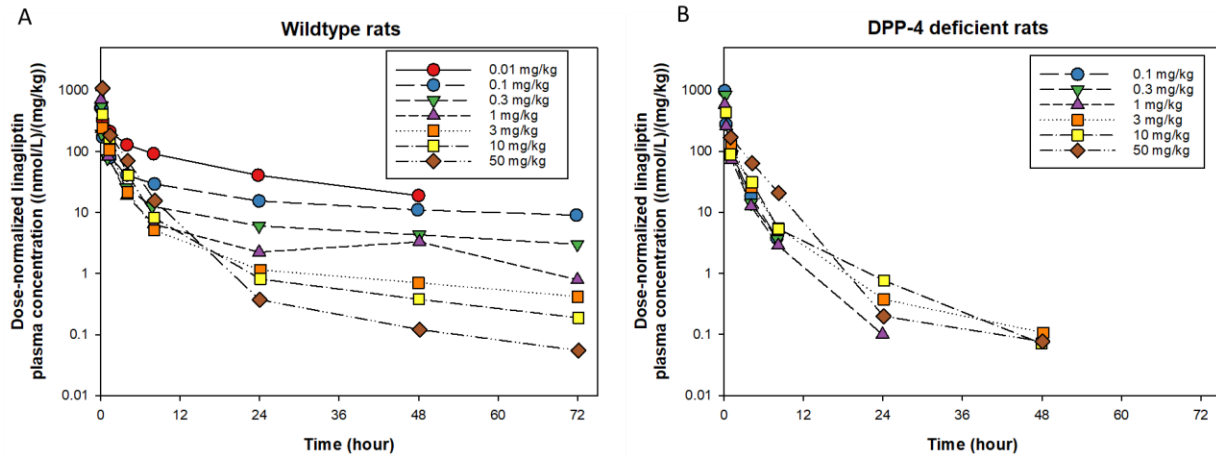


Figure 1-2. Dose-normalized linagliptin mean plasma concentration-time profiles after single intravenous bolus administration of linagliptin to (A) wild-type rats and (B) DPP-4-deficient rats.

Linagliptin exhibited significant nonlinearity in its pharmacokinetics when administered to wild-type rats, whereas it displayed linear pharmacokinetics in DPP-4-deficient rats. This figure is adapted from reference [14].

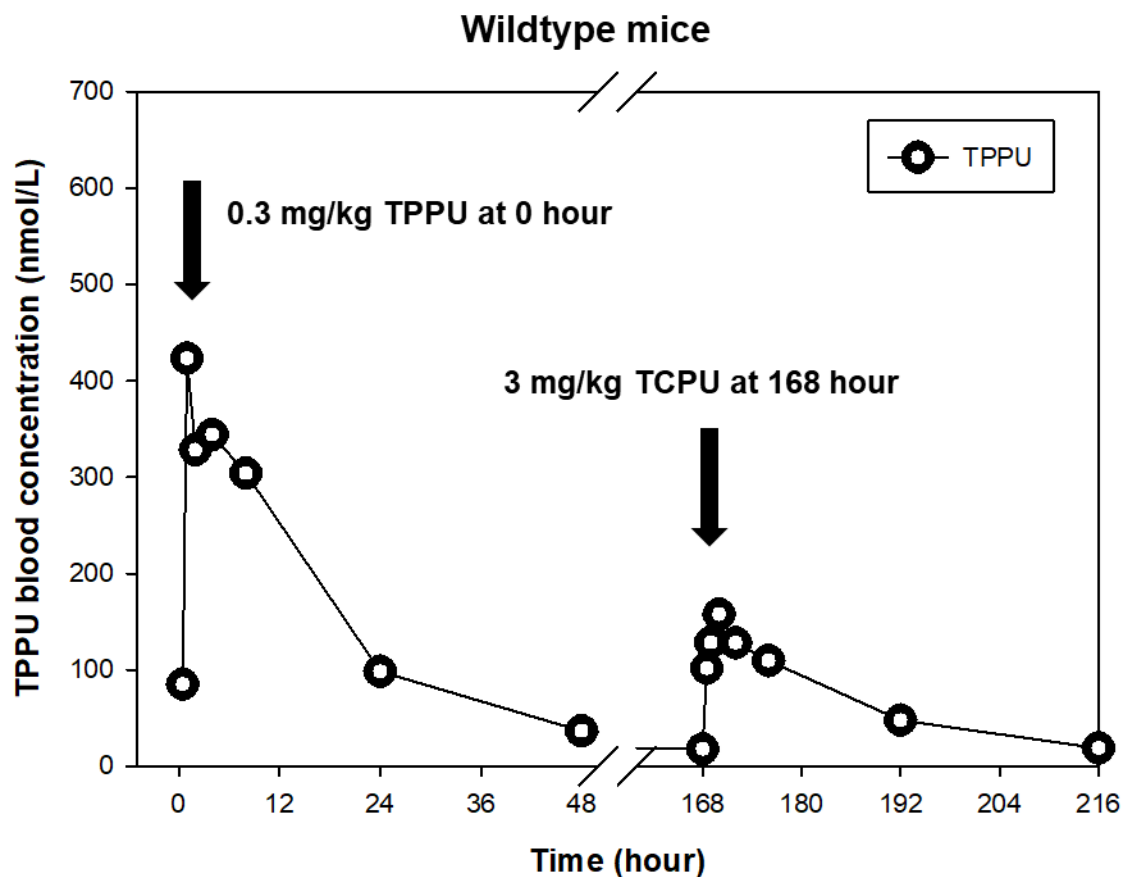


Figure 1-3. In vivo displacement assay of potent sEH inhibitors TPPU and TCPU conducted in mice.

TPPU, the compound under investigation, was administered at a dose of 0.3 mg/kg via subcutaneous injection at time point 0. Subsequently, TCPU, the displacing agent, was introduced at a dose of 3 mg/kg through subcutaneous injection at the 168-hour mark. The concentrations of TPPU were monitored within the timeframe of 0 to 216 hours. Notably, the second peak in TPPU levels was observed immediately following the administration of TCPU, suggesting the displacement of TPPU from its binding site on the sEH. This figure is adapted from reference [19].

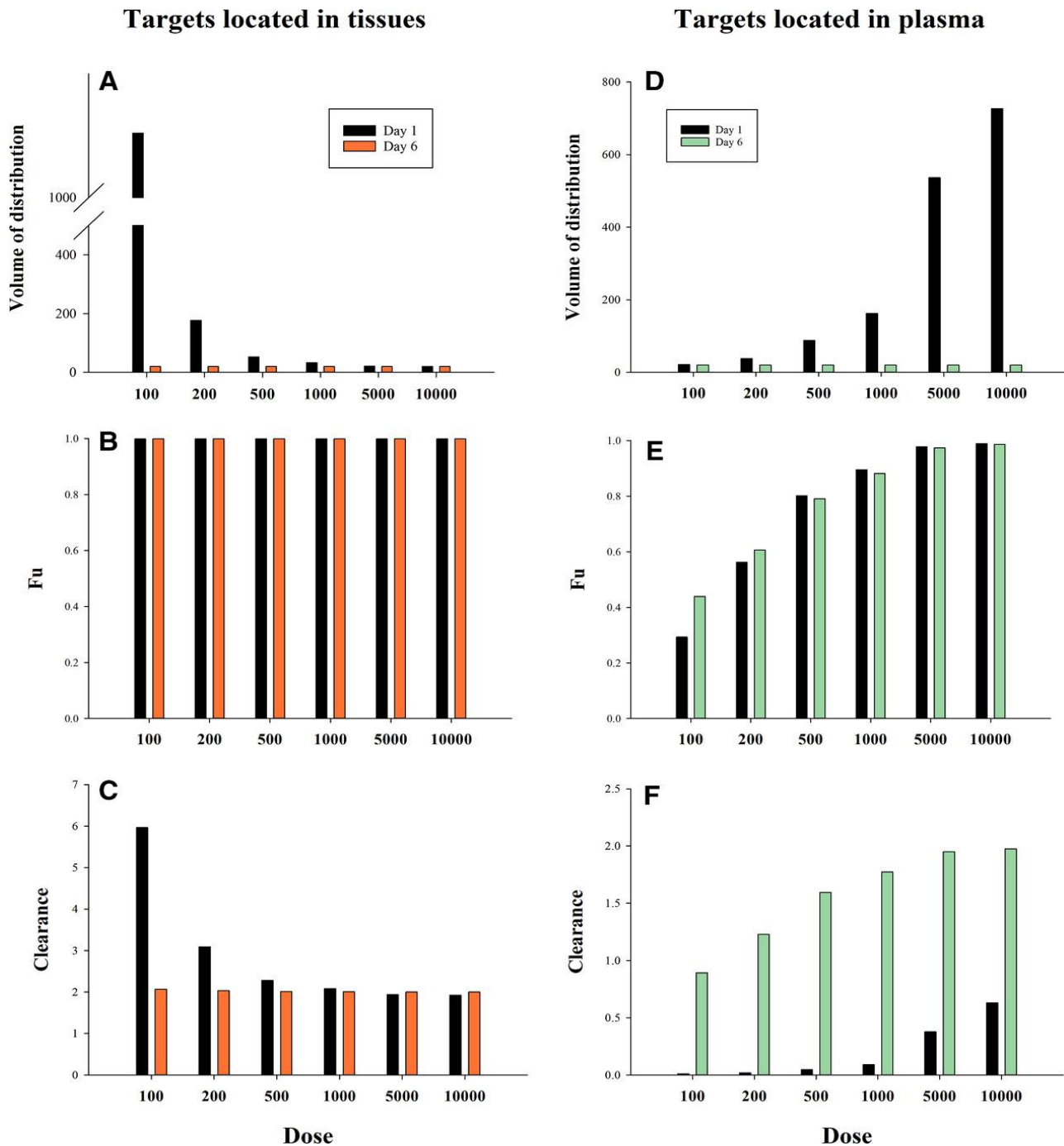


Figure 1-4. Effects of time and dose on V_{ss} , f_u , and CL for small molecule compounds with (A-C) saturable and specific binding in tissues and (D-F) saturable and specific binding in plasma, following single and multiple escalating IV bolus doses.

This figure is reused from reference [20].

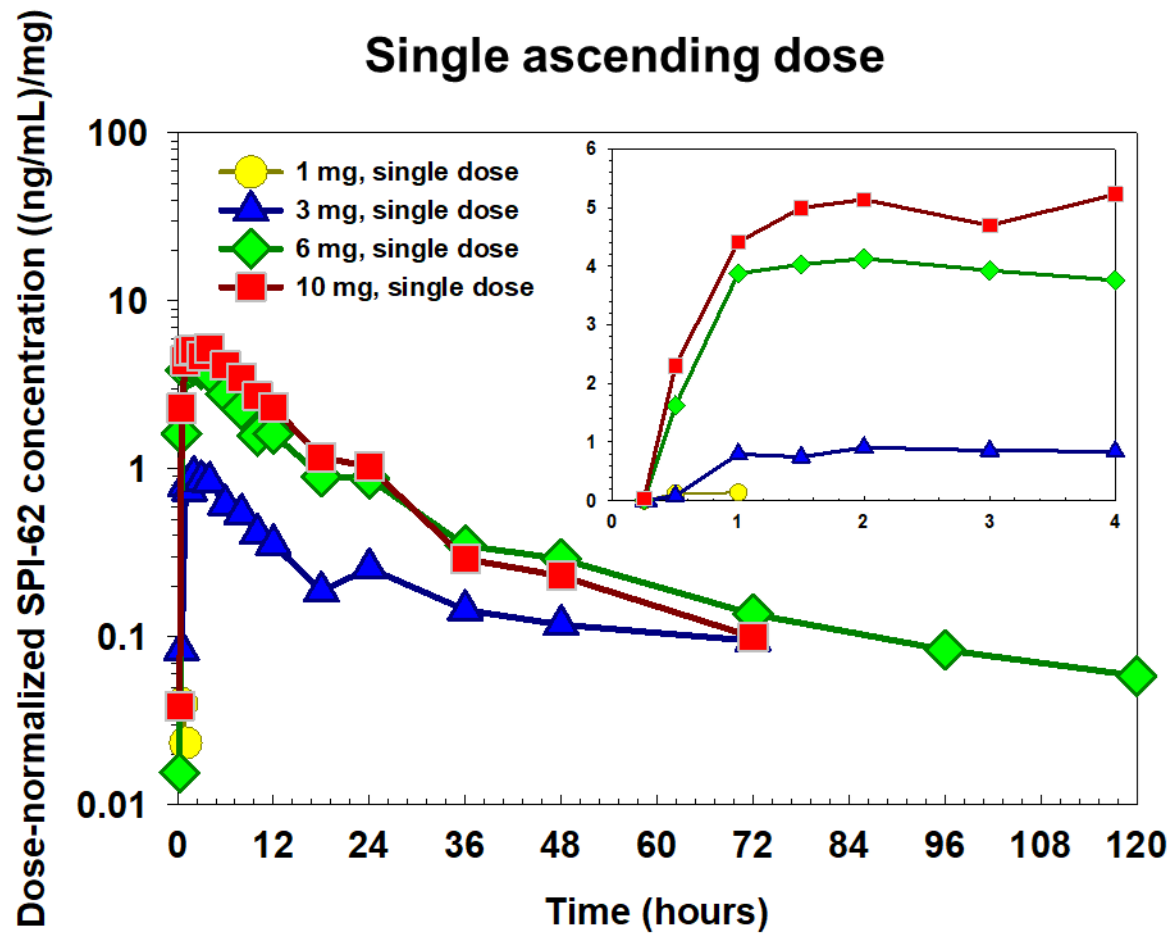


Figure 1-5. Dose-normalized mean plasma concentration-time course of SPI-62 following single oral doses of SPI-62.

This figure is adapted from reference [26].

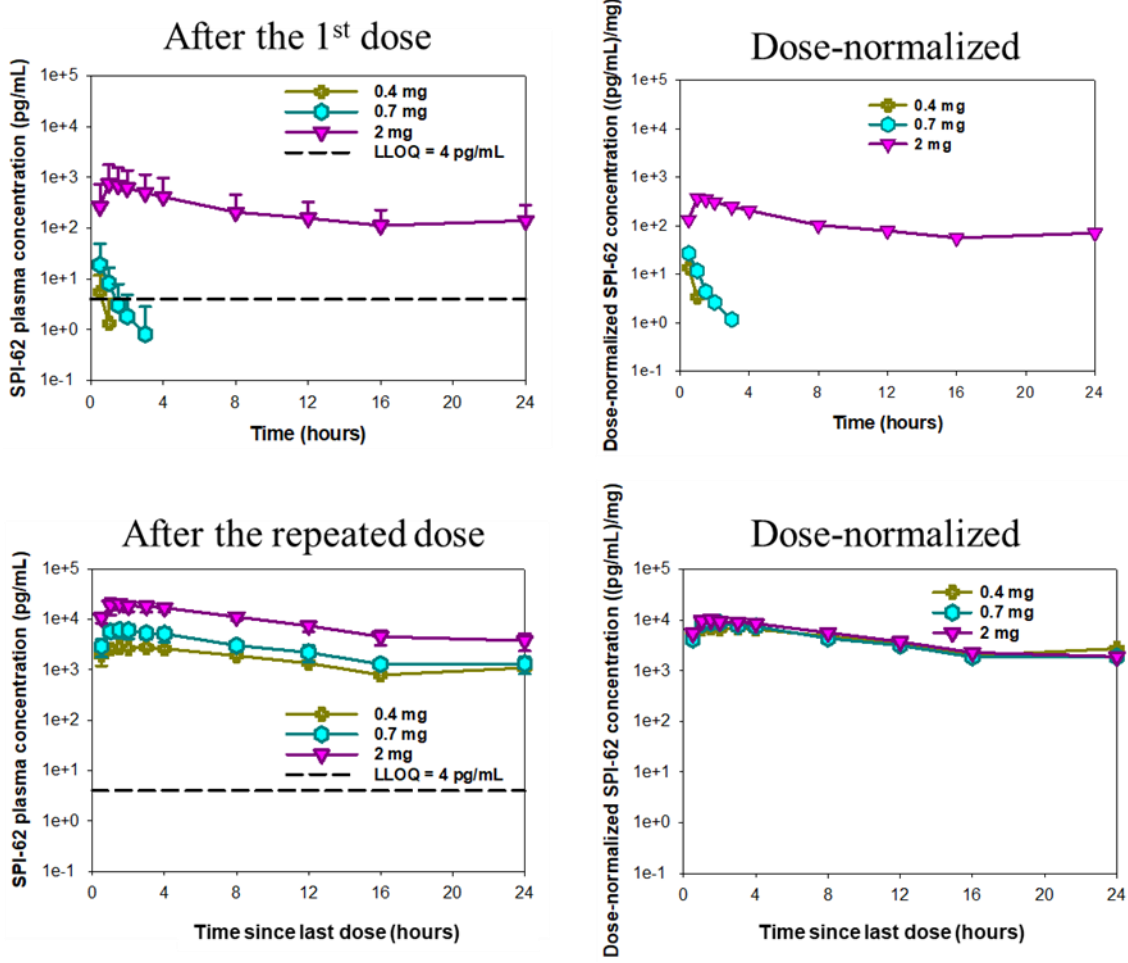


Figure 1-6. In a multiple ascending dose study of SPI-62 conducted in healthy adults, both dose-normalized (right panel) and original (left panel) mean plasma concentration-time profiles were examined following the initial and last dose.

This figure is adapted from reference [26].

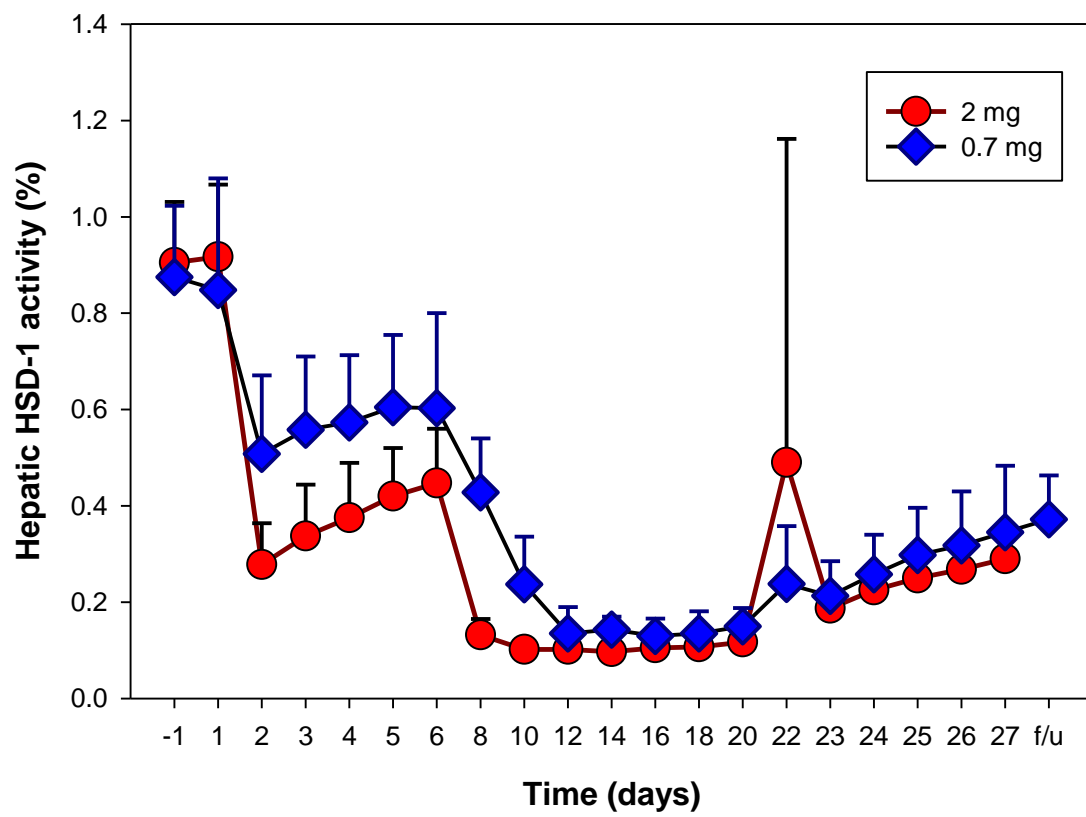


Figure 1-7. Urine 11 β -hydroxysteroid dehydrogenase type 1 (11 β -HSD1) activity from first morning void in healthy adults following 0.7 or 2 mg multiple doses. HSD1 activity, ratio of 5 α tetrahydrocortisol + 5 β tetrahydrocortisol to tetrahydrocortisone.

This figure is adapted from reference [26].

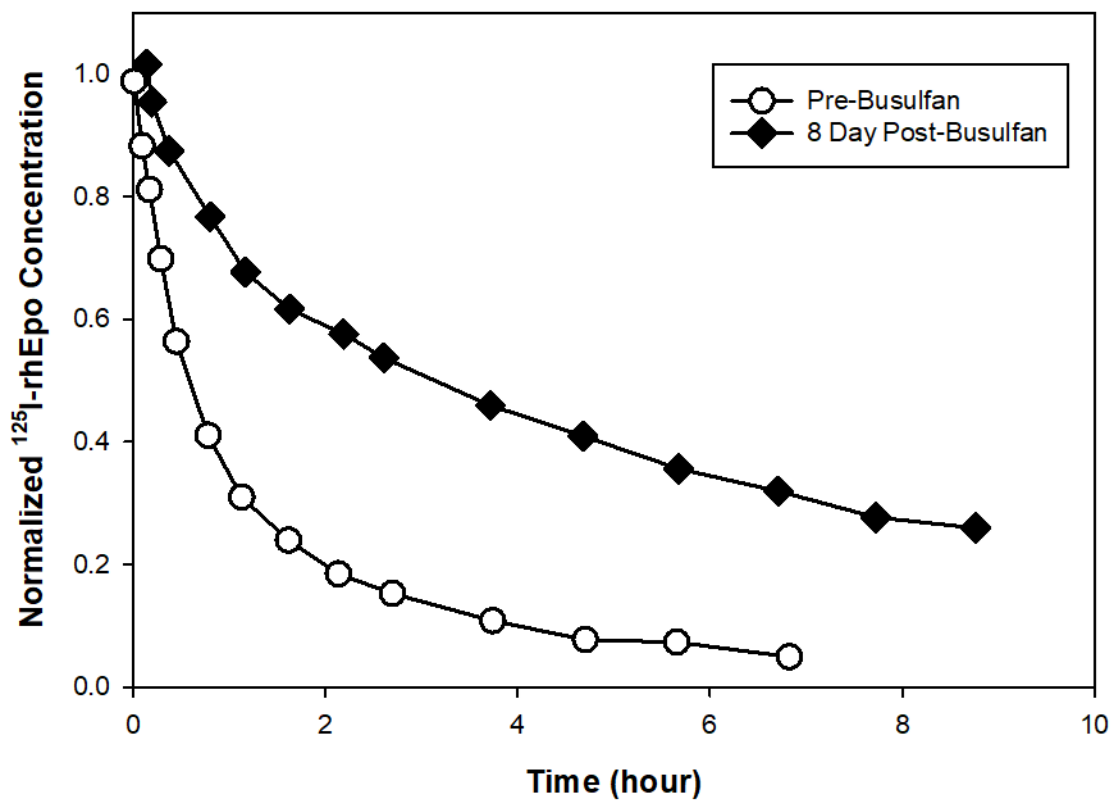


Figure 1-8. Representative plasma ^{125}I -rhEPO concentration-time profiles in a sheep before and after busulfan administration.

This figure is adapted from reference [44].

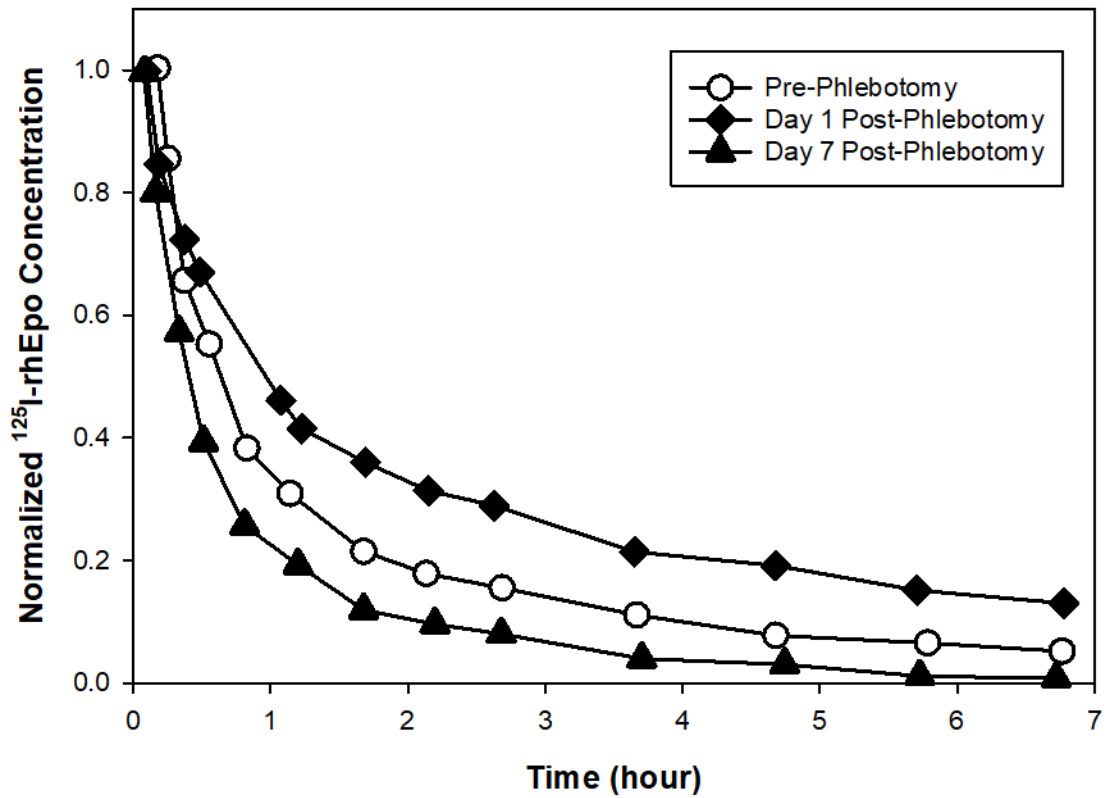


Figure 1-9. Representative plasma ^{125}I -rhEPO concentration-time profiles in a sheep during 3 study phases (i.e., before phlebotomy, day 1 post-phlebotomy, and day 7 post-phlebotomy).

This figure is adapted from reference [46].

**CHAPTER 2: POPULATION TARGET-MEDIATED
PHARMACOKINETICS/PHARMACODYNAMICS MODELING TO EVALUATE SPI-
62 EXPOSURE AND HEPATIC 11 β -HYDROXYSTEROID DEHYDROGENASE TYPE 1
(HSD-1) INHIBITION IN HEALTHY ADULTS**

Most of this chapter has been published in Clinical Pharmacokinetics.

(Wu N, Katz DA, An G. *Clin Pharmacokinet*. 2023 Sep;62(9):1275-1288.)

2.1. Abstract

SPI-62 is a small-molecule 11 β -hydroxysteroid dehydrogenase type 1 (HSD-1) inhibitor exhibiting complicated nonlinear pharmacokinetics (PK) in human. Previously, we developed a target-mediated drug disposition (TMDD) model to characterize the substantial nonlinear PK of SPI-62.

The aim of the current analysis was to perform population PK/PD analysis to further link SPI-62 exposure (i.e., PK) with its response (i.e., inhibition of hepatic HSD-1 activity) to gain a quantitative understanding of the SPI-62 dose-exposure-response relationship.

PK and PD data from the first-in-human (FIH) clinical trials, including single ascending dose (SAD) and multiple ascending dose (MAD) studies, were used for model development. During the model development process, the final model selection was based on biological and physiological plausibility, goodness-of-fit plots, stability of parameter estimates, and objective function value. The nonlinear-mixed effect modeling (NONMEM) software was used for both the implementation of the PK/PD model and model simulation. SPI-62 plasma levels and hepatic HSD-1 inhibition over time following various dose regimens were simulated.

The final model was a two-compartment TMDD model component for SPI-62 and an inhibitory Imax model component for hepatic HSD-1 activity. The TMDD-hepatic PD model that we established adequately characterized all remarkable PK and PD behaviors of SPI-62, such as extremely low plasma exposures following the first low doses, nonlinear PK turned into linear PK after repeated low doses, and substantial and long-lasting hepatic HSD-1 inhibition following low doses. SPI-62 was estimated to bind to the target with a second-order association rate constant (Kon) of 8.43 nM⁻¹ h⁻¹ and first-order dissociation rate constant (Koff) value of 0.229 h⁻¹, indicating that SPI-62 binds rapidly to, and dissociates slowly from, its pharmacological target.

The estimated target capacity (R_{tot}) of 5460 nmol corresponds to approximately 2.2 mg of SPI-62, which comports well with the dose range in which PK nonlinearity is prominent. Model simulation results reveal that a 6 mg once-daily regimen can lead to long-lasting and substantial hepatic HSD-1 inhibition.

A population TMDD-PD model that explains SPI-62 nonlinear PK and hepatic HSD-1 inhibition following different dose regimens in healthy adults was successfully established. Our simulation results provide a solid foundation for model-informed development of SPI-62.

2.2. Introduction

The 11β -hydroxysteroid dehydrogenases (HSDs) regulate the intracellular levels of glucocorticoids. There are two isoforms: HSD-1 converts inactive cortisone to active cortisol, and HSD-2 converts cortisol to cortisone [75]. HSD-2 protects mineralocorticoid-sensitive tissues (e.g., distal tubule of the kidney) from acute cortisol toxicity. HSD-1 is abundantly expressed in tissues in which glucocorticoid signaling serves physiological functions (e.g., liver, fat, muscle, skin, eye, and brain) at normal levels and can have pathological effects when in excess. In addition to endogenous glucocorticoids, HSDs act similarly on the glucocorticoid medicines by interconverting their inactive (e.g., prednisone) and active (e.g., prednisolone) forms [76]. Chronic elevation of the endogenous glucocorticoid cortisol can result in Cushing's syndrome and autonomous cortisol secretion (ACS), conditions associated with excess mortality and serious morbidity including diabetes, cardiovascular disease, obesity, osteoporosis, mood disorders, and cognitive impairments [77-79]. Glucocorticoid medicines are associated with approximately 10% of all drug adverse events including those that result in hospitalization [80]. The important role of HSD-1 in the biology of cortisol and the corticosteroid medicines makes it an attractive therapeutic target for the diseases and drug side effects mentioned above [81, 82].

SPI-62 (formerly known as ASP3662, CAS# 1204178-50-6), is a potent and selective small-molecule HSD-1 inhibitor (as shown in **Figure 2-1**) with high affinity against human HSD-1 and minimal activity on HSD-2 [26]. Currently SPI-62 is in clinical development for Cushing's syndrome and ACS, and as adjunctive therapy to prednisolone in patients with polymyalgia rheumatica. As part of the clinical development of SPI-62, the safety, pharmacokinetics (PK) and pharmacodynamics (PD) of SPI-62 in healthy adults were evaluated in a single ascending dose (SAD) trial as well as a multiple ascending dose (MAD) trial [26]. The PK results from these two Phase 1 clinical trials showed that SPI-62 has substantial and complex nonlinear PK in humans, which appeared to be caused by the specific and saturable binding of a highly potent small molecule, SPI-62, to its low-capacity pharmacological target HSD-1, known as TMDD [1, 2]. The key nonlinear PK behaviors of SPI-62 are: 1) following single doses, SPI-62 demonstrated linear PK at high doses but pronounced nonlinear PK at low doses; 2) following multiple doses, nonlinear PK observed following first low doses turned into linear PK with unusually high accumulation ratios for low doses that cannot be explained by SPI-62's elimination half-life [26]. Based on the PK data from SAD and MAD trials, we established a TMDD model to characterize SPI-62 nonlinear PK in humans [83].

In MAD trial low dose cohorts, in addition to PK, exploratory PD assessments were also performed. Cortisol and cortisone are converted by sequential action of 5α - and 5β -steroid reductases followed by 3-steroid reductase to form tetrahydrocortisol, allotetrahydrocortisol, and tetrahydrocortisone that are excreted in urine [84, 85]. The urinary ratio of cortisol metabolites (tetrahydrocortisol + allotetrahydrocortisol) to cortisone metabolite (tetrahydrocortisone) is commonly referred as urinary HSD-1 ratio since it represents HSD-1 inhibition in liver. The urinary HSD-1 ratio data showed clearly that substantial HSD-1 inhibition was observed even after

the first dose of 0.7 mg [26]. After repeated doses, full HSD-1 inhibition was achieved by all dose levels evaluated (0.2 mg with a 3 mg loading dose, 0.4 mg, 0.7 mg, and 2 mg). In addition, HSD-1 inhibition was long lasting, as reflected by the incomplete return of the urinary HSD-1 ratio to baseline approximately 16 days after the last dose even with the lowest dose tested, 0.2 mg[26]. The data of the time course of the HSD-1 activity are informative and valuable – they serve not only as strong evidence of HSD-1 mediated nonlinear PK of SPI-62 (i.e., pharmacological TMDD) but also provide opportunity to evaluate quantitatively the exposure-response relationship between SPI-62 and hepatic HSD-1 inhibition. As noted earlier, we previously developed a TMDD model to characterize the relationship between dose and exposure of SPI-62 in human. The aim of the current analysis was to perform population PK-PD analysis to further link SPI-62 exposure (i.e., PK) with its response (i.e., inhibition of hepatic HSD-1 activity) using the pooled PK data from the SAD and MAD trials and PD data from the MAD trial.

2.3. Methods

2.3.1. Data source

The modeling work was conducted based on the key PK and PD data from two Phase I clinical trials (SAD and MAD) conducted in healthy adults [26]. The data included in the analysis are summarized in **Table 2-1** and briefly described below.

In the SAD trial, 48 subjects were randomized into six dose cohorts: 1, 3, 6, 10, 30, and 60 mg. In each cohort, subjects were randomized to receive either placebo (n=2) or SPI-62 oral administration (n=6). Data used for the model development were from 1, 3, 6, and 10 mg cohorts. For PK evaluation, serial blood samples were collected at 0.5, 1, 1.5, 2, 3, 4, 6, 8, 10, 12, 18, 24, 36, 48, and 72 hours after oral dose administration for the 1, 3, and 10 mg cohorts, while two

additional blood samples were collected at 96 and 120 hours after dose administration for the 6 mg cohort. SPI-62 plasma concentrations were determined by a validated high-performance liquid chromatography with tandem mass spectrometry methods. The lower limit of quantification (LLOQ) was 0.1 ng/mL [26].

The MAD trial investigated high oral doses (10, 20, and 50 mg) and low oral doses (0.2, 0.4, 0.7, and 2 mg) separately. As high dose data were not included in our analysis, here we only describe the low dose design. Four subjects received a 3 mg loading dose on Day 1 and then 0.2 mg QD doses on Days 2-14. Four subjects received 0.4 mg QD doses on Days 1-14. Twelve subjects (six each at 0.7 and 2 mg doses) received a single dose of SPI-62 on Day 1, followed by a 6-day washout period, and then QD doses on Days 7-20. For the PK assessment, serial blood samples were obtained at 0.5, 1, 1.5, 2, 3, 4, 8, 12, 16, and 24 hours after the first dose, as well as 0.5, 1, 1.5, 2, 3, 4, 8, 12, 16, 24, 48, 72, 96, 120, 144 and 168 hours after the last dose. Six additional PK samples were collected at 36, 48, 72, 96, 120, 144 hours after the first dose of 0.7 or 2 mg. SPI-62 plasma concentrations were determined by a validated high-performance liquid chromatography with tandem mass spectrometry (LC/MS/MS) assay. The LLOQ was 4 pg/mL[26]. For PD assessment, urine samples from the first-morning void were collected at pre-dose, and on Days 1, 2, 3, 4, 5, 6, 8, 10, 12, 14, 16, 18, 20, 22, 23, 24, 25, 26, and 27 from subjects dosed with 0.7 or 2 mg SPI-62. Urine samples from the first morning void were collected at pre-dose, and on Days 1, 8, 10, 12, 14, 16, 18, 20, 21 from subjects dosed with 0.2 or 0.4 mg SPI-62 [26]. First-morning urine void samples were collected before the morning SPI-62 dose. The urine samples for steroid analysis were analyzed using validated liquid chromatographic-tandem mass spectrometric methods [26, 86]. The hepatic activity of HSD-1 was calculated as the urinary ratio of (tetrahydrocortisol + allotetrahydrocortisol) / tetrahydrocortisone.

In the population modeling analysis, there were 996 plasma concentrations, with 222 below LLOQ, and 279 observed baseline-corrected hepatic HSD-1 activity (%) data, with one outlier excluded. The PK and PD data were from 44 healthy subjects, including 24 subjects from the SAD study and 20 subjects from the low dose cohort of the MAD study. SPI-62 BLQ data were replaced with LLOQ/2 considering it was shown to provide the best model fitting [83].

2.3.2. Pharmacokinetics (PK) and pharmacodynamics (PD) modeling

Simultaneous pharmacokinetics and pharmacodynamics modeling was performed using the nonlinear mixed effect modeling approach with NONMEM (Version 7.4.3; Icon Development Solutions, Ellicott City, Maryland) using the first-order conditional estimation method with interaction (FOCEI) and a user-defined subroutine (ADVAN13). Simulations were performed in NONMEM (version 7.4.3; ICON Development Solutions, Ellicott City, Maryland) using the final PK-PD model. Data formatting, simulation data set creation, and simulation postprocessing were performed using R software version 3.4.0. Graphical analyses were conducted using SigmaPlot 13.0 (Systat Software, San Jose, CA) and R software.

We previously established a two-compartment TMDD model with 3 transit compartments to characterize nonlinear PK of SPI-62 in healthy adults [83]. In the current analysis, SPI-62 plasma concentrations from the SAD (≤ 10 mg dose groups) and MAD (≤ 2 mg dose groups) trials, as well as HSD-1 activity data from the MAD trial were pooled together for simultaneous fitting. The TMDD model structure is identical to the one we have published [83]. Only a brief description of model structure with key equations for that reported TMDD model is provided here. In our reported model, SPI-62 in the depot was absorbed into the central compartment through 3 transit compartments, which were parameterized using four identical transfer rate constants (k_{tr}). SPI-62 was distributed between the central compartment and the peripheral compartment following a

distribution flow (Q). Linear elimination of SPI-62 from the central compartment was characterized by clearance (CL). SPI-62 distributed in the central compartment could bind with HSD-1 to form a drug-target complex with a second-order association rate constant k_{on} , and in turn, the complex could dissociate to free drug and HSD-1 with a first-order dissociation rate constant k_{off} . The total amount of HSD-1 (R_{total}) was assumed to be a constant. No target synthesis or degradation processes were included in that model. Following are the equations used to characterize the PK data.

The equations for the depot and the 3 transit compartments were:

$$\frac{dA_{depot,SPI-62}}{dt} = -k_{tr} \times A_{depot,SPI-62} \quad (2.1)$$

$$A_{depot,SPI-62}(0) = \text{Dose} \times F \quad (2.1)$$

$$\frac{dA_{trans1,SPI-62}}{dt} = k_{tr} \times A_{depot,SPI-62} - k_{tr} \times A_{trans1,SPI-62}$$

$$A_{trans1,SPI-62}(0) = 0 \quad (2.2)$$

$$\frac{dA_{trans2,SPI-62}}{dt} = k_{tr} \times A_{trans1,SPI-62} - k_{tr} \times A_{trans2,SPI-62}$$

$$A_{trans2,SPI-62}(0) = 0 \quad (2.3)$$

$$\frac{dA_{trans3,SPI-62}}{dt} = k_{tr} \times A_{trans2,SPI-62} - k_{tr} \times A_{trans3,SPI-62}$$

$$A_{trans3,SPI-62}(0) = 0 \quad (2.4)$$

Where $A_{depot,SPI-62}$, $A_{trans1,SPI-62}$, $A_{trans2,SPI-62}$, $A_{trans3,SPI-62}$ represents the amount of SPI-62 in depot and transit compartments 1, 2, 3, respectively. k_{tr} represents transit absorption rate constant. F represents the bioavailability of SPI-62.

The equation for the central compartment was:

$$\begin{aligned}\frac{dA_{cen,SPI-62}}{dt} &= k_{tr} \times A_{Trans3,SPI-62} - k_{on} \times C_{cen,SPI-62} \times (R_{total} - RC) + k_{off} \times RC - CL/ \\ V_{cen,SPI-62} \times A_{cen,SPI-62} - Q/V_{cen,SPI-62} \times A_{cen,SPI-62} + Q/V_{peri,SPI-62} \times A_{peri,SPI-62} \\ A_{cen,SPI-62}(0) &= 0\end{aligned}\tag{2.5}$$

The equation for the peripheral compartment was:

$$\begin{aligned}\frac{dA_{peri,SPI-62}}{dt} &= Q/V_{cen,SPI-62} \times A_{cen,SPI-62} - Q/V_{peri,SPI-62} \times A_{peri,SPI-62} \\ A_{peri,SPI-62}(0) &= 0\end{aligned}\tag{2.6}$$

The equation for the binding with the high-affinity-low-capacity site compartment was:

$$\begin{aligned}\frac{dRC}{dt} &= k_{on} \times C_{cen,SPI-62} \times (R_{total} - RC) - k_{off} \times RC \\ RC(0) &= 0\end{aligned}\tag{2.7}$$

Where $A_{cen,SPI-62}$ and $C_{cen,SPI-62}$ represent the amount and concentration of SPI-62 in the central compartment, respectively. $A_{peri,SPI-62}$ represents the amount of SPI-62 in the peripheral compartment. $V_{cen,SPI-62}$ and $V_{peri,SPI-62}$ represents the volume distribution of central and peripheral compartment. CL and Q represent the clearance and distribution flow, respectively. k_{on} and k_{off} represents the association and dissociation rate constants, respectively. RC represents the amount of SPI-62:R complex and R_{total} represents the total amount of HSD-1.

2.3.2.1. PD structural model

Hepatic HSD-1 activity was measured as the urinary ratio of (tetrahydrocortisol + allotetrahydrocortisol) / tetrahydrocortisone. For modeling convenience, observed baseline-corrected HSD-1 activity was used and calculated as the following formula:

$$\text{Observed baseline-corrected HSD-1 activity} = \frac{\text{HSD-1 activity in specific sampling timepoint}}{\text{baseline}} \times 100 (\%) \quad (2.8)$$

Accordingly, the pharmacologic effect of SPI-62 on hepatic HSD-1 is calculated as

$$\text{Hepatic HSD-1 inhibition (\%)} = 100 - \text{Observed baseline-corrected HSD-1 activity} \quad (2.9)$$

Exploratory graphical analysis was performed first to examine the relationship between the observed HSD-1 activity and SPI-62 exposure. Urine samples for PD assays and blood samples for SPI-62 assay were not collected at the same times. Hence, time-matched SPI-62 plasma concentrations were predicted using the established TMDD model. Time-matched model-predicted SPI-62 concentrations were then plotted against the HSD-1 activity to better visualize the potential relation between each other. As a nonlinear relationship was observed, several different inhibitory I_{max} models were evaluated to describe the exposure-response relationship between SPI-62 concentrations and hepatic HSD-1 activities (**Table 2-2**). The final PK-PD model contains a TMDD model with 3 transit absorption compartments for SPI-62 PK and an inhibitory I_{max} model to link SPI-62 concentrations with HSD-1 activities. Hepatic HSD-1 activity (%) was modelled as the following:

$$\text{Predicted hepatic HSD-1 activity (\%)} = 100 \times \left(1 - \frac{I_{max} \times C^r}{IC_{50}^r + C^r}\right) \quad (2.10)$$

Inter-individual variability (IIV) were estimated using exponential model which was assumed to be normally distributed with a mean of 0 and a variance of ω^2 .

Additive, proportional, and a combined proportional and additive residual variability (RV) models were tested for both PK and PD structural models. RV was assumed to be normally distributed with a mean of 0 and a variance of σ^2 .

After the structural PK-PD model was constructed, covariate analyses were conducted. Individual estimates of IIVs for several PK-PD parameters (V_{central} , CL, k_{tr} , k_{off} , R_{total} and IC_{50}) were plotted against covariates including age, body weight, and race to visualize the potential relationships. Formal covariate analysis was to be performed using stepwise covariate modeling with an alpha level of 0.05 ($\Delta OFV > 3.84$, $\Delta df = 1$) for forward addition and an alpha level of 0.001 ($\Delta OFV > 10.83$, $\Delta df = 1$) for backward deletion.

2.3.2.2. Model evaluation

The final model was selected mainly based on graphical diagnostics and objective function values. When models are nested, ΔOFV is nominally χ^2 distributed, and a difference of -3.84 corresponds approximately to a $p < .05$ for 1 degree of freedom. Graphical diagnostics included standard goodness-of-fit plots (population-predicted concentrations (PRED) vs observed concentrations (DV), individual-predicted concentrations (IPRED) vs DV, conditional weighted residuals (CWRES) vs PRED and CWRES vs time), model fitting for time course, and prediction-corrected visual predictive check (pcVPC).

2.3.2.3. Simulations

PK sampling timepoints included prior to dosing (i.e., 0) and 0.5, 1, 1.5, 2, 3, 4, 8, 12, 16, and 24 hours after the first dose, as well as 0.5, 1, 1.5, 2, 3, 4, 8, 12, 16, 24, 48, 72, 96, 120, 144, 168 hours after the last dose. PD samples were scheduled to be collected immediately before each daily dosing (trough) and collected for one week after the last dose. Using the final model and its parameter estimates, 1000 virtual observations at each sampling time point were simulated. Variability in the simulation results was contributed by IIV in PK parameters. The 5th, 50th, and 95th percentiles of the simulated data were then plotted.

The following dosing scenarios were simulated:

Scenario 1. 0.4, 1, 2, 3, 6, 10 mg once-daily dose on Days 1 -14.

Scenario 2. 3 mg loading dose on Day 1 followed by 0.4 mg or 1 mg once-daily dose on Days 2 – 14.

2.4. Results

2.4.1. Observed data

Figure 2-1 shows the time course of hepatic HSD-1 inhibition, calculated based on the observed remaining HSD-1 activity, and time-matched SPI-62 concentrations predicted using the TMDD model established using PK data alone. As shown in **Figure 2-2**, following low doses of SPI-62, substantial HSD-1 inhibition was observed, even though the plasma exposure of SPI-62 was extremely low. After the last dose of SPI-62, the HSD-1 inhibitory effect persisted for many days. In addition, there was no time delay between C_{max} of SPI-62 and maximal HSD-1 inhibition, indicating a direct relationship between SPI-62 exposure and response. **Figure 2-3** shows the relationship between observed hepatic HSD-1 activity and time-matched SPI-62 concentrations predicted using the final TMDD model established using PK data alone. As shown in **Figure 2-3**, a clear inhibitory nonlinear relationship was demonstrated.

2.4.2. Final model structure

During model development phase, TMDD model component for the PK part and different types of I_{max} model component for the PD part were explored. In addition to the structural model, we also optimized the statistical model component by testing IIV on different parameters as well as error models. Among the different models tested, TMDD model with 3 transit absorption compartments for PK and an inhibitory I_{max} model ($100 \times \left(1 - \frac{I_{max} \times C^r}{IC_{50}^r + C^r}\right)$) with IIV on IC_{50} for

PD was found to be the best PK-PD model structure (**Figure 2-4**). Exploratory covariate analysis showed that there was no meaningful impact of age, sex, body weight or race on any model parameters ($P>0.05$ for all plots) (data not shown). Accordingly, formal standard forward addition and backward elimination covariate testing was not performed. Since there were no covariates, the final PK-PD model was identical to the base PK-PD model.

2.4.3. Parameter estimates

The parameter estimates for the final simultaneous PK-PD model are presented in **Table 2-3**. SPI-62 bound to its target with k_{on} of $8.43 \text{ nM}^{-1}\text{h}^{-1}$ and dissociated from SPI-62:R complex with k_{off} of 0.229 h^{-1} . These PK parameters estimated using combined PK and PD data are very close to those estimated using the PK data alone. The capacity of the target (R_{max}) was estimated to be 5460 nmol, which is similar to the value estimated using PK data alone (6070 nmol). The IC_{50} of SPI-62 on hepatic HSD-1 inhibition was estimated to be 0.0787 nM (i.e., 0.0334 ng/mL), within two-fold of the average C_{max} of a single dose of 0.7 mg SPI-62 (0.0185 ng/mL). Estimated IC_{50} is close to the estimated k_d (0.0272 nM) calculated as the ratio of k_{off} and k_{on} and is far less than the k_i (5.3 nM) value measured in vitro. As shown in **Table 2-3**, the standard errors of the estimated typical structural PK/PD parameters were all estimated with sufficient precision as suggested by low RSEs.

2.4.4. Model evaluation

The time courses of observed versus population predicted (PRED) plasma concentrations of SPI-62 after single- or multiple-dose in healthy adults are presented in **Figure 2-5**. Concentration-time profiles of SPI-62 after various single-dose levels (1-10 mg) administration were captured by the final model adequately. This model also provided a good fit for SPI-62 PK

profiles in the multiple-dose study, except for a slight overprediction for concentrations measured on Day 1 of the 0.7 mg dose group.

The time course of mean observed versus population predicted SPI-62 concentrations and HSD-1 activity after 0.2, 0.4, 0.7, and 2 mg multiple-dose in healthy adults are presented in **Figure 2-6**. The final model characterized the HSD-1 activity time profiles after multiple-dose administrations adequately. There is a good agreement between the observed and predicted data, except for slight overprediction for HSD-1 activity on Day 1 of both 0.7 and 2 mg dose groups.

Additional goodness-of-fit plots, presented in **Figure 2-7**, further confirmed that the final model described SPI-62 PK and PD adequately at both the population and individual levels. The pcVPC plots, which show the adequacy of the final TMDD-liver PD model, are shown in **Figure 2-8**.

2.4.5. Simulation profiles

To better understand the PK-PD relationship, simulations for PK and PD (HSD-1 activity) under different dose regimens were conducted. The results are shown in **Figures 2-9 and 2-10**.

Substantial HSD-1 inhibition was predicted for all simulated doses, with full inhibition being achieved when SPI-62 is given ≥ 2 mg QD. The inhibitory effect of SPI-62 on hepatic HSD-1 is long lasting, as reflected by the substantial inhibition through 7 days after the last dose. The time to reach maximum PD effect is dose-dependent. For example, it took around 10 days to reach steady-state after 0.4 QD dose and only about 1 day to reach steady-state after 4 mg QD dose. Administration of a loading dose, as shown in **Figure 2-10**, could bring HSD-1 inhibition to its maximum level within the first dose interval. The variability of simulated HSD-1 activity became smaller as SPI-62 dose increased.

2.5. Discussion

For small molecules exhibiting TMDD with targets located in tissues, although TMDD model has been developed for several of them [15, 69, 87], reports on TMDD-PD model are quite limited, possibly due to the lack of time course PD data. Extensive time course hepatic HSD-1 activity data, together with the unusual and complex nonlinear PK of SPI-62, enabled construction of a population TMDD-PD model that adequately captured SPI-62 nonlinear PK and hepatic HSD-1 inhibition following different dose regimens in healthy adults. The final model structure contains a 2-compartment TMDD model with 3 transit absorption compartments for SPI-62 disposition and an inhibitory I_{max} model for hepatic HSD-1 activity. SPI-62 was estimated to bind to the target with a second order association rate constant k_{on} $8.43 \text{ nM}^{-1}\text{h}^{-1}$ and dissociate back to free enzyme and drug with k_{off} value of 0.229 h^{-1} , indicating a rapid binding and slow dissociation of SPI-62 to its pharmacological target, HSD-1. The estimated target capacity (R_{tot}) 5460 nmol corresponds to approximately 2.2 mg of SPI-62, which comports well with the dose range in which pharmacokinetic nonlinearity is prominent. Both estimated dissociation equilibrium constant (k_{off}/k_{on}) 27.2 pM from the TMDD model component and estimated IC_{50} 78.7 pM from the PD model component are consistent with very high SPI-62 potency and observed achievement of substantial HSD-1 inhibition at steady state with SPI-62 daily doses substantially lower than would be predicted from measured k_i 5.3 nM .

Our results provide a compelling example showing that TMDD, mediated by its pharmacological target, does occur in small-molecule compounds. TMDD is a term to describe nonlinear PK that is caused by the interaction between a drug and its pharmacological target [1]. Although TMDD in large-molecule compounds is well accepted, its occurrence in small molecules has not been widely recognized [13, 88]. One reason for this oversight is that mechanistic studies

or PD investigation often are not conducted for many small molecules which exhibit TMDD. As a result, whether the observed nonlinear PK is truly caused by the interaction with the drug's pharmacological target might remain unverified. For small molecules exhibiting TMDD with target located in tissues, they demonstrate linear PK at high doses and substantial nonlinear PK following single low doses, as reflected by unusually low plasma exposures [13, 20]. The explanation for this nonlinear PK behavior is that, after a first low dose, a large fraction of the dose is trapped to a high-affinity-low-capacity site so that only a small amount of drug molecules is present in systemic circulation, resulting in extremely low plasma exposures [20]. If this "site" is truly the drug's pharmacological target, significant PD effect should be observed following the first dose no matter how low the plasma exposure is. In addition, the PD effect would last long after the last dose since drug molecules bind tightly to the pharmacological target. That is exactly what was observed in SPI-62 in these two Phase I clinical trials. For example, more than 40% of hepatic HSD-1 inhibition was observed following a single dose of 0.7 mg SPI-62, when the average C_{max} of SPI-62 was only 0.02 ng/mL and concentrations were undetectable at many time points [26]. In addition, inhibition of hepatic HSD-1 persisted even after 6-day wash out, with >30% inhibition being observed on Day 6. Similarly, full HSD-1 inhibition was observed after repeated doses in all low dose groups (0.2 to 2 mg), and the inhibition lasted many days after the last dose even with the lowest dose tested, 0.2 mg [26]. The TMDD-hepatic PD model that we established adequately characterized all remarkable PK and PD behaviors of SPI-62, such as extremely low plasma exposures following the first low doses, nonlinear PK turned into linear PK after repeated low doses, as well as substantial and long-lasting hepatic HSD-1 inhibition following low doses.

The nonlinear PK behavior of SPI-62 in human is not unique. Other HSD-1 inhibitors, including ABT-384 [15], MK-0916 [27], and BMS-823778 [28], showed strikingly similar nonlinear PK patterns in SAD and MAD trials when drug PK across a wide dose range, starting from a very low dose, was evaluated in healthy adults. For ABT-384 nonlinear PK, we previously performed population PK modeling. The best model was found to be a 2-compartment TMDD model with 3 transit absorption compartments [15], a model structure that is identical to the one we established for SPI-62 in the current analysis. In ABT-384 MAD trial daily doses of 1 mg to 100 mg were evaluated, but HSD-1 activity was evaluated only prior to the first dose (Day -1) and on last day of dosing (Day 7 or 14). Although not as informative as time course HSD-1 activity data available for SPI-62, ABT-384 PD results clearly showed that full hepatic HSD-1 inhibition was achieved following the lowest daily dose of 1 mg ABT-384 [86]. That observation is consistent with SPI-62 results. These interesting PK and PD behaviors of HSD-1 inhibitors indicate that small-molecule TMDD might be a class effect. The nonlinear PK observed at those low doses should not be ignored as they provide a strong sign of target engagement.

After the final TMDD-PD model was established, we performed comprehensive simulation to predict SPI-62 PK and time course of hepatic HSD-1 activity following various dose regimens, including those that haven't been evaluated in the clinical trials. The simulation results showed substantial and long-lasting HSD-1 inhibition in all dose groups evaluated, including the lowest presented daily dose of 0.4 mg; full hepatic HSD-1 inhibition can be achieved following ≥ 2 mg QD. The time needed to reach maximum HSD-1 inhibition is dose dependent. For example, it takes around 10 days to reach PD steady state with 0.4 mg SPI-62 QD but only 2 days with 2 mg SPI-62 QD. To rapidly reach maximal HSD-1 inhibition, a loading dose as shown in **Figure 2-10** could be administered. It's worth pointing out that the simulated work only predicts hepatic HSD-

1 inhibition and cannot necessarily be extrapolated to target inhibition of HSD-1 located in other tissues. Work to establish PK-PD models for HSD-1 inhibition by SPI-62 in human brain and adipose is ongoing. When available, the results of the three models together will inform dose selection for SPI-62 clinical trials..

2.6. Conclusions

The TMDD-PD modeling and simulation results provide a strong foundation for model-informed development of SPI-62. In addition, since TMDD has been reported to be a class effect of HSD-1 inhibitors [12], the TMDD-PD model that we developed for SPI-62 has potential to be utilized for other members of the class to facilitate interpretation of their PK and PD data as well as future clinical trial design.

Table 2-1. Overview of SPI-62 PK and hepatic HSD-1 activity data included in the population PK-PD analysis.

Study	Dosing regimens	Data type	Sampling time points
SAD (n = 6 for each dose)	1-, 3-, 6-, 10- mg single dose	PK	0.5, 1, 1.5, 2, 3, 4, 6, 8, 10, 12, 18, 24, 36, 48, and 72 h post-dose; additional 96 and 120 h post-dose for 6 mg dose (LLOQ = 0.1 ng/mL).
MAD (n = 4 for 0.2- and 0.4- mg. n = 6 for 0.7- and 2- mg)	3 mg loading dose on Day 1, 0.2 mg QD doses on Days 2-14	PK	0.5, 1, 1.5, 2, 3, 4, 8, 12, 16, and 24 hours after the first dose; 0.5, 1, 1.5, 2, 3, 4, 8, 12, 16, 24, 48, 72, 96, 120, 144, and 168 hours after the last dose (LLOQ = 4 pg/mL).
		PD	Pre-dose and Days 1, 8, 10, 12, 14, 16, 18, 20, and 21 from the first morning void.
	0.4 mg QD doses on Days 1-14	PK	0.5, 1, 1.5, 2, 3, 4, 8, 12, 16, and 24 hours after the first dose; 0.5, 1, 1.5, 2, 3, 4, 8, 12, 16, 24, 48, 72, 96, 120, 144, and 168 hours after the last dose (LLOQ = 4 pg/mL).
		PD	Pre-dose and Days 1, 8, 10, 12, 14, 16, 18, 20, and 21 from the first morning void.
	0.7- and 2- mg single dose on Day 1, QD doses on Days 7-20	PK	0.5, 1, 1.5, 2, 3, 4, 8, 12, 16, 24, 36, 48, 72, 96, 120, and 144 hours after the first dose and 0.5, 1, 1.5, 2, 3, 4, 8, 12, 16, 24, 48, 72, 96, 120, 144, and 168 hours after the last dose (LLOQ = 4 pg/mL).
		PD	Pre-dose and Days 1, 2, 3, 4, 5, 6, 8, 10, 12, 14, 16, 18, 20, 22, 23, 24, 25, 26, and 27 from the first morning void.

Table 2-2. Model development history for PD model.

No.	PD link	IV	Minimization	Covariance step	RSE	Model fitting	OFV	ΔOFV
1	$Activity = (100 - E_0) \times \left(1 - \frac{I_{max} \times C^r}{IC_{50} + C^r}\right) + E_0$ $IC_{50} = \theta + \exp(\eta);$ $\tau = \theta;$	$I_{max} = \theta; E_0 = \theta + \eta;$	Yes	No	-	Good	151.128	-
2		$I_{max} = \theta; E_0 = 0;$	Terminated	-	-	-	-	-
3		$I_{max} = \theta + \eta; (\theta \text{ was fixed to } 1);$ $E_0 = \theta + \eta;$	Yes	Yes	High	Good	151.042	-0.086
4		$I_{max} = \theta + \eta; (\theta \text{ was fixed to } 1);$ $E_0 = \theta + \exp(\eta);$	Yes	Yes	High	Good	150.806	-0.236
5		$I_{max} = \theta + \eta; (\theta \text{ was fixed to } 1);$ $E_0 = \theta;$	Terminated	-	-	-	-	-
6		$I_{max} = \theta + \eta; E_0 = \theta + \eta;$	Yes	No	-	Good	151.743	0.937
7		$I_{max} = \theta + \eta; E_0 = 0;$	Terminated	-	-	-	-	-
8		$I_{max} \text{ was fixed to } 1; E_0 = \theta + \eta;$	Terminated	-	-	-	-	-
9		$I_{max} \text{ was fixed to } 1;$ $E_0 = \theta + \exp(\eta);$	Yes	No	-	Good	149.817	-1.926
10		$I_{max} \text{ was fixed to } 1; E_0 = 0;$	Terminated	-	-	-	-	-
11	$Activity = 100 \times \left(1 - \frac{I_{max} \times C^r}{IC_{50} + C^r}\right)$ $\tau = \theta;$	$I_{max} = \theta + \eta; IC_{50} = \theta + \exp(\eta);$	Yes	No	-	Good	152.860	3.043
12		$I_{max} = \theta + \exp(\eta); IC_{50} = \theta + \exp(\eta);$	Yes	Yes	High	Good	150.620	-2.240
13-final		$I_{max} = \theta; IC_{50} = \theta + \exp(\eta);$	Yes	Yes	Good	Good	153.312	2.692
14		$I_{max} = \theta; IC_{50} = \theta + \exp(\eta);$ Additive residual error	Yes	Yes	Good	Good	234.094	80.782
15		$I_{max} = \theta; IC_{50} = \theta;$	Terminated	-	-	-	-	-
16		$I_{max} = \theta + \exp(\eta); IC_{50} = \theta;$	Terminated	-	-	-	-	-
17		$I_{max} = \theta + \eta; IC_{50} = \theta;$	Terminated	-	-	-	-	-
18	$Activity = 100 \times \left(1 - \frac{A_{SP162-HSD1} \times I_{max}}{R_{max}}\right)$	$I_{max} = \theta + \eta;$	Yes	Yes	Good	Over-prediction of the higher end and underprediction of the lower end of HSD-1 activity.	492.364	258.27
19		$I_{max} = \theta;$	Yes	Yes	Good		517.467	25.103

OFV, objective function value; RSE, relative standard errors. ΔOFV were calculated comparing the model with the previous one.

Table 2-3. Parameter estimation from the final PK-PD model.

Parameter	Unit	Definition	Estimates	RSE (%)	Shrinkage (%)
$V_{cen}^{\#}$	L	Volume of distribution of central compartment	152	16	
$CL^{\#}$	L/h	Clearance	10.1	6	
$Q^{\#}$	L/h	Distribution flow	2.38	12	
$V_{peri}^{\#}$	L	Volume of distribution of peripheral compartment	116	6	
k_{tr}	h^{-1}	Transit absorption rate constant	8.82	11	
k_{on}	$nM^{-1} h^{-1}$	Association rate constant	8.43	6	
k_{off}	h^{-1}	Dissociation rate constant	0.229	31	
R_{total}	nmol	Total amount of HSD-1 enzyme	5460	7	
γ		Power coefficient	0.441	7	
I_{max}	%	Maximum inhibition effect	99.9	2	
IC_{50}	nM	The half maximal inhibitory concentration	0.0787	16	
$IIV_{Vcentral}$	%	Interindividual variability on $V_{central}$	51.9%	33	14
IIV_{CL}	%	Interindividual variability on CL	19.2%	84	21
IIV_{ktr}	%	Interindividual variability on K_{tr}	50.2%	38	7
IIV_{koff}	%	Interindividual variability on K_{off}	119%	55	15
IIV_{Rtotal}	%	Interindividual variability on R_{total}	27.5%	31	9
IIV_{IC50}	%	Interindividual variability on IC_{50}	39.5%	63	37
σ_{PK}	%	Proportional residual variability for PK	27.4%	3	7
σ_{PD}	%	Proportional residual variability for PD	19.3%	12	5

#Please note these are apparent parameters as bioavailability (F) is unknown.

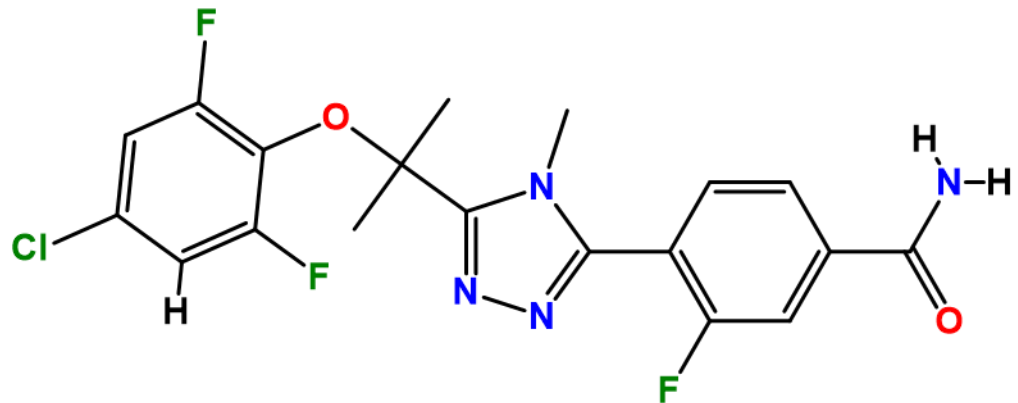


Figure 2-1. Chemical structure of SPI-62, a potent and highly selective HSD-1 inhibitor.

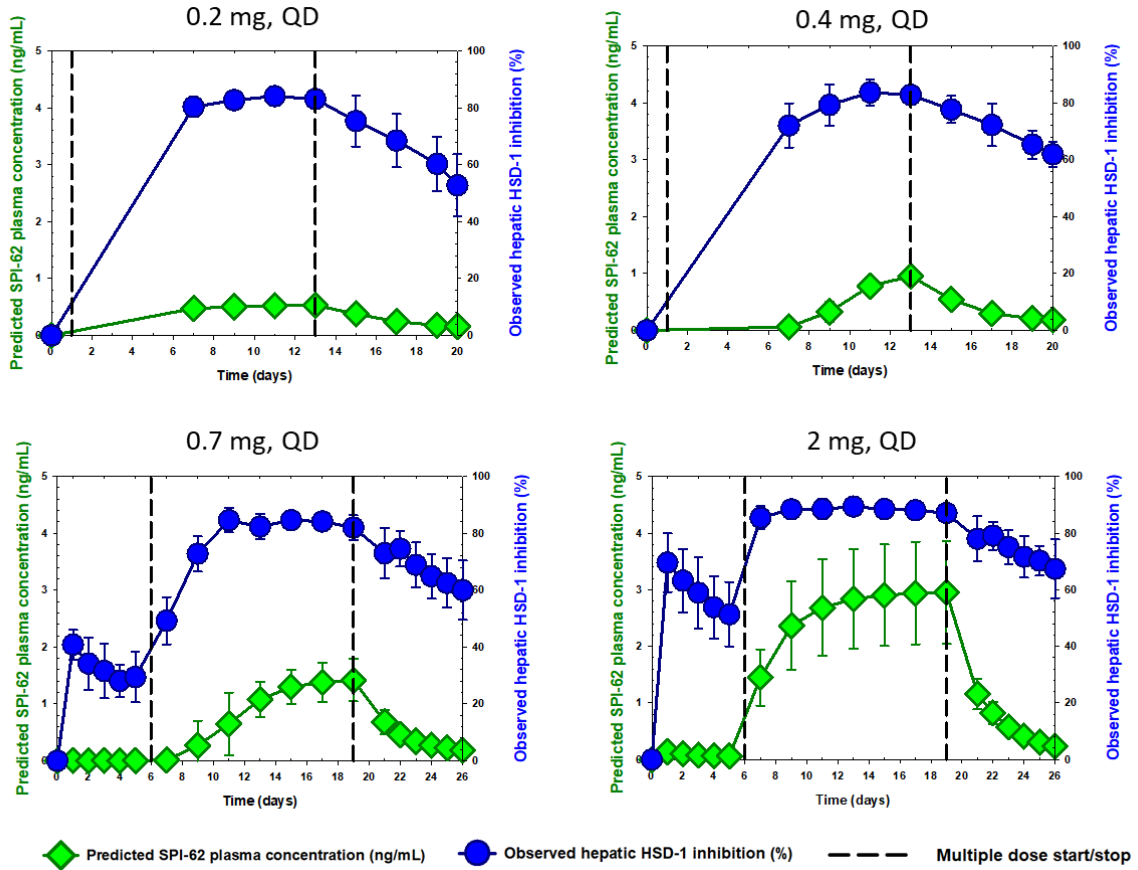


Figure 2-2. Time courses of mean \pm SD observed hepatic HSD-1 inhibition and mean \pm SD of individual model- predicted SPI-62 plasma concentrations following 0.2, 0.4, 0.7, and 2 mg oral multiple doses of SPI-62.

Vertical black solid lines represent the start and stop of multiple doses. For subjects who received 0.2 mg SPI-62, a loading dose of 3 mg was administered. For subjects who received 0.7 mg or 2 mg, a single dose of SPI-62 was followed by a 6-day washout before the start of the QD dose regimens.

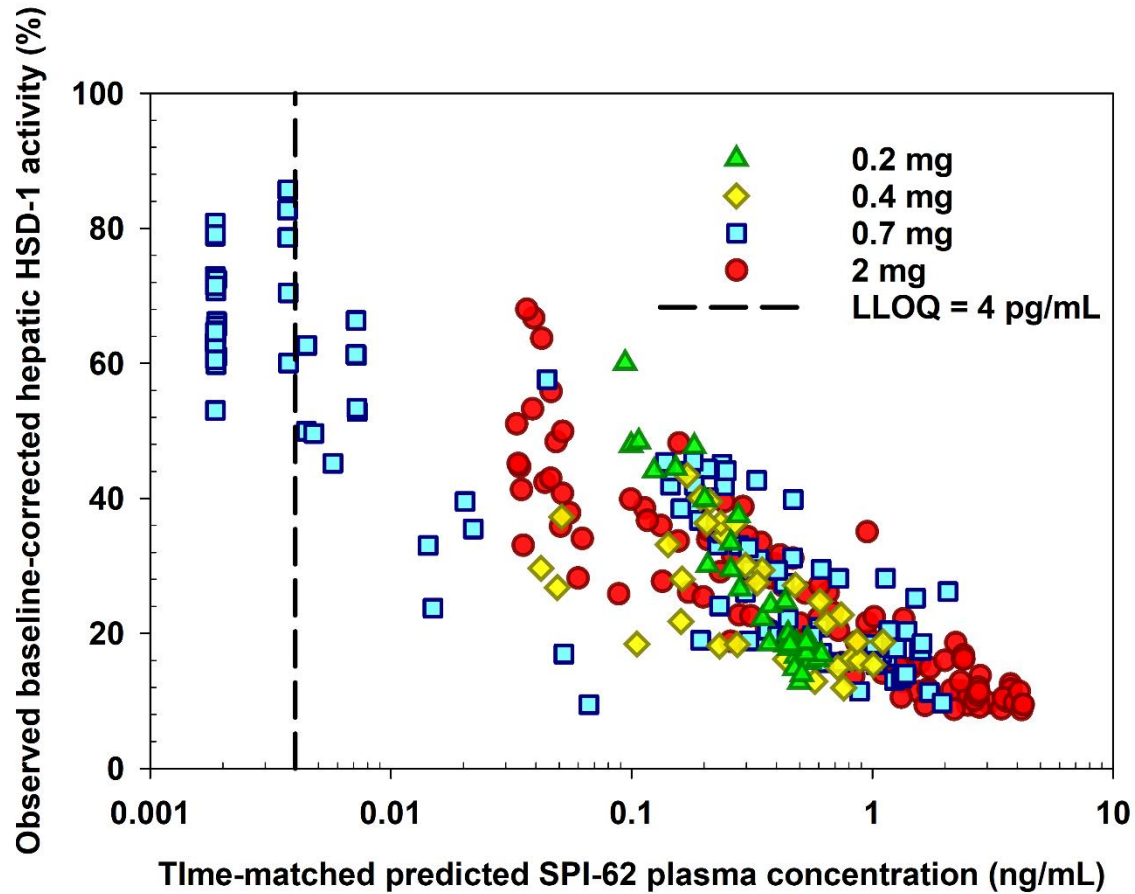


Figure 2-3. Log-scale scatter plot of the relationship between time-matched SPI-62 plasma concentrations predicted using the established TMDD model and the percentage of the observed baseline-corrected hepatic HSD-1 activity.

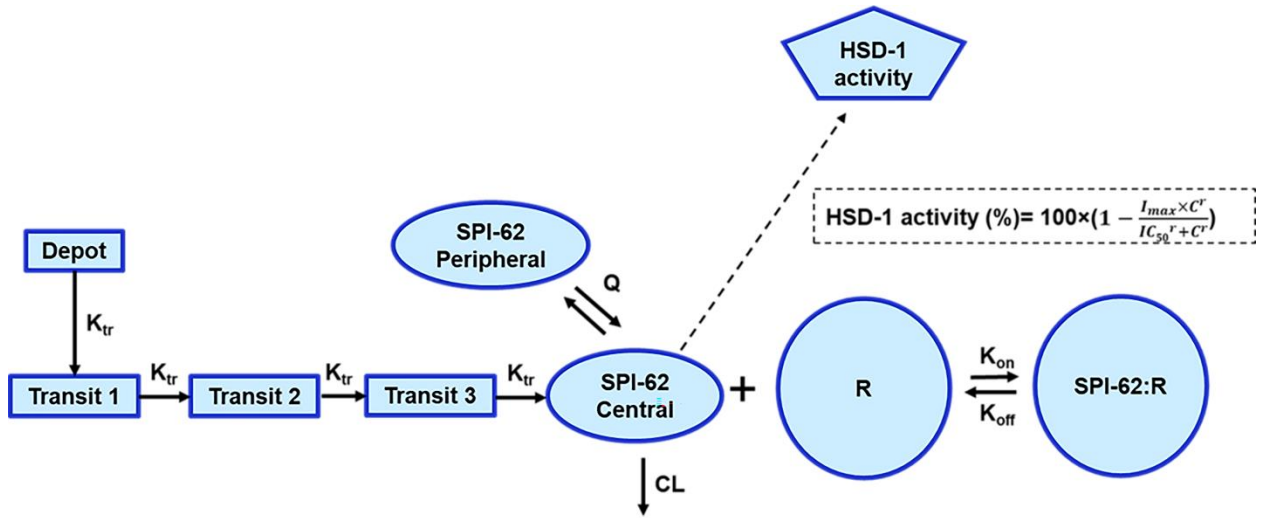


Figure 2-4. Final TMDD model describing the pharmacokinetics and pharmacodynamics of SPI-62.

The absorption process of SPI-62 was characterized by 4 sequential first-order transition rate constants (k_{tr}). SPI-62 in the central compartment ($C_{central}$, $V_{central}$) can distribute to the peripheral compartment ($C_{peripheral}$, $V_{peripheral}$) by distribution flow (Q) and be eliminated by a linear elimination pathway that is characterized by CL/V . SPI-62 can bind with HSD-1 (i.e., R) with second-order association rate constant (k_{on}) to form SPI-62:R complexes. SPI-62:R can dissociate back to free drug and free HSD-1 target with the first-order dissociation rate constant (k_{off}). The total amount of HSD-1 in human (R_{max}) is assumed to be constant. The relation between HSD-1 inhibition versus SPI-62 plasma concentrations was described by a sigmoid I_{max} model. I_{max} represents the maximum drug inhibition effect, IC_{50} represents the SPI-62 plasma concentration at 50% of I_{max} . In the sigmoid I_{max} model, the sigmoid character of the curve is determined by the power coefficient γ .

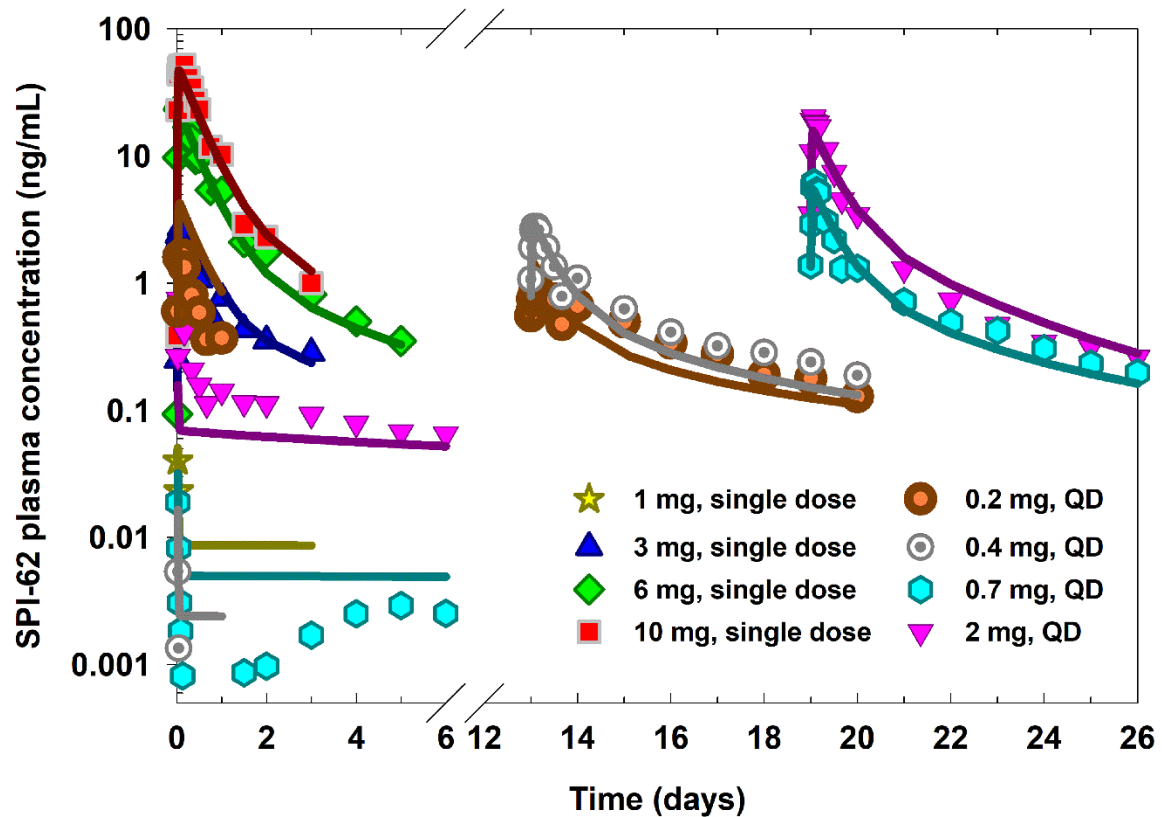


Figure 2-5. Time courses of mean observed (symbols) and population model-predicted (lines) SPI-62 plasma concentrations following 1, 3, 6, and 10 mg single oral doses of SPI-62; as well as 0.2, 0.4, 0.7, and 2 mg oral once-daily doses of SPI-62.

Subjects who received 0.2 mg SPI-62 also received a loading dose of 3 mg. Subjects who received 0.7 mg or 2 mg SPI-62 were administered a single dose of SPI-62, followed by 6-day washout before the start of 14-day QD dosing. Error bars were omitted to maintain the clarity of the image.

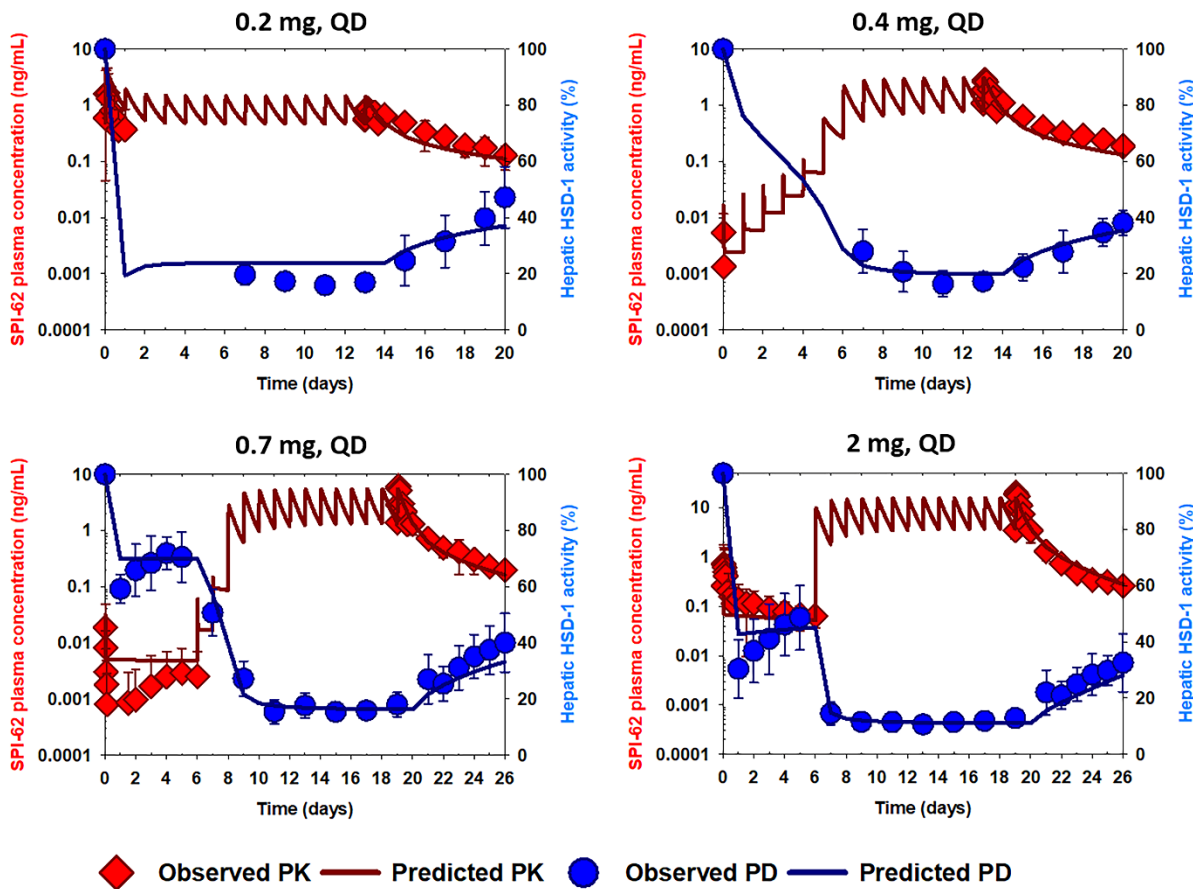


Figure 2-6. Time courses of mean observed (symbols) and population model-predicted (lines) SPI-62 plasma concentrations and hepatic HSD-1 activity following 0.2, 0.4, 0.7, and 2 mg oral once-daily doses of SPI-62.

Subjects who received 0.2 mg SPI-62 also received a loading dose of 3 mg. Subjects who received 0.7 mg or 2 mg SPI-62 were administered a single dose of SPI-62, followed by 6-day washout before the start of 14-day QD dosing.

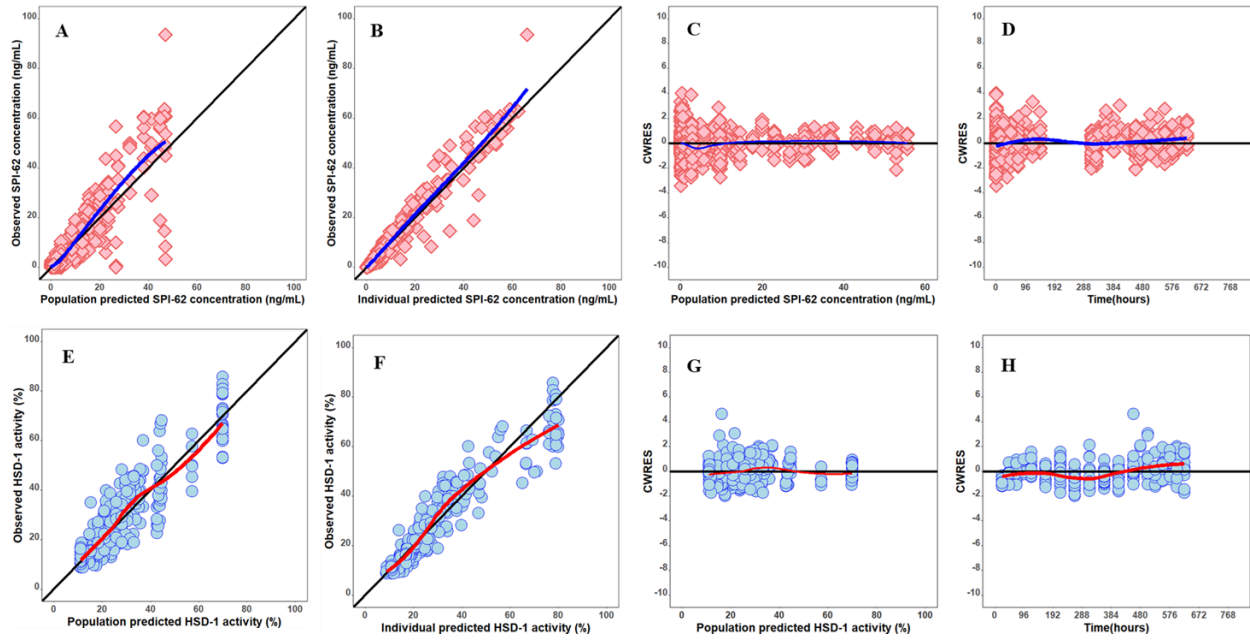


Figure 2-7. Goodness-of-fit plots for the final model of SPI-62.

(A) Observed versus population-predicted SPI-62 plasma concentrations, (B) observed versus individual-predicted SPI-62 plasma concentrations, (C) weighted conditional residuals versus time, (D) weighted conditional residuals versus population-predicted SPI-62 plasma concentrations, (E) observed versus population-predicted hepatic HSD-1 activity, (F) observed versus individual-predicted hepatic HSD-1 activity, (G) weighted conditional residuals versus time, (H) weighted conditional residuals versus population-predicted hepatic HSD-1 activity. Solid black lines represent lines of identity in (A), (B), (E), (F) and zero residuals in (C), (D), (G), (H). LOWESS lines are provided in (A), (B), (C), (D) using in blue solid lines and in (E), (F), (G), (H) using red solid lines.

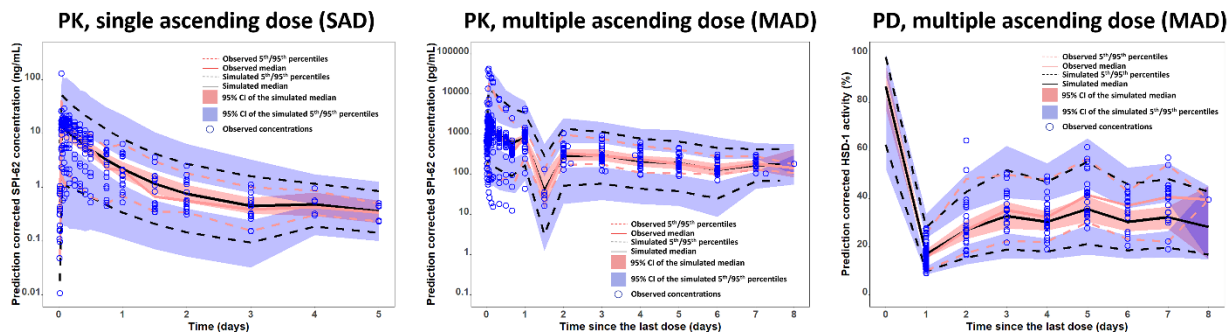


Figure 2-8. Prediction-corrected visual predicted check (pcVPC) of SPI-62 PK and PD.

The observed prediction-correct data are represented by blue circles. The median of prediction-corrected observed and simulated data are represented by the solid red and black lines. The semitransparent red field represents a simulation-based 95% confidence interval for the median. The observed and simulated 5% and 95% percentiles are presented with dashed red and black lines. The 95% confidence intervals for the corresponding model-predicted percentiles are shown as semitransparent blue fields.

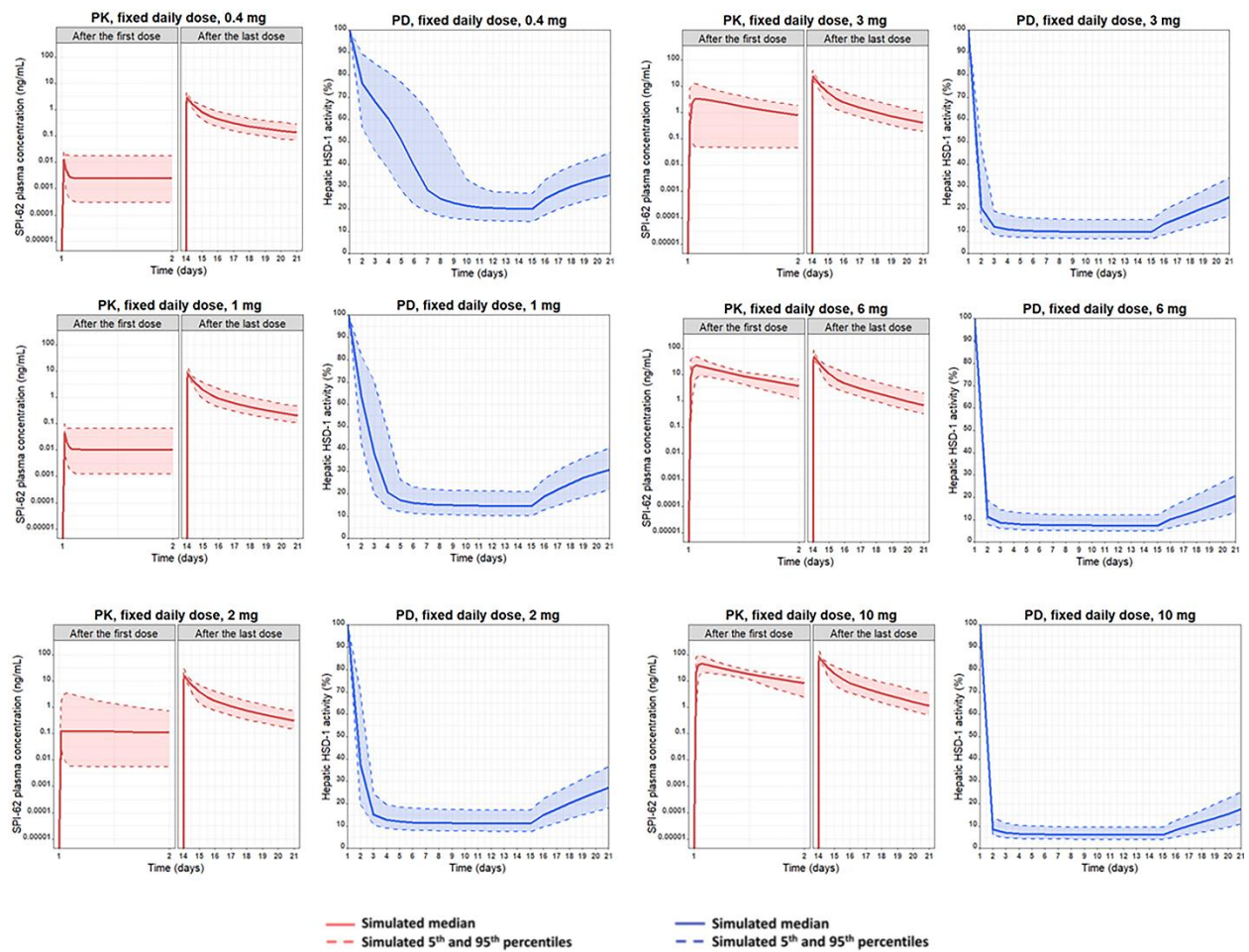


Figure 2-9. The time course of median, 5th and 95th percentile of the simulated SPI-62 plasma concentration and hepatic HSD-1 activity in 1000 virtual subjects receiving 0.4, 1, 2, 3, 6, or 10 mg SPI-62 once-daily on Days 1-14.

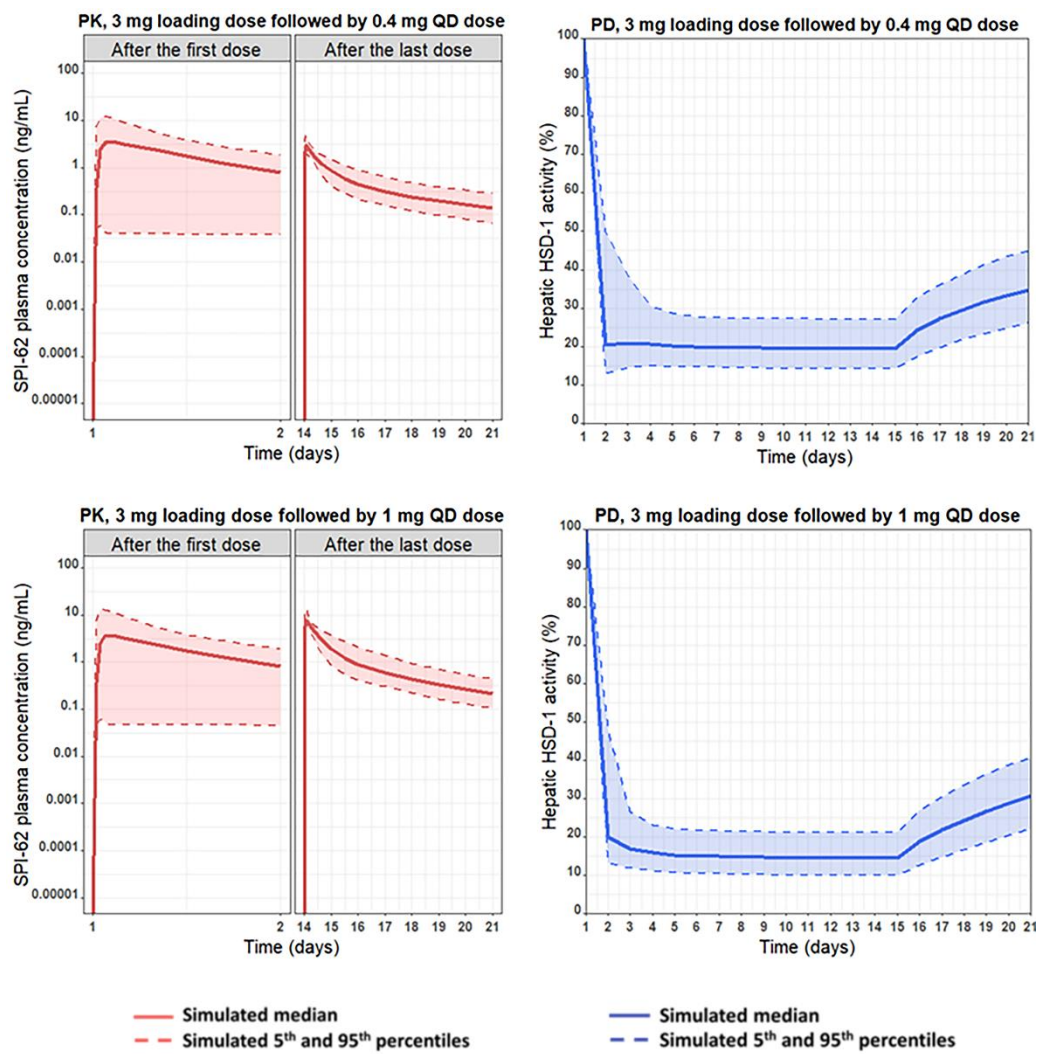


Figure 2-10. The time course of median, 5th and 95th percentage of the simulated SPI-62 plasma concentration and hepatic HSD-1 activity in 1000 virtual subjects receiving 3 mg loading dose on Day 1 followed by 0.4 mg or 1 mg SPI-62 once-daily on Days 2-14.

**CHAPTER 3: SIMULTANEOUS TARGET-MEDIATED DRUG DISPOSITION MODEL
FOR TWO SMALL-MOLECULES COMPOUNDS COMPETING FOR THEIR
PHARMACOLOGICAL TARGET: SOLUBLE EPOXIDE HYDROLASE**

Most of this chapter has been published in Journal of Pharmacology and Experimental Therapeutics.

(Wu N, Hammock BD, Lee KSS, An G. *J Pharmacol Exp Ther.* 2020 Jul;374(1):223-232.)

3.1. Abstract

1-(1-propanoylpiperidin-4-yl)-3-[4-(trifluoromethoxy)phenyl]urea (TPPU) and 1-(4-trifluoro-methoxy-phenyl)-3-(1-cyclopropanecarbonyl-piperidin-4-yl)-urea (TCPU) are potent inhibitors of soluble epoxide hydrolase (sEH) that have much better efficacy in relieving nociceptive response than the Food and Drug Administration-approved drug gabapentin in a rodent model of diabetic neuropathy. Experiments conducted in sEH knockout mice or with coadministration of a potent sEH displacer demonstrated that the pharmacokinetics of TPPU and TCPU were influenced by the specific binding to their pharmacologic target sEH, a phenomenon known as target-mediated drug disposition (TMDD). To quantitatively characterize the complex pharmacokinetics of TPPU and TCPU and gain better understanding on their target occupancy, population pharmacokinetics analysis using a nonlinear mixed-effect modeling approach was performed in the current study. The final model was a novel simultaneous TMDD interaction model, in which TPPU and TCPU compete for sEH, with TCPU binding to an additional unknown target pool with larger capacity that we refer to as a refractory pool. The total amount of sEH enzyme in mice was predicted to be 16.2 nmol, which is consistent with the experimental value of 10 nmol. The dissociate rate constants of TPPU and TCPU were predicted to be 2.24 and 2.67 hours⁻¹, respectively, which is close to the values obtained from in vitro experiments. Our simulation result predicted that 90% of the sEH will be occupied shortly after a low dose of 0.3 mg/kg TPPU administration, with ≥40% of sEH remaining to be bound with TPPU for at least 7 days. Further efficacy experiments are warranted to confirm the predicted target occupancy.

Although target-mediated drug disposition (TMDD) models have been well documented, most of them were established in a single compound scenario. Our novel model represents the first

TMDD interaction model for two small-molecule compounds competing for the same pharmacological target.

3.2. Introduction

Soluble epoxide hydrolase (sEH) is a major enzyme involved in metabolizing epoxy-polyunsaturated fatty acids such as epoxyeicosatrienoic acids (EETs) into much less active dihydroxyeicosatrienoic acids (DHETs) [29], leading to partial or complete loss of their initial biological activities. sEH is highly expressed in the liver, kidney, heart, lung, intestine, brain, and vasculature of mammals, and its increased expression is associated with inflammation and several diseases [89, 90]. sEH is also presented in red blood cell in small amount [19]. Because inhibition of sEH stabilizes endogenous EETs, sEH represents a promising therapeutic target for the treatment of inflammation, pain, cardiovascular diseases, and a variety of other disease usually involving mitochondrial dysfunction and endoplasmic reticulum stress [29, 30, 91, 92].

Effort has been made toward the discovery of the sEH inhibitors in the past decades. Among the various sEH inhibitors identified, 1-(1-propanoylpiperidin-4-yl)-3-[4-(trifluoromethoxy)phenyl]urea (TPPU) and 1-(4-trifluoro-methoxy-phenyl)-3-(1-cyclopropanecarbonyl-piperidin-4-yl)-urea (TCPU) (as shown in **Figure 3-1**) represent two particularly promising candidates due to their potent inhibition on sEH [31, 93-95]. Both TPPU and TCPU have demonstrated much better efficacy in relieving nociceptive response than the FDA-approved drug, gabapentin, in a rodent model of diabetic neuropathy [19]. *In vitro* binding kinetics experiments showed that TPPU and TCPU have small dissociation rate constants ($k_{off} = (8.52 \pm 0.47) \times 10^{-4} \text{ s}^{-1}$ and $(9.9 \pm 0.1) \times 10^{-4} \text{ s}^{-1}$ respectively), which indicates their tight binding with sEH [30, 96]. In addition, both TPPU and TCPU have high affinity to sEH ($k_d = 2.5 \text{ nM}$ and 0.9 nM , respectively).

Interesting characteristics in the pharmacokinetic profiles of TPPU and TCPU were observed in our novel displacement experiment conducted recently in both wild-type mice and sEH-global knockout mice [19]. We have the following key observations: 1) TPPU plasma concentration decreased rapidly in sEH-knockout mice and cannot be measured after 48 hrs using a highly sensitive mass spectrometry method with the limit of detection \leq 0.4 nM. In contrast, TPPU pharmacokinetics in wild-type mice has a much longer terminal phase, with TPPU plasma concentrations being measurable past 312 hours. This phenomenon may be explained by the tight binding of TPPU with sEH, and the corresponding slow dissociation process of TPPU from the TPPU-sEH complex in tissues. 2) When the wild-type mice dosed with TPPU at time 0 followed by a dose of TCPU at 168 hours (i.e., 1 week later), the TPPU plasma profile showed two peaks, with the first TPPU peak (~ 2 hours) observed shortly after TPPU dose and the second TPPU peak (~170 hours) observed shortly after the TCPU dose. The second peak was not observed in sEH-knockout mice following the same dosing regimen. 3) Interestingly, we observed TCPU plasma concentration peaks right after time 0 (TPPU added) in one group of re-used mice that was administrated TCPU 2 weeks previously, which accidentally supported the hypothesis that TCPU could also be displaced by TPPU reversely. Our findings strongly suggested that the pharmacokinetics of TPPU and TCPU were influenced by the specific binding to their pharmacologic target sEH, a phenomenon known as target-mediated drug disposition phenomenon (TMDD) [1, 2].

It is known that compounds exhibiting TMDD usually have complex and nonlinear pharmacokinetics, and the dose regimen selection can be quite challenging since the relationship among dose, drug exposure, and response is no longer intuitive. To optimize the dose regimen, it is important to utilize pharmacometric modeling approaches to elucidate the quantitative

relationship between drug exposure and response. The goal of the current study was to develop a TMDD mathematical model to quantitatively characterize the complex pharmacokinetics of TPPU and TCPU we observed in mice and gain better understanding on their target occupancy. The first TMDD mathematical model was proposed by Mager and Jusko in 2001 [69]. Several different TMDD models have been published since then [48, 97-100]. However, most reported TMDD models were developed in a single compound scenario, and therefore cannot be adapted directly to characterize the TPPU and TCPU data we have. In the current study we present a novel simultaneous TMDD interaction model, where TPPU and TCPU compete for their pharmacologic target sEH with TCPU unexpectedly binding to an additional unknown target pool with larger capacity which we refer to a refractory to degradation pool.

3.3. Methods

3.3.1. Data source

TPPU and TCPU pharmacokinetics displacement data in mice came from a published study and were used for development of the TMDD pharmacokinetics model [19]. As shown in **Figure 3-2**, two experiments were conducted, with four treatment groups in experiment 1 and three treatment groups in experiment 2 (four to six mice/group). In experiment 1, wild-type mice received a 0.3 mg/kg dose of TPPU subcutaneously at time 0 on the 1st day followed by either blank vehicle (group 1) or 3 mg/kg TCPU (group 2) at 168 hours on the 7th day. Similarly, sEH knockout mice in experiment 1 received 0.3 mg/kg s.c. dose of TPPU at time 0 on the 1st day followed by either blank vehicle (group 3) or 3 mg/kg TCPU (group 4) at 168 hours on the 7th day. In experiment 1, blood samples were collected at 0, 0.25, 0.5, 1, 2, 4, 6, 8, 24, 48, 72, 96, 120, 144, 168, 168.25, 168.5, 168, 169, 170, 172, 174, 176, 192, 216, 264, and 312 hours. In experiment 2, wild-type mice received a 0.3 mg/kg s.c. dose of TPPU at time 0 on the 1st day followed by

TCPU 1 (group 1), 10 (group 2), or 0.3 mg/kg (group 3) at 168 hours on the 7th day. The wild-type mice used in group 3 of experiment 2 were reused from a previous experiment, in which the mice were given a weak sEH inhibitor, mTPPU at 1 mg/kg s.c. 3 weeks ago followed by 3 mg/kg TCPU s.c. 1 week from the administration of mTPPU. Blood samples from experiment 2 were collected through tail nick at similar time points as those in experiment 1. The concentrations of TPPU and TCPU in mice plasma were quantified using a well characterized and quantitative liquid chromatography–tandem mass spectrometry assay as published previously [19]. Lower limit of quantification for both TPPU and TCPU was 0.49 nM. The interday and intraday accuracy and precision of TPPU and TCPU were all within 15%. Detailed bioanalytical assay information has been previously reported [19].

3.3.2. Population pharmacokinetics modeling

All pharmacokinetics data for TPPU and TCPU from both in vivo displacement experiments were analyzed simultaneously using the nonlinear mixed-effect modeling approach with NONMEM (version 7.4.3; Icon Development Solutions, Ellicott City, MD) interfaced with Pirana (version 2.9.9, <http://www.pirana-software.com/>). The first-order conditional estimation method with interaction and a user-defined subroutine (ADVAN13) were used to estimate the population mean values of the pharmacokinetics parameters, interindividual variability (IIV) and residual variability (RV) between observed and individually predicted blood TPPU and TCPU concentrations. SigmaPlot and RStudio (version 1.0.143, <https://www.rstudio.com/>) were used for graphical analysis and data handling. Data from the reused mice (experiment 2, third group) were excluded to avoid the potential inference from the previous experiment, even though this group accidentally revealed the TMDD characteristics of TCPU. TCPU data in knockout mice were also excluded because of the small sample size with outlier data. BLQ data were also excluded.

3.3.2.1. Structural model evaluated

TPPU data from sEH knockout mice were used to build the TPPU base structure model. Among the different models tested (e.g., one- or two-compartment models), the one compartment model with first-order absorption and linear elimination was found to best characterize TPPU disposition in sEH knockout mice. This base structure was then incorporated with the TMDD component(s) to characterize TPPU pharmacokinetics from the wild-type mice. During the model-building process, various TMDD model structures for TPPU and TCPU were evaluated. The following are several representative models (model structure is shown in **Figure 3-3**).

Model with one TMDD component (Figure 3-3 (a)).

In this model, both TPPU and TCPU have the same central pharmacophore (i.e., one-compartment, first-order absorption and elimination), but only TPPU has a TMDD component. TPPU interacted with sEH with a second-order association rate constant (k_{on}) to form a TPPU-sEH complex. TPPU-sEH complex dissociated back to free sEH target and free drug with the first-order dissociation rate constant (k_{off}). The compacity of sEH target (R_{max1}) remained constant. The TCPU plasma concentration was assumed to directly affect the k_{off} of TPPU.

Model with two TMDD components (Figure 3-3 (b)).

In this model, in addition to their base structure, both TPPU and TCPU have TMDD components. TPPU and TCPU can interact with sEH with a second-order association rate constant ($k_{on,TPPU}$ and $k_{on,TCPU}$, respectively) to form a drug-sEH complex. TPPU-sEH and TCPU-sEH can dissociate back to free drug and free sEH target with the first-order dissociation rate constants ($k_{off,TPPU}$ and $k_{off,TCPU}$, respectively).

Model with two TMDD components plus MM process (Figure 3-3 (c)).

This model was built on top of the model with two TMDD components, with an additional M-M elimination pathway for TCPU being incorporated in the model. The M-M kinetics were characterized by maximum rate of elimination and the Michaelis constant (k_m) for elimination, not overall pharmacokinetics.

Model with two TMDD components mixing with a competitive and noncompetitive mechanism (Figure 3-3 (d)).

This model was similar to the model with two TMDD components. The difference lies in the TPPU and TCPU replacement process. In addition to competing with free sEH enzyme, in this model, we assumed that TCPU and TPPU can also interact and replace those molecules in the bound drug-sEH complex. TCPU could bind to TPPU-sEH complex with the rate constant $k_{TCPU \rightarrow TPPU}$ to release free TPPU and generate TCPU-sEH receptor at the same time. Inversely, TPPU could also bind to TCPU-sEH complexes with a rate constant $k_{TPPU \rightarrow TCPU}$ to release free TCPU and generate TPPU-sEH complexes at the same time.

Model with three TMDD components (final model) (Figure 3-4).

This model was built on top of the model with two TMDD components, with an additional TMDD component for TCPU being incorporated in the model. In this model, both TPPU and TCPU can bind to sEH target (R1). In addition, TCPU can also bind to an unknown target termed a refractory pool (R2) with a different k_{onTCPU} value and dissociate from the TCPU-R2 complex with a different $k_{offTCPU}$ value. We assume the total amount of this unknown target (R_{max2}) in mice is also a constant.

This model was our final model. The equations used to characterize this complicated TMDD model are as follows:

$$\frac{dA_{TPPU,depot}}{dt} = -k_{a1} \times A_{TPPU,depot}$$

$$A_{TPPU,depot}(0) = \text{Dose} \times F \quad (3.1)$$

$$\begin{aligned} \frac{dA_{TPPU,central}}{dt} &= k_{a1} \times A_{TPPU,depot} - k_{on,TPPU,R1} \times (R_{max1} - A_{[TPPU-R1]} - A_{[TCPU-R1]}) \times \\ &C_{TPPU,central} + k_{off,TPPU,R1} \times A_{[TPPU-R1]} - k_{e1} \times A_{TPPU,central} \end{aligned}$$

$$A_{TPPU,central}(0) = 0 \quad (3.2)$$

$$\frac{dA_{TCPU,depot}}{dt} = -k_{a2} \times A_{TCPU,depot}$$

$$A_{TCPU,depot}(0) = \text{Dose} \times F \quad (3.3)$$

$$\begin{aligned} \frac{dA_{TCPU,central}}{dt} &= k_{a2} \times A_{TCPU,depot} - k_{on,TCPU,R1} \times (R_{max1} - A_{[TPPU-R1]} - A_{[TCPU-R1]}) \times \\ &C_{TCPU,central} + k_{off,TCPU,R1} \times A_{[TCPU-R1]} - k_{on,TCPU,R2} \times (R_{max2} - A_{[TCPU-R2]}) \times \\ &C_{TCPU,central} + k_{off,TCPU,R2} \times A_{[TCPU-R2]} - k_{e2} \times A_{TCPU,central} \end{aligned}$$

$$A_{TCPU,central}(0) = 0 \quad (3.4)$$

$$\begin{aligned} \frac{dA_{[TPPU-R1]}}{dt} &= k_{on,TPPU,R1} \times (R_{max1} - A_{[TPPU-R1]} - A_{[TCPU-R1]}) \times C_{TPPU,central} - \\ &k_{off,TPPU,R1} \times A_{[TPPU-R1]} \end{aligned}$$

$$A_{[TPPU-R1]}(0) = 0 \quad (3.5)$$

$$\begin{aligned} \frac{dA_{[TCPU-R1]}}{dt} &= k_{on,TCPU,R1} \times (R_{max1} - A_{[TPPU-R1]} - A_{[TCPU-R1]}) \times C_{TCPU,central} - \\ &k_{off,TCPU,R1} \times A_{[TCPU-R1]} \end{aligned}$$

$$A_{[TCPU-R1]}(0) = 0 \quad (3.6)$$

$$\frac{dA_{[TCPUR2]}}{dt} = k_{on,TCPUR2} \times (R_{max2} - A_{[TCPUR2]}) \times C_{TCPU,central} - k_{off,TCPUR2} \times A_{[TCPUR2]}$$

$$A_{[TCPUR2]}(0) = 0 \quad (3.7)$$

3.3.2.2. Stochastic models evaluated

Interindividual variability (IV)

IV was evaluated using an exponential model, which is assumed to be normally distributed with a mean of 0 and a variance of ω^2 .

Residual variability (RV)

Additive, proportional, and combined proportional and additive RV models were evaluated. The residual error is assumed to be normally distributed with a mean of 0 and a variance of σ^2 .

3.3.2.3. Model evaluation

Final model selection was based on biologic and physiologic plausibility, goodness-of-fit plots, individual fitted plots, stability of parameter estimates, and objective function value. The likelihood ratio test was used for comparing nested models, for which a decrease in the NONMEM objective function ($-2 \log \text{likelihood}$) of 3.84 points was necessary to consider the improvement in model performance statistically significant at $\alpha = 0.05$.

A visual predictive check, stratified by TPPU/TCPU and murine strain (WT/KO), was performed to evaluate the predictive ability of the final model. Using the original data set, along with the final model and its parameter estimates, 1000 virtual observations at each sampling time point were simulated. The observed data were then plotted with the 5th, 50th, and 95th percentiles

of the simulated data. If the model is consistent and appropriate, the observed concentrations should fall within the 5th, 50th, and 95th percentiles of the simulated concentrations. The condition (calculated from the ratio of the largest and the smallest eigenvalues) was calculated to evaluate if the model is overparametrized or ill-conditioned.

3.3.3. Target occupancy simulation

Target binding kinetics help to evaluate the time of drug action *in vivo* [101]. The formula of fraction of target occupancy is provided as following.

$$\text{Target occupancy} = \frac{\text{The amount of [TPPU-sEH complex]}}{\text{The amount of sEH}} \quad (3.8)$$

Using the above formula, the fraction of the sEH enzyme that are occupied by TPPU can be estimated. We used our final TMDD model to simulate the time course of fraction of sEH enzyme occupied by TPPU following different doses of TCPU displacement.

Simulations were performed in NONMEM (version 7.4.3; ICON Development Solutions, Ellicott City, Maryland) using the structural models detailed in the previous section. The following conditions were simulated:

(1) At time 0, 0.3 mg/kg dose of TPPU was given subcutaneously to the wild-type mice, and at the time 168 hours, 1 mg/kg dose of TCPU was given subcutaneously.

(2) At time 0, 0.3 mg/kg dose of TPPU was given subcutaneously to the wild-type mice, and at the time 168 hours, 3 mg/kg dose of TCPU was given subcutaneously.

(3) At time 0, 0.3mg/kg dose of TPPU was given subcutaneously to the wild-type mice, and at the time 168 hours, 10 mg/kg dose of TCPU was given subcutaneously.

3.4. Results

In experiment 1, the pharmacokinetics of TPPU had a very long terminal phase in wild-type mice (**Figure 3-5**, middle panel), and this feature was not observed in the sEH knockout mice (**Figure 3-5**, top panel), indicating that the binding of TPPU to its pharmacological target sEH affected the disposition of TPPU. In line with this mechanism, a high dose of TCPU given at 168 hours displaced those TPPU molecules bound to sEH, resulting in a TPPU second peak that occurred at 170 hours (**Figure 3-5**, bottom panel). These data provided direct and strong evidence that TPPU undergoes pharmacological TMDD. Based on the data from experiment 1, the initial model we built has a TMDD component for TPPU only, with TCPU blood concentration affecting the k_{off} of TPPU (i.e., dissociation of TPPU). However, this model was unstable and could not capture the full TCPU data set, indicating that this is not an appropriate model. Similar to TPPU, TCPU is also a potent sEH inhibitor, and therefore its disposition may also be affected by the sEH concentration and distribution. Indeed, as shown in **Figure 3-6**, when a group of mice receiving a single dose of 3 mg/kg TCPU were administered TPPU 2 weeks later, a small TCPU peak was observed shortly after a low dose of TPPU was given, indicating that TPPU can also displace those TCPU bound to sEH. Based on this observation, we updated our model by adding a TMDD component on both TPPU and TCPU (i.e., model with two TMDD components). However, the updated model can characterize TPPU data and TCPU data from the low-dose groups (1 mg/kg) but cannot capture the TCPU data from high-dose groups (3 and 10 mg/kg). Because a total of four different doses of TCPU was evaluated (3 mg/kg from experiment 1 and 0.3, 1, and 10 mg/kg from experiment 2), we evaluated TCPU pharmacokinetics linearity and found that the nonlinearity still existed at the highest dose (i.e., 10 mg/kg) (**Figure 3-7**). Because the capacity of sEH was predicted to be low, the nonlinearity of TCPU observed at high doses cannot be explained by the binding to

its low-capacity high-affinity pharmacological target sEH. To characterize the nonlinearity of TCPU, on top of the model with two TMDD components, we tested additional nonlinear sources of TCPU disposition, such as an M-M elimination pathway or an additional unknown target with large capacity. The different types of models that we have tested, along with their convergence status, model stability, and the objective function values, can be found from the model development history listed in **Table 3-1**. Among the different types of models that we have constructed, the best model was found to be the model with three TMDD components, in which TPPU and TCPU compete for their pharmacologic target sEH (R1), with TCPU binding to an additional unknown target pool or refractory pool (R2) with a larger capacity. The model structure of this final model is shown in **Figure 3-4**.

The final model estimated parameters of TPPU and TCPU pharmacokinetics are presented in **Table 3-2**. Based on the model estimation, TPPU and TCPU have similar absorption rate constants (0.961 vs. 0.730 hour⁻¹, respectively), volume of distribution (0.0231 vs. 0.0158 L, respectively) and clearance (0.0017 vs. 0.0014 L/h, respectively). When TPPU and TCPU competed for sEH binding site, both the association rate constant and dissociate rate constant of TCPU (0.0779 nM⁻¹ hour⁻¹ and 2.67 hour⁻¹, respectively) were similar with that of TPPU (0.0918 nM⁻¹ hour⁻¹ and 2.24 hour⁻¹, respectively). The binding of TCPU to the unknown target is much weaker, as reflected by the smaller k_{on} of 0.0275 nM⁻¹ hour⁻¹ and large k_{off} of 11.9 hour⁻¹. The capacity of sEH (R_{max1}) and the unknown target (R_{max2}) were estimated to be 16.2 and 46.6 nmol, respectively. In the final model, IIV terms were placed on the volume distribution, clearance, and absorption rate constant of TPPU and TCPU; a combined proportional and additive residual error model best described the unexplained RV. Interindividual variability estimates on V, CL, and k_a of TPPU and TCPU can be found from **Table 3-3**. The calculated shrinkage for interindividual

variability estimates in the final model ranges from 2% to 67%. Shrinkage above 30% may influence the power of the diagnostics for individual predicted parameters and concentrations. However, removing the IIV on V , k_a , and k_{off} of TCPU negatively impacts the model stability and fit. Condition number (calculated from the ratio of the largest and the smallest eigenvalues) of the final model is 161. Because this value is less than 1000, it indicates that the model is not overparametrized or ill-conditioned.

To further evaluate the model performance, the model predicted TPPU and TCPU parameters, including maximum concentration, area under the concentration time curve from predose extrapolated to infinity, and terminal elimination half-life, were compared with those obtained from noncompartmental analysis using the observed data. As shown in **Table 3-3**, the model predicted values are in line with those from the noncompartmental analysis. In addition, the model-predicted k_{off} as well as the capacity of sEH (i.e., R_{max1}) were also consistent with the experimental determined values (**Table 3-3**).

The standard goodness-of-fit plot of the final model for TPPU and TCPU are shown in **Figure 3-8**, a and b, respectively. The population- and individual-predicted concentrations versus the observed concentrations were evenly distributed around the line of identity without bias, indicating that the final model characterized both TPPU and TCPU pharmacokinetics adequately at both the population and individual levels. Additionally, the conditional weighted residuals appear distributed uniformly around the zero line when plotted either by population-predicted concentrations or by time, further indicating the absence of significant bias in the model fit.

The time course of mean observed versus population-predicted blood concentrations of TPPU and TCPU are presented in **Figure 3-9**, **Figure 3-10** and **Figure 3-11**. As shown in **Figure 3-9**, the final model was able to adequately characterize TPPU pharmacokinetics in both sEH

knockout mice (top panel) and wild-type mice without or with TCPU displacement (middle panel and bottle panel, respectively) simultaneously. This model also captured the dose-dependent displacement effect of TCPU on TPPU pharmacokinetics, which is reflected by the higher second peak of TPPU with increase in TCPU dose (**Figure 3-10**). In addition, the final model also provided favorable fitting on TCPU pharmacokinetics following different TCPU doses (**Figure 3-11**). To evaluate the predictive ability of the final model, a visual predictive check was performed. As shown in VPC plots (data not shown), the solid lines, depicting the 2.5th, 50th, and 97.5th percentiles of the predicted TPPU and TCPU concentrations, cover most of the observed data and are also in close agreement with the 2.5th, 50th, and 97.5th percentiles of the observed data, confirming the adequacy of the final model.

The simulation result for the time course of sEH target occupancy for TPPU with different doses of TCPU displacement is shown in the **Figure 3-12**. Following 0.3 mg/kg TPPU, sEH occupancy reaches 90% shortly after TPPU administration and starts to decline after 24 hours. Based on the simulation, about 40% of sEH is still bound with TPPU after 7 days. The fraction of sEH occupied by TPPU drops dramatically shortly after TCPU is administered, and it happens in a dose-dependent manner, indicating the target displacement by TCPU.

3.5. Discussion

TMDD is a term to describe the phenomenon where the interaction between drug and its pharmacologic target, a pharmacodynamics process, affects drug disposition, a pharmacokinetics process. Although the concept of TMDD was raised by Levy 25 years ago based on the unusual nonlinear pharmacokinetics of a number of small-molecule drugs, TMDD only became a widely-known concept with the proliferation of large-molecule biologics because numerous protein drugs

demonstrate nonlinear pharmacokinetics imparted by TMDD due to their specific binding to their pharmacological targets [1, 97]. Due to the relatively low prevalence of TMDD in small-molecule drugs, it has been an overlooked area [13, 88], misunderstanding has evolved that “TMDD cannot occur in small-molecule compounds”. This is a clear misconception and our study has provided direct evidence that TMDD can occur in small-molecule compounds. To verify the occurrence of pharmacological TMDD, a number of mechanism experiments have been recommended, including pharmacokinetic experiment using pharmacological target knock-out animals as well as *in vivo* displacement experiment with co-administration of pharmacological target binding [2, 13, 14, 102]. So far only a few groups have done such mechanism experiments to verify TMDD in large-molecule and small-molecule compounds but none of them have done both experiments within the same study [14, 102]. Both recommended experiments have been performed in our study, which represent an advantage of our work. Our observations of long terminal phase of TPPU in wild-type mice while not in sEH-knockout mice, along with the occurrence of second TPPU peak following administration of TCPU provide clear and direct evidence of pharmacological TMDD of TPPU, a potent small-molecule sEH inhibitor.

Based on the TPPU and TCPU pharmacokinetics data from both mechanism experiments, we developed a novel simultaneous TMDD interaction model, where TPPU and TCPU compete for their pharmacologic target sEH. Based on our final model, the total amount of sEH enzyme (R_{max1}) in mice was predicted to be around 16.2 nmol, which is consistent with the experimental value of 10 nmol [19]. The dissociation rate constants (k_{off}) of TPPU and TCPU were predicted to be 2.24 h^{-1} and 2.67 h^{-1} , respectively, which is close to the values (2.09 h^{-1} and 1.76 h^{-1} , respectively) obtained from the *in vitro* experiment. Regarding the k_d predicted by pharmacokinetic model, which is calculated by k_{off} over k_{on} , were predicted to be 24.4 nM for

TPPU and 34.3 nM for TCPU. These estimates are higher than those experimentally determined k_d values (2.5 nM for TPPU and 0.92 nM for TCPU) [19]. This discrepancy is not surprising since k_d values determined *in vitro* is usually measured in a closed system which is different from the *in vivo* situation where a drug is exposed to an open system. Recently, a number of studies have suggested that drug-target residence time (t_R), which is calculated as $1/k_{off}$, is a better *in vitro* parameter to predict *in vivo* efficacy than those standard *in vitro* potency parameters, including K_d [19, 103]. Our model results indirectly support this recommendation considering that the k_{off} values determined *in vitro* are consistent with those estimated from the mathematical modeling using the *in vivo* data, while the K_d values determined *in vitro* are much smaller than the model predicted values. The disconnection between model predicted and *in vitro* determined k_d has been reported before for other compounds [97]. Although TMDD models have been well documented, most of them were established in a single compound scenario. Our novel model represents the first TMDD interaction model for small-molecule compounds.

In our final TMDD interaction model, in addition to TPPU and TCPU competing for sEH enzyme, TCPU was predicted to bind to an additional target pool. Based on the model prediction, the capacity of this unknown target is 46.6 nmol, which is higher than sEH (16.2 nmol). In addition, TCPU was predicted to be dissociated from this target with k_{off} value of 11.9 h^{-1} , which is much faster than its dissociation from sEH. We anticipate that TCPU has specific binding to this unknown target as a second TMDD component for TCPU is required in the model in order to capture TCPU nonlinear pharmacokinetics observed in our experiment. It would be interesting to know what this unknown target is. In addition to sEH, many other epoxide hydrolase isozymes, including mEH, EH3, EH4, are known to be expressed in mammals. These isozymes share the similar protein structure with sEH enzyme with similar hydrolysis activity but different tissue

expression and substrate preferences [104]. Theoretically, if TCPU has broad inhibitory effect on epoxide hydrolase isozymes, then this model predicted second target pool could be one of these isozymes. TCPU has potent inhibitory effect on sEH. Whether TCPU has inhibitory effect on other epoxide hydrolase isozymes or other unknown targets warrants further investigation.

As noted earlier, TMDD is a consequence of PD affecting pharmacokinetics. Accordingly, for compounds exhibiting TMDD, valuable information on drug binding to its pharmacological target can be extracted from the observed pharmacokinetics profile. For the TMDD interaction model that we developed for TPPU and TCPU, it can be used not only for pharmacokinetics characterization but also for sEH target occupancy prediction. Our simulation result predicted that, 90% of the sEH will be occupied shortly after a low dose of 0.3 mg/kg TPPU administration, with $\geq 40\%$ of sEH remaining bound with TPPU for at least 7 days. If sEH target occupancy is directly correlated with the pharmacodynamics effect, then long-lasting efficacy is expected following a single dose of TPPU. Further efficacy experiments are warranted to confirm the predicted target occupancy.

Changes in the magnitude and time course of TPPU/TCPU exposure and drug action in tissues of interest other than blood are also required to be investigated. Physiologically based pharmacokinetic (PBPK) model is commonly used to integrate the system components (e.g. body fluid dynamics, tissue size and composition, abundance and distribution of drug receptors, and membrane transporters in various organ and tissue compartments) and the drug-dependent component to enables the study of ADME processes and mechanisms of action at the cellular level [105]. Our long-term goal is to use TPPU as a model drug to build a PBPK-TMDD model to better describe the pharmacokinetics and target occupancy of sEH inhibitors, which could facilitate the

drug design of sEH inhibitors and clinical dosage regime design of those small molecule drugs with strong TMDD characteristics.

3.6. Conclusions

Although TMDD models have been well documented, most of them were established in a single compound scenario. Our novel model represents the first TMDD interaction model for two small-molecule compounds competing for the same pharmacological target. TPPU and TCPU PK data in all mice was well described by our TMDD model. Our simulation result predicted that 90% of the sEH will be occupied shortly after a low dose of 0.3 mg/kg TPPU administration, with $\geq 40\%$ of sEH remaining to be bound with TPPU for at least 7 days. Further efficacy experiments are warranted to confirm the predicted target occupancy.

Table 3-1. Model development history.

No.	Dataset	Description	Fit goodness	OFV
1	Data only from experiment 1	5 compartmental model; Only TPPU shows TMDD; TPPU k_{off} was affected by TCPU plasma concentration;	Minimization successfully; Fit well with high RSE	3013.497
2	Data only from group experiment 1	6 compartmental model; TPPU and TCPU both show TMDD binding with R1 competitively;	Minimization successfully; Fit well with high RSE	2992.667
3	Data from group experiment 1 and 2 (experiment 2 group 3 was excluded)	6 compartmental model; TPPU and TCPU both show TMDD binding with R1 competitively;	Minimization successfully; Did not capture TCPU high dose	5811.443
4	Data from group experiment 1 and 2 (experiment 2 group 3 was excluded)	7 compartmental model; TPPU and TCPU both show TMDD binding with R1 competitively; TCPU and TPPU could also bind with each other's receptor complex; TCPU has another specific binding pool R2;	Terminated	
5	Data from group experiment 1 and 2 (experiment 2 group 3 was excluded)	6 compartmental model; TPPU and TCPU both show TMDD binding with R1 competitively; TCPU and TPPU could also bind with each other's receptor complex;	Terminated	

Table 3-1 (Continued)

6	Data from group experiment 1 and 2 (experiment 2 group 3 was excluded)	7 compartmental model; TPPU and TCPU both show TMDD binding with R1 competitively; TCPU has peripheral compartment;	Minimization successfully; Did not capture TCPU high dose with high RSE	5770.227
7	Data from group experiment 1 and 2 (experiment 2 group 3 was excluded)	6 compartmental model; TPPU and TCPU both show TMDD binding with R1 competitively; TCPU also have M-M elimination;	Minimization successfully; Fit well with high RSE	5921.653
8	Data from group experiment 1 and 2	7 compartmental model; TPPU and TCPU both show TMDD binding with R1 competitively; TCPU has another specific binding pool R2;	Minimization successfully; Did not capture TCPU high dose with high RSE	6227.922
Final Model	Data from group experiment 1 and 2 (experiment 2 group 3 was excluded)	7 compartmental model; TPPU and TCPU both show TMDD binding with R1 competitively; TCPU has another specific binding pool R2;	Minimization successfully; Good	5744.069

Table 3-2. Estimated parameters from the final TMDD model.

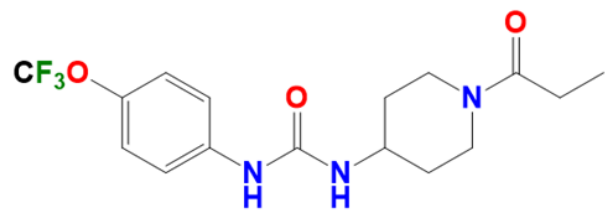
Parameters (unit)	Definition	Estimate	RSE (%)	Shrinking (%)
V_2 (L)	TPPU central volume of distribution	0.0231	13	
V_4 (L)	TCPUs central volume of distribution	0.0158	18	
CL_2 (L/h)	TPPU clearance	0.0017	8	
CL_4 (L/h)	TCPUs clearance	0.0014	17	
k_{a1} (h ⁻¹)	TPPU first-order absorption rate constant	0.961	10	
k_{a2} (h ⁻¹)	TCPUs first-order absorption rate constant	0.73	12	
$k_{\text{on TPPU}, R1}$ (nM ⁻¹ h ⁻¹)	TPPU second-order association rate constant to sEH	0.0918	20	
$k_{\text{off TPPU}, R1}$ (h ⁻¹)	TPPU first-order dissociation rate constant from sEH	2.24	20	
$k_{\text{on TCPU}, R1}$ (nM ⁻¹ h ⁻¹)	TCPUs second-order association rate constant to sEH	0.0779	44	
$k_{\text{off TCPU}, R1}$ (h ⁻¹)	TCPUs first-order dissociation rate constant from sEH	2.67	91	
$k_{\text{on TCPU}, R2}$ (nM ⁻¹ h ⁻¹)	TCPUs second-order association rate constant to unknown receptor	0.0275	96	
$k_{\text{off TCPU}, R2}$ (h ⁻¹)	TCPUs first-order dissociation rate constant from unknown receptor	11.9	92	
$R_{\text{max}1}$ (nmol)	Total sEH amount	16.2	4	
$R_{\text{max}2}$ (nmol)	Total unknown receptor amount	46.6	20	
ω^2_{V2}	Variance of inter-individual variability on V_2	0.353	31	5
ω^2_{V4}	Variance of inter-individual variability on V_4	0.178	42	35
ω^2_{CL2}	Variance of inter-individual variability on CL_2	0.17	46	2
ω^2_{CL4}	Variance of inter-individual variability on CL_4	0.315	36	28
ω^2_{ka1}	Variance of inter-individual variability on k_{a1}	0.195	42	9
ω^2_{ka2}	Variance of inter-individual variability on k_{a2}	0.0459	55	46
$\omega^2_{koff, TCPU,R1}$	Variance of inter-individual variability on $k_{\text{off, TCPU,R1}}$	3.74	60	42
$\omega^2_{koff, TCPU,R2}$	Variance of inter-individual variability on $k_{\text{off, TCPU,R2}}$	0.31	121	67
σ_1^2	Proportional variance of residual variability of TPPU PK	0.083	15	11
σ_2^2	Proportional variance of residual variability of TCPU PK	0.0557	38	17
σ_3^2	Additive variance of residual variability of TPPU PK	18.5	52	11
σ_4^2	Additive variance of residual variability of TCPU PK	0.0381	14	17

Table 3-3. Parameters comparison between observed and predicted values.

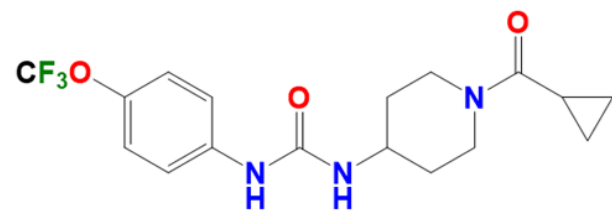
Compound	Dose (mg/kg)	C _{max} (nM)		AUC _{inf} (nM•h)		t _{1/2} (h)		k _{off} (h ⁻¹)		sEH _{total} (nmol)	
		Observed	Predicted	Observed	Predicted	Observed	Predicted	Observed	Predicted	Observed	Predicted
TPPU	0.3	436±319	390±250	12100±4630	12700±3360	54.3±1 7.5	58.6±9. 33	2.09 [92]	2.24	10.0	16.2
TCPU	1.0	853±207	971±196	22800±3720	21900±3340	15.2±2. 64	16.3±1. 68	1.76 [92]	2.67	[19]	
	3.0	9220±294	8740±31	159000±178	144000±334	10.5±4. 00	11.6±2. 00	67 15			
	10.0	57300±11 600	49800±9 570	1200000±85 500	102000±162 000	11.6±0. 86	11.7±0. 56				

data are presented as mean ± SD.

k_{off}, first-order dissociation rate constant; AUC_{inf}, area under the concentration-time curve from predose extrapolated to infinity; C_{max}, maximum concentration, t_{1/2}, terminal elimination half-life; sEH_{total}, sEH total amount in rat body.



TPPU



TCPU

Figure 3-1. Chemical structure of TPPU and TCPU, two potent sEH inhibitors.

Experiment 1

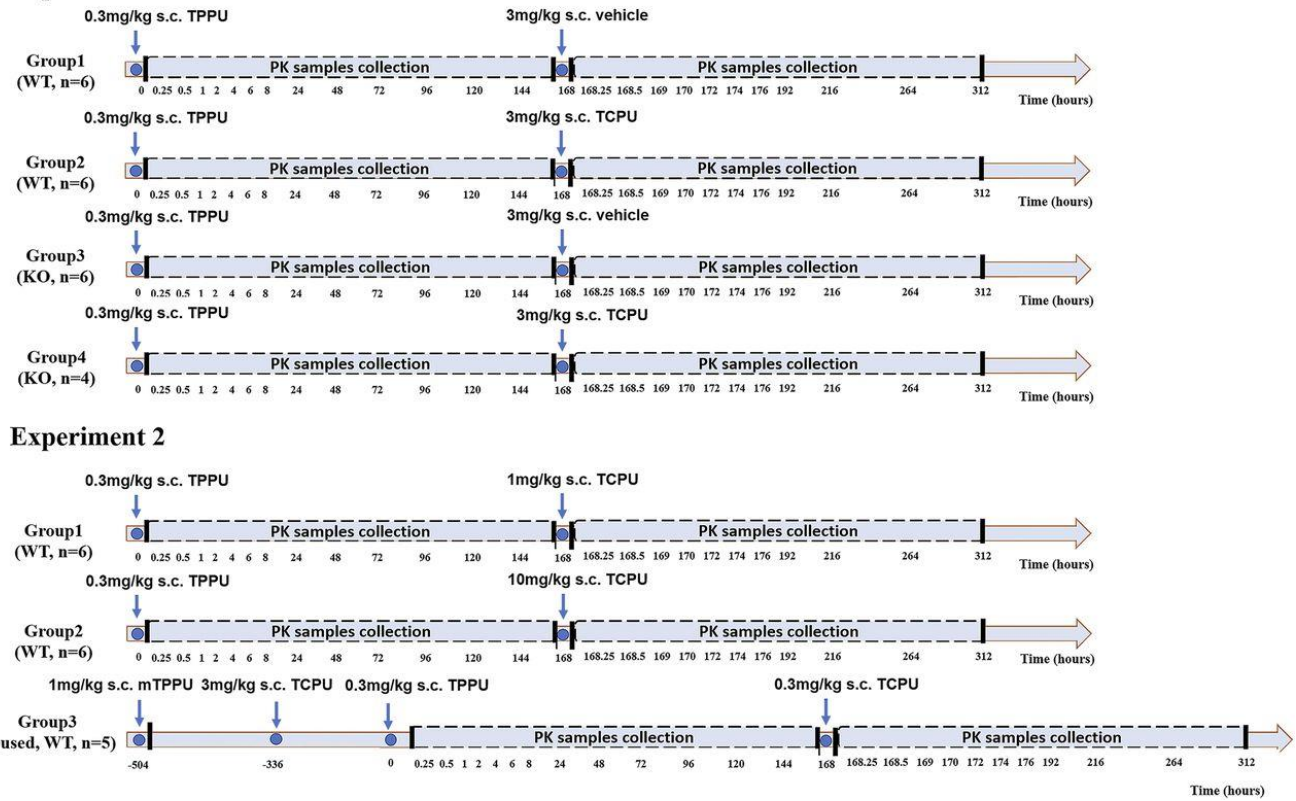


Figure 3-2. Schematic flow diagram of animal study protocol in experiment 1 and experiment 2.

Four treatment groups from wild-type or sEH-deficient mice were included in experiment 1. Three treatment groups from wild-type mice were included in experiment 2.

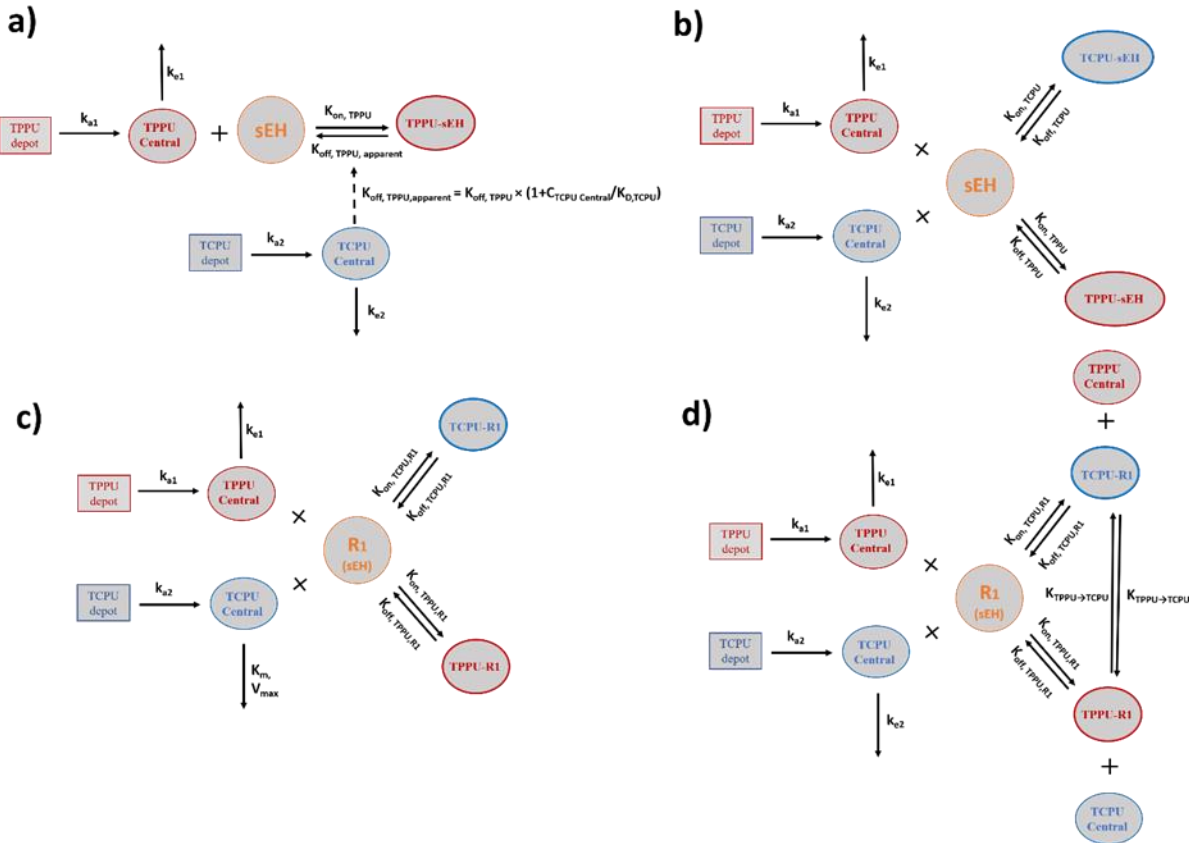


Figure 3-3. Model structures in model development history.

Model with one TMDD component. b) Model with two TMDD components. c) Model with two TMDD components plus MM process. d) Model with two TMDD components mixing with competitive and non-competitive mechanism.

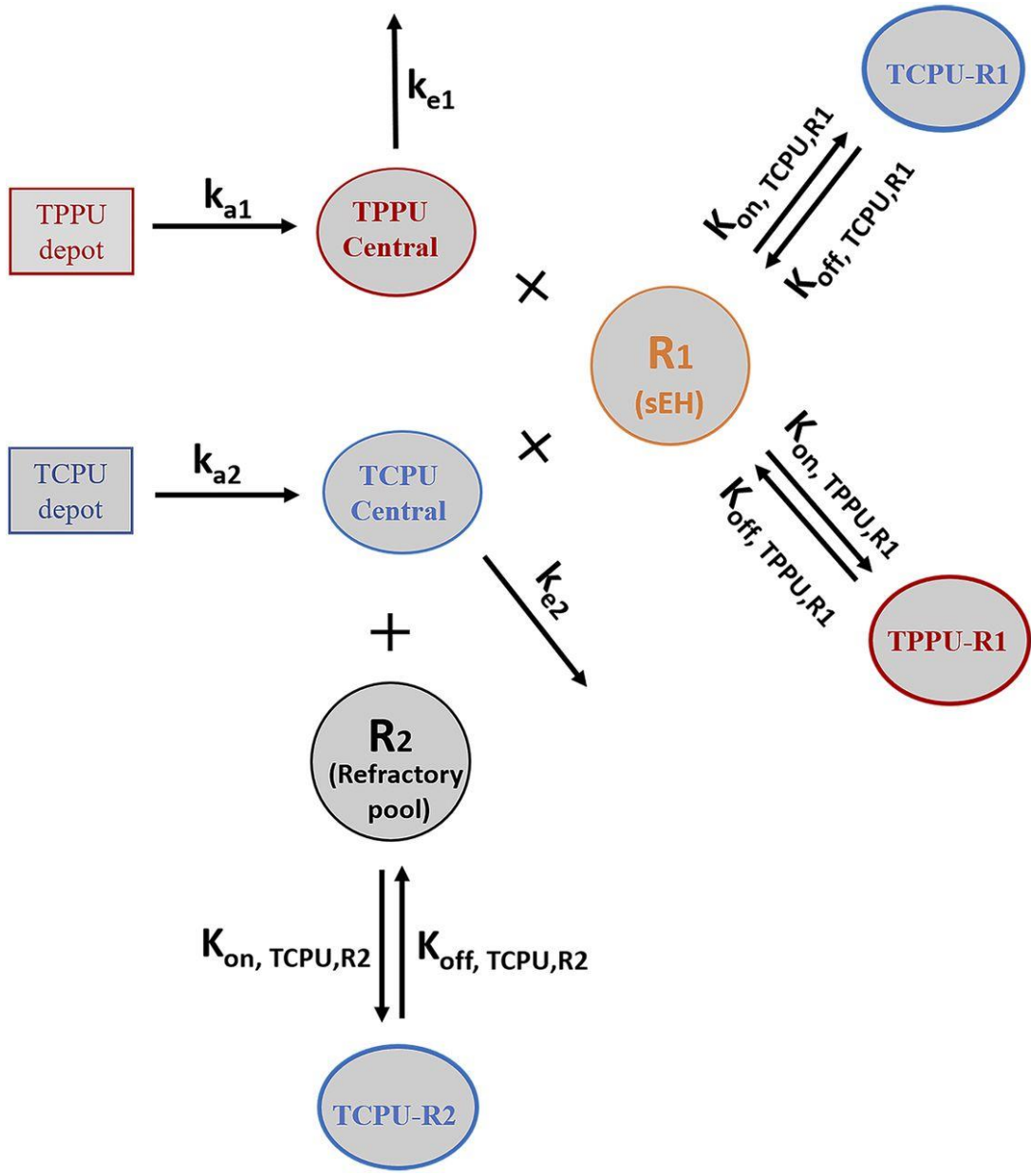


Figure 3-4. Final TMDD model describing the pharmacokinetics of TPPU and TCPUs.

Both TPPU and TCPUs were absorbed from the depot with first-order absorption rate constants (k_{a1} and k_{a2} , respectively) and eliminated from the central compartment with first-order elimination rate constants (k_{e1} and k_{e2} , respectively). Both TPPU and TCPUs can bind with sEH (i.e., R1) with second-order association rate constant ($k_{on, TPPU, R1}$ and $k_{on, TCPUs, R1}$, respectively) to form drug-sEH complexes. TPPU-sEH and TCPUs-sEH can dissociate back to free drug and free sEH target with the first-order dissociation rate constants ($k_{off, TPPU, R1}$ and $k_{off, TCPUs, R1}$, respectively). In addition, TCPUs can also bind to an unknown target termed a refractory pool (R2) with a different $k_{on, TCPUs, R2}$ value and dissociate from the TCPUs-R2 complex with a different $k_{off, TCPUs, R2}$ value. The total amounts of sEH (R_{max1}) and refractory pool (R_{max2}) in mice are assumed to be constant.

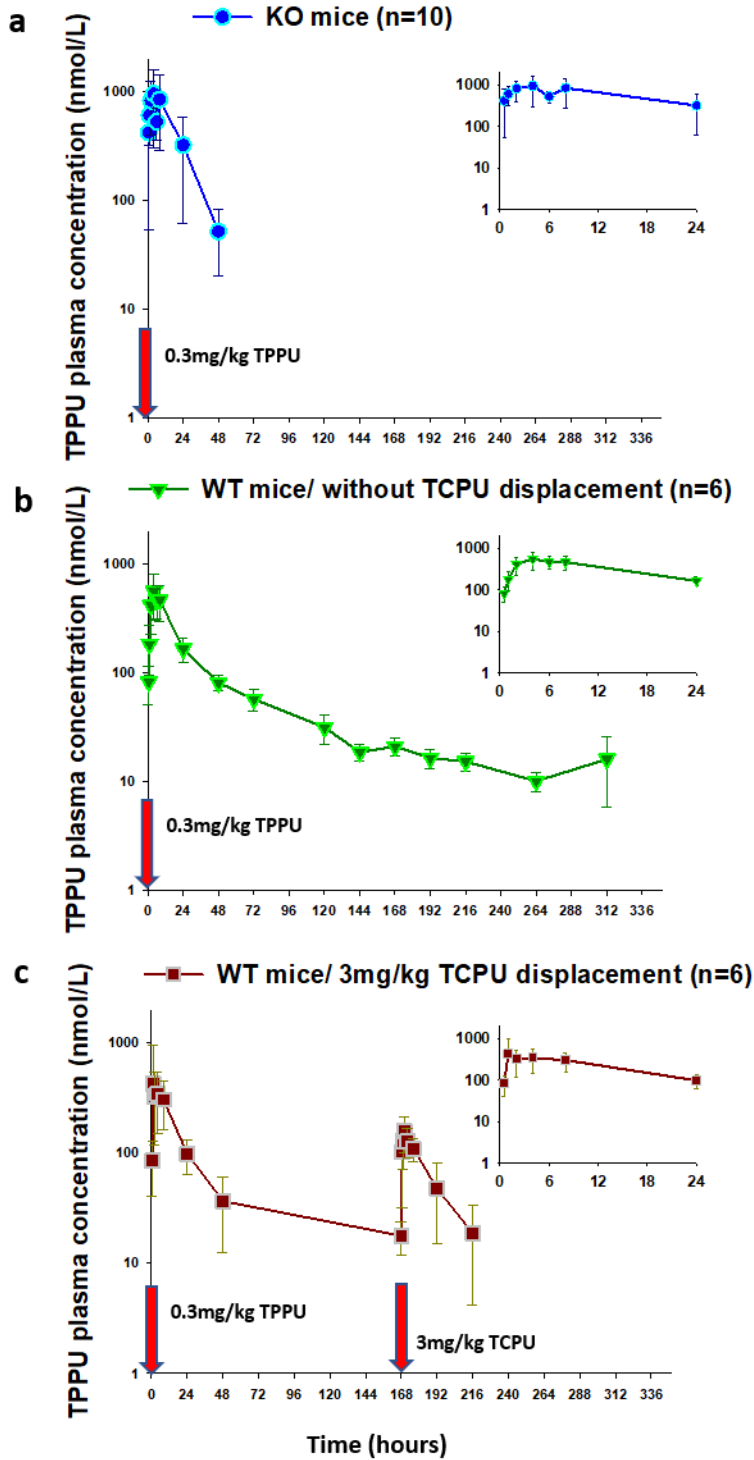


Figure 3-5. Time courses of mean observed (symbols) and model-predicted (lines) TPPU blood concentrations following 0.3 mg/kg TPPU at time 0 in (a) sEH knock-out mice without TCPU displacement, (b) wild-type mice without TCPU displacement, and (c) wild-type mice with 3 mg/kg TCPU displacement at 168 hours.

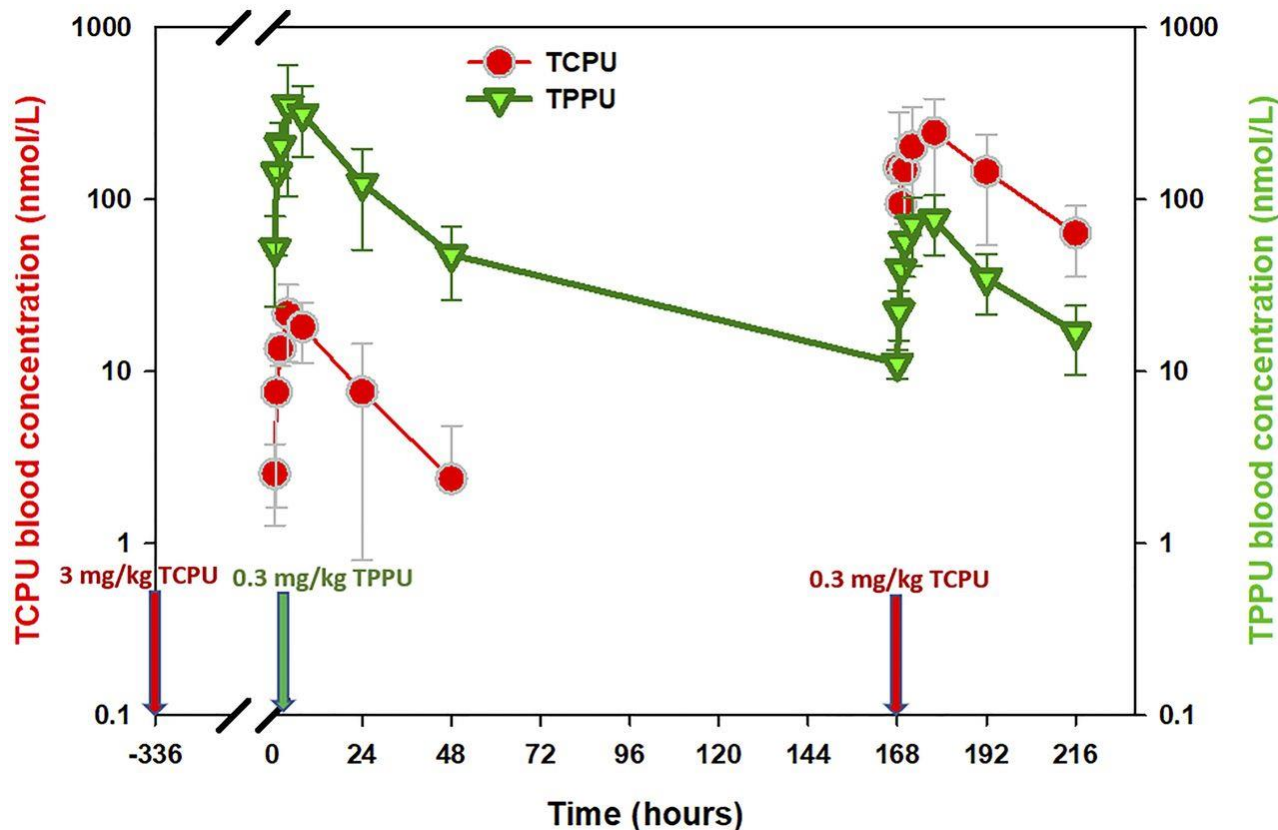


Figure 3-6. Time courses of the mean observed TPPU and TCPU blood concentrations in wild-type mice following 0.3 mg/kg TPPU at time 0 and 0.3 mg/kg TCPU at time 168 hours.

The mice used in this experiment were reused from a previous experiment, in which the mice were given a weak sEH inhibitor, mTPPU, at 1 mg/kg s.c. 3 weeks ago followed by 3 mg/kg TCPU s.c. 1 week from the administration of mTPPU.

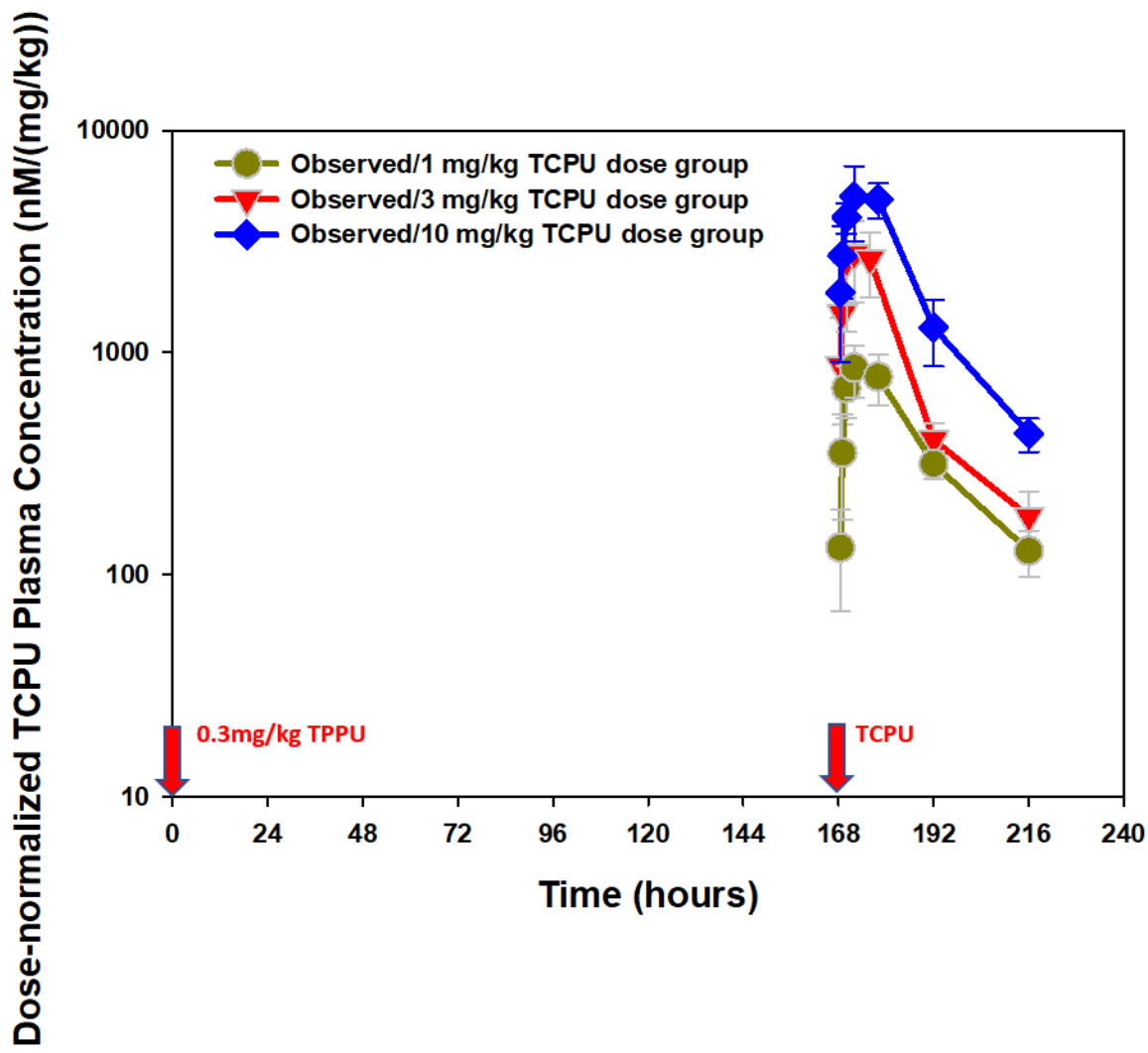


Figure 3-7. Time courses of mean observed TCPU plasma concentrations following 0.3 mg/kg TPPU at time 0 in wild-type mice with 1,3, 10 mg/kg TCPU displacement at 168 hours.

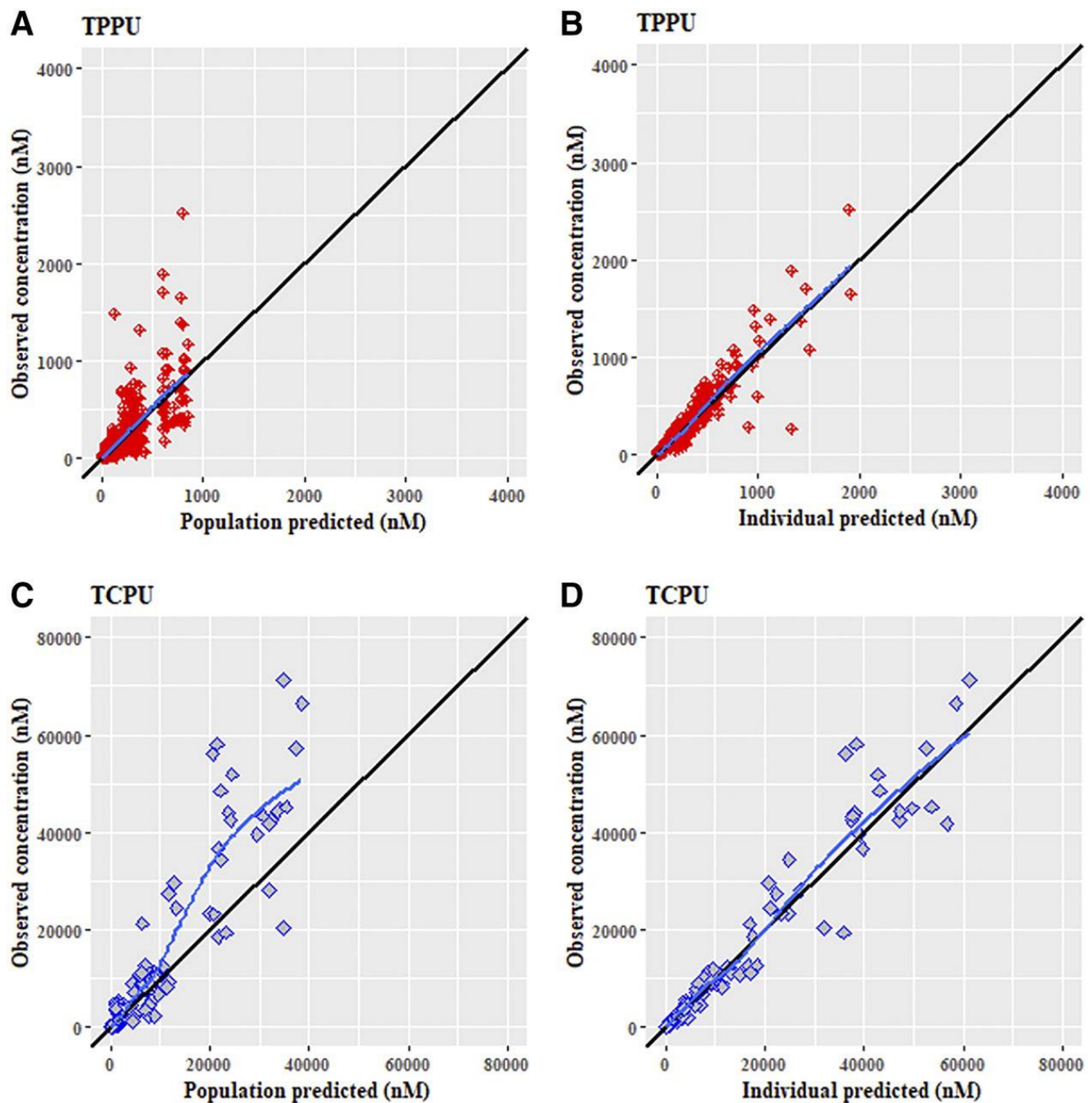


Figure 3-8. Goodness fit plots for the final population pharmacokinetics modeling.

(A) TPPU observed vs. population-predicted, (B) TPPU observed vs. individual-predicted, (C) TCPU observed vs. population-predicted, and (D) TCPU observed vs. individual-predicted. Solid black lines represent the lines of identity. Solid blue lines represent lowess line.

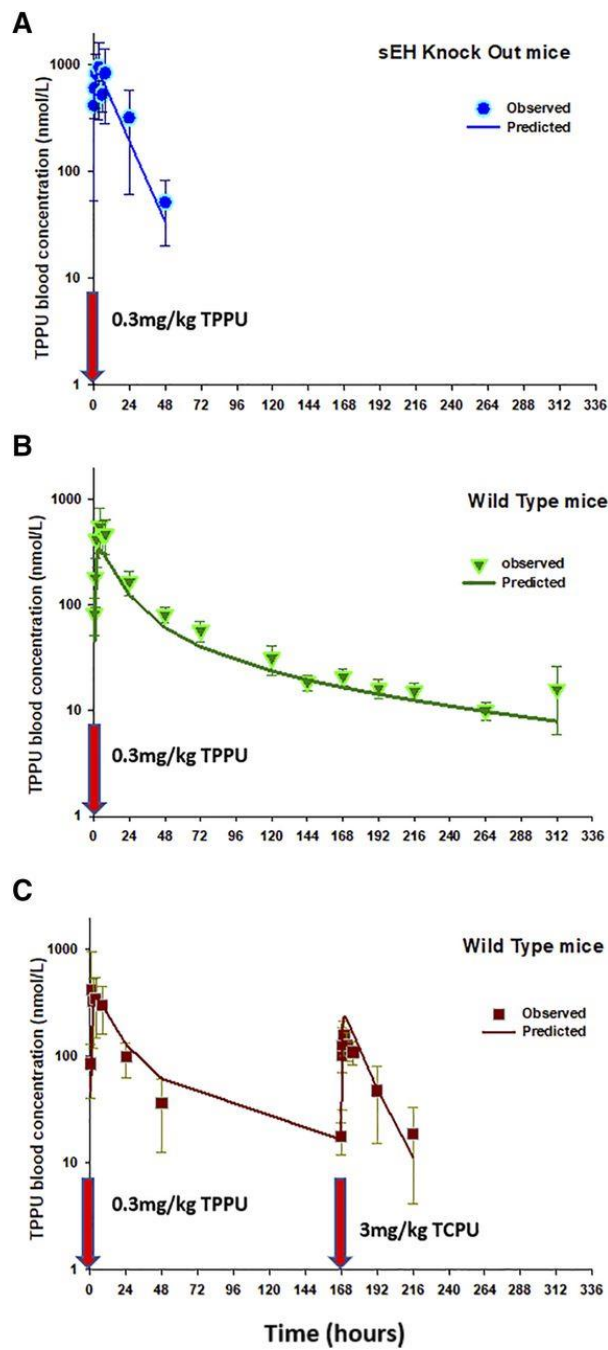


Figure 3-9. Time courses of mean observed (symbols) and model-predicted (lines) TPPU blood concentrations following 0.3 mg/kg TPPU at time 0.

(a) sEH-deficient mice without TCPU displacement, (b) wild-type mice without TCPU displacement, and (c) wild-type mice with 3 mg/kg TCPU displacement at 168 hours.

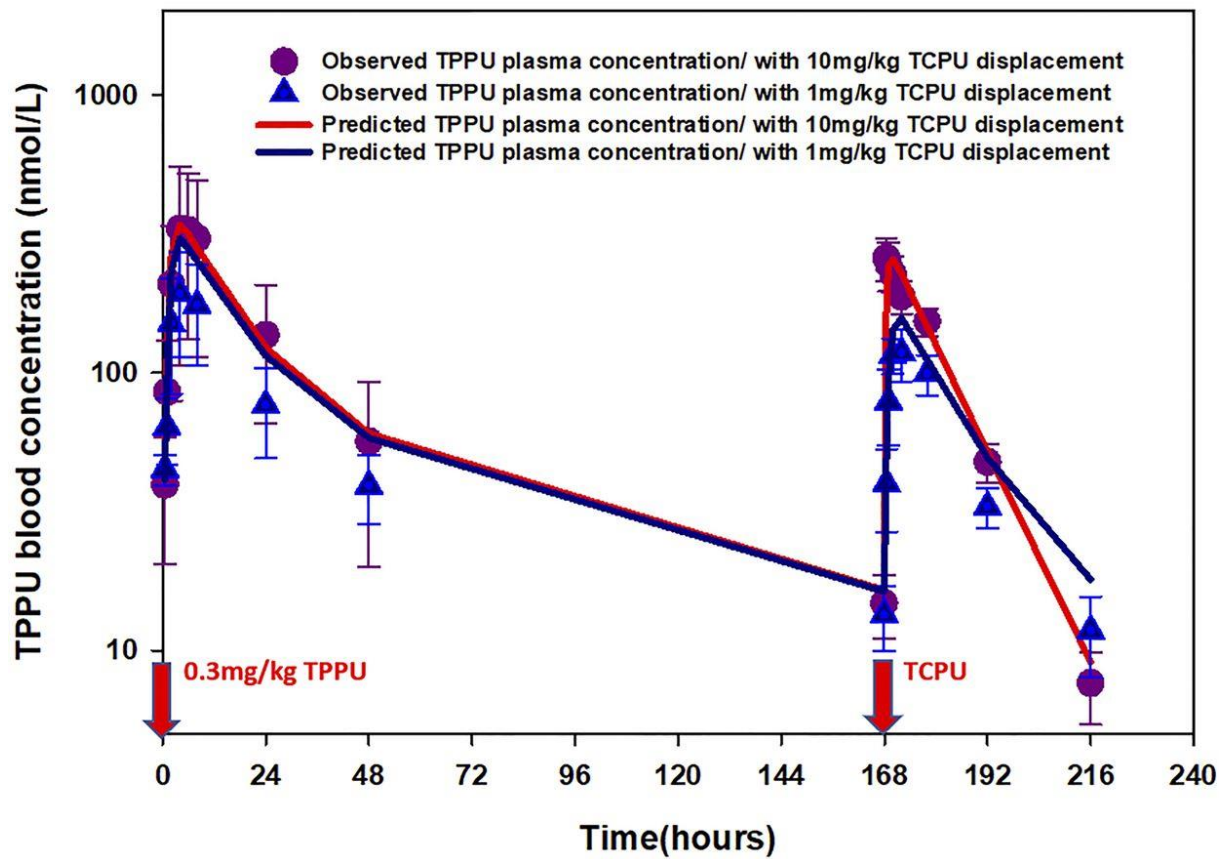


Figure 3-10. Time courses of mean observed (symbols) and model-predicted (lines) TPPU blood concentrations when wild-type mice received 0.3 mg/kg TPPU at time 0 and different doses of TCPU (1 or 10 mg/kg) at 168 hours ($n = 6$ per group).

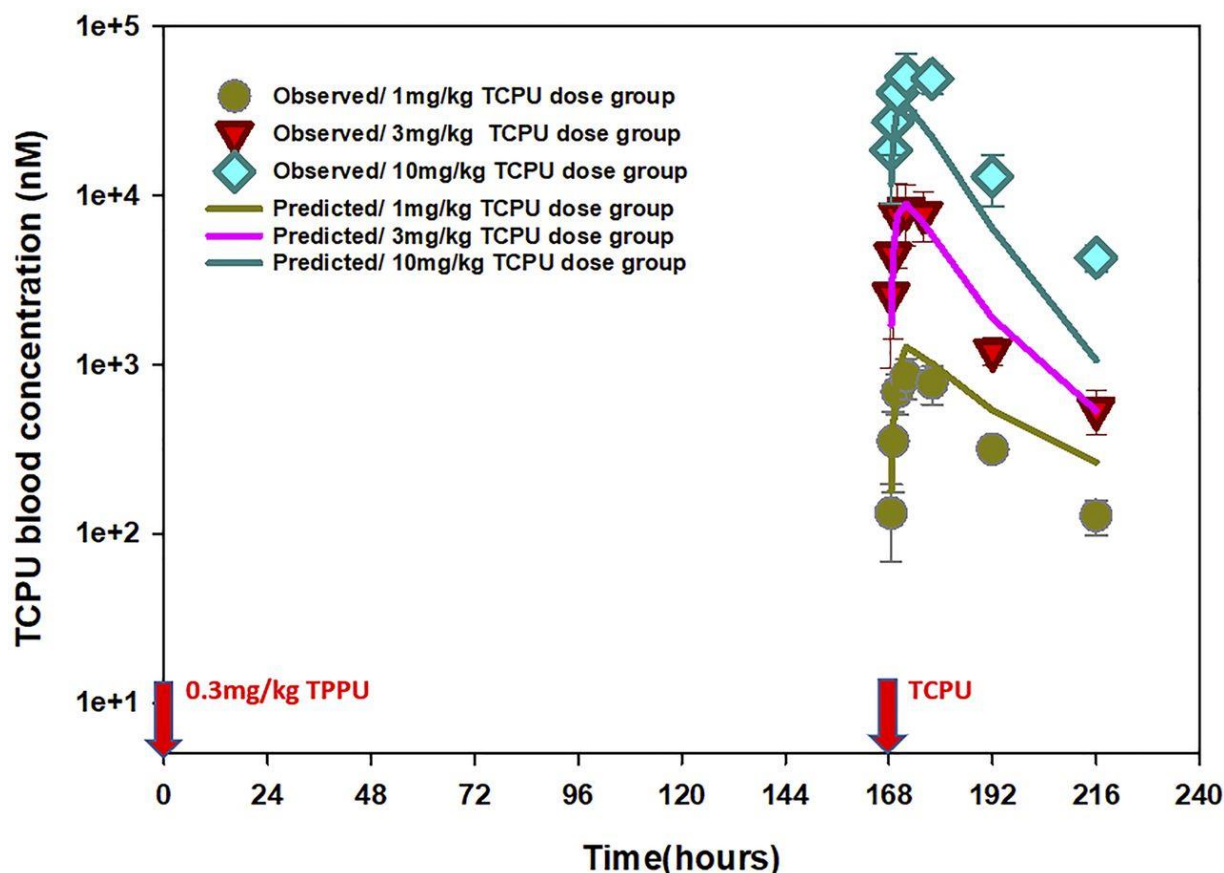


Figure 3-11. Time courses of mean observed (symbols) and model-predicted (lines) TCPU blood concentrations when wild-type mice received 0.3 mg/kg TPPU at time 0 and different doses of TCPU (1, 3, or 10 mg/kg) at 168 hours ($n = 6$ per group).

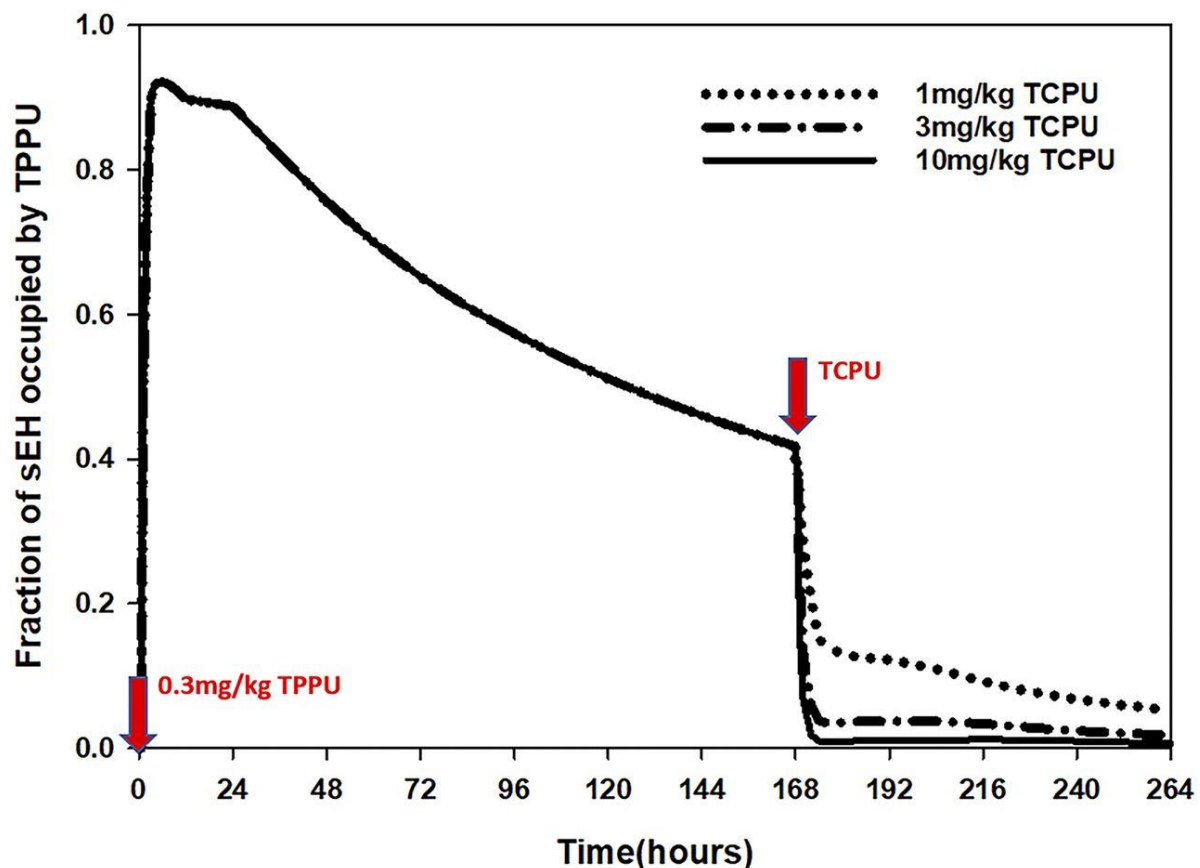


Figure 3-12. Simulated time course of fraction of sEH occupied by TPPU when wild-type mice receive 0.3 mg/kg TPPU at time 0 and different doses of TCPU (1, 3, or 10 mg/kg) at 168 hours.

**CHAPTER 4: INCORPORATING PHARMACOLOGICAL TARGET-MEDIATED
DRUG DISPOSITION IN A PHYSIOLOGICALLY BASED PHARMACOKINETIC
MODEL OF LINAGLIPTIN IN RAT AND SCALE-UP TO HUMAN**

Most of this chapter has been published in The AAPS Journal.

(Wu N, An G. *AAPS J*. 2020 Sep 29;22(6):125.)

4.1. Abstract

Linagliptin demonstrates substantial nonlinear pharmacokinetics due to its saturable binding to its pharmacological target dipeptidyl peptide 4 (DPP-4), a phenomenon known as target-mediated drug disposition (TMDD). In the current study, we established a novel whole-body physiologically-based pharmacokinetic (PBPK)-TMDD model for linagliptin. This comprehensive model contains plasma and 14 tissue compartments, among which TMDD binding process was incorporated in 9 of them, namely the plasma, kidney, liver, spleen, lung, skin, salivary gland, thymus, and reproductive organs. Our final model adequately captured the concentration-time profiles of linagliptin in both plasma and various tissues in both wildtype rats and DPP4-deficient rats following different doses. The association rate constant (k_{on}) in plasma and tissues were estimated to be 0.943 and $0.00680 \text{ nM}^{-1}\text{h}^{-1}$, respectively, and dissociation rate constant (k_{off}), in plasma and tissues were estimated to be 0.0698 and 0.00880 h^{-1} , respectively. The binding affinity of linagliptin to DPP-4 (K_d) was predicted to be higher in plasma (0.0740 nM) than that in tissue (1.29 nM). When scaled up to a human, this model captured the substantial and complex nonlinear pharmacokinetic behavior of linagliptin in human adults that is characterized by less-than dose-proportional increase in plasma exposure, dose-dependent clearance and volume of distribution, as well as long terminal half-life with minimal accumulation after repeated doses. Our modeling work is not only novel but also of high significance as the whole-body PBPK-TMDD model platform developed using linagliptin as the model compound could be applied to other small-molecule compounds exhibiting TMDD to facilitate their optimal dose selection.

4.2. Introduction

Linagliptin is a competitive and highly selective dipeptidyl peptide 4 (DPP-4) inhibitor that was licensed in the US, Europe, Japan and other territories in 2011 for the treatment of type 2 diabetes mellitus (T2DM) (as shown in **Figure 4-1**) [36, 38]. DPP-4, a serine type protease widely distributed in mammalian tissues as a membrane-bound form and in plasma as a soluble protein, is responsible for cleavage of glucagon-like peptide-1 (GLP-1), and thus inactivates GLP-1 mediated insulin secretion [106]. Therefore, inhibition of DPP-4 enhances GLP-1 level and prolongs the action of GLP-1, and subsequently restores the beneficial effect of GLP-1 on lowering plasma glucose levels [107-109]. Among the various pharmacological options available for T2DM, DPP-4 inhibitors represent a new and promising class of oral antihyperglycemic agents that are characterized by low risk of hypoglycemic episodes and neutral effect on body weight [110].

Thomas et al reported that linagliptin inhibited DPP-4 activity in vitro with an IC_{50} of 1 nM, which is more potent than other licensed gliptins, including sitagliptin (19 nM), alogliptin (24 nM), saxagliptin (50 nM) and vildagliptin (62 nM) [38]. In addition, the binding of linagliptin to the DPP-4 enzyme is tight, with a k_i of 1 nM, and long lasting, with a dissociation rate constant (k_{off}) of 0.108 h^{-1} that is approximately 10-fold slower than the off-rate for vildagliptin [38]. Coupled with its high-affinity and long lasting binding to the DPP-4 enzyme, linagliptin exhibits a unique nonlinear pharmacokinetic profile that is different from the linear pharmacokinetics observed in other DPP-4 inhibitors [14, 34, 39, 111, 112]. Several lines of evidence strongly indicate that the substantial nonlinear pharmacokinetics of linagliptin is caused by the interaction of linagliptin with its pharmacological target DPP-4, a phenomenon known as target-mediated drug disposition (TMDD) [1, 2]. Followings are the key evidence: 1) Linagliptin exhibited

nonlinear pharmacokinetics in wildtype rats, with less than dose-proportional increase in exposure as well as long terminal half-life. In contrast, linagliptin pharmacokinetics in DPP-4 deficient rats was dose proportional (i.e. linear pharmacokinetics) with much shorter half-life [14]; 2) In vitro experiment showed that linagliptin exhibited concentration-dependent protein binding in plasma from human, wildtype mouse and rat (99% at 1 nM to 70-80% at >30 nM) but concentration-independent protein binding in plasma from DPP-4 knockout mice and DPP-4-deficient rats (~70% across all concentrations evaluated) [35]. This indicated that the observed concentration-dependent plasma protein binding is due to the binding of linagliptin to its high-affinity but readily saturable (i.e., low-capacity) target DPP-4 that is presented in plasma. 3) Saturable binding of linagliptin to its target DPP-4 occurs not only in plasma but also in tissues, especially in those with high DPP-4 expression. Fuchs et al determined the tissue distribution of linagliptin in wild-type and DPP-4 deficient rats at different dose levels using whole body autoradiography and they found that in wild-type rats, linagliptin concentrations in tissues with DPP-4 expression, including kidney, lung, liver, spleen, thymus, salivary gland, skin, and reproductive organs, were much higher than that the respective tissues from DPP-4 deficient rats [113].

Consistent with the target-mediated nonlinear pharmacokinetics observed in vitro and in animals, linagliptin exhibits substantial and complex nonlinear pharmacokinetics in human that is characterized by less-than dose proportional increase in plasma exposure, concentration-dependent plasma protein binding, as well as long terminal half-life (110-130 hours) with minimal accumulation after repeated doses [39]. Although TMDD has been observed in several other small-molecule compounds whose pharmacological targets are located in tissues [15, 21, 69, 87, 114], the TMDD profile in linagliptin is more complicated and unique in certain aspect as its

pharmacological target DPP-4 presents not only in tissues but also in plasma, and the target in both locations plays a significant role in linagliptin disposition.

To characterize the complicated pharmacokinetics of linagliptin, several pharmacometric models, including a TMDD model, have been developed to elucidate its dose-exposure relationship [14, 34, 115]. However, the pharmacometric models reported so far only focus on the plasma exposure of linagliptin. Considering the important role of DPP-4 in linagliptin tissue distribution, changes in the magnitude and time course of linagliptin exposure in tissues of interest other than blood are also required to be investigated. To meet this need, establishing a physiologically-based pharmacokinetics (PBPK) model for linagliptin is highly valuable since it can be used to evaluate and predict the disposition of a compound of interest in various organs. However, traditional PBPK model does not provide mechanistic insight as usually well-stirred model is assumed for each organ [73, 116]. As a result, it does not provide reliable prediction if the concentration of drug in the organ is not in equilibrium with that in the emergent blood (i.e., situations where well-stirred model is invalid); An example for this type of situation is those drugs with potent and long-lasting target binding (such as DPP-4 inhibitor linagliptin that we study here), where the equilibrium may never be reached. Therefore, in order to predict linagliptin's pharmacokinetics and tissue distribution more accurately, a mechanistic PBPK model that incorporates DPP-4 binding affinity and binding kinetics (i.e., TMDD process) is needed. The development of such mechanistic model, which has never been done before, represented the major goal of the present study. Based on the literature reported rat data, a whole-body PBPK model incorporating TMDD components was developed to quantitatively characterize the time-course of linagliptin in plasma and various tissues in both wildtype and DPP-4 deficient rats simultaneously. The PBPK-TMDD model developed in rats was then extrapolated to human by taking into account

the interspecies physiology differences, and the scale up potential of this model was evaluated by comparing model simulated vs literature reported human pharmacokinetic profiles.

4.3. Methods

4.3.1. Data source

4.3.1.1. Data source for PBPK-TMDD model development in rat

The data used for whole-body PBPK-TMDD model development came from three published studies conducted in rats [14, 113, 117]. The study design of these studies is summarized in **Table 4-1**. Rat study No.1 determined the concentrations of linagliptin in various tissues using whole body autoradiography following different doses of [¹⁴C] linagliptin in both wild-type and DPP-4 deficient rats. This study contained three parts. Part I determined linagliptin concentrations in various tissues of wildtype and DPP-4 deficient rats at different time points (3, 24 and 168 hours) after an i.v. dose of 2 mg/kg. Part II determined linagliptin concentrations in various tissues at a single time point (72 hours) after iv administration of linagliptin at various doses ranging from 0.01 to 50 mg/kg. Part III determined linagliptin concentrations in various tissues of wildtype rats at different time points (24, 96, 168, 240 and 336 hours) after 2 mg/kg oral dose once daily (QD) for 14 days. Rat study No.2 reported linagliptin plasma concentration-time profiles following single iv doses of 0.01, 0.1, 0.3, 1, 3, 10, and 50 mg/kg of [¹⁴C] linagliptin in both wild-type and DPP-4 deficient rats. Blood samples were collected at 0.033, 0.167, 1, 4, 8, 24, 48, and 72 hours. Rat study No.3 evaluated linagliptin plasma concentrations at various time points (13 time points ranging from 0.25 to 72 hours) following a single oral dose of 1 or 15 mg/kg linagliptin in wildtype rats. In Rat study No.1, mean concentrations of linagliptin at each time point, each tissue, and each dose were reported in their tables, and these values were used directly in our analysis. As Rat study

No.2 and No.3 presented their pharmacokinetics data using plots. Mean plasma concentrations of linagliptin at each time point and each dose were digitized using Engauge Digitizer (<https://markummitchell.github.io/engauge-digitizer/>).

4.3.1.2. Data source for PBPK-TMDD model extrapolation in human

After PBPK-TMDD model was established in rat, it was scaled up to human to simulate linagliptin plasma concentration – time profiles. The simulated profiles were then compared with those published linagliptin human pharmacokinetic profiles following the same dose regimen and sampling time schedule. Two human reports were used for comparison [39, 118]. Human study No.1 evaluated the pharmacokinetics of linagliptin at various time points following single oral doses of 1, 2.5, 5, or 10 mg linagliptin in Japanese healthy volunteers [118]. Human study No.2 evaluated the pharmacokinetics of linagliptin at various time points following oral doses of 0.5, 2.5, or 10 mg linagliptin once daily for 28 days in Japanese patients with T2DM [39]. The study design of these studies is summarized in **Table 4-1**. Mean plasma concentrations of linagliptin at each time point and each dose from these two studies were digitized using Engauge Digitizer.

4.3.2. Whole-body PBPK- TMDD model development in rats

4.3.2.1. Analysis software and estimation method

All pharmacokinetics and tissue distribution data for linagliptin following different doses in both wildtype and DPP-4 deficient rats were analyzed simultaneously using the nonlinear mixed effect modeling approach with NONMEM (Version 7.4.3; Icon Development Solutions, Ellicott City, Maryland) interfaced with Pirana (version 2.9.9, <http://www.pirana-software.com/>). The first-order conditional estimation method with interaction (FOCEI) and a user-defined subroutine (ADVAN13) were used to estimate the parameters. Since only mean data were used in the analysis,

inter-subject variability (IIV) is not applicable and therefore was not included. The residual variability (RV) was evaluated, and it was assumed to be normally distributed with a mean of 0 and a variance of σ^2 . Additive, proportional and a combined proportional and additive RV models were evaluated. SigmaPlot and RStudio (version 1.0.143, <https://www.rstudio.com/>) were used for graphical analysis and data handling.

4.3.2.2. Structure of the whole-body PBPK-TMDD model

The whole-body PBPK-TMDD model was developed with linagliptin data from plasma and 14 organs, namely lung, liver, kidney, heart, spleen, pancreas, thymus, muscle, skin, fat, salivary gland, adrenal, bone marrow, and reproductive organs. A schematic diagram for the structure of the developed whole-body PBPK-TMDD model is shown in **Figure 4-2**. In this model, each organ was represented by one compartment, and all compartments were interconnected through organ blood flow. In addition to plasma and those 14 tissue compartments, a “remainder” compartment was included in the model to account for linagliptin concentrations in those organs that were not determined. Among the 14 organs included in the model, TMDD component was incorporated in 8 of them, including kidney, liver, spleen, lung, skin, salivary gland, thymus, and reproductive system. Since DPP-4 is presented not only in various tissues but also in plasma, TMDD process was also incorporated in the plasma compartment. As shown in **Figure 4-2**, in plasma and those 8 organs with DPP-4 expression, linagliptin molecules interacted with the DPP-4 enzyme with a second-order association rate constant (k_{on}) to form a linagliptin-DPP4 complex. Linagliptin-DPP4 complex dissociated back to free DPP-4 target and free drug with a first-order dissociation rate constant (k_{off}). Only linagliptin molecules not bound to DPP-4 target could enter and leave each compartment and be eliminated. For those organs without TMDD process, well-stirred model was used in which K_p values were incorporated. As linagliptin has been reported to

be eliminated predominantly through biliary excretion [36, 117, 119], clearance of linagliptin via the liver was assumed to be the only elimination pathway in our model.

4.3.2.3. Representative equations

Our whole-body PBPK-TMDD model contains plasma and 15 tissue compartments with a total of 26 differential equations. Since the format of the differential equations in many compartments is similar, only several representative equations are listed as follows. The equation for the rate transfer of linagliptin in the plasma compartment is

$$\frac{dA_{\text{linagliptin,plasma}}}{dt} = k_{\text{absorption}} \times A_{\text{linagliptin,depot}} - Q_{\text{lung}} \times C_{\text{linagliptin,plasma}} + \sum(Q_{\text{tissue}} \times \frac{C_{\text{linagliptin,tissue}}}{Kp_{\text{tissue}}}) - k_{\text{on,linagliptin,plasma}} \times (R_{\text{max,plasma}} - A_{[\text{linagliptin-DPP4}],\text{plasma}}) \times C_{\text{linagliptin,plasma}} + k_{\text{off,linagliptin,plasma}} \times A_{[\text{linagliptin-DPP4}],\text{plasma}}$$

$$A_{\text{linagliptin,plasma}}(0) = \begin{cases} \text{Dose; i.v} \\ 0; p.o \end{cases} \quad (4.1)$$

$$\frac{dA_{[\text{linagliptin-DPP4}],\text{plasma}}}{dt} = k_{\text{on,linagliptin,plasma}} \times (R_{\text{max,plasma}} - A_{[\text{linagliptin-DPP4}],\text{plasma}}) \times C_{\text{linagliptin,plasma}} - k_{\text{off,linagliptin,plasma}} \times A_{[\text{linagliptin-DPP4}],\text{plasma}}$$

$$A_{[\text{linagliptin-DPP4}],\text{plasma}}(0) = 0 \quad (4.2)$$

The equation for the rate transfer of linagliptin in lung is:

$$\begin{aligned}
\frac{dA_{linagliptin,lung}}{dt} = & Q_{lung} \times C_{linagliptin,plasma} - Q_{lung} \times \frac{C_{linagliptin,lung}}{Kp_{lung}} - k_{on,linagliptin,tissue} \times \\
& (R_{max,lung} - A_{[linagliptin-DPP4],lung}) \times C_{linagliptin,lung} + k_{off,linagliptin,tissue} \times \\
& A_{[linagliptin-DPP4],lung} \\
A_{linagliptin,lung}(0) = & 0
\end{aligned} \tag{4.3}$$

$$\begin{aligned}
\frac{dA_{[linagliptin-DPP4],lung}}{dt} = & k_{on,linagliptin,tissue} \times (R_{max,lung} - A_{[linagliptin-DPP4],lung}) \times \\
& C_{linagliptin,lung} - k_{off,linagliptin,tissue} \times A_{[linagliptin-DPP4],lung} \\
A_{[linagliptin-DPP4],lung}(0) = & 0
\end{aligned} \tag{4.4}$$

The equation for the rate transfer of linagliptin in eliminating organ liver is:

$$\begin{aligned}
\frac{dA_{linagliptin,liver}}{dt} = & (Q_{liver} - Q_{spleen} - Q_{pancreas}) \times \frac{C_{linagliptin,lung}}{Kp_{lung}} + Q_{spleen} \times \frac{C_{linagliptin,spleen}}{Kp_{spleen}} + \\
& Q_{pancreas} \times \frac{C_{linagliptin,pancreas}}{Kp_{pancreas}} - Q_{liver} \times \frac{C_{linagliptin,liver}}{Kp_{liver}} - k_{on,linagliptin,tissue} \times (R_{max,liver} - \\
& A_{[linagliptin-DPP4],liver}) \times C_{linagliptin,liver} + k_{off,linagliptin,tissue} \times A_{[linagliptin-DPP4],liver} - \\
& CL_{int} \times \frac{C_{linagliptin,liver}}{Kp_{liver}} \\
A_{linagliptin,liver}(0) = & 0
\end{aligned} \tag{4.5}$$

$$\begin{aligned}
\frac{dA_{[linagliptin-DPP4],liver}}{dt} = & k_{on,linagliptin,tissue} \times (R_{max,liver} - A_{[linagliptin-DPP4],liver}) \times \\
& C_{linagliptin,liver} - k_{off,linagliptin,tissue} \times A_{[linagliptin-DPP4],liver} \\
A_{[linagliptin-DPP4],liver}(0) = & 0
\end{aligned} \tag{4.6}$$

The general equation for the rate transfer of linagliptin in tissues or organs with TMDD process (except for liver) is:

$$\begin{aligned} \frac{dA_{\text{linagliptin,tissue}}}{dt} = & Q_{\text{tissue}} \times \frac{C_{\text{linagliptin,lung}}}{K_p \text{ lung}} - Q_{\text{tissue}} \times \frac{C_{\text{linagliptin,tissue}}}{K_p \text{ tissue}} - k_{\text{on,linagliptin,tissue}} \times \\ & (R_{\text{max,tissue}} - A_{[\text{linagliptin-DPP4}],\text{tissue}}) \times C_{\text{linagliptin,tissue}} + k_{\text{off,linagliptin,tissue}} \times \\ & A_{[\text{linagliptin-DPP4}],\text{tissue}} \\ A_{\text{linagliptin,tissue}}(0) = 0 \end{aligned} \quad (4.7)$$

$$\begin{aligned} \frac{dA_{[\text{linagliptin-DPP4}],\text{tissue}}}{dt} = & k_{\text{on,linagliptin,tissue}} \times (R_{\text{max,tissue}} - A_{[\text{linagliptin-DPP4}],\text{tissue}}) \times \\ & C_{\text{linagliptin,tissue}} - k_{\text{off,linagliptin,tissue}} \times A_{[\text{linagliptin-DPP4}],\text{tissue}} \\ A_{[\text{linagliptin-DPP4}],\text{tissue}}(0) = 0 \end{aligned} \quad (4.8)$$

The general equation for the rate transfer of linagliptin in tissues or organs without TMDD process is:

$$\begin{aligned} \frac{dA_{\text{linagliptin,tissue}}}{dt} = & Q_{\text{tissue}} \times \frac{C_{\text{linagliptin,lung}}}{K_p \text{ lung}} - Q_{\text{tissue}} \times \frac{C_{\text{linagliptin,tissue}}}{K_p \text{ tissue}} \\ A_{\text{linagliptin,tissue}}(0) = 0 \end{aligned} \quad (4.9)$$

Here C represents concentration, A represents amount, Q represents organ flow rate, K_p represents partition coefficients, k_{on} represents binding rate constant, k_{off} represents dissociation rate constant, R_{max} represents the total amount of DPP-4 in rat plasma, or each tissue/ organ.

4.3.2.4. Parameters that were fixed during PBPK-TMDD model fitting

During the model fitting process, all physiological parameters such as organ blood flow and organ weight were fixed based on the literature reports [120-125]. **Table 4-2** lists the reported organ weight and organ flow rate for a 250 g rat. Blood flow rate fraction (Q_{fraction}) and tissue volume fraction (V_{fraction}) in each organ was also included in **Table 4-2**. The relationship between Q_{fraction} and the flow rate $Q_{\text{rat tissue}}$ in each tissue or organ is expressed as following:

$$Q_{\text{rat tissue}} = Q_{\text{fraction}} \times CO_{\text{total}} \quad (4.10)$$

Cardiac output (CO_{total}) value was fixed to 3.06 L/hour for rats weighing from 0.169~0.25 kg [120]. Since the average body weight of the rats used in animal study No.1 was different from 250 g (**Table 4-1**), their organ volume used in the model was calculated based on the fraction (i.e. V_{fraction}) listed in **Table 4-2** and average weight reported in animal study No.1. As animal study No.2 and No.3 did not report the bodyweight of the rats used in their studies, mean weight of 250 g was assumed and accordingly the organ flow rate and organ weight listed in **Table 4-2** was used directly when analyzing data collected from those two studies.

4.3.2.5. Parameters that were estimated during PBPK-TMDD model fitting

The parameters that were estimated in the data fitting include partition coefficients (K_p) in each tissue, bioavailability (F), first-order absorption rate constant (k_a), intrinsic clearance ($CL_{\text{int,b}}$), as well as those TMDD process related parameters, including association rate constant in plasma or tissue ($k_{\text{on,plasma}}$ and $k_{\text{on,tissue}}$), dissociation rate constant in plasma or tissue ($k_{\text{off,plasma}}$ and $k_{\text{off,tissue}}$), and amount of DPP-4 enzyme in plasma ($R_{\text{max,plasma}}$) or each of those 8 organs ($R_{\text{max,organ}}$). Our model assumed that the total amount of DPP-4 in rat plasma, each tissue or organ per rat body weight is a constant value.

$$R_{\max,\text{rat}} = R_{\max,\text{normalized}} \times BW_{\text{rat}} \quad (4.11)$$

$R_{\max,\text{rat}}$ represents the total amount of DPP-4 targets in rat plasma, each tissue or organ. BW_{rat} represents rat body weight. $R_{\max,\text{normalized}}$ represents total amount of DPP4 targets in rat plasma, each tissue or organ per kg rat body weight, respectively. $R_{\max,\text{normalized}}$ is a model estimated parameter.

4.3.3. PBPK-TMDD model scaling up to human

The final linagliptin PBPK-TMDD model established in rat was further extrapolated to humans to simulate the concentrations of linagliptin in human plasma. Clinical data from two published studies in both Japanese healthy volunteers and T2DM patients following oral single or multiple doses were used to evaluate the model extrapolation capability [39, 118]. The study design of these two published reports has been described in early section and summarized in **Table 4-1**.

4.3.3.1. *Simulation scenario*

In order to have a head to head comparison, linagliptin human pharmacokinetics were simulated using the same dose regimen and sampling time schedules, and in human adults with same average bodyweight as that in those two published reports [39, 118]. Following was the simulation scenarios:

Scenario 1. Simulate human pharmacokinetics of linagliptin at various time points following single oral doses of 1, 2.5, 5, or 10 mg linagliptin in human adults with average body weight of 61.2 kg. Linagliptin concentrations were predicted at following time points: 0.5, 1, 1.5, 2, 3, 4, 6, 8, 12, 24, 48, 72-, 96-, 144-, and 192-hours following drug administration. The simulated result was compared with observed data reported in Human study No.1.

Scenario 2. Simulate human pharmacokinetics of linagliptin at various time points following oral doses of 0.5, 2.5, or 10 mg linagliptin once daily for 28 days in human adults with average body weight of 64.5 kg for 0.5 mg dose, 69.9 kg for 2.5 mg dose, and 63.5 for 10 mg dose. Linagliptin concentrations were predicted at following time points: 0.5, 1, 1.5, 2, 4, 6, 8, and 12 hours after drug administration on days 1 and 28, and at 30 minutes before drug administration on days 2 to 14. The simulated result was compared with observed data reported in Human study No.2.

The PBPK-TMDD model simulation was performed in NONMEM (Version 7.4.3; Icon Development Solutions, Ellicott City, Maryland). Sigmashift and RStudio (version 1.0.143, <https://www.rstudio.com/>) were used for graphical analysis and data handling.

4.3.3.2. Parameters used in the PBPK-TMDD model scale up to human

Human physiological parameters, including human organ weight, and blood flow rate, were fixed based on literature reports [123, 126-129] and these values for a 70 kg human are shown in **Table 4-3**. Blood flow rate fraction ($Q_{fraction}$) and tissue volume fraction ($V_{fraction}$) in each human organ are also included in **Table 4-3** and these fraction values were used when bodyweight included in the model simulation was different from 70 kg. Intrinsic clearance and absorption rate constant of linagliptin were scaled up to humans by means of allometric scaling:

$$CL_{int,human} = CL_{int,rat} * \left(\frac{\text{mean human body weight}}{\text{mean rat body weight}} \right)^{0.75} \quad (4.12)$$

$$k_{absorption,human} = k_{absorption,rat} * \left(\frac{\text{mean human body weight}}{\text{mean rat body weight}} \right)^{-0.25} \quad (4.13)$$

A fixed value of 0.75 was used for clearance and -0.25 was used for absorption rate constant [130, 131]. Amount of DPP-4 in human ($R_{max,plasma}$) and the linagliptin-DPP4 complex

dissociation rate constant in plasma ($k_{off,plasma}$) were fixed to 22.6 nmol and 0.108 hr⁻¹ respectively; these values were obtained in vitro in binding kinetics experiments [35]. For R_{max} in human tissues and organs, it was assumed that the DPP-4 targets concentration levels ($C_{DPP-4,total}$) in each tissue or organ has been conserved between mammalian species. Total amount of DPP-4 targets in human tissues and organs ($R_{max,human\ tissue}$) are fixed in the simulation based on the following equation:

$$C_{DPP-4,total} = \frac{R_{max,rat}}{V_{rat\ tissue}} \quad (4.14)$$

$$R_{max,human\ tissue} = C_{DPP-4,total} \times V_{human\ tissue} \quad (4.15)$$

Here $C_{DPP-4,total}$ represents DPP-4 targets concentration levels in each tissue, which were estimated from the rat PBPK-TMDD model. $R_{max,human\ tissue}$ represents the total amount of DPP-4 targets in human each tissue or organ, $V_{human\ tissue}$ represents volume of human each tissue or organ. All other parameters including bioavailability (F), K_p values in each tissue, and plasma or tissue binding rate constant ($k_{on,plasma}$ $k_{on,tissue}$), and tissue dissociation rate constant ($k_{off,tissue}$) in human were fixed to those values obtained from the rat PBPK-TMDD model fitting.

4.3.3.3. Evaluation of the model scale-up capability

To evaluate the model performance, the time course of the model simulated linagliptin concentrations were compared with those pharmacokinetic profiles reported in clinical studies No.1 and No.2 [39, 118]. In addition, noncompartmental analysis of the simulated linagliptin human plasma pharmacokinetic profiles was performed using Phoenix WinNonlin (version 8.1; Certara USA, Inc., Princeton, NJ), then the pharmacokinetic parameters obtained were compared with those values reported in those two clinical studies. The evaluated parameters included area

under the curve (AUC), maximum concentration (C_{max}), apparent clearance (CL/F), apparent volume of distribution (V/F), terminal half-life ($t_{1/2}$), and accumulation ratio (AR).

4.4. Results

4.4.1. Whole-body PBPK- TMDD model development in rats

4.4.1.1. *Goodness of model fitting*

A comprehensive whole-body PBPK-TMDD model comprising plasma and 14 tissue compartments has been successfully established to characterize linagliptin pharmacokinetics and tissue distribution in wildtype rats and DPP-4 deficient rats. As shown in **Figure 4-3**, the proposed whole-body PBPK-TMDD model adequately captured the linagliptin concentration-time profiles in various tissues in both wildtype rats and DPP4-deficient rats following a single iv dose of 2 mg/kg. The model predicted linagliptin concentrations were in close agreement with the experimental observations in most tissues. In our model, the TMDD component, a process reflecting the tight and long lasting binding between linagliptin and its pharmacological target, were incorporated in plasma, lung, kidney, salivary gland, reproductive organs, thymus, liver, skin and spleen since these tissues are known to have high level DPP-4 expression [106, 132]. Our model estimated that linagliptin concentrations in these 8 tissues in wildtype rats were much higher than that in the respectively tissues in DPP-4 deficient rats; this prediction is in line with the observed data (**Figure 4-3**). Our model also showed that, the difference in linagliptin concentrations in kidney, lung and thymus between wildtype and DPP-4 deficient rats was bigger than that in the remaining organs. In addition to 2 mg/kg, the robustness of our model in estimating the tissue distribution of linagliptin in various other doses, ranging from 0.01 to 50 mg/kg, were also evaluated. Our whole-body PBPK-TMDD model adequately captured the concentrations of

linagliptin in various tissues in both wildtype and DPP-4 deficient rats at 72 hours after iv administration of linagliptin at various doses (data not shown). Furthermore, our model accurately predicted the drug accumulation in various tissues after repeated 2 mg/kg oral administration once daily for 14 days in wildtype rats. As shown in **Figure 4-4**, the model predicted linagliptin trough concentrations were in close agreement with the experimental observations in most tissues at 24, 96, 168, 240 and 336 hours. Our model accurately captured the time course of linagliptin concentrations not only in various tissues, but also in plasma. As shown in **Figure 4-5 (a)**, the proposed whole-body PBPK-TMDD model sufficiently characterized linagliptin plasma concentration time profiles in both wildtype and DPP-4 deficient rats at low dose levels. At high doses, the proposed model tends to overestimate linagliptin plasma concentrations at the terminal phase, indicating that additional nonlinear processes may exist which were not accounted for in the current model. . In addition, our model predicted that linagliptin plasma concentrations in wildtype rats were higher than that in DPP-4 deficient rats when low doses were given, while there was no pharmacokinetics difference between these two types of rats when linagliptin was given at doses higher than 10 mg/kg. **Figure 4-5 (b)** showed comparison between the model estimated and the observed linagliptin plasma concentrations in wildtype rats at different time points following 1 mg/kg or 15 mg/kg oral doses. As it shows, the model estimated linagliptin pharmacokinetics was in good agreement with the observed one in wildtype rats following oral doses.

4.4.1.2. Parameter estimation

The final model estimated parameters of linagliptin is presented in **Table 4-4**. Based on the model estimation, linagliptin has extensive tissue distribution, as reflected by high K_p values in most tissues. The model estimated K_p values in various tissues range from 3.94 in fat to 575 in the liver. It should be noted that, the estimated K_p values in those 8 tissues with TMDD process

only represent tissue-to-plasma partition coefficient of non-specific bound linagliptin in those tissues. Accordingly, these K_p values will be smaller than the K_p values calculated as the ratio of AUC_{tissue} to AUC_{plasma} . The intrinsic clearance of linagliptin in rats was estimated to be 2.2 L/h. Since DPP-4 presents in tissues and plasma with different forms, our model assumed that membrane bound DPP-4 and soluble DPP-4 interact with linagliptin with different association rate constants and dissociation rate constants. Based on the final model, k_{on} , in plasma and tissues were estimated to be 0.943 and 0.0068 $nM^{-1}h^{-1}$, respectively, and k_{off} , in plasma and tissues were estimated to be 0.0698 and 0.0088 h^{-1} , respectively. Bioavailability estimated by our model is 0.405, which is close to the reported value (0.3) [34]. The amount of DPP-4 in plasma and each of those 8 tissues (R_{max} , plasma or tissue) were also estimated, and the values normalized to a 250 g rat are shown in **Table 4-4**. Based on the estimated amount of DPP-4 and the literature reported volume of each organ, concentrations of DPP-4 in those 8 organs/tissues were calculated and those values are presented in **Table 4-5**. In addition, the percentage of DPP-4 concentrations in tissues relative to that in kidney is also evaluated. As shown in **Table 4-5**, the concentration of DPP-4 was estimated to be highest in kidney, followed by lung, liver, salivary gland, thymus, spleen, skin and reproductive system. The predicted DPP-4 concentration in plasma for a 0.25 kg rat is 0.928 nmol/L, which is close to the experimental value (3.84 nmol/L) obtained from protein binding study in rat plasma [35].

4.4.2. PBPK-TMDD model scale-up to human

The final PBPK-TMDD model developed in rat was further scaled up to human using human physiological parameters, such as organ volume and organ blood flow rate. The model simulated linagliptin human pharmacokinetics were then compared with the observed human plasma concentration-time profiles documented in two published studies [39, 118]. **Figure 4-6**

(a) shows the model simulated versus observed time course of linagliptin plasma concentrations in human adults following different single oral doses (1, 2.5, 5, or 10 mg). **Figure 4-6 (b)** presents the model simulated versus observed linagliptin plasma concentrations-time profiles on Day 1 and Day 28 in human adults following the oral administration of multiple ascending doses at 0.5, 2.5 and 10 mg once daily for 28 days.

To further evaluate the model performance, the model predicted linagliptin pharmacokinetics parameters in human adults, obtained via noncompartmental analysis (NCA) using the simulated data, were compared with those obtained from NCA using the observed data [39, 118]. As shown in **Table 4-6**, in general the model predicted linagliptin pharmacokinetic parameters are in line with those literature reported values. **Table 4-6** compares the model predicted parameters following single dose regimens, including AUC_{inf} , C_{max} , CL/F , V/F , and $t_{1/2}$, with the correspondingly values reported from Human Study No.1.

As shown in **Table 4-6**, linagliptin was predicted to have a long half-life ranging from 107 to 132 hours, which is in line with the observed range (96.9 – 113 hours). Following single doses, CL/F followed dose-dependent increase with increase in doses, with the predicted values ranging from 7.10 L/h in the 1 mg group to 12.0 L/h in the 10 mg group, which is in a good agreement with observed range (8.40 – 18.8 L/h). V/F was also predicted to follow dose-dependent increase with increase in doses, and the predicted trend is in close agreement with the reported one.

Table 4-6 compares the model predicated versus literature reported pharmacokinetics parameters of linagliptin following multiple dose regimens in human adults. The parameters that were evaluated included AUC_{24} and C_{max} on Days 1 and 28, CL_{ss}/F , as well as the accumulation ratios (AR) calculated using AUC_{day28}/AUC_{day1} or $C_{max_day28}/C_{max_day1}$. As shown in **Table 4-6**, the predicted linagliptin exposure (AUC_{24} and C_{max} on Days 1 and 28) in each dose group were

fall within the same range of those reported values following the same dose. Following repeated daily doses, the accumulation ratio of linagliptin was predicted to be low (AR <2), which is in line with the observed values [39, 118].

4.5. Discussion

Pharmacological target-mediated drug disposition (TMDD) represents a special source of nonlinear pharmacokinetics and it is caused by saturable binding of a compound to its high-affinity, low-capacity pharmacological target [1, 2]. Although both large-molecule and small-molecule compounds exhibiting TMDD have been reported, TMDD in small-molecule compounds has not been well appreciated due to its low prevalence [2, 88]. With more and more potent small-molecule compounds acting on highly specific targets being developed, together with the increasingly sensitive analytical techniques, the prevalence of TMDD in small-molecule compounds has considerably increased over the last decade [13, 133]. As small-molecule compounds exhibiting TMDD usually demonstrate substantial and complex nonlinear pharmacokinetics, dose regimen design can be particularly challenging due to the nonlinear relationship among dose, exposure and response. To facilitate the optimal dose selection, recently there has been a growing interest in developing mathematical models to quantitatively characterize TMDD in small-molecule compounds. TMDD models have been developed for many small-molecule compounds, such as warfarin [21], imirestat [69], bosentan [114], ABT-384 [15] linagliptin [14], as well as soluble epoxide hydrolase (sEH) inhibitors (TPPU and TCPU) [87]. However, most of the TMDD models reported so far only focus on plasma pharmacokinetics. For small molecule compounds whose TMDD is caused by their pharmacological targets located in tissues, it is known that there is a nonlinear relationship between drug plasma concentration and the drug concentration in tissues expressing the pharmacological targets. Therefore, it is highly

valuable to develop a pharmacometric model which can characterize the time course of drug disposition in tissues, especially in those with pharmacological target expression. Whole-body PBPK model are commonly used to evaluate and predict the disposition of a compound of interest in various tissues. However, traditional whole-body PBPK models usually assume well-stirred condition for each organ and consequently are not able to capture the tight and long last binding of drug with its pharmacological target that is expressed in specific organs. To address the limit of the current TMDD model and traditional PBPK model, in the current study we established a novel whole-body PBPK-TMDD model using DPP-4 inhibitor linagliptin as the model compound.

As our model was developed using literature reported linagliptin plasma and tissue distribution data in rats, we carefully evaluated the data quality before we performed the modeling. In Rat studies No.2 and No.3, plasma concentrations of linagliptin were measured using validated LC/MS/MS methods [14, 117]. In Rat Study No.1, concentrations of total radioactivity of [¹⁴C]linagliptin in various tissues were measured using TriCarb2900 TR scintillation counter [113]. A common concern of using radioactivity data is that the measured concentrations include both parent compound and its metabolites. Therefore, radioactivity data will not be a reliable data source for those compounds undergo extensive metabolism. However, this won't be a significant concern for linagliptin as it undergoes minimum metabolism and is mainly eliminated via biliary excretion as an unchanged form [117]. Based on above information, in our analysis we assumed that the concentrations of total radioactivity in each tissue reported in Animal study No.1 can reliably represent concentrations of parent linagliptin in each tissue.

Based on the literature reported data, a novel and comprehensive whole-body PBPK-TMDD model was successfully developed, which adequately captured the concentration-time profiles of linagliptin in both plasma and various tissues in both wildtype rats and DPP4-deficient

rats. The model was ultimately created using NONMEM software. Nevertheless, we have also been exploring the utility of the SimBiology tools integrated within MATLAB and ADAPT5 (BMSR Biomedical Simulations Resource). It's important to note that we achieve optimal convergence and model fitting when employing the FOCEI parameter estimation algorithm integrated within NONMEM. Our model indicated that the binding process of linagliptin to tissue DPP-4 is much slower than that to plasma DPP-4 ($k_{on,tissue} = 0.00680 \text{ nM}^{-1}\bullet\text{hr}^{-1}$ vs $k_{on,plasma} = 0.943 \text{ nM}^{-1}\bullet\text{hr}^{-1}$). Intuitively this is not surprising since linagliptin molecules may take some time to reach DPP-4 anchored in tissue cell membrane before binding occurs, which means that the estimated association rate constant $k_{on,tissue}$ for DPP-4 in tissue is reflective of diffusion within the tissue as well as binding. On the other hand, the interaction of linagliptin with soluble DPP-4 circulating in plasma does not involve the diffusion step. As a result, $k_{on,plasma}$ is a lot higher than $k_{on,tissue}$. Further studies are needed to investigate binding process differences between soluble and membrane-bound DPP-4. In addition, the dissociation process of linagliptin-DPP4 complex in tissue was estimated to be slower than that in plasma ($k_{off,tissue} = 0.00880 \text{ hr}^{-1}$ vs $k_{off,plasma} = 0.0698 \text{ hr}^{-1}$). In other words, the dissociation of linagliptin-DPP4 complex in plasma is estimated to be faster than that in tissues. The faster K_{off} of linagliptin-DPP4 in plasma is expected as the endogenous substrates of DPP4 are glucagon-like peptide (GLP1) and glucose-dependent insulinotropic polypeptide (GIP), both of which are incretin hormones that circulate in the blood. As these hormones are mainly present in systemic circulation instead of tissues, they could compete and displace the linagliptin-DPP4 complex in plasma, leading to the faster association of the complex in plasma than that in tissue. It's worth pointing out that our model estimated dissociation rate constant in plasma ($k_{off,plasma} = 0.0698 \text{ hr}^{-1}$) is in agreement with the value obtained from the in vitro experiment ($k_{off} = 0.108 \text{ hr}^{-1}$) [38]. The binding affinity of linagliptin to DPP-4 (i.e. k_d values),

which is calculated by k_{off} over k_{on} , were predicted to be 1.29 nM for tissue DPP-4 binding and 0.0740 nM for plasma DPP-4 binding, indicating that linagliptin has higher binding affinity in plasma than that in tissues.

Based on the model estimated DPP-4 amount (i.e. R_{max}) in those 8 organs and the literature reported organ volume, we calculated the tissue concentration of DPP-4, and then compared them with the literature reported gene expression level of DPP-4 in those organs; these literature data was obtained using transcriptomics experiment in rat [132]. Our model predicted that the protein DPP-4 concentration was highest in kidney compared with other organs, which is in line with the literature reported data as the gene expression of DPP-4 was also found to be the highest in kidney (**Table 4-5**). Since what our model predicted was DPP-4 protein expression level and what literature reported was DPP-4 gene expression level, comparing the absolute values is not appropriate. In this case, we calculated the percentage of DPP-4 expression in other organs relative to its expression in kidney, and then compared those values between model predicted and literature reported data. As shown in **Table 4-5**, except for thymus, the difference between the percentage of DPP-4 expression in most tissues relative to kidney was within 2-fold between model predicted and literature reported data. For example, our model predicted that DPP-4 protein concentration in the liver was 12.1% of the kidney value. Similarly, the literature reported DPP-4 gene expression in the liver was 21.1% of the kidney value [132].

After the mechanistic whole-body PBPK-TMDD model was developed in rat, it was further scaled up to human to evaluate the model extrapolation capability. Linagliptin pharmacokinetics in human was simulated and then compared with literature reported data [39, 118]. It's worth emphasizing that linagliptin human pharmacokinetics profiles were simulated based entirely on human physiological parameters (i.e. human organ flow rate and human organ weight), parameters

obtained from linagliptin rate PBPK-TMDD model, as well as a few parameters obtained from in vitro experiments (such as DPP-4 amount in human plasma). Overall, our model accurately predicted following substantial and complex nonlinear pharmacokinetic behavior of linagliptin in human: a) less-than dose proportional increase in plasma exposure; b) dose-dependent increase in CL and V with increase in dose; and c) long terminal half-life (on average ~130 h) with minimal accumulation after repeated doses (AR<2).

Our modeling work has a number of limitations. First, for those organs with low or no DPP-4 expression, well-stirred condition for each organ was assumed in our model. While this is appropriate for those highly perfused organs, such as heart and pancreas, it is less ideal for those poorly perfused tissues, such as fat and bone marrow. For poorly perfused organs, usually interstitial fluid and tissue cells are separated in the model, with permeability being included to capture the permeability limited drug distribution. However, due to the very limited tissue data, we were not able to incorporate permeability in those poorly perfused organs. This explains why the current model did not capture well the initial phase of linagliptin disposition in fat and bone marrow (**Figure 4-3s**). Secondly, during model scale-up to human, we were able to fix DPP-4 amount in plasma ($R_{max, plasma}$) using in vitro experimental value. However, there is no literature report on DPP-4 amount in each tissue ($R_{max, tissue}$). We assumed that the DPP-4 concentration in each tissue is conserved across different species, and we estimated DPP-4 amount in each human tissue based on its concentration in rat and human organ weight. As the assumption of conserved tissue DPP-4 concentrations across species may not hold true, the model scale-up potential for linagliptin concentrations in tissues need to be evaluated carefully.

4.6. Conclusions

In conclusion, a novel and comprehensive whole-body PBPK-TMDD model for linagliptin was successfully developed in rat and scaled up to human. This model adequately captured the concentration-time profiles of linagliptin in both plasma and various tissues in both wildtype rats and DPP4-deficient rats. In addition, this model accurately predicted the substantial and complex nonlinear pharmacokinetic behavior of linagliptin in human adults that is characterized by less-than dose proportional increase in plasma exposure, dose-dependent clearance and volume of distribution, as well as long terminal half-life with minimal accumulation after repeated doses. Our modeling work is not only novel but also of high significance as the whole-body PBPK-TMDD model platform developed using linagliptin as the model compound can be applied to other small-molecule compounds exhibiting TMDD to facilitate the optimal dose selection of those compounds.

Table 4-1. Data source used for linagliptin whole-body PBPK-TMDD model development and model scale-up.

Study No.	PMID	Dose Regimen	Subject	Mean Body Weight	Sampling Time (hours)	Tissue vs Plasma	Reference
Data Source for PBPK-TMDD Model Development in Rat							
Rat study # 1a	19562682	2 mg/kg, i.v, single dose	Wildtype & DPP-4 deficient rat	153-186 g	3, 24, 168	Tissue	[113]
Rat study # 1b	19562682	0.01, 0.1, 0.3, 1, 3, 10, or 50 mg/kg, i.v, single dose	Wildtype & DPP-4 deficient rat	246 g	72	Tissue	[113]
Rat study #1c	19562682	2 mg/kg, p.o, QD for 14 days	Wildtype rat only	200 g	24, 96, 168, 240, 336	Tissue	[113]
Rat study #2	19771584	0.01, 0.1, 0.3, 1, 3, 10, or 50 mg/kg, i.v, single dose	Wildtype & DPP-4 deficient rat	Not reported*	0.033, 0.167, 1, 4, 8, 24, 48, 72	Plasma	[14]
Rat study #3	22198311	1 or 15 mg/kg p.o, single dose	Wildtype rat only	Not reported*	0.25, 0.5, 1, 2, 3, 4, 5, 6, 7, 8, 24, 48, 72	Plasma	[117]

Table 4-1 (Continued)

Data Source for Scale-up-to Human Validation							
Human study #1	20637971	1 mg, 2.5 mg, 5 mg, 10 mg single dose, p.o	Japanese healthy volunteers	61.2 kg	30 minutes before dose and 0.5,1, 1.5, 2, 3, 4, 6, 8, 12, 24, 48, 72, 96, and 144, 192 hours after administration	Plasma	[118]
Human Study #2	21723606	0.5, 2.5, or 10 mg multiple dose, once daily for 28 days, p.o	Japanese patients with T2DM	64.5 kg /0.5 mg group; 69.9 kg /2.5 mg group; 63.5 kg /10 mg group;	30 minutes before dose on Days 1-14; and 0.5, 1, 1.5, 2, 4, 6, 8, and 12 hours after dose on Day 1 and Day 28.	Plasma	[39]

*Bodyweight of 250 g was assumed in our model.

Table 4-2. Physiological and kinetic parameters for modeling linagliptin pharmacokinetics and tissue distribution in rat

Organ	Flow rate (L/h) ^c	Cardio output fraction	Organ weight (kg) ^c	Organ weight fraction	Reference
Lung	3.06	1	0.00155	0.0062	[120]
Liver	0.612	0.20	0.0118	0.047	[120]
Kidney ^a	0.398	0.13	0.00200	0.0080	[120]
Heart	0.162	0.053	0.000830	0.0033	[120]
Muscle	1.01	0.33	0.0950	0.38	[120, 123]
Fat	0.0153	0.005	0.0200	0.08	[120, 123]
Skin	0.315	0.103	0.0400	0.16	[120]
Thymus	0.0214	0.007	0.000250	0.0010	[124]
Salivary gland	0.0520	0.017	0.000430	0.0017	[120-122]
Pancreas	0.0428	0.014	0.00125	0.0050	[124]
Spleen	0.0245	0.008	0.000750	0.0030	[123]
Reproductive organs ^b	0.0260	0.0085	0.00288	0.0115	[120]
Adrenal	0.00643	0.0021	0.0000500	0.00020	[120]
Bone marrow	0.165	0.054	0.0192	0.077	[120]
Plasma	3.06		0.0100	0.040	[125]
Remainder	0.277	0.0904	0.0440	0.176	

^a, mean concentration of inner medulla, outer medulla and kidney cortex. ^b, mean concentration of testis and epididymis. ^c, parameters calculated for a 250g rat

Table 4-3. Physiological and kinetic parameters for linagliptin PBPK simulations in human.

Organ	Flow rate (L/h)^a	Cardio output fraction	Organ weight (kg)^a	Organ weight fraction	Reference
Lung	336	1	1.00	0.014	[123]
Liver	87.0	0.26	1.80	0.026	[123]
Kidney	74.4	0.22	0.310	0.0044	[123]
Heart	14.4	0.043	0.330	0.0047	[123]
Muscle	45.0	0.13	28.0	0.40	[123, 126]
Fat	15.6	0.046	11.6	0.16	[123, 126]
Skin	18.0	0.054	2.60	0.037	[123, 126]
Thymus	0.201	0.00060	0.0240	0.00034	[126]
Salivary gland	0.104	0.00031	0.0810	0.0012	[126, 127]
Pancreas	3.36	0.010	0.134	0.0019	[126]
Spleen	4.62	0.014	0.180	0.0026	[123]
Reproductive organs	1.04	0.0031	0.0374	0.00053	[123, 128]
Adrenal	1.00	0.003	0.0140	0.0002	[123, 126]
Bone marrow	10.0	0.03	1.12	0.016	[126]
Plasma	336		3.46	0.049	[129]
Remainder	69.1	0.18	19.3	0.28	

^a, parameter calculated for 70 kg human.

Table 4-4. Estimated parameters from the final whole-body PBPK-TMDD model of linagliptin.

Parameter	Unit	Definition	Final model	RSE ^a (%)
$K_{p,\text{lung}}$		lung-to-plasma partition coefficient	9.66	20
$K_{p,\text{liver}}$		liver-to-plasma partition coefficient	575	42
$K_{p,\text{kidney}}$		kidney-to-plasma partition coefficient	42.0	16
$K_{p,\text{heart}}$		heart-to-plasma partition coefficient	12.1	19
$K_{p,\text{muscle}}$		muscle-to-plasma partition coefficient	4.37	10
$K_{p,\text{fat}}$		fat-to-plasma partition coefficient	3.94	13
$K_{p,\text{skin}}$		skin-to-plasma partition coefficient	4.72	16
$K_{p,\text{thymus}}$		thymus-to-plasma partition coefficient	10.6	19
$K_{p,\text{salivary gland}}$		salivary gland-to-plasma partition coefficient	27.4	24
$K_{p,\text{pancreas}}$		pancreas-to-plasma partition coefficient	22.9	17
$K_{p,\text{spleen}}$		spleen-to-plasma partition coefficient	26.2	17
$K_{p,\text{reproductive organs}}$		reproductive organs-to-plasma partition coefficient	19.0	27
$K_{p,\text{adrenal}}$		adrenal-to-plasma partition coefficient	31.6	18
$K_{p,\text{bone marrow}}$		bone marrow-to-plasma partition coefficient	39.6	13
$K_{p,\text{remainder}}$		remainder-to-plasma partition coefficient	764	21
k_a	h^{-1}	first-order absorption rate constant	0.897	14
$CL_{\text{int,b}}$	L/hr	intrinsic clearance	2.20	37
F		absolute bioavailability	0.405	8
$k_{\text{on,tissues}}$	$\text{nM}^{-1} \bullet \text{h}^{-1}$	association rate constant to tissue DPP-4	0.00680	59
$k_{\text{off,tissues}}$	h^{-1}	dissociation rate constant to tissue DPP-4	0.00880	68
$k_{\text{on, plasma}}$	$\text{nM}^{-1} \bullet \text{h}^{-1}$	association rate constant to plasma DPP-4	0.943	79
$k_{\text{off, plasma}}$	h^{-1}	dissociation rate constant to plasma DPP-4	0.0698	44
$R_{\text{max,plasma}}^b$	nmol	total amount of DPP-4 in plasma	0.00928	23
$R_{\text{max,lung}}^b$	nmol	total amount of DPP-4 in lung	0.693	17
$R_{\text{max,liver}}^b$	nmol	total amount of DPP-4 in liver	4.53	24
$R_{\text{max,kidney}}^b$	nmol	total amount of DPP-4 in kidney	6.35	14
$R_{\text{max,skin}}^b$	nmol	total amount of DPP-4 in skin	2.23	22
$R_{\text{max,thymus}}^b$	nmol	total amount of DPP-4 in thymus	0.0460	19
$R_{\text{max,salivary gland}}^b$	nmol	total amount of DPP-4 in salivary gland	0.0460	46
$R_{\text{max,spleen}}^b$	nmol	total amount of DPP-4 in spleen	0.146	22
$R_{\text{max,reproductive organs}}^b$	nmol	total amount of DPP-4 in reproductive organs	0.187	46
RV		proportional residual variability	0.440	11

^aRSE: Relative standard error; ^bRmax values normalized to 250 g rat.

Table 4-5. DPP-4 expression level prediction in different rat tissues.

Tissue	Predicted protein expression level (nmol/L)	Predicted Percentage (%)	Reported Gene Expression Level (TPM)*	Reported Percentage (%)	Reference
Kidney	3175	100.0	307	100.0	[132]
Lung	447	14.1	99	32.2	[132]
Liver	385	12.1	65	21.1	[132]
Salivary gland	108	3.4	NA	NA	
Thymus	184	5.8	72	23.4	[132]
Spleen	195	6.1	36	11.7	[132]
Skin	56	1.8	NA	NA	
Reproductive Organs	65	2.0	7	2.3	[132]

Kidney as reference, NA, not investigated

DPP-4 gene expression data was obtained from Expression Atlas:

(https://www.ebi.ac.uk/gxa/genes/ENSRNOG0000030763?bs=%7B%22rattus%20norvegicus%22%3A%5B%22ORGANISM_PART%22%5D%7D&ds=%7B%22kingdom%22%3A%5B%22animals%22%5D%7D#baseline)

Table 4-6. Comparison of model predicted vs literature reported pharmacokinetics parameters of linagliptin in human.

Pharmacokinetics parameters	Unit	Human Study No.1 (PMID: 20637971)							
		1 mg		2.5mg		5 mg		10 mg	
		Observed	Predicted	Observed	Predicted	Observed	Predicted	Observed	Predicted
AUC _{inf}	nM•h/L	253	297	517	671	765	1130	1120	1770
C _{max}	nM	4.27	5.68	5.92	7.79	9.00	9.82	23.1	13.2
V _{d/F}	L	1260	1160	1430	1250	2090	1450	3060	2290
CL/F	L/h	8.40	7.10	10.3	7.87	13.9	9.40	18.8	12.0
t _{1/2}	h	104	113	96.9	110	105	107	113	132

	Human Study No.2 (PMID: 21723606)							
	0.5 mg		2.5 mg		10 mg			
	Observed	Predicted	Observed	Predicted	Observed	Predicted		
AUC _{24,Day1}	nM•h/L	29.9	63.7	129	120	323	216	
AUC _{24,Day28}	nM•h/L	89.4	125	164	178	373	309	
C _{max,Day1}	nM	2.81	3.77	8.84	6.89	35.1	12.9	
C _{max,Day28}	nM	5.02	5.88	11.0	8.72	44.0	17.7	
CL/F,ss	L/h	11.8	8.41	32.2	29.7	56.7	178	
AR _{AUC}		2.98	1.96	1.27	1.48	1.16	1.43	
AR _{Cmax}		1.78	1.56	1.23	1.26	1.25	1.37	

data are presented as mean. AUC_{inf} = area under the concentration-time curve from time 0 to infinity; C_{max} = maximum concentration; V_{d/F} = apparent oral volume of distribution; CL/F = apparent oral clearance; AUC_{0-24h} = area under the concentration-time curve from 0 extrapolated to 24 hours; t_{1/2} = terminal elimination half-life; AUC_{24,Day1} = area under plasma concentration-time curve over 24 h interval on day 1; AUC_{24,Day28} = area under the steady-state plasma concentration-time curve to the dosing interval; C_{max,Day1} = maximum plasma concentration over 24 h interval on day 1; C_{max,Day28} = steady-state maximum plasma concentration; CL/F,ss = apparent oral clearance at steady-state; AR_{AUC} = accumulation ratio calculated based on AUC; AR_{Cmax} = accumulation ratio calculated based on C_{max}.

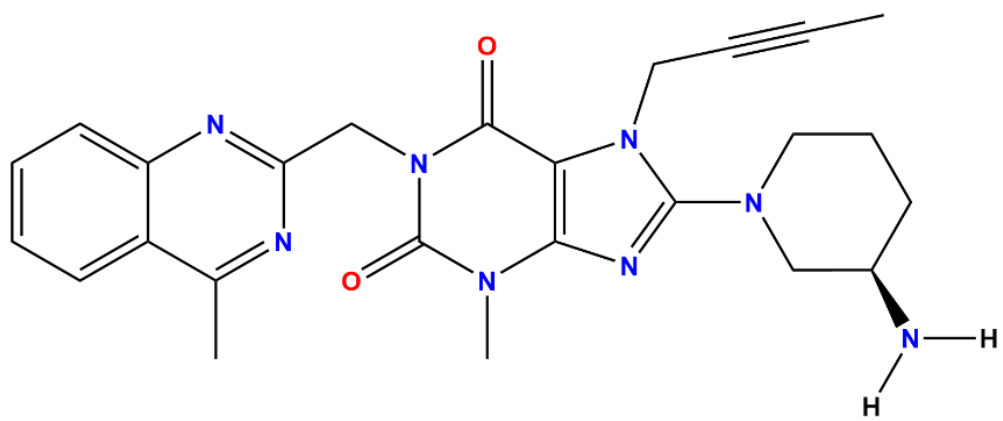


Figure 4-1. Chemical structure of linagliptin, an approved DPP-4 inhibitor for the treatment of T2DM.

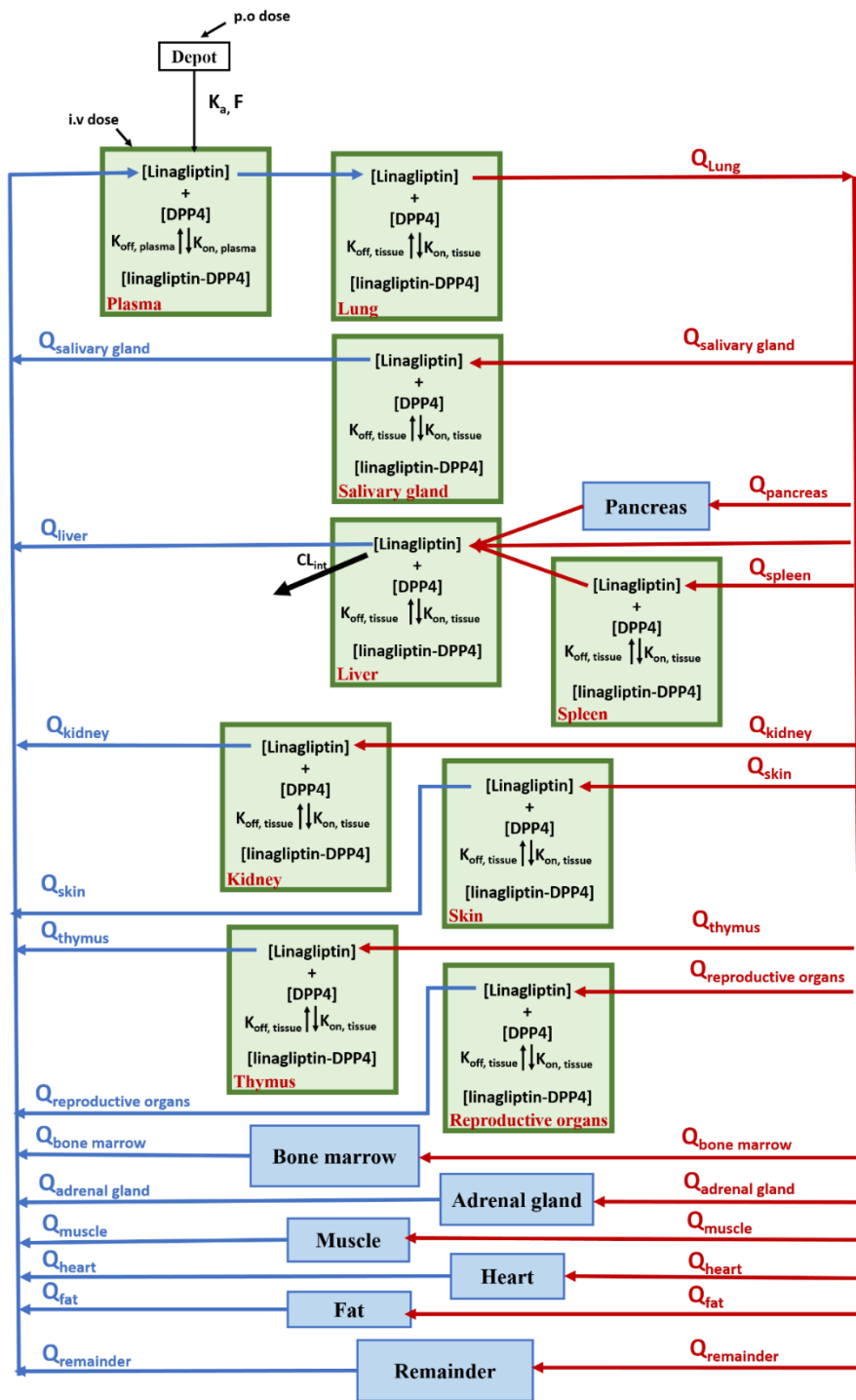


Figure 4-2. Schematic representation of the whole-body PBPK-TMDD model for linagliptin in rats.

The PBPK-TMDD model incorporates plasma and 14 tissue compartments (lung, liver, kidney, heart, spleen, pancreas, thymus, muscle, skin, fat, salivary gland, adrenal, bone marrow, reproductive organs), among which 9 compartments containing TMDD binding process.

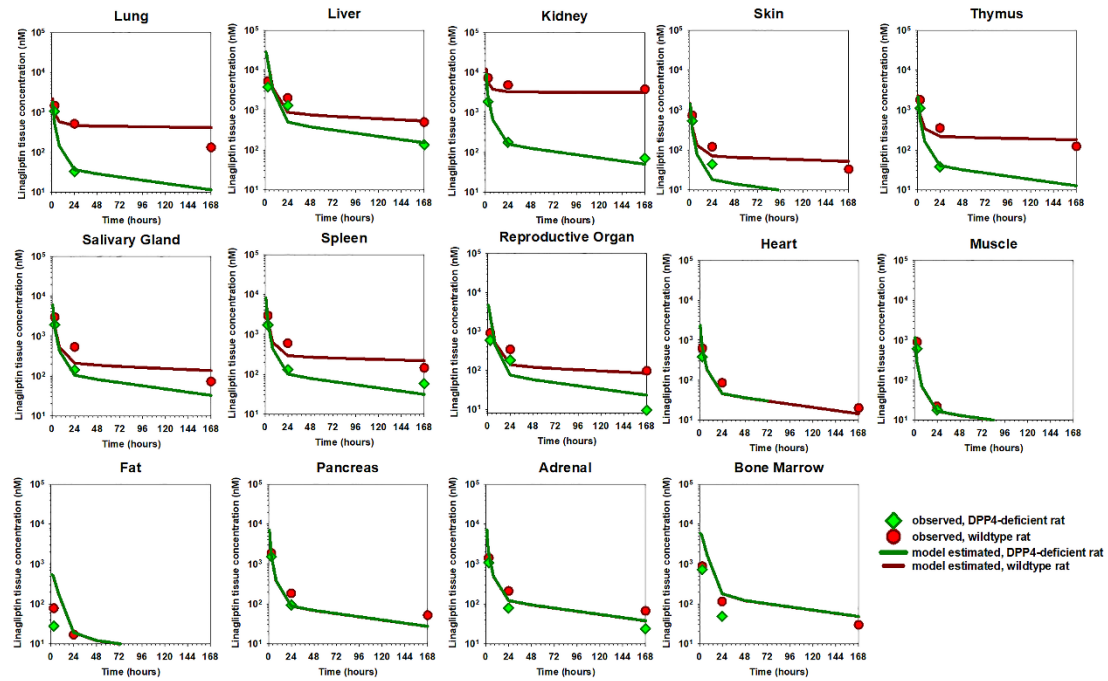


Figure 4-3. Goodness of fit plots for the final whole-body PBPK-TMDD model for linagliptin observed versus model-predicted concentrations in 14 different tissues in both wildtype and DPP4-deficient rat after a single 2 mg/kg intravenous dose.

Symbols represent observed linagliptin tissue concentration in rats (circles for wildtype rats and diamond for DPP4-deficient rats). Solid lines represent model predicted linagliptin tissue concentrations in rats.

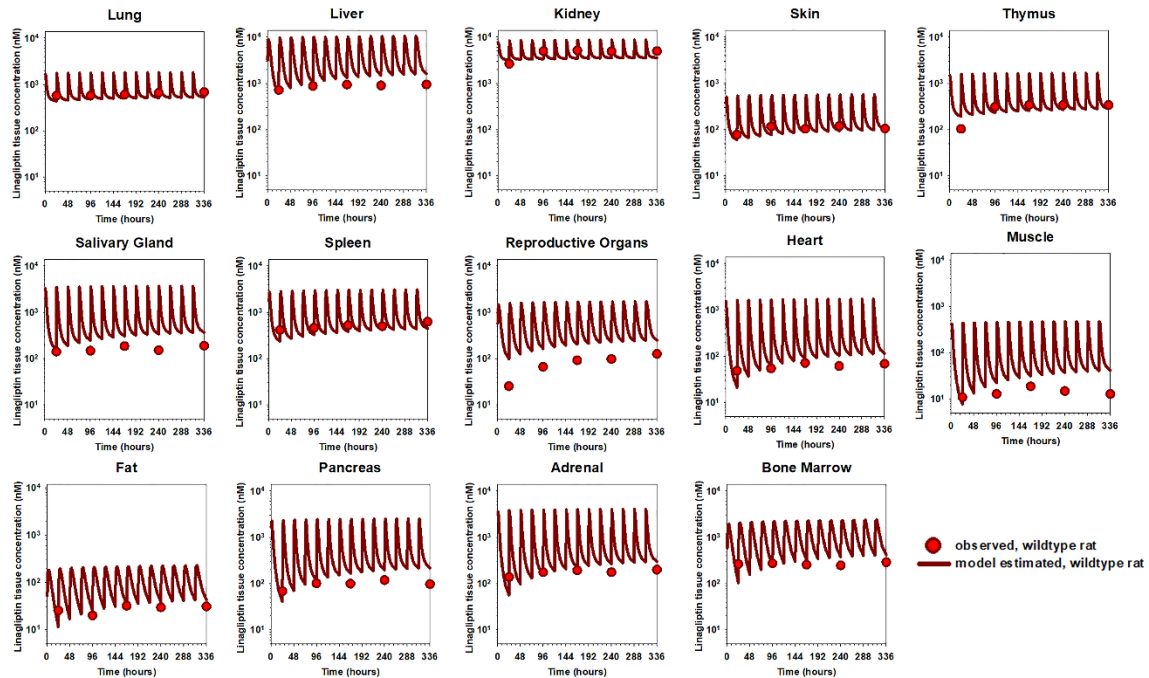


Figure 4-4. Goodness of fit plots for the final whole-body PBPK-TMDD model for linagliptin observed versus model-predicted concentrations in 14 different tissues in wildtype rat after 2 mg/kg oral dose once daily for 14 days.

Circles represent observed linagliptin tissue concentration. Triangles represent predicted linagliptin tissue concentration.

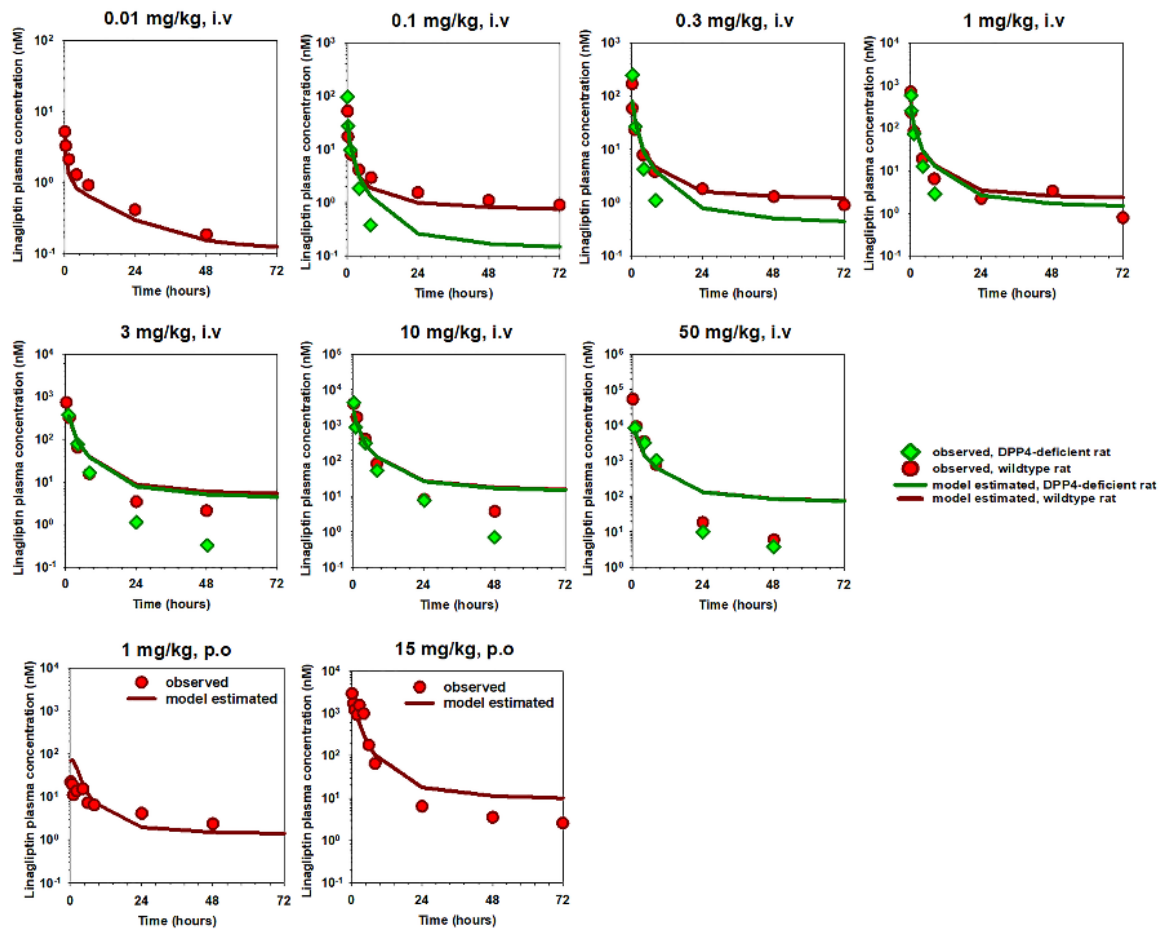
A

Figure 4-5. Goodness of fit plots for the final whole-body PBPK-TMDD model for linagliptin observed versus model-predicted plasma concentrations in both wild type and DPP4-deficient rats.

Doses of linagliptin were administered at (A) different i.v. doses (0.01, 0.1, 0.3, 1, 3, 10, 50 mg/kg) and (B) 1 or 15 mg/kg oral dose. Circles represent observed linagliptin plasma concentration in rats. Symbols represent observed linagliptin plasma concentration in rats (circles for wildtype rats and diamond for DPP4-deficient rats). Solid lines represent model predicted linagliptin plasma concentrations in rats.

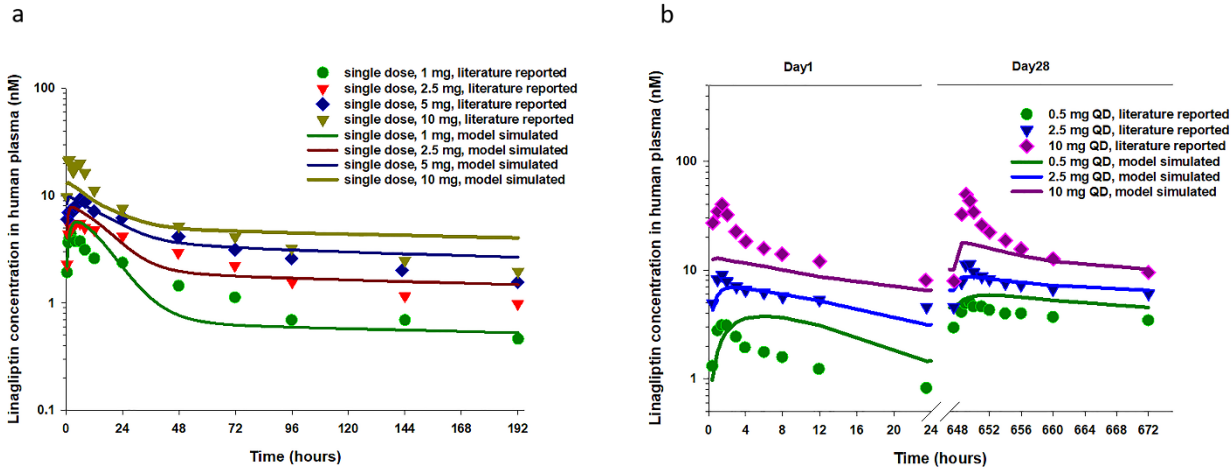


Figure 4-6. Observed (symbols) vs simulated (solid lines) linagliptin plasma-time concentration profiles in human adults.

Linagliptin oral doses were given at (a) single doses of 1, 2.5, 5, or 10 mg and (b) multiple doses of 0.5, 2.5, or 10 mg linagliptin once daily for 28 days. Observed data were obtained from literature reports as listed in Table 4-1. Simulated data were obtained from our final whole-body PBPK-TMDD model that was scaled up to human.

**CHAPTER 5: A QUANTITATIVE SYSTEM PHARMACOLOGY MODEL OF THE
INCRETIN HORMONES GIP AND GLP-1, GLUCAGON, GLUCOSE, INSULIN AND
THE SMALL MOLECULE DPP-4 INHIBITOR, LINAGLIFTIN**

Most of this chapter has been accepted by Journal of Pharmaceutical Sciences and the article is in press.

(Wu N, An G. *J Pharm Sci.* 2023 Sep 14:S0022-3549(23)00369-6.)

5.1. Abstract

In the current study, we established a comprehensive quantitative systems pharmacology (QSP) model using linagliptin as the model drug, where drug disposition, drug intervention on dipeptidyl peptidase-4 (DPP-4), glucose-dependent insulinotropic peptide (GIP), Glucagon-like peptide-1 (GLP-1), glucagon, glucose, and insulin are integrated together with the cross talk and feedback loops incorporated among the whole glycemic control system. In the final linagliptin QSP model, the complicated disposition of linagliptin was characterized by a 2-compartment pharmacokinetic (PK) model with an enterohepatic cycling (EHC) component as well as target-mediated drug disposition (TMDD) processes occurring in both tissues and plasma, and the inhibitory effect of linagliptin on DPP-4 was determined by the linagliptin-DPP-4 complex in the central compartment based on target occupancy principle. The integrated GIP-GLP1-glucagon-glucose-insulin system contains five indirect response models as the "skeleton" structure with 12 feedback loops incorporated within the glucose control system. Our model adequately characterized the substantial nonlinear PK of linagliptin, time course of DPP-4 inhibition, as well as the kinetics of GIP, GLP-1, glucagon, and glucose simultaneously in humans. Our model provided valuable insights on linagliptin pharmacokinetics/pharmacodynamics and complicated glucose homeostasis. Since the glucose regulation modeling framework within the QSP model is "drug-independent", our model can be easily adopted by others to evaluate the effect of other DPP-4 inhibitors on the glucose control system. In addition, our QSP model, which contains more components than other reported glucose regulation models, can potentially be used to evaluate the effect of combination antidiabetic therapy targeting different components of glucose control system.

5.2. Introduction

Type 2 diabetes mellitus (T2DM) is a chronic progressive disease marked by hyperglycemia resulting from insulin resistance and β -cell dysfunction. In the U.S., approximately 30 million adults are affected by T2DM, and this number is projected to rise to around 39 million by 2050 [134].

Approved therapies for type 2 diabetes mellitus (T2DM) encompass a variety of drug classes, including metformin, sulfonylureas, DPP-4 inhibitors, SGLT-2 inhibitors, GLP-1 receptor agonists, and insulin [135, 136]. Among these options, DPP-4 inhibitors occupy a unique position due to their minimal risk of causing hypoglycemia [110, 137]. DPP-4 inhibitors work by reducing the activity of the enzyme DPP-4, which exists in both soluble form in plasma and membrane-bound form throughout various organs. This adjustment slows down the DPP-4-mediated degradation of glucagon-like peptide-1 (GLP-1) and glucose-dependent insulinotropic peptide (GIP). Consequently, these inhibitors prolong the drug action of GLP-1 and GIP, leading to enhanced outcomes in lowering glucose levels [107-109, 138].

Linagliptin, an FDA-approved DPP-4 inhibitor, has been approved by FDA in 2011 to treat T2DM. Its pharmacokinetics (PK) exhibit nonlinearity due to target-mediated drug disposition (TMDD) in wildtype animals and human. To understand this phenomenon, we have established a novel whole-body physiologically based pharmacokinetic (PBPK)-TMDD model in rats and scaled it up to human [139]. Additionally, a number of pharmacometrics models have been developed to characterize linagliptin's plasma PK and DPP-4 inhibition relationships in both rats and human [14, 34, 115, 140].

Much like other DPP-4 inhibitors, linagliptin effectively reduces glucose levels by extending the impact of crucial incretins, namely GLP-1 and GIP. These incretins are released at

specific intestinal sites in response to exogenous glucose, such as food, and are degraded by the DPP-4 enzyme. In healthy individuals, these incretins indirectly lower glucose by enhancing insulin secretion, with GLP-1 additionally inhibiting glucagon release [141, 142]. However, in individuals with T2DM, GIP's insulinotropic effect diminishes while it retains its capacity to stimulate glucagon production [143, 144]. The intricate glycemic control system involves a dynamic interplay between insulin, glucose, and glucagon to tightly regulate blood sugar levels, thereby influencing glucose levels.

Numerous quantitative models have been developed to elucidate glycemic control and the impact of drug interventions. Initially, models focused primarily on the glucose-insulin relationship [145-149]. However, as clinical studies began to test glucagon more extensively, these models expanded to incorporate insulin-glucose-glucagon regulation [150-152]. Subsequently, researchers have created models that incorporate drug interventions to glycemic control system [153-156]. These modeling efforts play a crucial role in facilitating drug development.

Incretin-based therapeutics represent a novel category of antidiabetic drugs. Models have been crafted to elucidate how incretins respond to glucose absorption [146, 157]. In addition, because substantial clinical trial data is readily accessible, and the abundance of data presents us with a unique opportunity to construct mathematical models that can quantitatively elucidate the impact of this drug class on glycemic control. Notably, a quantitative system pharmacology (QSP) model has been documented in a study by Balazki et al., shedding light on the effects of sitagliptin on glycemic control [155]. However, constructed with PKsim and Mobi, this model lacks the transparency of ODEs to depict dynamics and a clearly presented model structure. Consequently, comprehending the model's evolution and its integration of drug pharmacokinetics/pharmacodynamics (PK/PD) and regulatory signaling pathways into glycemic

control becomes challenging to readers. Furthermore, the adaptability of this model to different T2DM therapeutic interventions is limited.

To further enhance dose selection optimization for linagliptin, the current research aims to establish a comprehensive QSP model that captures linagliptin's PK/PD modulation for glycemic control involving key factors like GLP-1, GIP, glucagon, glucose, and insulin. By integrating these components into a coherent QSP model, a deeper understanding of the complex interactions governing glycemic control and the specific effects of linagliptin can be achieved, facilitating the development of more effective treatments for type 2 diabetes mellitus.

5.3. Methods

5.3.1. Data source

The mean concentrations of important incretin hormones (GIP and GLP-1), glucagon, glucose, as well as pharmacokinetic (PK) data and plasma DPP-4 inhibition data from various time points were extracted from published clinical trials, as summarized in **Table 5-1**. These datasets were digitized using Engauge Digitizer (<https://markummitchell.github.io/engauge-digitizer/>) [39, 111, 118, 158].

Study #1 involved the administration of linagliptin to healthy subjects using both single escalating doses (1, 2.5, 5, and 10 mg) and multiple escalating doses (2.5, 5, and 10 mg) once daily for 12 days. Pharmacokinetic (PK) and pharmacodynamic (PD, i.e., DPP-4 plasma inhibition) samples were collected at multiple time points, including 30 minutes before dosing, and at 30 minutes, 1, 1.5, 2, 3, 4, 6, 8, 12, 24, 48, 72, 96, 144, and 192 hours after dosing for single doses. For multiple doses, PK and PD samples were obtained 30 minutes before administration and at 30 minutes and 1, 1.5, 2, 3, 4, 6, 8, and 12 and 23.5 hours after administration on day 1 and day 12, and at 30 minutes before administration on day 2 through 11. In study #2, individuals with type 2

diabetes mellitus (T2DM) were administered different doses of linagliptin (1, 2.5, 5, and 10 mg) once daily for 12 days. PK and PD samples were collected at the same time points as in the multiple-dose group of study #1, i.e., on day 1, day 12, and day 2 through 11. Study #3 enrolled T2DM patients who received oral doses of linagliptin (0.5, 2.5, or 10 mg) once daily for 28 days. PK and PD data were collected at different time points, including 0, 0.5, 1, 1.5, 2, 3, 4, 6, 8, 12, and 23.5 hours after the first dose (day 1) and at steady-state condition (day 28). In study #4, T2DM patients received the once-daily dose of 5 mg linagliptin or placebo for 28 days. Meal tolerance tests (MTT) were performed on days 1, 28, 29, and 30, one hour after linagliptin/placebo administration. Plasma glucagon, GLP-1, and GIP were measured right before the drug/placebo administration and right before the MTT was performed, and at 0.25, 0.5, 12, and 2 hours following the MTT test on day 28. Plasma glucose concentrations were determined right before drug/placebo administration and right before the MTT was performed, and at 0.25, 0.5, 1, 1.5, 2, 3, 5, 6, 7, 8, 11, 12, 13, 15, 18, and 23 hours after the MTT on day 28.

5.3.2. Model description

All data were simultaneously fitted into our proposed QSP model, which comprises three distinct parts for narrative convenience: the linagliptin pharmacokinetics-plasma DPP-4 inhibition sub-model, the glucose-GLP-1-GIP sub-model, and the glucose-glucagon-insulin sub-model. Further details on each sub-model can be found below:

5.3.2.1. Linagliptin pharmacokinetics-plasma DPP-4 inhibition model

Initial model:

A published model structure was modified to serve as our foundational framework for characterizing linagliptin pharmacokinetics (PK) [140]. The base model, depicted in **Figure 5-2**,

illustrates linagliptin's absorption from the depot compartment into the central compartment through a first-order rate constant k_a . The systemic distribution of linagliptin occurs across central and peripheral spaces. Linear elimination of linagliptin from the central compartment is represented by k_e (i.e., $CL/V_{linagliptin,central}$). Within the central compartment, linagliptin engages with soluble DPP-4 in plasma, forming a linagliptin-DPP-4 complex through a second-order association rate constant (k_{on}). The dissociation of the linagliptin-DPP-4 complex results in the release of free DPP-4 target and free drug, characterized by first-order dissociation rate constants k_{off} . Concurrently, linagliptin in the peripheral compartment can also interact with membrane-bound DPP-4 in tissues using the same k_{on} and k_{off} values. The binding capacity of both soluble and membrane-bound DPP-4 targets, represented by $R_{max,plasma}$ and $R_{max,tissue}$, respectively, remains constant.

Given that linagliptin's function involves inhibiting DPP-4 activity, plasma DPP-4 inhibition is modeled as the product of the target occupancy (i.e., the ratio of plasma DPP-4 bound to linagliptin to the total amount of DPP-4) and the maximum inhibition potential achievable by linagliptin. As linagliptin binds to DPP-4, the level of DPP-4 inhibition progressively increases until saturation, at which point all DPP-4 molecules are engaged by linagliptin, resulting in a target occupancy of 100% and attainment of the maximum effect (I_{max}). DPP-4 activity is the complement of DPP-4 inhibition, where it is calculated as 100% minus the extent of inhibition.

Nevertheless, the foundational model exhibited a tendency to underestimate linagliptin pharmacokinetics in individuals receiving a single oral dose of 10 mg. To address this, we explored additional modifications.

Tested modifications on top of base model:

The base model was enhanced by integrating an enterohepatic recirculation (EHC) component, accounting for the circular movement of linagliptin from the liver to the bile, then into the small intestine, absorption by enterocytes, and subsequent transport back to the liver [159]. The rate constant for linagliptin transit from the liver to bile was denoted as k_{cb} , while the rate constant from bile to intestine was denoted as k_{bg} .

Final model:

This refinement resulted in improved model fitting and a reduced objective function value (OFV), as detailed in **Table 5-2** and was included in our final model.

Our final sub model is a dual target-mediated drug disposition (TMDD) model, encompassing the interaction of linagliptin with its pharmacological target, DPP-4, in both tissues and plasma, and augmented with the enterohepatic recirculation (EHC) component. DPP-4 activity is inversely related to DPP-4 inhibition, which is proportional to the target occupancy, with the coefficient of maximal inhibition denoted as I_{max} . The essential equations are presented below:

$$\frac{dA_{linagliptin,gut}}{dt} = -k_{a,linagliptin} \times A_{linagliptin,gut} + k_{bg} \times A_{linagliptin,bile}$$

$$A_{linagliptin,gut}(0) = \text{Dose} \times F \quad (5.1)$$

$$\frac{dA_{linagliptin,central}}{dt} = k_{a,linagliptin} \times A_{linagliptin,depot} - k_{on} \times (R_{max,plasma} -$$

$$A_{[linagliptin-DPP4],plasma}) \times C_{linagliptin,central} + k_{off} \times A_{[linagliptin-DPP4],plasma} -$$

$$A_{linagliptin,central} \times CL/V_{linagliptin,central} + A_{linagliptin,peripheral} \times Q/V_{linagliptin,peripheral} -$$

$$A_{linagliptin,central} \times Q/V_{linagliptin,central} - k_{cb} \times A_{linagliptin,central}$$

$$A_{linagliptin,central}(0) = 0 \quad (5.2)$$

$$\begin{aligned}
\frac{dA_{linagliptin,peripheral}}{dt} = & -k_{on} \times (R_{max,tissue} - A_{[linagliptin-DPP4],tissue}) \times C_{linagliptin,peripheral} + \\
& k_{off} \times A_{[linagliptin-DPP4],tissue} - A_{linagliptin,peripheral} \times Q/V_{linagliptin,peripheral} + \\
& A_{linagliptin,central} \times Q/V_{linagliptin,central} \\
A_{linagliptin,peripheral}(0) = & 0
\end{aligned} \tag{5.3}$$

$$\begin{aligned}
\frac{dA_{linagliptin,bile}}{dt} = & k_{cb} \times A_{linagliptin,central} - k_{bg} \times A_{linagliptin,bile} \\
A_{linagliptin,bile}(0) = & 0
\end{aligned} \tag{5.4}$$

$$\begin{aligned}
\frac{dA_{[linagliptin-DPP4],plasma}}{dt} = & k_{on} \times (R_{max,plasma} - A_{[linagliptin-DPP4],plasma}) \times C_{linagliptin,central} - \\
& k_{off} \times A_{[linagliptin-DPP4],plasma} \\
A_{[linagliptin-DPP4],plasma}(0) = & 0
\end{aligned} \tag{5.5}$$

$$\begin{aligned}
\frac{dA_{[linagliptin-DPP4],tissue}}{dt} = & k_{on} \times (R_{max,tissue} - A_{[linagliptin-DPP4],tissue}) \times C_{linagliptin,peripheral} - \\
& k_{off} \times A_{[linagliptin-DPP4],tissue} \\
A_{[linagliptin-DPP4],tissue}(0) = & 0
\end{aligned} \tag{5.6}$$

$$DPP4_{activity}(\%) = 100 - \frac{A_{[linagliptin-DPP4],plasma}}{R_{max,plasma}} \times I_{max} \tag{5.7}$$

5.3.2.2. Glucose-GLP-1 and GIP sub-model

Initial model:

In our initial model, illustrated in **Figure 5-1**, the concentrations of both GLP-1 and GIP were characterized using indirect response models, employing zero-order rate constants for production ($k_{in,GLP-1}$ and $k_{in,GIP}$), while $k_{out,GLP-1,DPP4-dependent}$ and $k_{out,GIP,DPP4-dependent}$ delineated the first-order rate constants for the elimination of GLP-1 and GIP, respectively. The presence of

endogenous GLP-1 and GIP was stimulated by glucose originating from dietary intake and degraded by DPP-4. To capture this interplay, the uptake of glucose from ingested food was modeled through a depot compartment, wherein an increase in depot glucose content yielded proportional elevations in the production rates of GLP-1 and GIP. The degradation rates of both GLP-1 and GIP exhibited a proportionate relationship with DPP-4 activity, signifying that the extent of endogenous degradation for GLP-1 and GIP was contingent upon the residual DPP-4 activity.

However, the model exhibited inadequate fitting, as indicated in **Table 5-2**. Consequently, two modifications were explored to enhance model performance.

Tested modifications on top of base model:

- The initial models exhibited an overestimation of both the maximum plasma glucose concentration and the time taken for plasma glucose to reach its peak, indicating a potential time delay in glucose absorption. To address this, a transit compartment representing the small intestine was introduced between the glucose depot compartment and the central compartment. Meanwhile, an increase in glucose concentration within the transit compartment led to proportional enhancements in the production rates of GLP-1 and GIP, characterized by their respective slopes, SLGLP and SLGIP.
- Additionally, recent findings indicate that GLP-1 and GIP are metabolized not only by DPP-4 but also by neutral endopeptidase (NEP) [160], which is characterized by the incorporation of additional DPP-4 independent elimination pathways for both GLP-1 and GIP. These pathways were characterized by two first-order rate constants, $k_{out,GLP-1,DPP4-independent}$, and $k_{out,GIP,DPP4-independent}$.

Final model:

These two attempted modifications resulted in improved model fitting and a reduction in the objective function value (OFV) (**Table 5-2**) and our final model incorporated these.

Subsequent to food intake, glucose go through the stomach and intestine before entering the plasma. In emulation of this process, our model encompasses three compartments—stomach, intestine, and plasma. This configuration effectively captures the absorption of exogenous glucose, with the transition from the stomach to the intestine characterized by the first-order rate constant $k_{a,\text{glucose}}$, and the transition from the intestine to the bloodstream denoted by the distinct first-order rate constant, k_{tr} .

Crucial incretin hormones, glucagon-like peptide-1 (GLP-1), and glucose-dependent insulinotropic peptide (GIP), released from distinct intestinal sites under glucose stimulation and undergo degradation via both DPP-4 and NEP enzymes. In correspondence, both GLP-1 and GIP are described by indirect response models, characterized by zero-order endogenous production rate constants ($k_{in, \text{GLP-1}}$ and $k_{in, \text{GIP}}$). Elevated intestinal glucose concentrations yield proportionate increments in the production rates of GLP-1 and GIP, each governed by linear slopes (SLGLP and SLGIP). Moreover, the decline of GLP-1 and GIP aligns with DPP-4 dependent pathways, demarcated by $k_{out, \text{GLP-1,DPP4-dependent}}$ and $k_{out, \text{GIP,DPP4-dependent}}$, while NEP enzyme-mediated metabolism is encapsulated through $k_{out, \text{GLP-1,DPP4-independent}}$ and $k_{out, \text{GIP,DPP4-independent}}$.

In bridging the PK-PD model with the glucose-GLP-1-GIP sub-model, the resultant DPP-4 dependent rate constants are determined by the product of remaining DPP-4 activity (%)—reflecting the fraction of the intrinsic DPP-4 dependent degradation rate constant unaltered by linagliptin intervention—and the baseline DPP-4 degradation rate constants ($k_{out, \text{GLP-1,DPP4-dependent}}$ and $k_{out, \text{GIP,DPP4-dependent}}$).

The essential equations are outlined below:

$$\frac{dC_{GLP-1}}{dt} = k_{in,GLP-1} \times (1 + SLGLP \times A_{glucose,intestine}) - k_{out,GLP-1,DPP4-dependent} \times C_{GLP-1} \times DPP4_{activity} - k_{out,GLP-1,DPP4-independent} \times C_{GLP-1}$$

$$C_{GLP-1}(0, SS) = \frac{k_{in,GLP-1}}{k_{out,GLP-1,DPP4-dependent} + k_{out,GLP-1,DPP4-independent}} \quad (5.8)$$

$$\frac{dC_{GIP}}{dt} = k_{in,GIP} \times (1 + SLGIP \times A_{glucose,intestine}) - k_{out,GIP,DPP4-dependent} \times C_{GIP} \times DPP4_{activity} - k_{out,GIP,DPP4-independent} \times C_{GIP}$$

$$C_{GIP}(0, SS) = \frac{k_{in,GIP}}{k_{out,GIP,DPP4-dependent} + k_{out,GIP,DPP4-independent}} \quad (5.9)$$

5.3.2.3. Glucose-insulin-glucagon sub-model

Initial model:

As depicted in our initial model, plasma glucose originates from two primary sources: dietary intake (exogenous) and hepatic production (endogenous). Dietary glucose enters the central compartment from the depot compartment through the first-order rate constant k_a , glucose. The hepatic contribution to glucose is represented by the zero-order rate constant k_{in} , glucose. Conversely, glucose elimination involves two distinct pathways: one involves the consumption by brain and nerve cells, which is insulin-independent, and the other entails uptake by various tissue cells like muscles, kidneys, and adipose tissues, which is insulin-dependent. Thus, our base model incorporates dual parameters for glucose elimination from the central compartment: the second-order rate constant $k_{out, glucose, insulin-dependent}$, and the first-order rate constant $k_{out, glucose, insulin-independent}$.

Two indirect response models were employed to quantitate insulin and glucagon concentrations, respectively. In these models, $k_{in,insulin}$ and $k_{in,glucagon}$ denote the zero-order rate

constants governing endogenous production, while $k_{out,insulin}$ and $k_{out,glucagon}$ characterize the first-order rate constants governing degradation.

The base model structure reveals regulatory pathways among insulin, glucagon, and glucose within the central compartment, summarized as follows:

- Both GLP-1 and GIP exert a strong stimulatory effect on insulin secretion from pancreatic islet β -cells, while GLP-1 inhibits glucagon secretion in T2DM patients [141, 142].
- Glucose has the ability to elevate the insulin release rate ($k_{in,insulin}$) from pancreatic β -cells in T2DM patients [161].
- Glucagon is capable of increasing the hepatic glucose production rate ($k_{in,glucose}$) [161].
- Insulin can effectively suppress glucagon secretion in healthy subjects [162, 163].
- Amino acids uptake from a high-protein meal act as potent stimulators of glucagon secretion [164].

Insulin-dependent glucose elimination rate constant is proportional to the insulin concentration. Meanwhile in the initial model, the interplay of other biomarkers was assumed to follow a simple linear relationship, where a unit increase in the concentration of one biomarker leads to a proportionate increase or decrease in the rate constant that governs the synthesis or degradation processes of another biomarker regulated by the former.

Tested modifications on top of base model:

However, the model exhibited inadequate fitting, as indicated in **Table 5-2**. To address these limitations, adjustments were made to the base model and are summarized as follows:

- In T2DM patients, the insulinotropic effect of GIP is notably diminished [144], while its glucagonotropic effect remains significant [143]. To reflect this physiological difference, we opted to remove the simulation of GIP on insulin release, while incorporating its impact on glucagon secretion.
- Recent findings indicate that insulin can inhibit glucagon secretion in healthy individuals but not in those with T2DM [162]. Consequently, the insulin-mediated inhibition of glucagon secretion was omitted.
- For a more comprehensive representation of insulin secretion, the model was augmented with a circadian variation component [146].

Final model:

We incorporated modifications into our initial model. Therefore, in our final model, plasma glucose concentration arises not only from the absorption of glucose from exogenous sources like food but also from endogenous hepatic production, represented by the zero-order rate constant, $k_{in, glucose}$. The utilization of glucose relies on its uptake by adipose, kidney, and muscle cells, which is insulin-dependent and described by the second-order rate constant, $k_{out, glucose, insulin-dependent}$. Additionally, glucose uptake by brain and nerve cells, which is insulin-independent, is characterized by $k_{out, glucose, insulin-independent}$. Not only glucose, insulin and glucagon are also incorporated into the final model, and they are represented through indirect response models with secretion rate constants ($k_{in, insulin}$ and $k_{in, glucagon}$) and degradation rate constants ($k_{out, insulin}$ and $k_{out, glucagon}$).

To establish the connection between incretin effects and the glucose-glucagon-insulin system in T2DM patients, it is crucial to recognize that GIP stimulates glucagon secretion, while GLP-1 stimulates insulin secretion and suppresses glucagon secretion. An incremental rise in GIP

concentration results in a proportionate increase in the glucagon secretion rate constant, denoted by the slope SLGN. Similarly, a unit increase in GLP-1 concentration corresponds to a proportional rise in the insulin secretion rate constant with a slope (SLIG), and a reduction in glucagon production rate with a slope SLGN.

Moreover, glucose has been shown to stimulate insulin production, especially at elevated concentrations in T2DM patients. Additionally, glucagon has been observed to enhance hepatic glucose production through the activation of the enzyme glycogen phosphorylase. Reflecting this, an incremental rise in glucose concentration induces a linear increase in the insulin secretion rate constant, defined by the slope SLG. Conversely, an incremental increase in glucagon concentration triggers a linear augmentation in hepatic glucose production rate, quantified by the slope PGNG. Furthermore, the influence of protein is also integrated into the model, as it stimulates glucagon secretion. A unit increase in protein concentration leads to a linear escalation in the glucagon production rate, characterized by the slope SLP.

The essential equations are outlined below:

$$\frac{dC_{\text{glucagon}}}{dt} = k_{\text{in,glucagon}} \times (1 - SLGN \times C_{\text{GLP-1}}) \times (1 + SLGN \times C_{\text{GIP}}) \times (1 + SLP \times A_{\text{protein}}) - k_{\text{out,glucagon}} \times C_{\text{glucagon}}$$

$$C_{\text{glucagon}}(0, \text{SS}) = \frac{k_{\text{in,glucagon}}}{k_{\text{out,glucagon}}} \quad (5.10)$$

$$\frac{dC_{\text{insulin}}}{dt} = k_{\text{in,insulin}} \times (1 + SLIG \times C_{\text{GLP-1}}) \times (1 + SLG \times C_{\text{glucose}}) - k_{\text{out,insulin}} \times C_{\text{insulin}}$$

$$C_{\text{insulin}}(0, \text{SS}) = \frac{k_{\text{in,insulin}}}{k_{\text{out,insulin}}} \quad (5.11)$$

$$\frac{dC_{\text{glucose,central}}}{dt} = k_{\text{tr}} \times A_{\text{glucose,intestine}} / V_{\text{glucose,central}} + k_{\text{in,glucose}} \times (1 + PGNG \times C_{\text{glucagon}}) - k_{\text{out,insulin-dependent}} \times C_{\text{insulin}} \times C_{\text{glucose}} - k_{\text{out,insulin-independent}} \times C_{\text{glucose}}$$

$$C_{\text{glucose,central}}(0, \text{steady-state}) =$$

$$\frac{k_{\text{in,glucose}}}{k_{\text{out,insulin-dependent}} \times C_{\text{insulin}}(0, \text{SS}) + k_{\text{out,insulin-independent}}} \quad (5.12)$$

$$\frac{dA_{\text{glucose,depot}}}{dt} = -k_{a,\text{glucose}} \times A_{\text{glucose,depot}}$$

$$A_{\text{glucose,depot}}(0) = \text{Exogenous glucose intake} \quad (5.13)$$

$$\frac{dA_{\text{glucose,intestine}}}{dt} = k_{a,\text{glucose}} \times A_{\text{glucose,depot}} - k_{\text{tr}} \times A_{\text{glucose,intestine}}$$

$$A_{\text{glucose,intestine}}(0) = 0 \quad (5.14)$$

$$\frac{dA_{\text{protein}}}{dt} = -k_{\text{deg,protein}} \times A_{\text{glucose,depot}}$$

$$A_{\text{protein}}(0) = \text{Exogenous protein intake} \quad (5.15)$$

Insulin secretion:

An established "surge function," previously published, was employed to depict insulin secretion [146]. This modulating function (M), detailed below, is defined by four parameters that determine whether a model term or parameter subject to circadian variation experiences stimulation or inhibition: the amplitude (MA) of modulation, its width (MW), and the time of maximum modulation (MT_{max}).

$$M(t) = \frac{MA}{(\frac{t-MT_{\text{max}}}{MW})^N + 1} \quad (5.16)$$

$$P(t) = P_0(1 + M(t)) \quad (5.17)$$

P₀ denotes the respective original term or parameter before modulation.

The final model offers excellent model fitting, parameter estimation with minimal RSEs, and a low OFV, as demonstrated in **Table 5-2**.

5.3.3. Model implementation

The model was constructed using the nonlinear mixed-effects modeling approach in NONMEM (Version 7.4.3; Icon Development Solutions, Ellicott City, Maryland) in conjunction with Pirana (version 2.9.9, <http://www.pirana-software.com/>) for interfacing. The first-order conditional estimation method with interaction (FOCEI) was employed, along with a user-defined subroutine (ADVAN13). For graphical analysis and data management, Sigmashow was utilized.

5.3.4. Model evaluation

Final model selection was based on biological and physiological plausibility, goodness-of-fit plots, stability of parameter estimates and objective function value. The likelihood ratio test was used for comparing nested models where a decrease in the NONMEM objective function (-2 log likelihood) of 3.84 points was necessary to consider the improvement in model performance statistically significant at $\alpha= 0.05$.

5.4. Results

5.4.1. Final model structure

A comprehensive quantitative system pharmacology model has been successfully established (**Figure 5-2**).

Firstly, the ideal characterization of linagliptin's PK and PD data employs a dual TMDD model. This comprehensive framework encompasses linagliptin's interaction with DPP-4 in tissues and plasma, along with enterohepatic recirculation (EHC). DPP-4 inhibition is proportional to target occupancy with the coefficient of maximal inhibition (I_{max}). GLP-1 and GIP both are characterized by indirect response models with zero-order production (k_{in}) and DPP-4 activity dependent degradation ($k_{out, DPP4-dependent}$), as well as DPP4-independent degradation ($k_{out, DPP4-independent}$).

independent). Secondly, glucose is absorbed from the depot compartment (stomach) into the transit compartment (intestine), where it stimulates GLP-1 and GIP with distinct slopes (SLGLP and SLGIP) before being absorbed into the plasma. Furthermore, plasma glucose is determined by hepatic glucose production ($k_{in, glucose}$) and intestinal absorption (k_{tr}), along with insulin and insulin-independent degradation pathways ($k_{out, glucose, insulin-dependent}$ and $k_{out, glucose, insulin-independent}$). Insulin and glucagon follow indirect response models with secretion ($k_{in, insulin}$ and $k_{in, glucagon}$) and degradation ($k_{out, insulin}$ and $k_{out, glucagon}$) rate constants. GIP stimulates glucagon secretion, GLP-1 stimulates insulin secretion while inhibiting glucagon production. GIP concentration increase leads to proportional glucagon secretion rate change (slope SLIGN). Similarly, GLP-1 concentration change affects insulin secretion (slope SLIG) and glucagon production (slope SLGN). Glucose concentration change stimulate insulin secretion (slope SLG), while glucagon concentration change increase hepatic glucose production (slope PGNG). Protein stimulates glucagon secretion with a proportional rate (slope SLP).

5.4.2. Goodness of model fitting

As depicted in **Figures 5-3** and **5-4**, the model proficiently captured linagliptin concentration (**Figures 5-3 A and B**) and plasma DPP-4 inhibition (**Figures 5-4 A and B**) profiles in healthy subjects, receiving single escalating doses (1, 2.5, 5, and 10 mg) and multiple escalating doses (2.5, 5, and 10 mg) once daily for 12 days. Model-predicted data closely aligned with experimental data. Moreover, the model accurately characterized linagliptin concentration (**Figures 5-3 C and D**) and plasma DPP-4 inhibition (**Figures 5-4 C and D**) time profiles in T2DM patients, encompassing oral doses of linagliptin (0.5, 2.5, or 10 mg) once daily for 28 days or ascending doses (1, 2.5, 5, or 10 mg) once daily for 12 days. The standard goodness-of-fit plots

confirm the adequacy of the PK/PD model in describing linagliptin plasma concentration, plasma DPP-4 activity, as well as the concentrations for GLP-1, GIP, glucose and glucagon (**Figure 5-5**).

Figure 5-6 demonstrates the effective characterization by our proposed model of the 24-hour blood glucose, 3-hour GLP-1 and GIP, and glucagon profiles in T2DM patients undergoing an MTT after 28 days of treatment with either 5 mg linagliptin once-daily doses or placebo. The close alignment between observed and model-predicted data highlights this success. Initially, our model adeptly captures the post-MTT glucose concentration increase, mainly driven by exogenous glucose uptake, followed by a decline due to tissue uptake in both the linagliptin QD dose group and placebo group (**Figure 5-6 A**). Furthermore, the model accurately reproduces the reduced glucose AUC and C_{max} resulting from 28-day linagliptin QD dosing compared to the placebo group, evident at each time point within the 24-hour period. This alignment between observed and model-predicted data reaffirms the model's reliability (**Figure 5-6 A**). Secondly, our model accurately predicts the rise in GLP-1 and GIP concentrations in both the 5 mg QD linagliptin group and placebo group post-MTT, attributable to exogenous glucose stimulating incretin secretion, in agreement with observations (**Figure 5-6 B and C**). Moreover, the increased AUC and C_{max} of GLP-1 and GIP in the 5 mg linagliptin QD dose group compared to placebo arises from linagliptin's pharmacological impact on DPP-4 inhibition, effectively decelerating DPP-4 mediated degradation and thereby extending the duration of their presence in the plasma. Our model effectively captures these group differences (**Figure 5-6 B and C**). Finally, it's noteworthy that our model effectively captures the post-MTT increase in glucagon, attributed to the stimulation of glucagon production by amino acids from the MTT meal (**Figure 5-6 D**). Additionally, our model accurately predicts lower glucagon concentrations in the 5 mg QD linagliptin dose group compared to the placebo group (**Figure 5-6 D**). This reduction could

potentially be influenced by the combined effects of the two incretins on the glucagon production rate.

5.4.3. Parameter estimation

Moreover, our model provides insightful perspectives on linagliptin's PK/PD dynamics (**Table 5-3**). Remarkably, our estimation for the linagliptin peripheral volume of distribution is 226 L, signifying substantial tissue distribution, and corresponds to literature values of 380–1540 L reported in healthy males receiving single doses of 0.5–10 mg [34]. Additionally, the estimated clearance of 33.1 L/hr closely resembles literature-reported values [34, 119, 165, 166]. Linagliptin's interaction with DPP-4 is characterized by a second-order rate constant (k_{on}) of 0.739 $nM^{-1}h^{-1}$, leading to complex formation, which subsequently dissociates back into the free drug and target at a first-order rate constant (k_{off}) of 0.204 h^{-1} . These estimations closely mirror in vitro experimental findings ($k_i = 1 nM$, $k_{off} = 0.108 h^{-1}$) [38]. Pharmacokinetic parameters remain consistent across both healthy and T2DM subjects. Furthermore, the estimated tissue DPP-4 content (1120 nmol) aligns with previous modeling results of 1990 nmol [140]. Linagliptin's maximum inhibition effect (I_{max}) is estimated at 90.7%, closely resembling the reported literature value of 93.5% [140].

Our model offers well-justified parameter estimations related to the dynamics of incretins, glucose, glucagon, and insulin., notably the estimated endogenous insulin-dependent glucose degradation rate at $4.59 nM^{-1}h^{-1}$, which align closely with the value reported by Jauslin et al of $4.15 nM^{-1}h^{-1}$ [146]. Likewise, the estimated endogenous glucose production rate of 4.11 mM/h harmonizes with other literature-reported values (2.23 mM/h) [153]. Our model estimated insulin-dependent glucose degradation rate constant is $4.59 nM^{-1}h^{-1}$, which is approximately two-fold lower than Jauslin et al reported value ($7.96 nM^{-1}h^{-1}$).

Moreover, our model predicts the proportion of DPP-4 dependent elimination in the overall clearance of GLP-1 and GIP, both of which undergo metabolism by DPP-4 and neutral endopeptidase (NEP). The model estimates the DPP-4 independent elimination rates for GLP-1 and GIP as 2.05 and 3.66 h^{-1} , respectively, constituting 20.0% and 50.8% of the total clearance, which our model calculates to be 10.2 and 7.2 h^{-1} , respectively. These findings highlight the greater relevance of DPP-4 dependent elimination for GLP-1 compared to GIP, with 80.0% of GLP-1 elimination attributed to DPP-4, while only 49.2% of GIP elimination relies on DPP-4.

5.5. Discussion

A quantitative system pharmacology model was developed successfully to characterize the linagliptin intervention on DPP-4 plasma inhibition, and dynamics of two important hormones, GLP-1 and GIP, in addition to glucose, glucagon.

Mathematical models have been employed to investigate glycemic control systems. Bergman's 1979 "minimal model" is a pivotal tool for assessing insulin sensitivity and glucose metabolism. This approach mathematically captures glucose and insulin dynamics within the first two hours of an intravenous glucose tolerance test [145, 149]. Subsequently, various insulin-glucose models have emerged, featured by intricate structures and extended experimental timeframes [146-148]. For instance, in 2011, Jauslin et al. introduced a comprehensive insulin-glucose model that characterizes 24-hour glucose and insulin profiles in T2DM patients [146]. Their model enhances physiological fidelity in representing insulin and glucose disposition, incorporating circadian insulin secretion and the influence of incretins. The model describes glucose absorption from the stomach to the plasma via the intestine, involving compartments for depot, transit, and central components. It also accounts for endogenous glucose generation from the liver and plasma glucose elimination through insulin-dependent and -independent pathways. Insulin is depicted using a single-compartment model, integrating circadian secretion and linear elimination. The model also encompasses glucose's impact on insulin production and insulin's effect on glucose degradation, incorporating "effect compartments." Notably, in this model, the absorption rate of glucose was intricately tied to insulin secretion through a linear function to describe the incretin effect. It's important to note that the model did not differentiate between the effects of glucose on GLP-1 and GIP, nor did it distinguish the individual impacts of GLP-1 and GIP on insulin secretion in patients with type 2 diabetes mellitus (T2DM). Nevertheless, this report

supplied crucial parameter values, notably the insulin-independent glucose degradation rate constant, which we retained as a fixed parameter during our model development. Our model structure for the insulin-glucose portion closely resembles the published model, except for two aspects. Firstly, we employed a straightforward linear relationship to represent the impact of insulin on glucose elimination and glucose-induced stimulation on insulin secretion, opting for simplicity over the effect compartment utilized in Jauslin's model. Furthermore, we did not incorporate a peripheral compartment into our model, as the one-compartment model adequately captured the fitting for the present glucose data.

However, up to 2011, numerous physiological models of glucose homeostasis published overlooked the influence of glucagon on the intricate dynamics of glucose and insulin. In 2019, Masroor et al. addressed this gap by augmenting Bergman's insulin-glucose model with the inclusion of another hormone in glycemic control: glucagon [151]. In this enhanced model, insulin is characterized through a one-compartment model, encompassing its distinct production and clearance processes. Glucose dynamics entail a hepatic production rate and dual elimination pathways, insulin-dependent and insulin-independent. Notably, glucose stimulates insulin production, while glucagon prompts glucose production. Conversely, insulin stimulates glucose elimination, and low glucose levels (<80 mg/dL) trigger glucagon production. A pioneering aspect of this model is the incorporation of glucagon binding kinetics with the glucagon receptor positioned on the hepatocyte membrane surface, followed by internalization upon glucagon stimulation—a phenomenon known as TMDD of glucagon. Nevertheless, our model did not include kinetics that describe the binding of glucagon to its receptor, primarily due to limitations in available data. Our model did not include the glucose-stimulated production of glucagon, unlike

Masroor's model. This omission is due to the fact that this effect becomes negligible when glucose concentrations exceed 100 mg/dL or 5.6 mmol/L in T2DM patients.

In addition, Liu et al. constructed an intricate glucose-insulin-glucagon model that delves into molecular intricacies, including glycogen conversion within the liver [150]. This comprehensive model yields valuable insights, offering crucial parameters such as degradation rate constants for insulin and glucagon.

While existing models have tackled the quantitative interplay among crucial glycemic control hormones—glucose, insulin, and glucagon—there remains a gap in integrating drug intervention. This integration is vital for establishing a link between drug pharmacokinetics/pharmacodynamics and glycemic control. Such a connection would enable the prediction of not only the drug's impact on its direct pharmacological target but also on other essential biomarkers and clinical endpoints within glycemic control. This holistic approach aids in facilitating drug dose selection, aligning with the overarching objective of quantitative system pharmacology models. These models aim to bridge pharmacokinetics/pharmacodynamics and system pharmacology, thereby fostering a comprehensive understanding of diseases like type 2 diabetes mellitus (T2DM).

For instance, Schneck et al. crafted a semi-mechanistic integrated glucose-insulin-glucagon model to aid in the dose selection of an oral glucokinase activator, LY2599506 [153]. However, they did not incorporate the incretin effect in their study as it was not directly relevant to the drug's mechanism of action. Similarly, Peng et al. developed an insulin-glucose-glucagon model to elucidate the effects of a novel glucagon receptor antagonist, MK-3577, on glycemic control [154]. Yet, like the previous example, they also did not differentiate the incretin effect. In contrast, Røge et al. introduced a GLP-1-GIP-glucose model to distinguish the influence of glucose

on the two incretins, GLP-1 and GIP, by considering their release locations within the intestine [157]. However, this model did not encompass the impact of GLP-1 and GIP on other vital biomarkers such as insulin and glucagon.

Our proposed model provides a comprehensive quantitative analysis of two critical aspects: (1) the distinct effects of glucose on GLP-1 and GIP, and (2) the unique impacts of GLP-1 and GIP on insulin and glucagon. Notably, our model demonstrates that a 1 mmol increase in glucose results in a substantial 0.0160-fold increase in GLP-1 production rate, a value comparable to the estimate by Moller et al (0.0472 mmol^{-1}) [167].

On the other hand, our model distinguishes the separate effects of GLP-1 and GIP on insulin secretion in T2DM patients. GLP-1 primarily stimulates insulin secretion and has a minor inhibitory effect on glucagon concentration. This is supported by our model, where a 1 pM increase in GLP-1 concentration leads to a 0.0226-fold increase in the insulin secretion rate constant—higher than the 0.0166-fold decrease in the glucagon secretion rate constant caused by the same GLP-1 increase. Recent reports suggest that while GLP-1 can inhibit glucagon secretion, GIP can stimulate glucagon secretion. According to our model, a 1 pM increase in GLP-1 concentration results in a significant 0.0166-fold decrease in the glucagon secretion rate constant, while a 1 pM increase in GIP concentration leads to a 0.0014-fold increase in the glucagon secretion rate. This highlights that GLP-1's inhibition of glucagon secretion is over 10-fold more profound than GIP's stimulation of glucagon secretion.

In 2013, Schaller et al. established a comprehensive physiologically based whole body model for the glucose-insulin-glucagon system using PK-sim and MoBi [152]. Building upon this foundation, Balazki et al. further extended the model's scope by incorporating the action of a DPP-4 inhibitor named sitagliptin, thereby creating a quantitative system pharmacology (QSP)

framework in 2020 [155]. While this model appears to encompass the intricate dynamics of incretin effects and the interplay among glucose, insulin, and glucagon, it is worth noting that it remains a simulation-based study. In this study, all parameters were either derived from existing literature or estimated based on the chemical and physiological attributes of the compounds integrated into the model. While the model demonstrates promise in elucidating the effects of sitagliptin intervention, its applicability to diverse classes of therapeutic compounds for type 2 diabetes mellitus (T2DM) may be limited. The absence of explicit equations and a transparent model structure could potentially hinder investigators from readily adapting this model to different therapeutic scenarios within the realm of T2DM management. In contrast to the aforementioned model, our proposed Quantitative Systems Pharmacology (QSP) framework offers a distinct advantage by presenting transparent and well-defined mathematical differential equations, coupled with a clear and easily comprehensible model structure. This approach enhances accessibility for readers seeking a comprehensive understanding of the model's intricacies and dynamics.

Given the prevalent use of combination therapy in the treatment of type 2 diabetes mellitus (T2DM), our QSP model holds particular relevance. Having already established a system that incorporates key biomarkers relevant to T2DM, our forthcoming endeavors involve the application of this model to forecast the glucose-lowering effects resulting from the synergistic interaction of diverse classes of T2DM therapeutics.

5.6. Conclusions

In conclusion, we have developed a comprehensive QSP model integrating GIP-GLP1-glucagon-glucose-insulin system using linagliptin as the model drug for therapeutic intervention. Our model, containing a dual TMDD model structure for linagliptin and extensive feedback loops for the glucose regulation system, adequately characterized the substantial nonlinear PK of

linagliptin, time course of DPP-4 inhibition, as well as the kinetics of GIP, GLP-1, glucagon and glucose simultaneously in human. Our model provided valuable insights on linagliptin PK/PD and complicated glucose homeostasis and has the potential to be adopted by others to evaluate the antidiabetic effect of other DPP-4 inhibitors or be used to evaluate the effect of combination antidiabetic therapy targeting different components of glucose control system.

Table 5-1. The data source used for linagliptin QSP model integrating GIP, GLP-1, glucagon, glucose and insulin.

No.	PMID	Dosing regime	Sampling time points	Subjects	Mean weight (kg)	Data Type	Reference
1a	20637971	Placebo, 1, 2.5, 5, and 10 mg, single oral dose	0, 0.5, 1, 1.5, 2, 3, 4, 6, 8, 12, 24, 48, 72, 96, 144, and 192 hours	Healthy Japanese volunteers (N=32)	61.2 kg	Linagliptin PK and plasma DPP-4 inhibition	[118]
1b	20637971	Placebo, 2.5, 5, and 10 mg, once daily for 12 days	0, 0.5, 1, 1.5, 2, 3, 4, 6, 8, 12, 23.5 hours on Day 1 and Day 12, 30 minutes before drug administration on Day 2 through Day 11	Healthy Japanese volunteers (N=24)	61.6 kg	Linagliptin PK and plasma DPP-4 inhibition	[118]
2	19476474	Placebo, 1, 2.5, 5, and 10 mg, once daily for 12 days	0, 0.5, 1, 1.5, 2, 3, 4, 6, 8, 12, 23.5 hours on Day 1 and Day 12, 30 minutes before drug administration on Day 2 through Day 11	T2DM Caucasian patients (N=48)	NA	Linagliptin PK and plasma DPP-4 inhibition	[111]
3	21723606	Placebo, 0.5, 2.5, and 10 mg, once daily for 28 days	0, 0.5, 1, 1.5, 2, 3, 4, 6, 8, 12, 23.5 hours on Day 1 and Day 28	T2DM Japanese patients (N=72)	64.5 kg	Linagliptin PK and plasma DPP-4 inhibition	[39]

Table 5-1 (Continued).

		5 mg and placebo once daily for 28 days,	GLP-1, GIP, Glucagon: -1 (i.e., pre-dose), 0, 0.25, 0.5, 1, 2 hours following MTT on Day 28	T2DM patients (N=80)	NA	Time course of glucose, glucagon, GLP-1, and GIP	[158]
4 22986920		MTT was performed on days 1, 28, 29, and 30 one hour after linagliptin or placebo administration	Glucose: -1 (i.e., pre-dose), 0, 0.25, 0.5, 1, 1.5, 2, 3, 5, 6, 7, 8, 11, 12, 13, 15, 18, and 23 hours following MTT on Day 28				

Table 5-2. Model development history.

No.	Description	Fit goodness	OFV
1	Base model;	Poor fitting for both glucose and DPP-4 plasma inhibition	2961.336
2	Add intestine compartment for glucose absorption	Glucose fitting got improved but still poor fitting for DPP-4 plasma inhibition	2872.581
3	Add EHC component	Fitting well	2835.101
4	Add independent elimination pathway for both GLP-1 and GIP	Fitting well but with high RSE of two parameters	2821.059
5	Add insulin circadian rhythm	Fitting well with low RSEs	2821.104
6	Add different k_{on} and k_{off} value for linagliptin tissue binding	Poor fitting for DPP-4 plasma inhibition with high RSE	2944.511
7	Proceed with model 5, the effect of glucose on insulin, the effect of glucagon on glucose and the effect of insulin on glucagon were described using a M-M function	Fitting well with high RSEs	2820.935
8	Proceed with model 5, the effect of glucose on insulin, the effect of glucagon on glucose and the effect of insulin on glucagon were described using a power function	Fitting well with high RSEs	2821.113
9-Final Model	Proceed with model 5, the effect of GIP on insulin secretion was removed and the effect of GIP on glucagon production is added, inhibitory effect of insulin on production of glucagon was removed	Fitting well with low RSEs	2821.896

Table 5-3. Final parameter estimations for the proposed QSP model of the incretin hormones GIP and GLP-1, glucagon, glucose, insulin and small-molecule DPP-4 inhibitor, linagliptin.

Parameter	Unit	Definition	Value	RSE (%)	Reference
$V_{\text{linagliptin, central}}$	L	Linagliptin central volume of distribution	4.36	4	
CL	L/hr	Linagliptin central clearance	33.1	6	
$V_{\text{linagliptin, peripheral}}$	L	Linagliptin peripheral volume of distribution	226	19	
Q	L/hr	Linagliptin distribution flow	418	27	
$k_a, \text{linagliptin}$	h^{-1}	Linagliptin absorption rate constant	0.79	21	
F		Bioavailability	0.3 FIX		[34]
k_{cb}	h^{-1}	Transit rate constant from central to bile	3.4	31	
k_{bg}	h^{-1}	Transit rate constant from bile to depot	0.0391	38	
k_{on}	$\text{nM}^{-1} \bullet \text{h}^{-1}$	Linagliptin association rate constant	0.739	17	
k_{off}	h^{-1}	Linagliptin dissociation rate constant	0.204	16	
$R_{\max, \text{plasma}}$	nmol	DPP-4 amount in plasma	22.6 FIX		[35]
$R_{\max, \text{tissue}}$	nmol	DPP-4 amount in tissue	1120	10	
I_{\max}	%	Maximum inhibition effect	90.7	2	
$k_{in, \text{GLP-1}}$	$\text{pM} \bullet \text{h}^{-1}$	Endogenous GLP-1 production rate constant	20.1 FIX		[157]
$k_{out, \text{GLP-1, total}}$	h^{-1}	Total GLP degradation rate constant	10.2 FIX		[157]
$k_{in, \text{GIP}}$	$\text{pM} \bullet \text{h}^{-1}$	Endogenous GIP production rate constant	72 FIX		[157]
$k_{out, \text{GIP, total}}$	h^{-1}	Total GIP degradation rate constant	7.2 FIX		[157]
$k_{out, \text{GLP-1, DPP4-independent}}$	h^{-1}	Endogenous DPP4-independent GLP-1 degradation rate constant	2.05	20	
$k_{out, \text{GIP, DPP4-independent}}$	h^{-1}	Endogenous DPP4-independent GIP degradation rate constant	3.66	17	
$k_{in, \text{insulin}}$	$\text{nM} \bullet \text{h}^{-1}$	Endogenous insulin production rate constant	0.0377 FIX		[150]
$k_{out, \text{insulin}}$	h^{-1}	Endogenous insulin degradation rate constant	0.6 FIX		[150]
$k_{in, \text{glucagon}}$	pg/mL/h	Endogenous glucagon production rate constant	42 FIX		[150]
$k_{out, \text{glucagon}}$	h^{-1}	Endogenous glucagon degradation rate constant	0.6 FIX		[150]
$k_{deg, \text{protein}}$	h^{-1}	Protein degradation rate constant	3.43	105	
$k_a, \text{glucose}$	h^{-1}	Glucose absorption rate constant	8.68	42	
V_{glucose}	L	Glucose volume of distribution	10 FIX		[146]
K_{tr}	h^{-1}	Glucose transition rate constant	0.313	29	
$k_{in, \text{glucose}}$	$\text{mM} \bullet \text{h}^{-1}$	Endogenous glucose production rate constant	4.11	57	
$k_{out, \text{glucose, insulin-dependent}}$	$\text{nM}^{-1} \bullet \text{h}^{-1}$	Endogenous insulin-dependent glucose degradation rate constant	4.59	93	
$k_{out, \text{glucose, insulin-independent}}$	h^{-1}	Endogenous insulin-independent glucose degradation rate constant	0.184 FIX		[146]

Table 5-3 (Continued).

SLGLP	mmol^{-1}	Effect of glucose on GLP-1 production	0.016	14
SLGIP	mmol^{-1}	Effect of glucose on GIP production	0.0354	16
SLGN	pM^{-1}	Effect of GLP-1 on glucagon production	0.0166	52
SLIG	pM^{-1}	Effect of GLP-1 on insulin production	0.0226	87
SLIGN	pM^{-1}	Effect of GIP on glucagon production	0.0014	135
PGNG	$(\text{pg/mL})^{-1}$	Effect of glucagon on glucose production	0.0077	92
SLG	mM^{-1}	Effect of glucose on insulin production	0.114	117
SLP	g^{-1}	Effect of protein on glucagon production	0.123	76
MA	%	Modulation amplitude on baseline insulin secretion	-24 FIX	[146]
MW	h	Modulation width on baseline insulin secretion	2.3 FIX	[146]
MTMAX	h	Time of maximal modulation of insulin secretion	18.7 FIX, 1:10 a.m.	[146]
RV		Residual error	0.0431	6

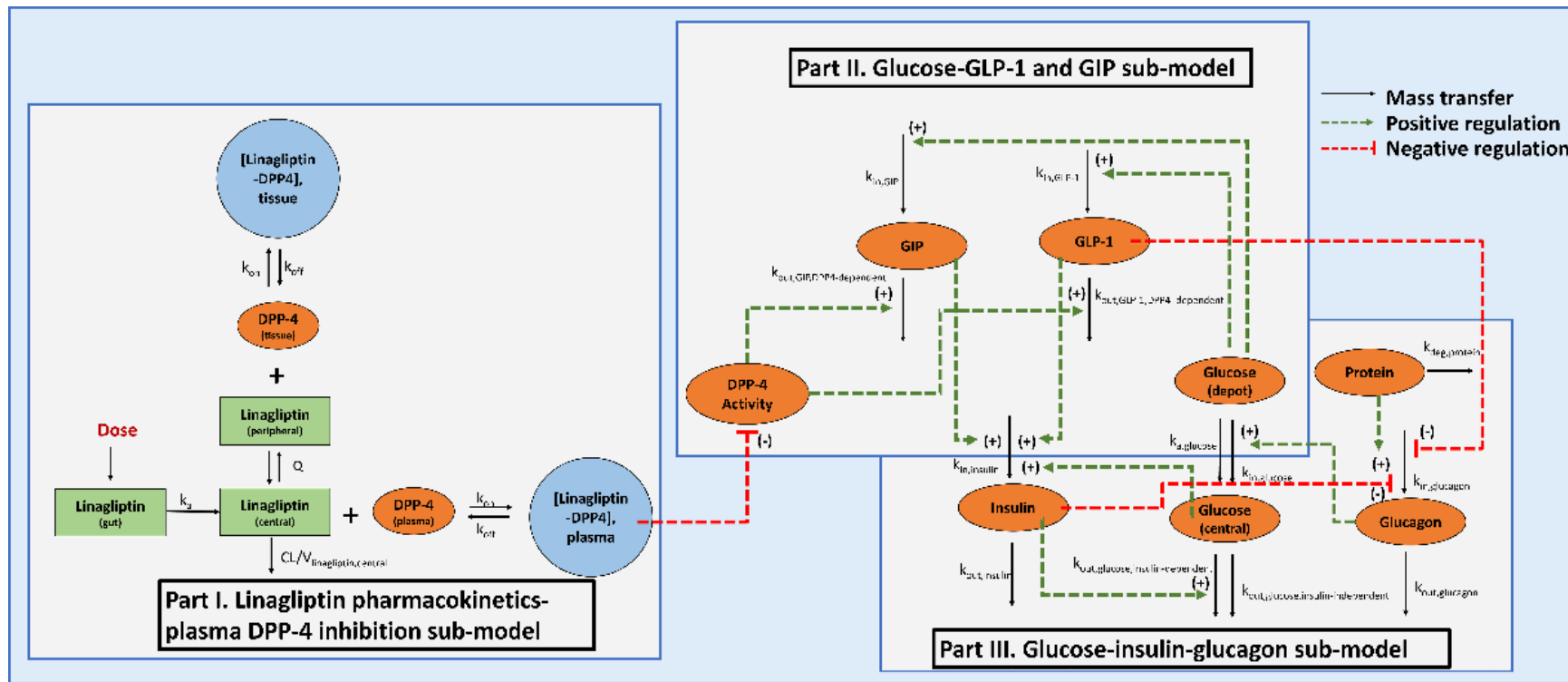


Figure 5-1. Model structure of base model.

Sub model 1: Linagliptin was absorbed from the depot compartment to the central compartment following a first-order rate constant k_a , linagliptin can distribute between central and peripheral compartments and have a linear elimination pathway characterized by k_e (i.e., $\text{CL}/V_{\text{central}}$). Linagliptin distributed in central compartment interacted with soluble DPP-4 located in plasma with the second-order association rate constant (k_{on}) to form a linagliptin-DPP-4 complex. Linagliptin-DPP-4 complex dissociated back to free DPP-4 target and free drug with the first-order dissociation rate constants k_{off} . Meanwhile the linagliptin distributed in the peripheral compartment can also interact with membrane-bound DPP-4 in tissue with the same association rate constant (k_{on}) and dissociation rate constant (k_{off}). The plasma DPP-4 activity was incorporated into the model in a semi-mechanistic way using receptor occupancy theory. **Sub model 2:** Both GLP-1 and GIP concentrations was described by indirect response models with the zero-order rate constants for production ($k_{in, \text{GLP-1}}$ and $k_{in, \text{GIP}}$), and DPP-4 elimination were characterized by two first-order rate constants $k_{out,GLP-1,\text{DPP4-dependent}}$ and $k_{out,GIP,\text{DPP4-dependent}}$, respectively. Endogenous GLP-1 and GIP were reported to be stimulated by glucose distributed in depot compartment. The DPP-4 dependent degradation rates for both GLP-1 and GIP are proportional with DPP-4 activity. **Sub model 3:** Glucose from food was

Figure 5-1 (Continued).

absorbed from the depot compartment to the central compartment following a first-order rate constant $k_{a, \text{glucose}}$ followed by transit rate constant k_{tr} . Protein can be degraded in a first order rate constant, $k_{deg, \text{protein}}$. Endogenous production rate of glucose from the liver was represented by a zero-order rate constant $k_{in, \text{glucose}}$. On the other hand, the elimination of glucose from the central compartment was characterized by two parameters which are the second-order rate constant $k_{out, \text{glucose, insulin dependent}}$ and the first-order rate constant $k_{out, \text{glucose, insulin-independent}}$. Two indirect response models were used to quantify insulin and glucagon concentrations, respectively, where $k_{in, \text{insulin}}$ and $k_{in, \text{glucagon}}$ represent the zero-order rate constants for endogenous production and $k_{out, \text{insulin}}$ and $k_{out, \text{glucagon}}$ define the first-order rate constants for degradation. Both GIP and GLP-1 can stimulate insulin release while GLP-1 can inhibit glucagon production. Insulin can inhibit glucagon production as well. Glucose stimulates insulin production and glucagon can stimulate glucose production. Protein can also stimulate glucagon production. All mass transfer processes are represented using black solid arrows. Simulation effects are represented by green dashed arrows and inhibition effects are represented by red dashed arrows.

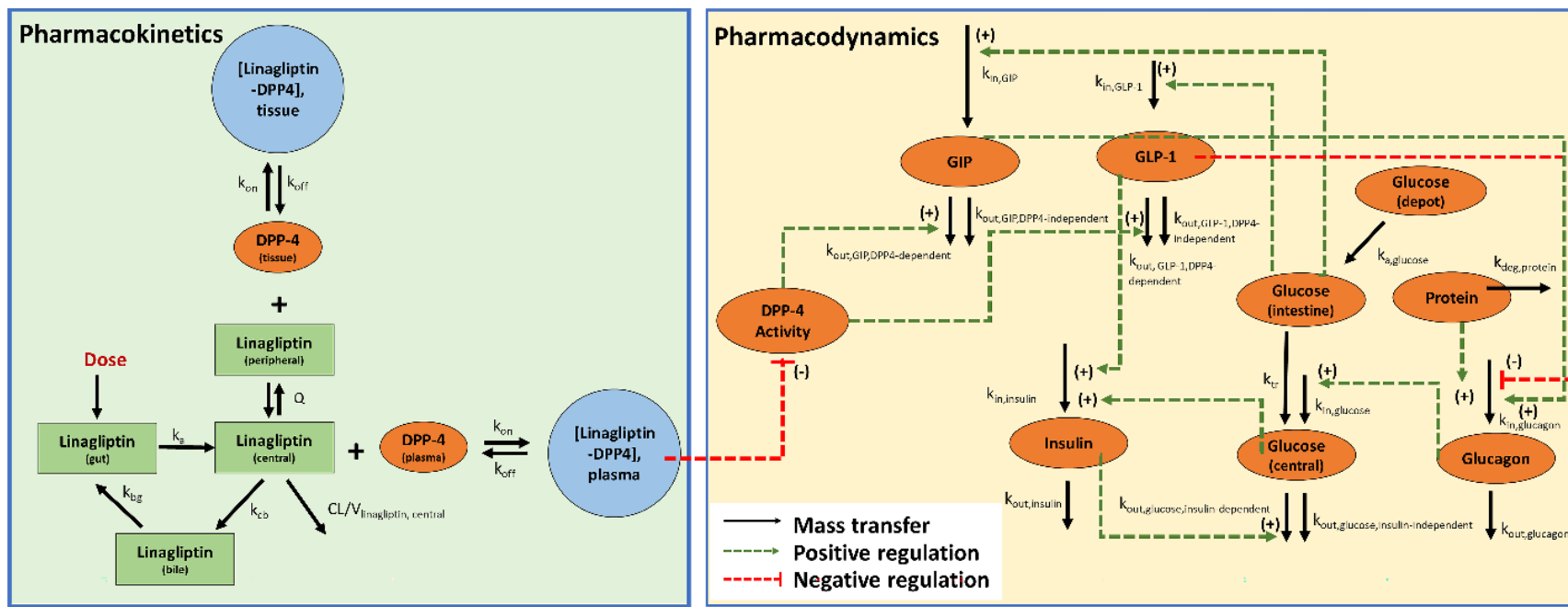


Figure 5-2. Model structure of the final QSP model.

Final model structure of quantitative system pharmacology model for linagliptin. Sub model 1: Linagliptin was absorbed from the depot compartment to the central compartment following a first-order rate constant k_a . Linagliptin circulation from central compartment to the bile, followed by entry into the small intestine, absorption by the enterocyte and transport back to the central compartment was characterized by the transit rate constant k_{cb} and k_{bg} . Linagliptin can distribute between central and peripheral compartments and have a linear elimination pathway characterized by k_e (i.e., $CL/V_{central}$). Linagliptin distributed in central compartment interacted with soluble DPP-4 located in plasma with the second-order association rate constant (k_{on}) to form a linagliptin-DPP-4 complex. Linagliptin-DPP-4 complex dissociated back to free DPP-4 target and free drug with the first-order dissociation rate constants k_{off} . Meanwhile the linagliptin distributed in the peripheral compartment can also interact with membrane-bound DPP-4 in tissue with the same association rate constant (k_{on}) and dissociation rate constant (k_{off}). The plasma DPP-4 activity was incorporated into the model in a semi-mechanistic way using receptor occupancy theory. Sub model 2: Both GLP-1 and GIP concentrations was described by indirect response models with the zero-order rate constants for production ($k_{in, GLP-1}$ and $k_{in, GIP}$), and DPP-4 dependent elimination were characterized by two first-order rate constants $k_{out,GLP-1,DPP-4\text{ dependent}}$ and $k_{out,GIP,DPP-4\text{ dependent}}$ and DPP-4 independent elimination pathways were represented by $k_{out,GLP-1,DPP-4\text{ independent}}$ and $k_{out,GIP,DPP-4\text{ independent}}$, respectively. Endogenous GLP-1 and GIP were reported to be stimulated by glucose distributed in

Figure 5-2 (Continued).

intestine compartment. The DPP-4 dependent degradation rates for both GLP-1 and GIP are proportional with DPP-4 activity. Sub model 3: Glucose from food was absorbed from the depot compartment to the central compartment following a first-order rate constant $k_{a,\text{glucose}}$ followed by transit rate constant k_{tr} . Protein can be degraded in a first order rate constant, $k_{\text{deg, protein}}$. Endogenous production rate of glucose from the liver was represented by a zero-order rate constant $k_{in,\text{glucose}}$. On the other hand, the elimination of glucose from the central compartment was characterized by two parameters which are the second-order rate constant $k_{out,\text{glucose, insulin-dependent}}$ and the first-order rate constant $k_{out,\text{glucose, insulin-independent}}$. Two indirect response models were used to quantify insulin and glucagon concentrations, respectively, where $k_{in,\text{insulin}}$ and $k_{in,\text{glucagon}}$ represent the zero-order rate constants for endogenous production and $k_{out,\text{insulin}}$ and $k_{out,\text{glucagon}}$ define the first-order rate constants for degradation. GLP-1 can stimulate insulin release while inhibiting glucagon production. GIP stimulate glucagon production. Glucose stimulates insulin production and glucagon can stimulate glucose production. Circadian rhythm of insulin is incorporated. Protein can also stimulate glucagon production. All mass transfer processes are represented using black solid arrows. Simulation effects are represented by green dashed arrows and inhibition effects are represented by red dashed arrows.

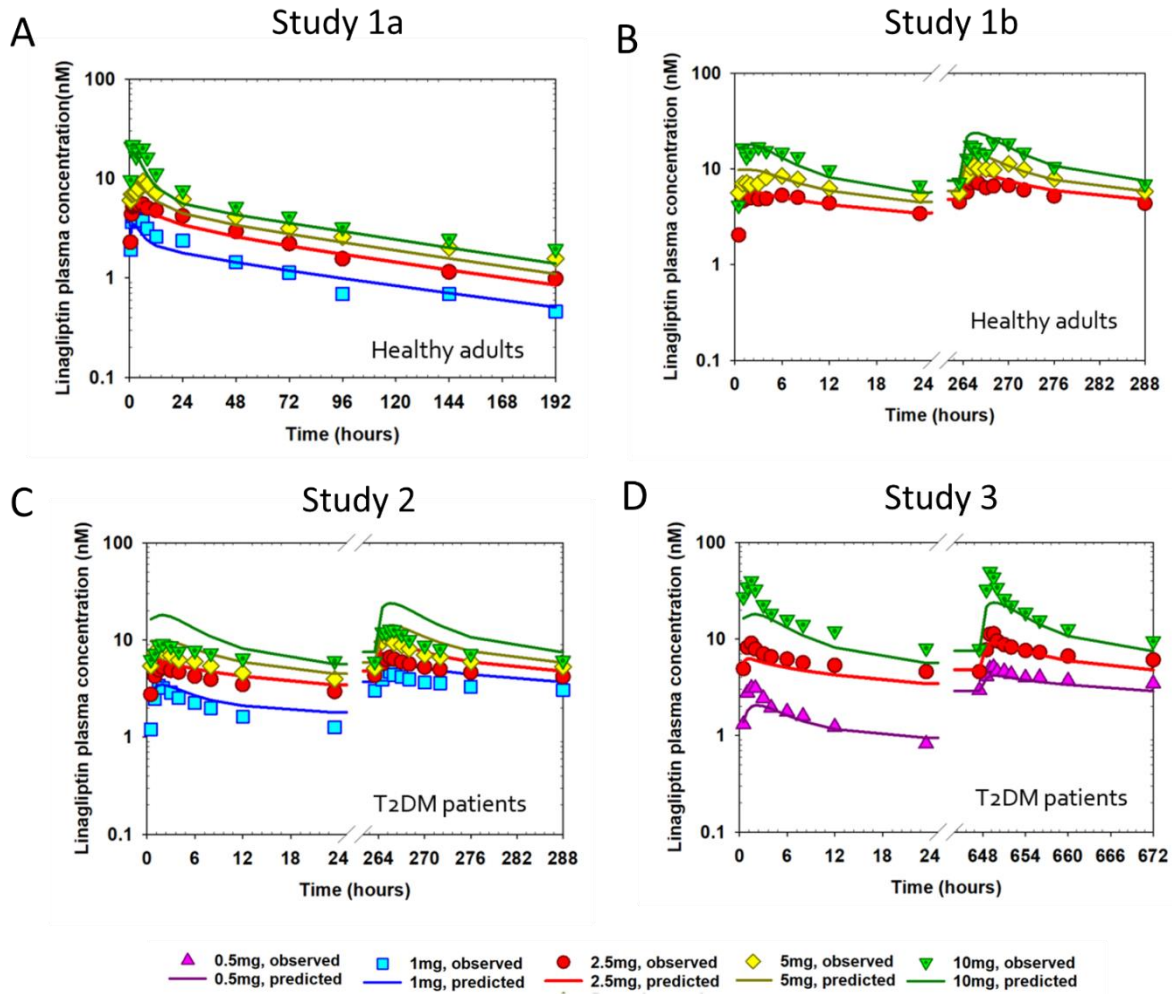


Figure 5-3. Time course of model predicted (lines) vs observed mean (symbols) linagliptin plasma concentrations in both healthy and T2DM patients.

In studies 1a (A), 1b (B), 2 (C), and 3 (D), subjects were administered linagliptin at various doses, including 0.5 mg (purple), 1 mg (cyan), 2.5 mg (red), 5 mg (yellow), and 10 mg (green).

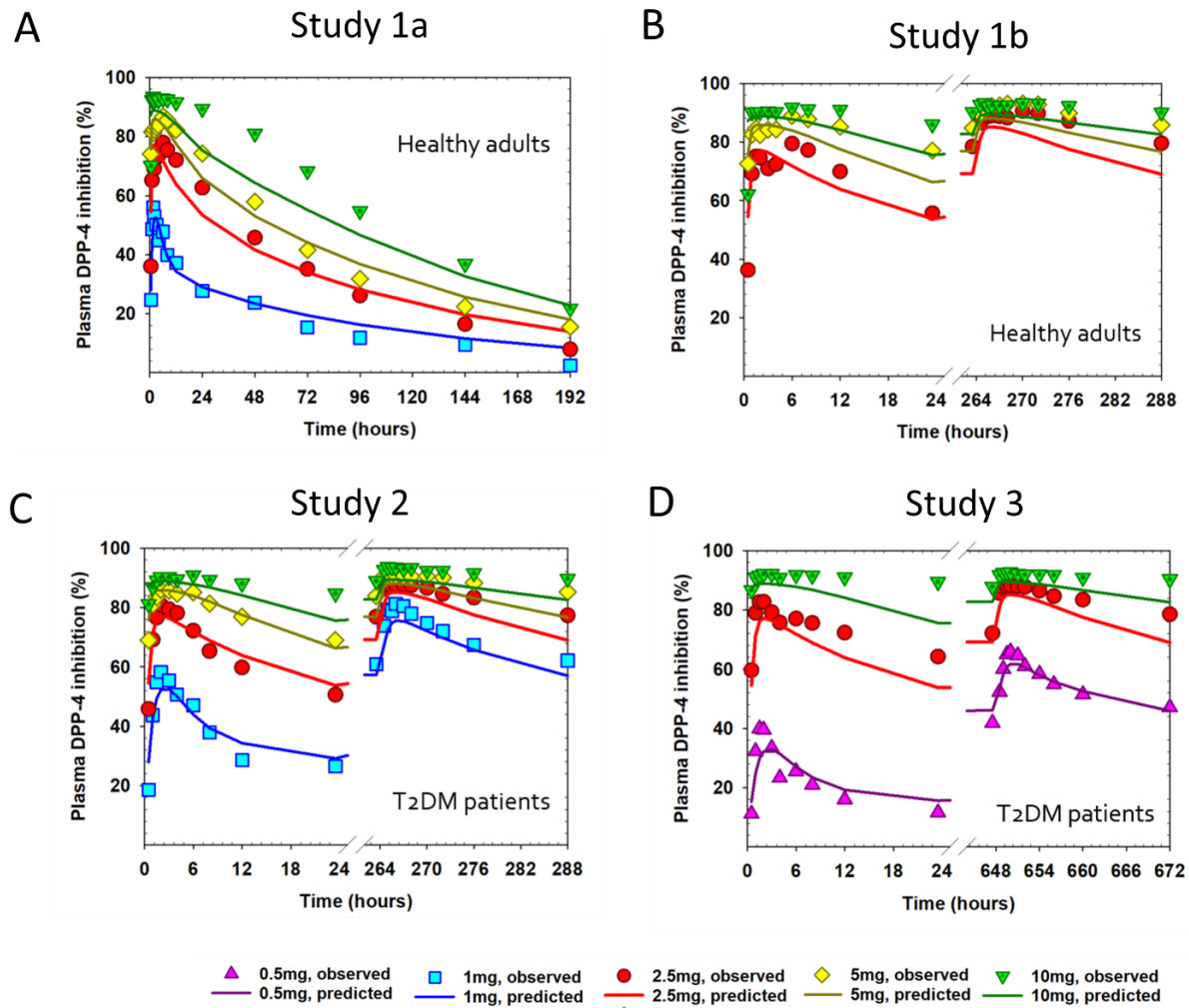


Figure 5-4. Time course of model predicted (lines) vs observed mean (symbols) plasma DPP-4 inhibition (%) in both healthy and T2DM patients.

In studies 1a (A), 1b (B), 2 (C), and 3 (D), subjects were administered linagliptin at various doses, including 0.5 mg (purple), 1 mg (cyan), 2.5 mg (red), 5 mg (yellow), and 10 mg (green).

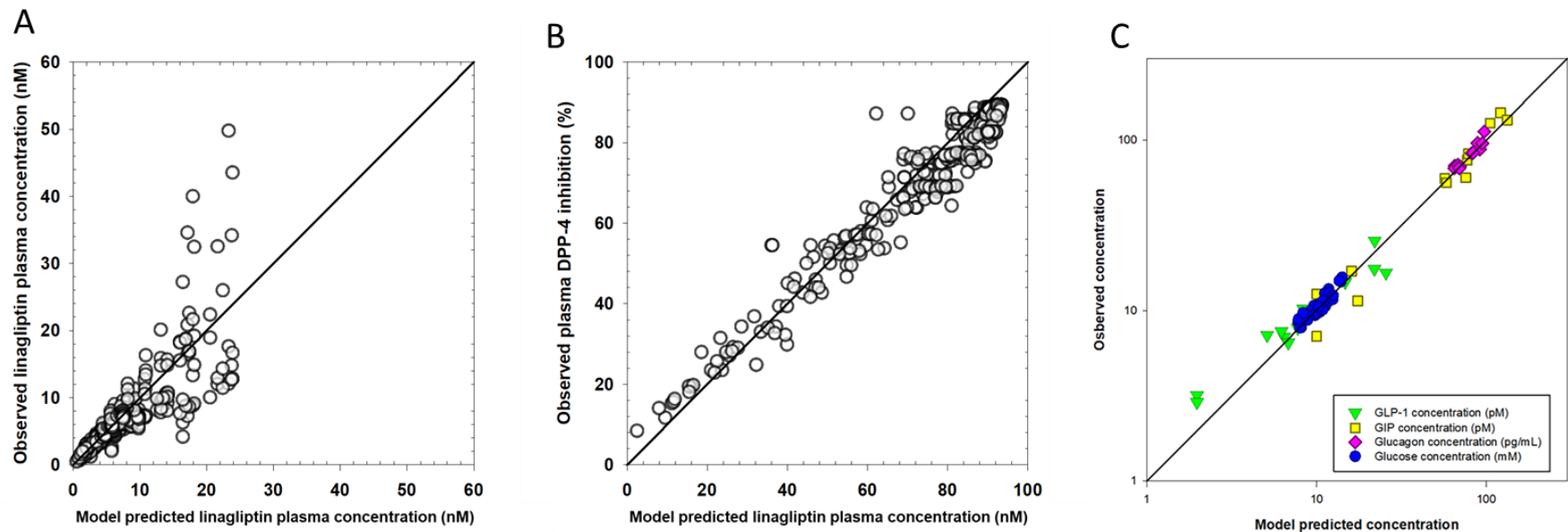


Figure 5-5. Goodness-of-fit plots for the final QSP model built for GLP-1, GIP, glucose, glucagon insulin and linagliptin. (A) Observed versus model-predicted linagliptin plasma concentrations. (B) Observed versus population-predicted plasma DPP-4 inhibition. (C) Observed versus population-predicted concentrations of GLP-1 (triangle), GIP (square), glucagon (diamond), and glucose (circle). Solid black lines represent lines of identity.

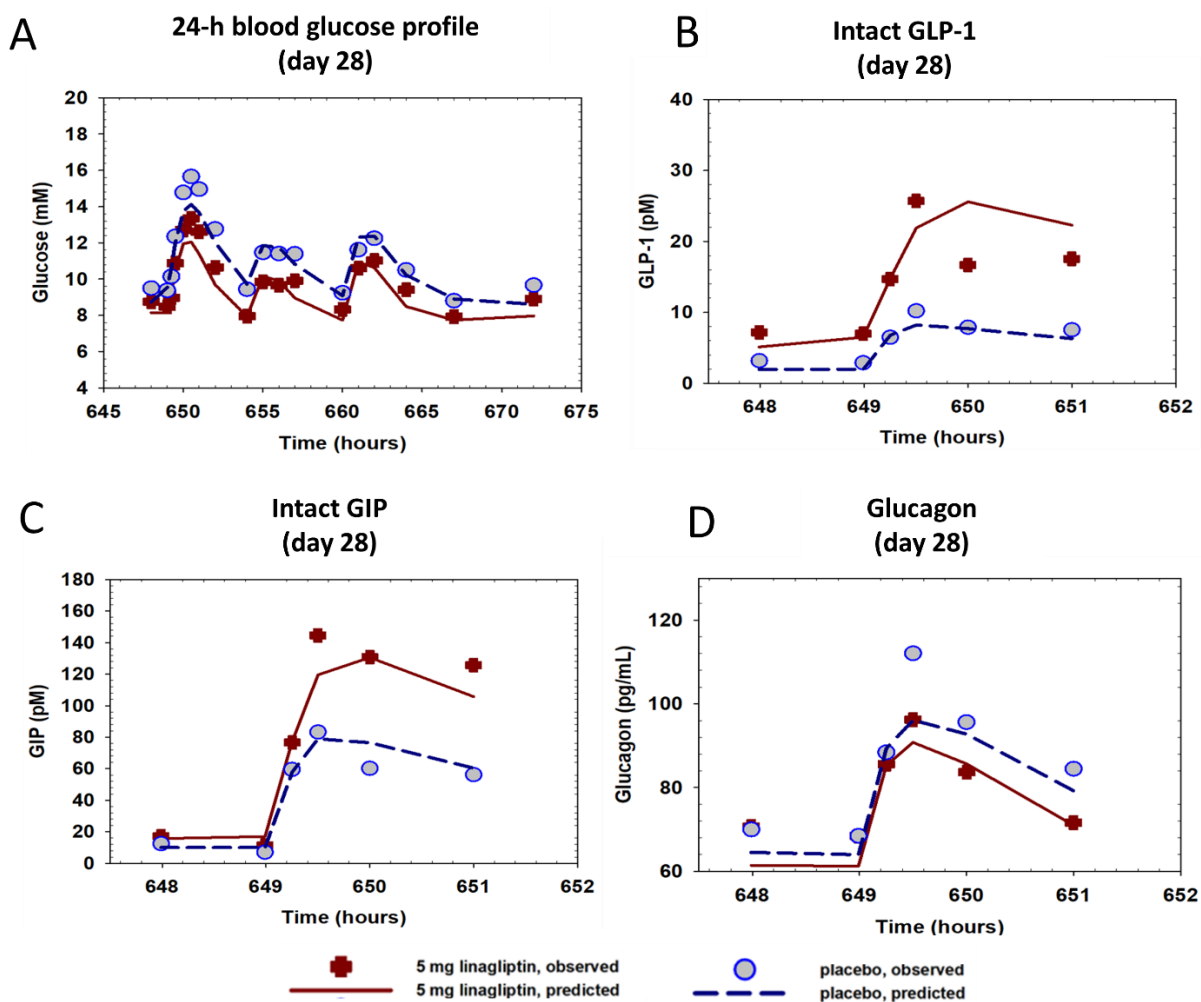


Figure 5-6. Time courses of mean observed (symbols) and population model-predicted (lines) concentrations of (A) glucose (B) GLP-1 (C) GIP and (D) GIP for T2DM patients after MTT test receiving 5 mg linagliptin (brown) and placebo (blue).

**CHAPTER 6: A FULL TARGET-MEDIATED DRUG DISPOSITION MODEL TO
EXPLAIN THE CHANGES IN RECOMBINANT HUMAN ERYTHROPOIETIN (rhEpo)
PHARMACOKINETICS IN PATIENTS WITH DIFFERENT BONE MARROW
INTERITY FOLLOWING HEMATOPOIETIC TRANSPLANTATION**

Most of this chapter has been published in Journal of Pharmaceutical Sciences.

(Wu N, Widness JA, Yan X, Veng-Pedersen P, An G. *J Pharm Sci.* 2022 Sep;111(9):2620-2629.)

6.1. Abstract

Our aim was to build a mechanistic full target-mediated drug disposition (TMDD) model for rhEpo to better understand rhEpo disposition, Epo receptor (EpoR) synthesis, and degradation in hematopoietic transplant patients with four distinct bone marrow conditions. All PK data were analyzed simultaneously using the nonlinear mixed effect modeling approach with NONMEM. The final model was a two-compartmental full TMDD model, which adequately characterizes rhEpo PK in patients and provides insight into the dynamics of free EpoR, rhEpo-EpoR, and total EpoR. The model predicted association rate constant (k_{on}), dissociation rate constant (k_{off}), and internalization rate constant (k_{int}) were $0.0276 \text{ pM}^{-1}\text{h}^{-1}$, 0.647 h^{-1} , and 0.255h^{-1} , respectively, which were supported by experimental data. Also, the EpoR degradation rate constant (k_{deg}) was estimated to be 0.461 h^{-1} . EpoR production rate was estimated to be 37.5 pM/h for adults at pre-ablation baseline and 5.91 pM/h , and 4.19 pM/h in the early post-transplant post-engraftment, and late post-transplant full engraftment. Our model provides extensive information on the dynamics of free EpoR, total EpoR and rhEpo-EpoR, and proven to be more robust and can provide more physiologically relevant binding parameters than previous models.

6.2. Introduction

Erythropoietin (Epo) plays a key role in the regulation of erythrocyte production (as shown in **Figure 6-1**). Under anemia-, ischemia-, or hypoxemia-induced tissue hypoxia in adults, Epo is stimulated with increased production in the kidneys. The produced Epo molecules are then transported to the bone marrow and bind to Epo receptors (EpoR) on erythroid progenitor cells to stimulate their proliferation and differentiation. Structurally and functionally very similar to Epo,

recombinant human Epo (rhEpo) has proven beneficial for the treatment of anemia caused by chronic kidney disease and chemotherapy [58-61].

rhEpo has been on the market for over 3 decades and its in vivo disposition across different species has been extensively studied. Nonlinear pharmacokinetics of rhEpo has been consistently observed in mice [62], rats [63], rabbit [64], sheep [65], and humans [66, 67], in which rhEpo clearance decreases with an increase in rhEpo doses, indicating saturation of the elimination process at high doses. This saturation process unlikely occurs in the liver and/or kidney as our previous mechanism study conducted in sheep confirmed that removal of liver and kidney had no impact on Epo elimination [168]. Multiple lines of evidence indicate that nonlinear pharmacokinetics of rhEpo is likely due to saturation of rhEpo elimination in bone marrow, where rhEpo binds to its high-affinity-low-capacity pharmacologic target EpoR located on erythroid progenitors and is subsequently eliminated by Epo-EpoR complex degradation [44, 46, 62, 68, 169]. This type of nonlinear phenomenon is known as target-mediated drug disposition (TMDD) and has been broadly observed in not only rhEpo but also many other protein drugs [1, 47, 49, 170].

To characterize the pharmacokinetics of rhEpo in human, population pharmacokinetic modeling has been performed by several research groups [171-175]. However, because of data limitation, caused by sparse/incomplete data and/or narrow dose evaluation, most of the reported models are either simple linear pharmacokinetic model or nonlinear Michaelis-Menton model [172-175] Recently, based on extensive and informative pharmacokinetic data that we have collected in preterm infants, we established a TMDD model that incorporated the mechanism of receptor binding and degradation to characterize rhEpo disposition in this vulnerable population [57]. We also used the TMDD model to characterize and compare rhEpo pharmacokinetics in

infant and adult populations [56]. Although our previous TMDD models provided valuable estimates on several important parameters, such as EpoR capacity and rhEpo-EpoR complex degradation rate, those parameters remain to be validated. In addition, our previous model is not a full TMDD model as the synthesis and degradation processes of the free EpoR were not included in the model due to data limitations. The limitations of our previous TMDD model motivated us to build a full TMDD model using data from a unique mechanism study that we previously carried out in patients receiving hematopoietic stem cell transplantation [45]. In that study, rhEpo pharmacokinetics were evaluated under four distinct bone marrow conditions: baseline pre-ablation, post-ablation pre-transplant, early post-transplant pre-engraftment, as well as late post-transplant full engraftment. Association of change in rhEpo elimination with decreased bone marrow activity was observed in our study, providing strong evidence that bone marrow serves as a key determinant of rhEpo elimination in humans. The original data, analyzed using non-compartmental analysis (NCA), has been published already [45]. The current work was a secondary data analysis, and our goal was to build a mechanistic full TMDD model so that we can use it to 1) validate the parameters estimated in our previous model, 2) better understand rhEpo disposition as well as EpoR synthesis and degradation, and 3) predict the changes of free EpoR, total EpoR, and rhEpo-EpoR over time following rhEpo administration.

6.3. Methods

6.3.1. Data source

In addition to rhEpo PK data in patients undergoing hematopoietic transplantation, we also included rhEpo PK data in healthy adults from a separate study [176]. Both clinical studies were conducted at the University of Iowa, and the NCA results of both studies have been published already [45, 176]. The study designs of these two clinical studies are briefly summarized below.

6.3.1.1. Study 1

The study design and the summary of the demographics of study participants are shown in the upper panel of **Figure 6-2** and **Table 6-1**, respectively. This study included four sequential rhEpo PK studies conducted in 10 healthy adults with washout period at least 14 days between adjacent studies. Single i.v. rhEpo doses of 10 IU/kg, 100 IU/kg, 500 IU/kg and 10 IU/kg were evaluated in the 1st, 2nd, 3rd, and 4th PK study, respectively. The PK samples were collected at 0.1, 0.267, 0.5, 1, 2, 3, 4, 6, 8, 12, and 24 hours after rhEpo administration in each PK study. Among the ten subjects who participated this study, 5 dropped out after the 3rd PK study (i.e., N=10 for the first three PK studies and N=5 for the 4th PK study).

6.3.1.2. Study 2

The study design and the summary of the demographics of study participants are shown in the lower panel of **Figure 6-2** and **Table 6-1**, respectively. This study included four sequential rhEpo PK studies conducted in 11 patients consisting of 8 adults and 3 pediatric subjects at the following different stages of hematopoietic transplantation: 1) pre-ablation baseline; 2) post-ablation pre-transplant; 3) early post-transplant post-engraftment, and 4) late post-transplant full engraftment. Among 11 subjects, two of them received 10 IU/kg rhEpo doses at the beginning of the 1st and 3rd period and 1000 IU/kg at the beginning of the 2nd and 4th period of transplantation. The remaining subjects received 100 IU/kg intravenous rhEpo doses at the beginning of each PK study (sample size varied due to drop out. See **Figure 6-2**) The PK samples were obtained at 0.0833, 0.25, 0.5, 1, 2, 3, 4, 6, 8, 12, and 24 hours after administration.

In both studies, the plasma rhEpo level was determined using a radioimmunoassay as previously described [177]. The lower limit of quantification was 1.15 mIU/mL. As endogenous

Epo cannot be distinguished by the assay from exogenously administered rhEpo, baseline-corrected Epo concentrations were used in our analysis. Total 788 baseline-corrected rhEpo concentrations was included in our population PK analysis.

6.3.2. Population pharmacokinetics modeling

All PK data were analyzed simultaneously using the nonlinear mixed effect modeling approach with NONMEM (Version 7.4.3; Icon Development Solutions, Ellicott City, Maryland) interfaced with Pirana (version 2.9.9, <http://www.pirana-software.com/>). The estimation of typical population PK parameters, inter-individual variability (IIV), and residual variability (RV) between predicted and observed plasma rhEPO concentrations were conducted by the first-order conditional estimation method with interaction (FOCEI) and a user-defined subroutine (ADVAN13). Plotting of NONMEM outputs was performed using SigmaPlot (version 14.0), R (version 4.1.3) interfaced with RStudio (<https://www.rstudio.com/>)

6.3.2.1. Population PK Base Structural Model

As rhEpo is known to have nonlinear PK due to target-mediated elimination and TMDD model has been used to characterize Epo PK [56, 57, 178], two- compartmental TMDD models with or without receptor dynamics were tested directly during the model development phase. In addition to the full TMDD model, a number of simpler TMDD model, such as quasi-steady-state (QSS) model and quasi-equilibrium (QE) model, were also evaluated. Model development history is shown in the **Table 6-2**. Among all models evaluated, the best model was found to be a two-compartment full TMDD model with EpoR turnover process (**Figure 6-3**). In this model, after injection rhEpo molecules distributed into central (C_{central} , V_{central}) and peripheral compartments ($C_{\text{peripheral}}$, $V_{\text{peripheral}}$) with the distribution flow (Q). rhEpo distributed in the central

compartment was eliminated from the system with first-order elimination rate constant k_e , calculated as the ratio of clearance to the central volume of distribution ($CL/V_{central}$). In addition, rhEpo could bind to its pharmacological target (i.e., EpoR) to form a complex (RC) with a second-order association rate constant k_{on} . The complex can be dissociated back to free drug and targets with a first-order dissociation rate constant (k_{off}). In addition, the rhEpo-EpoR complex (RC) could be degraded by the internalization process characterized by the parameter k_{int} . Furthermore, the turnover process of the free EpoR (R) was also included in our model with a zero-order production rate constant k_{syn} and a first-order degradation rate constant k_{deg} . Accordingly, the concentration of the free EpoR was modeled as an additional system variable. The synthesis rate of free EpoR in healthy adults was assumed to be same as that in patients at pre-bone marrow myeloablation baseline and was represented by $k_{syn,1,adults}$. The synthesis rate of free receptors in pediatric subjects was assumed to be different from that in adults and was represented by $k_{syn,1,children}$. The synthesis rate of the free receptor was fixed to 0 in patients undergoing the post-ablation/pre-transplant because erythroid progenitors would be absent at that time. The synthesis rates of free receptors in early post-transplant pre-engraftment and late post-transplant full engraftment recovery were represented by $k_{syn,3}$ and $k_{syn,4}$.

The equation for the central compartment was:

$$\frac{dC_{central}}{dt} = -k_{on} \times C_{central} \times R + k_{off} \times RC - CL/V_{central} \times C_{central} - Q/V_{central} \times C_{central} + Q/V_{central} \times C_{peripheral}$$

$$C_{central}(0) = \text{Dose}/V_{central} \quad (6.1)$$

The equation for the peripheral compartment was:

$$\frac{dC_{peripheral}}{dt} = Q/V_{peripheral} \times C_{central} - Q/V_{peripheral} \times C_{peripheral}$$

$$C_{\text{peripheral}}(0) = 0 \quad (6.2)$$

The equation for the free receptor was:

$$\frac{dR}{dt} = k_{\text{syn}} - k_{\text{on}} \times C_{\text{central}} \times R + k_{\text{off}} \times RC - k_{\text{deg}} \times R$$

$$R(0) = k_{\text{syn}}/k_{\text{deg}} \quad (6.3)$$

The equation for receptor-drug complex compartment was:

$$\frac{dRC}{dt} = k_{\text{on}} \times C_{\text{central}} \times R - k_{\text{off}} \times RC - k_{\text{int}} \times RC$$

$$RC(0) = 0 \quad (6.4)$$

Where C_{central} represented the rhEpo concentration in the central compartment, $C_{\text{peripheral}}$ represented the rhEpo concentration in the peripheral compartment. RC represented the concentration of Epo-R complex and R represented the concentration of free EpoR.

As the study population include both adult subjects and pediatric patients, allometric power model was used to accommodate the impact of bodyweight on the clearance (Q , CL) and volume of distribution terms (V_{central} , $V_{\text{peripheral}}$), with a fixed standard allometric exponent 0.75 and 1, respectively. Bodyweight was standardized to a 70 kg person.

6.3.2.2. Population PK stochastic model

Inter-individual variability (IIV): IIV for several PK parameters such as V_{central} and CL were estimated using an exponential model which is assumed to be normally distributed with a mean of 0 and a variance of ω^2 .

Residual variability (RV): Additive, proportional and a combined proportional and additive RV models were evaluated. The residual error is assumed to be normally distributed with a mean of 0 and a variance of σ^2 .

6.3.2.3. Covariate analysis

Prior to the formal covariate test, exploratory plots were performed to visualize the potential relationships between covariates and the individual estimates of IIVs. The following covariates were included in this descriptive analysis: age, gender, body weight, and disease state. The covariates with a potentially significant relationship, as reflected by $p < 0.05$ in those exploratory plots (**Figure 6-4**), were to be chosen for a formal covariate test which contains a forward addition ($\chi^2 = 3.84$, $p < 0.05$, $df = 1$) and a backward elimination ($\chi^2 = 10.83$, $p < 0.001$, $df = 1$) steps.

6.3.2.4. Model evaluation

Final model selection was based on goodness-of-fit plots, individual fitted plots, stability of parameter estimates, objective function value, condition number, and prediction-corrected visual predictive check (pcVPC). In addition, the likelihood ratio test was used for comparing nested models where a decrease in the NONMEM objective function (-2 log-likelihood) of 3.84 points (with one additional parameter, i.e., 1 df) or 5.99 (with two additional parameters, i.e., 2 df) was necessary to consider the improvement in model performance statistically significant at $\alpha = 0.05$.

6.3.2.5. Simulations

Dynamics of free receptors (R), drug-receptor complex (RC), and total receptors (R+RC) were simulated following 10, 100, 500, and 1000 IU/kg single dose of rhEpo for 168 hours in 1) adults in health condition or pre-ablation baseline; 2) pediatric subjects in health condition or pre-ablation baseline; 3) adults undergoing early post-transplant pre-engraftment and 4) adults undergoing late post-transplant full engraftment recovery. 70 kg and 20 kg body weight were assumed for adults and pediatric subjects, respectively. All the simulations were performed using NONMEM (Version 7.4.3; Icon Development Solutions, Ellicott City, Maryland) interfaced with Pirana (version 2.9.9, <http://www.pirana-software.com/>).

The time course of the rhEpo linear clearance, receptor-mediated clearance, total clearance, as well as fraction of receptor-mediated clearance over the total clearance were simulated following the same dosing regiments (i.e. 10, 100, 500, 1000 IU/kg i.v. doses) in the same populations as mentioned above.

rhEpo undergoes both linear elimination pathway and nonlinear saturable internalization process. Therefore, total clearance is calculated as the sum of the linear elimination rates and internalization rates (i.e. $A_{RC} \times k_{int} + A_{rhEpo,central} \times k_e$) divided by the concentration of drug in the plasma ($A_{rhEpo,central}/V_{central}$). After equation rearrange, total clearance is represented by the following equation:

$$CL_{total} = k_e \times V_{central} + k_{int} \times V_{central} \times \frac{A_{RC}}{A_{rhEpo,central}} \quad (6.5)$$

Where k_e represented first-order elimination rate constant, $V_{central}$ represented the central volume of distribution, k_{int} represented internalization rate of the drug-receptor complex, A_{RC} represented the amount of Epo-R complex and $A_{rhEpo,central}$ represented the amount of rhEpo in

the central compartment. The first term ($k_e \times V_{central}$) represented the linear clearance (CL). The receptor-mediated drug clearance was represented by the second term ($k_{int} \times V_{central} \times \frac{A_{RC}}{A_{rhEpo,central}}$). The ratio of receptor-mediated clearance to total clearance was also calculated.

6.4. Results

6.4.1. Parameter estimation

As shown in **Figure 6-3**, the best model to capture rhEpo PK data was a two-compartmental full TMDD model containing EpoR turnover process, linear elimination and a nonlinear target-mediated elimination pathway. The parameter estimates for this final model are presented in **Table 6-3**.

In the final model, the association rate constant k_{on} to form Epo-EpoR complex was estimated to be $0.0276 \text{ pM}^{-1}\text{h}^{-1}$. Once formed, the drug-receptor complex can either be intracellularly internalized at an estimated rate (k_{int}) of 0.255h^{-1} or dissociate back to the free EpoR and free rhEpo with k_{off} of 0.647 h^{-1} .

EpoR degradation rate constant (k_{deg}) was estimated to be 0.461 h^{-1} . Furthermore, at the pre-ablation baseline, adult subjects were predicted to have a six-fold higher synthesis rate of free EpoR (37.5 pM/h) than pediatric subjects (6.9 pM/h). The free EpoR synthesis rate was estimated to be 5.91 pM/h and 4.19 pM/h in patients undergoing early post-transplant pre-engraftment and late post-transplant full engraftment recovery, respectively. In other words, our model predicted the recovery rate of synthesis rate of free EpoR were 15.8% and 11.2% in the last two phases, respectively.

Referring to a 70-kg person, our final model predicted the central and peripheral volume of distribution to be 3.10 and 2.42 L, respectively, and the clearance and distribution flow of rhEpo

to be 0.223 and 0.174 L/h, respectively. Inter-individual variability (IIV) terms were attempted to be placed on several parameters including CL, $V_{central}$, k_{deg} , $k_{syn,1}$, $k_{syn,3}$, $k_{syn,4}$, k_{on} , k_{off} , k_{int} but it leaded to the failed model convergence (**Table 6-2**). Finally, IIVs were estimated only for $V_{central}$, CL, and k_{deg} . The magnitude of estimated IIV ranged from 18.4% for $V_{central}$ to 48.3% for k_{deg} . The estimate of IIV in CL was 20.6%. A proportional residual error model best described the unexplained residual variability. The estimate of residual variability was 16.3%. Most of the PK parameters were adequately estimated with the low relative standard error (RSE) (< 30%) and low shrinkage (< 30%).

No covariate was found to be significant from the initial exploratory analysis (**Figure 6-4**). Accordingly, formal covariate test containing forward selection and backward elimination procedure was not conducted.

6.4.2. Model fitting results

The time course of observed versus population predicted (PRED) plasma concentrations of rhEpo in healthy adults after 10, 100, and 500 IU/kg i.v. doses are presented in **Figure 6-5**. The time course of observed versus population predicted (PRED) plasma concentrations of rhEpo in patients undergoing hematopoietic transplantation after 10, 100, and 1000 IU/kg i.v. doses are presented in **Figure 6-6**. As shown in **Figure 6-5** and **Figure 6-6**, the final model adequately captured the PK of rhEpo following various doses in both healthy adults and patients during four periods of altered bone marrow integrity.

In addition to the observed and population predicted rhEpo plasma concentration-time profiles, other goodness-of-fit plots were also provided (**Figure 6-7**). As shown in **Figure 6-7**, the population-predicted concentrations versus the observed concentrations were symmetrically distributed around the line of identity, indicating the generally good performance of the model at

the population level. This conclusion was extended to the plot of individual-predicted concentrations versus the observed concentrations, which demonstrated even scatter around the line of identity. In addition, weighted residuals were distributed uniformly around the zero line when evaluated with the population-predicted concentrations or time.

The pcVPC plots of the final model are shown in **Figure 6-8**. The majority of the observed concentrations, except for some outliers (from one patient undergoing transplant (pre-ablation baseline) after receiving a very low dose (4.78 IU/kg)), were within the 95% prediction intervals from the simulation data, indicating that the model accurately captured the variability in observed data. There was a slight overprediction of the fifth percentile at late time points, probably due to the small sample size of the last two periods.

6.4.3. Dynamics of free receptors, drug-receptor complex and total receptors

As shown in **Figure 6-9**, dynamics of free receptors, drug-receptor complex and total receptors were simulated at the dose levels 10, 100, 500, and 1000 IU/kg in healthy subjects and patients.

An increase of the total receptor concentration was observed upon the drug administration, followed by a decrease returning to the baseline. The total receptor concentration at baseline was predicted to be 81.3 pM in adults in the healthy condition or at pre-ablation baseline, which is higher than 12.8 pM and 9.09 pM in adults at early post-transplant pre-engraftment and late post-transplant full engraftment, respectively. Pediatric subjects at pre-ablation baseline were estimated to have 15.0 pM total receptors.

6.4.4. Clearance vs. time profiles

The time course of the receptor-mediated clearance and the percentage of receptor-mediated clearance to the total clearance (CL_{total}) were simulated, as shown in **Figure 6-10**. The

linear clearance (CL) was 0.223 L/h for adults and 0.0871 L/h for pediatric subjects and was constant over time (plot not shown).

For all the populations and all dose levels, receptor-mediated clearance declines rapidly at first and then returns to baseline. In addition, at the pre-ablation baseline, the baseline receptor-mediated clearance was 0.676 L/h in adults and 0.126 L/h in pediatric subjects.. The baseline receptor-mediated clearance in adults during early post-transplant post-engraftment and late post-transplant full engraftment were 0.104 and 0.0739 L/h, respectively.

The time course of total clearance followed the same trend as that of receptor-mediated clearance. Take adults at pre-ablation baseline as an example; the ranges of the total clearance from the body were 0.514-0.926, 0.270-0.899, 0.233-0.899, and 0.228-0.899 L/h for 10, 100, 500, 1000 IU/kg rhEpo doses, respectively.

6.5. Discussion

Based on the rhEpo PK data collected from hematopoietic stem cell transplant patients with four distinct bone marrow conditions, we have successfully developed a two-compartmental full TMDD model that incorporated EpoR turnover process, a linear elimination pathway, and a nonlinear target-mediated elimination process. The novelty of this current model is that it not only provides insight of Epo kinetics but also the dynamics of free EpoR, total EpoR and rhEpo-EpoR complex. PK and target interaction information gained from this model are valuable as they could be used for rhEPO dose optimization in patients with different conditions of bone marrow integrity.

This full TMDD model validated the rationality and accuracy of our previous TMDD models built for infants and adults by providing similar estimation on a number of key parameters, such as rhEpo-EpoR complex degradation rate (k_{int}) and EpoR capacity (R_{total}) [56, 57]. For example, in the current analysis rhEpo-EpoR complex was predicted to be degraded at a rate of

0.255 h⁻¹, which is in line with the k_{int} of 0.172 h⁻¹ that was estimated from our previous TMDD model (0.172 h⁻¹) [56]. In addition, our full TMDD model predicted the baseline EpoR capacity in adults to be 81.3 nM (calculated from the ratio of a synthesis rate of free EpoR of 37.5 pM/h to a degradation rate constant of 0.461 h⁻¹), which is in close agreement with the R_{total} of 86.6 pM in adults predicted by previous TMDD model where total EpoR concentrations were assumed to be constant [56]. Based on the predicted EpoR concentration of 81.3 nM, we also calculated the number of EpoR molecules expressed per progenitor cell and then compared it with experimentally determined value to validate this parameter. As the progenitor cell volume is about 6000 μm³ based on the reported diameters (20-25 μm) [179], the average amount of EpoR within each progenitor cell is around $(81.3 \times 10^{-12} \text{ mol/L}) \times (6000 \times 10^{-18} \text{ m}^3) = 4.8 \times 10^{-22} \text{ mol}$ in order to have EpoR concentration of 81.3 nM. Accordingly, the estimated number of EpoR is $(6.02 \times 10^{23} \text{ molecules/mol}) \times (4.8 \times 10^{-22} \text{ mol}) = 289$ EpoR molecules per cell; this value is in close agreement to the experimental value (average 300 EpoR per cell) [180, 181].

In addition to k_{int} and R_{total} , both the current full TMDD model and our previous TMDD models provide similar estimates on rhEpo volume of distribution, clearance as well as distribution flow [56, 57]. However, there is a discrepancy in the estimation of parameters related to the binding process (i.e., k_{on} and k_{off}) between the current model and previous models. The association rate constant k_{on} was estimated to be 0.0276 pM⁻¹h⁻¹, which is a lot higher than k_{on} of 0.00410 pM⁻¹h⁻¹ estimated by our previous TMDD model [56]. Similarly, the dissociation rate constant k_{off} of 0.647 h⁻¹ estimated from the current model is also higher than the previous estimation (0.141 h⁻¹) with a similar magnitude of discrepancy [56]. To evaluate which set of binding parameters is more physiologically relevant, we compared them with experimentally determined values. Gross and Lodish conducted a series of *in vitro* experiments to investigate rhEpo receptor binding,

dissociation, and trafficking properties, where the direct dissociation assay was used to determine the dissociation rate constant (k_{off}) for rhEpo to EpoR and then association rate constant (k_{on}) was calculated based on k_{off} and experimentally measured the net binding rates, k_{obs} [182]. Their result showed that Epo binds to surface EpoR with k_{on} of $5 \times 10^8 \text{ M}^{-1} \text{ min}^{-1}$ (i.e. $0.0300 \text{ pM}^{-1}\text{h}^{-1}$) and k_{off} of 0.029 min^{-1} (i.e. 1.74 h^{-1}) [182]. These experimentally determined binding parameters are in close agreement with those estimated using our current full TMDD model ($k_{on} = 0.0276 \text{ pM}^{-1}\text{h}^{-1}$ and $k_{off} = 0.647 \text{ h}^{-1}$), indicating that the current model is more robust and can provide more physiologically relevant binding parameters than previous TMDD models.

Compared with the previous TMDD models characterizing rhEpo PK in infants and adults [56], our full TMDD model provided more mechanistic insight into dynamics of free EpoR, total EpoR and rhEpo-EpoR by incorporating EpoR turnover process. Following rhEpo administration, free EpoR concentration drops rapidly due to its quick binding to the rhEpo, which is accompanied by the increase of rhEpo-EpoR complex for different populations with different bone marrow integrity. The magnitude of the minimum concentration of free EpoR and the maximum of rhEpo-EpoR complex among different groups depended on both the dose levels and the different bone marrow conditions. Healthy adults and adult patients in 1st phase are predicted to have a higher EpoR baseline value (81.3 pM) than pediatric subjects (15.0 pM), as well as the adult patients in 3rd (12.8 pM) and 4th phases (9.09 pM). Adult patients are predicted to have the EpoR recovery rate of 15.7% and 11.2%, respectively, during the third and fourth phases, indicating that the EpoR does not ultimately return to the normal level even in the late post-transplant full engraftment phase (4th phase).

Simulation on the total receptor dynamics shows that the total EpoR is not constant across the study period, with the values higher than the baseline level in the presence of rhEpo. The

increase of total EpoR following rhEpo administration is expected as total receptor dynamics is determined by the difference between the degradation rate of the free receptors (k_{deg}) and the internalization rate (k_{int}) of rhEpo-EpoR complex. Based on our model estimate, the value of k_{int} (0.255 h^{-1}) is smaller than k_{deg} (0.461 h^{-1}), which means that rhEpo-EpoR is degraded slower than the degradation of free EpoR. As a result, in the presence of rhEpo, total EpoR increases compared with its baseline value when rhEpo is absent, with the magnitude of increase being both dose- and time-dependent.

Simulation on the contribution of receptor-mediated clearance shows that 75.2% of rhEpo molecules is eliminated by the EpoR-mediated clearance in adult subjects at pre-ablation baseline, which is higher than that in pediatric subjects (59.1%), adults during early post-transplant post-engraftment (31.9%), and late post-transplant full engraftment (24.9%). Following rhEpo administration, in the early phase due to high rhEpo concentrations and subsequent saturation of EpoR, linear clearance becomes the dominant elimination pathway. The time needed for receptor-mediated elimination to return to its baseline value is dose-dependent. Taking adults at pre-ablation as an example, the time needed to return to the baseline is approximately 12 hours at 10 IU/kg, whereas 144 hours at 1000 IU/kg.

6.6. Conclusions

In conclusion, we have successfully developed a mechanistic full TMDD model that adequately characterizes rhEpo PK in both healthy adults and patients with different bone marrow conditions. Our model provides extensive information on the dynamics of free EpoR, total EpoR and rhEpo-EpoR, and proven to be more robust and can provide more physiologically relevant binding parameters than previous TMDD models. The information gained from this study will be valuable in guiding and predicting future Epo dosing regimens for both children and adults. Results

from the current analysis provides a solid foundation for future work on establishing a mechanistic PK-PD model for rhEpo with available hemoglobin (Hb) data.

Table 6-1. Summary of demographics of study participants.

	Study 1		Study 2	
	Healthy Adults	Adult patients	Pediatric patients	
n	10	8	3	
Age (yr)	31.2 ± 8.5 (22.0 - 46.0)	40.2 ± 16.2 (19.0 - 60.9)	8.2 ± 3.0 (4.2 - 11.4)	
Weight (kg)	77.0 ± 15.6 (60.0 - 103)	87.1 ± 15.7 (58.6 - 110.9)	28.9 ± 11.6 (14.3 - 42.8)	
Gender				
Male	5 (50)	7 (88)	0 (0)	
Female	5 (50)	1 (12)	3 (100)	

Continuous variables are summarized as means ± SD (range); categorical variables are summarized as number (percentage) of patients

Table 6-2. Model development history.

No.	Model description	IIV	RSE	Model fitting	OFV	Δ OFV	Note
1	<ul style="list-style-type: none"> Two compartment TMDD model; Total amount of EpoR was assumed to be a constant with a inter-occasion variability (IOV); Amount of EpoR at 2nd stage was fixed to 0; 	CL, V _{central}	Low	Good	6306.394	-	Not mechanism interpretable
2	<ul style="list-style-type: none"> Two compartment TMDD model; Amount of EpoR is assumed to be different among those four stages, which was represented by four different parameters; Amount of EpoR at 2nd stage was fixed to 0; 	CL, V _{central} , R _{total,1}	Low	Good	6349.32	+42.93 (Compared to model #1)	
3	<ul style="list-style-type: none"> Two compartment full TMDD model; k_{syn,2} was fixed to 0; Adult and pediatric subjects are assumed to have the same EpoR production rate in 1st, 3rd, and 4th phase; 	CL, V _{central} , k _{deg} , k _{syn,1} , k _{syn,3} , k _{syn,4} , k _{on} , k _{off} , k _{int}	-	-	-	-	Terminated
4	<ul style="list-style-type: none"> Two compartment full TMDD model; k_{syn,2} was fixed to 0; Adult and pediatric subjects are assumed to have different EpoR production rate in 1st, 3rd, and 4th phase; 	CL, V _{central} , k _{deg}	High	Good	6309.452	-39.87 (Compared to model #2)	Over-fitting (suggested by condition number >1000)

Table 6-2 (Continued).

5-Final	<ul style="list-style-type: none"> • Two compartment full TMDD model; • $k_{syn,2}$ was fixed to 0; • Adult and pediatric subjects are assumed to have different EpoR production rate only in 1st phase; 	CL, $V_{central}$, k_{deg}	Low	Good	6332.831	-16.49 (Compared to model #2)	
6	<ul style="list-style-type: none"> • Two compartment TMDD model; • QE simplification; • $k_{syn,2}$ was fixed to 0; 	CL, $V_{central}$, k_{deg}	Low	Good	7992.788	+1659.96 (Compared to model #5)	
7	<ul style="list-style-type: none"> • Two compartment TMDD model; • QSS simplification; • $k_{syn,2}$ was fixed to 0; 	CL, $V_{central}$, k_{deg}	High	Good	7584.85	+1252.02 (Compared to model #5)	
8	<ul style="list-style-type: none"> • Two compartment full TMDD model; • Adult and pediatric subjects are assumed to have different EpoR production rate only in 1st phase; 	CL, $V_{central}$, k_{deg}	High	Good	6332.832	+0.00 (Compared to model #5)	

OFV, objective function value; RSE, relative standard errors. Δ OFV were calculated comparing the model with the indicated one.

Table 6-3. Estimated parameters from the final TMDD model for rhEpo.

Parameter	Unit	Definition	Estimate	RSE (%)	Shrinkage (%)
V_{central}	L	Central volume of distribution	$3.1 \times (\text{Wt kg}/70\text{kg})$	4	
$V_{\text{peripheral}}$	L	Peripheral volume of distribution	$2.42 \times (\text{Wt kg}/70\text{kg})$	4	
$CL^{\#}$	L/h	Clearance	$0.223 \times (\text{Wt kg}/70\text{kg})^{0.75}$	5	
Q	L/h	Inter-compartmental clearance	$0.174 \times (\text{Wt kg}/70\text{kg})^{0.75}$	6	
k_{on}	$\text{pM}^{-1}\text{h}^{-1}$	Second-order association rate constant	0.0276	28	
k_{off}	h^{-1}	First-order dissociation rate constant	0.647	20	
$k_{\text{syn},1,\text{adults}}$	pM/h	Synthesis rate of free receptor in healthy adults or adult patients at baseline	37.5	8	
$k_{\text{syn},1,\text{children}}$	pM/h	Synthesis rate of free receptor in pediatric patients at baseline	6.9	21	
$k_{\text{syn},3}$	pM/h	Synthesis rate of free receptor in subjects undergoing early post-transplant pre-engraftment	5.91	19	
$k_{\text{syn},4}$	pM/h	Synthesis rate of free receptor in subjects undergoing late post-transplant full engraftment	4.19	17	
k_{deg}	h^{-1}	Degradation rate of free receptor	0.461	24	
k_{int}	h^{-1}	Internalization rate of the drug-receptor complex	0.255	9	
$\text{IIV}_{V_{\text{central}}}$	%	inter-individual variability on V_{central}	18.4%	37	0
IIV_{CL}	%	inter-individual variability on CL	20.6%	51	2
$\text{IIV } k_{\text{deg}}$	%	inter-individual variability on k_{deg}	48.3%	41	12
σ	%	residual variability	16.3%	5	3

[#] CL represents linear clearance for a 70-kg adult

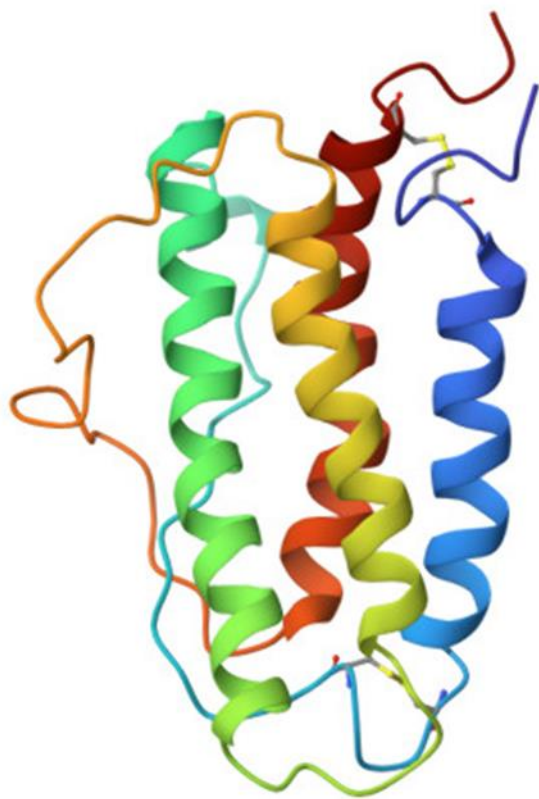
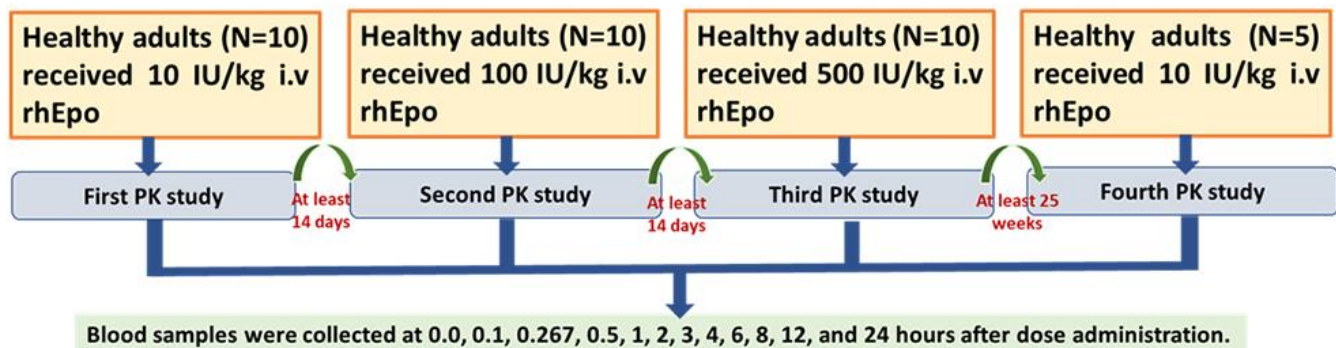


Figure 6-1. Structure of human erythropoietin, a 30.4 kDa glycoprotein hormone (PDB ID: 1BUY).

Study 1



Study 2

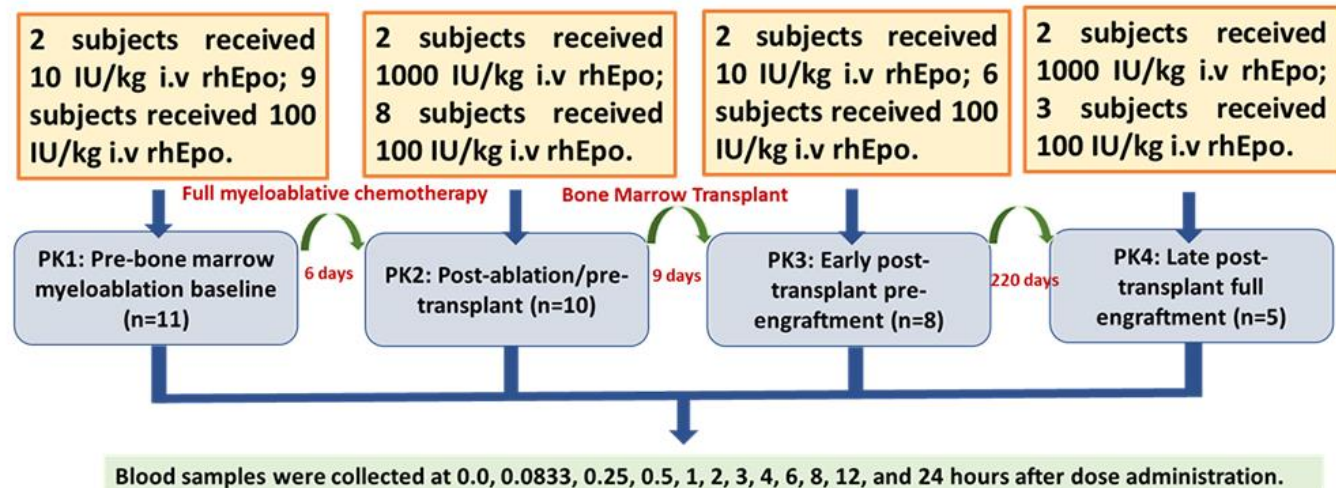


Figure 6-2.Schematic flow diagram of clinical study 1 and study 2.

Healthy subjects were included in study 1. Patients undergoing hematopoietic transplantation were included in study 2.

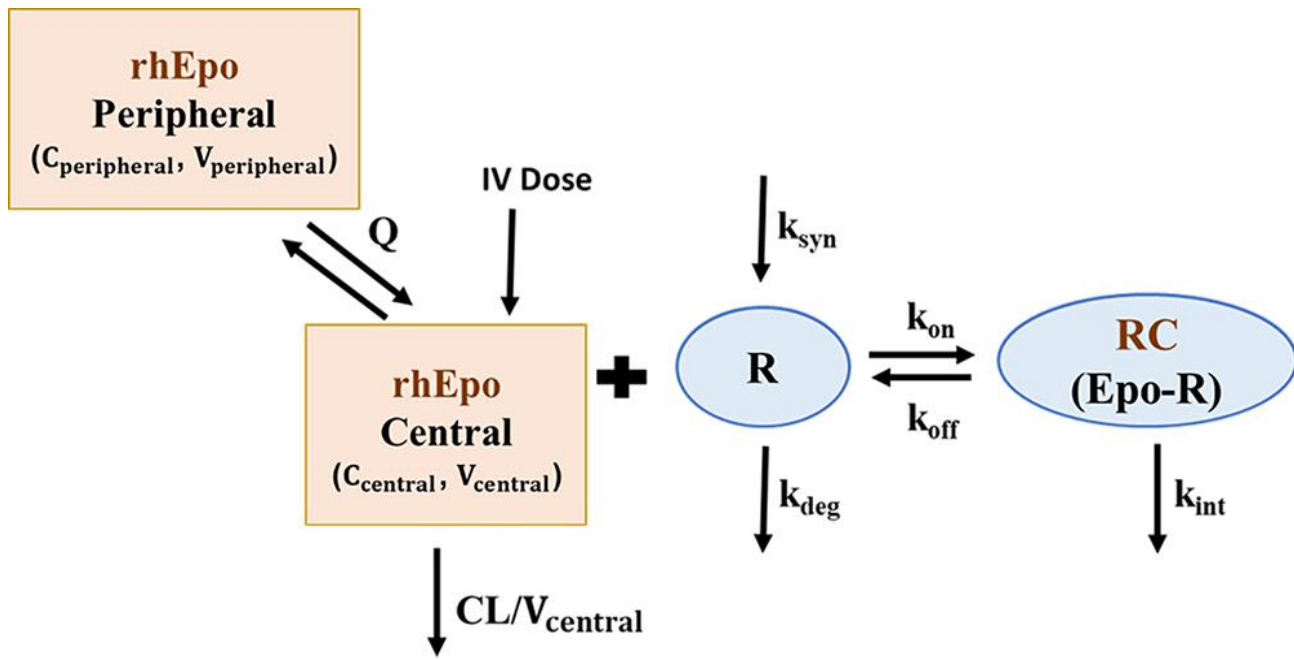


Figure 6-3.Final TMDD model structure describing the pharmacokinetics of rhEpo.

In this model, there is a dynamic distribution of exogenous rhEpo between a central compartment and a peripheral compartment. The elimination takes place from the central compartment via a linear pathway (CL/V), or via an interaction with Epo receptors (EpoR) with a second-order association rate constant (k_{on}) to form an Epo-R complex (RC). This complex can dissociate back to free rhEpo and free EpoR with a first-order dissociation rate constant (k_{off}), or the complex can undergo internalization and subsequent degradation with a first-order rate constant k_{int} . The turnover process of the free EpoR (R) is characterized with a zero-order production rate constant k_{syn} and a first-order degradation rate constant k_{deg} .

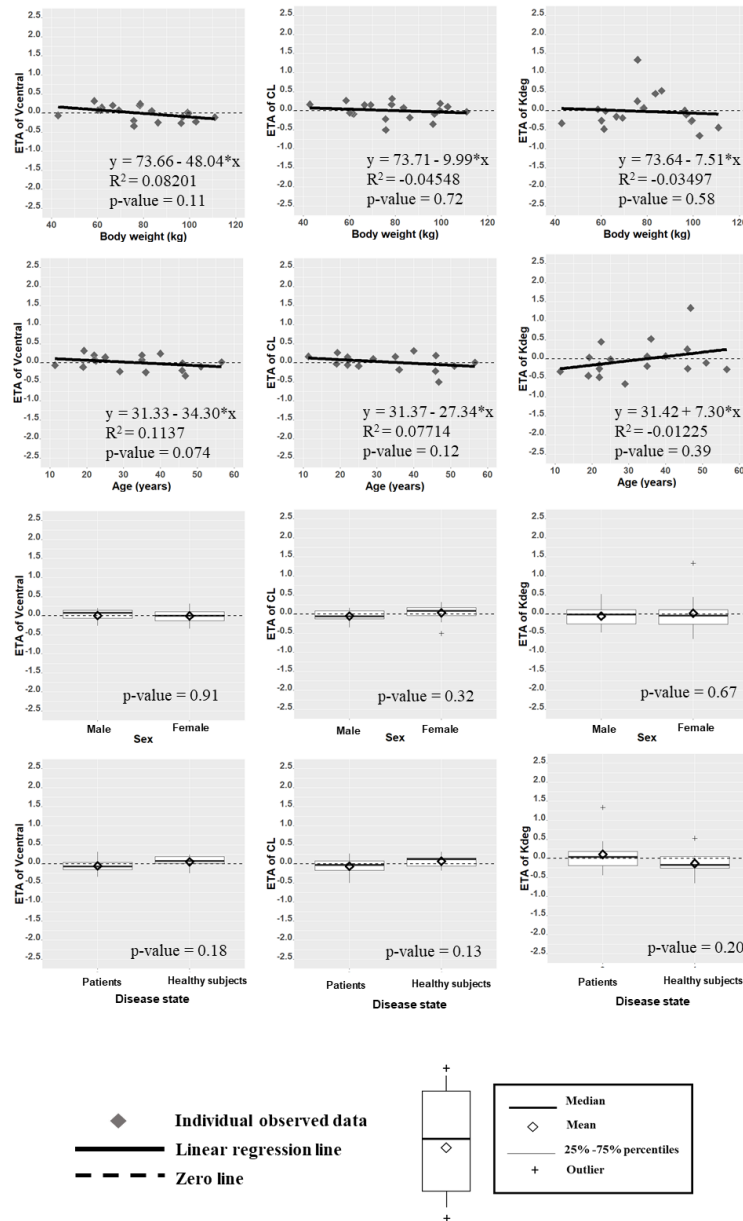


Figure 6-4. Exploratory test for covariates.

The potential relationship between continuous variables (age, and body weight) and individual estimates of IIV for three PK parameters (V_{central} , CL and k_{deg}) are presented in the scatter plots. The solid black lines represent the linear regression lines; The black diamonds represent observed values. The potential relationship between categorical variables (gender and disease state) and individual estimates of IIV for three PK parameters (V_{central} , CL and k_{deg}) are presented in those box plots. The solid horizontal black lines in bold represent the median values; the black open diamonds represent the mean values. The lower and upper hinges correspond to 25th and 75th percentiles. The black plus mean the outliers. The upper and lower notches extend to the largest and smallest values, respectively, excluding any outliers. The black dashed lines are the zero lines.

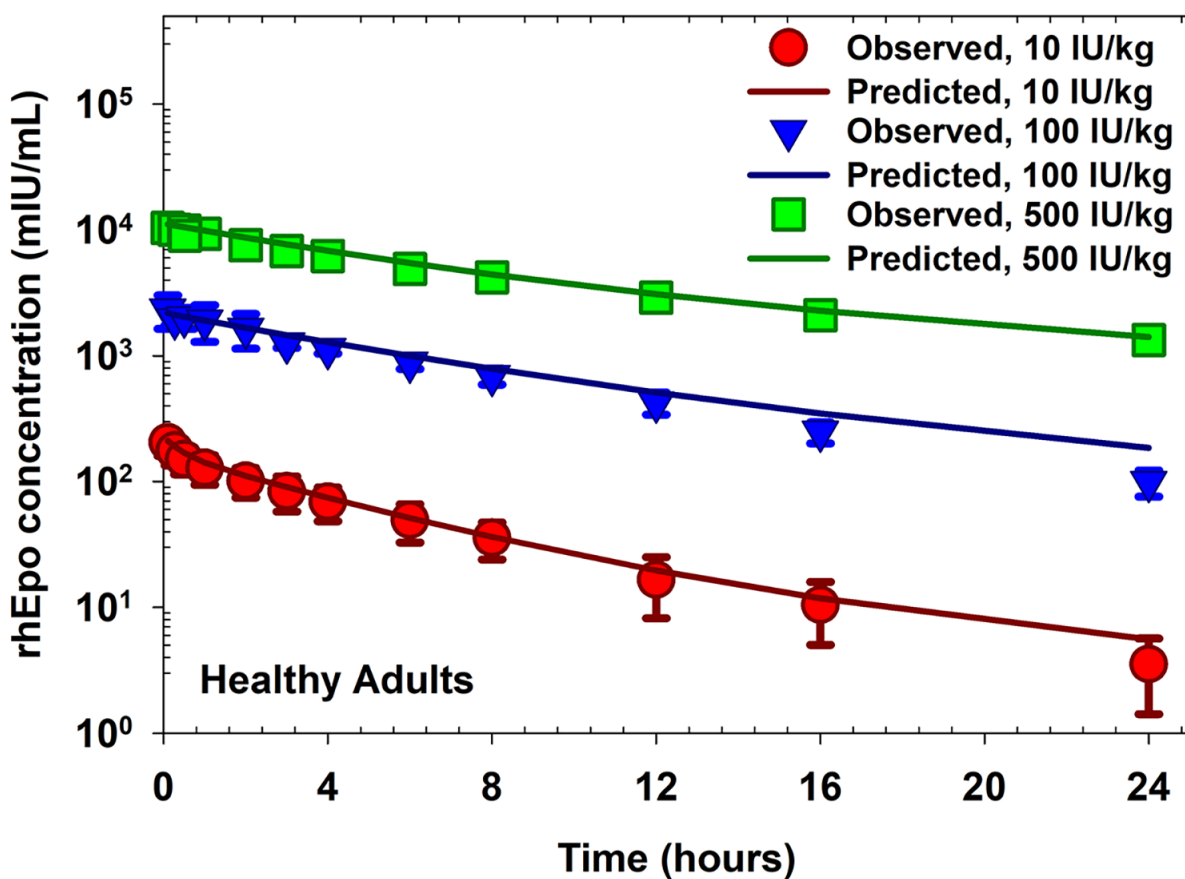


Figure 6-5. Time courses of mean \pm SD observed (symbols) and model predicted (lines) rhEpo plasma concentrations following 10, 100 and 500 IU/kg doses in healthy subjects.

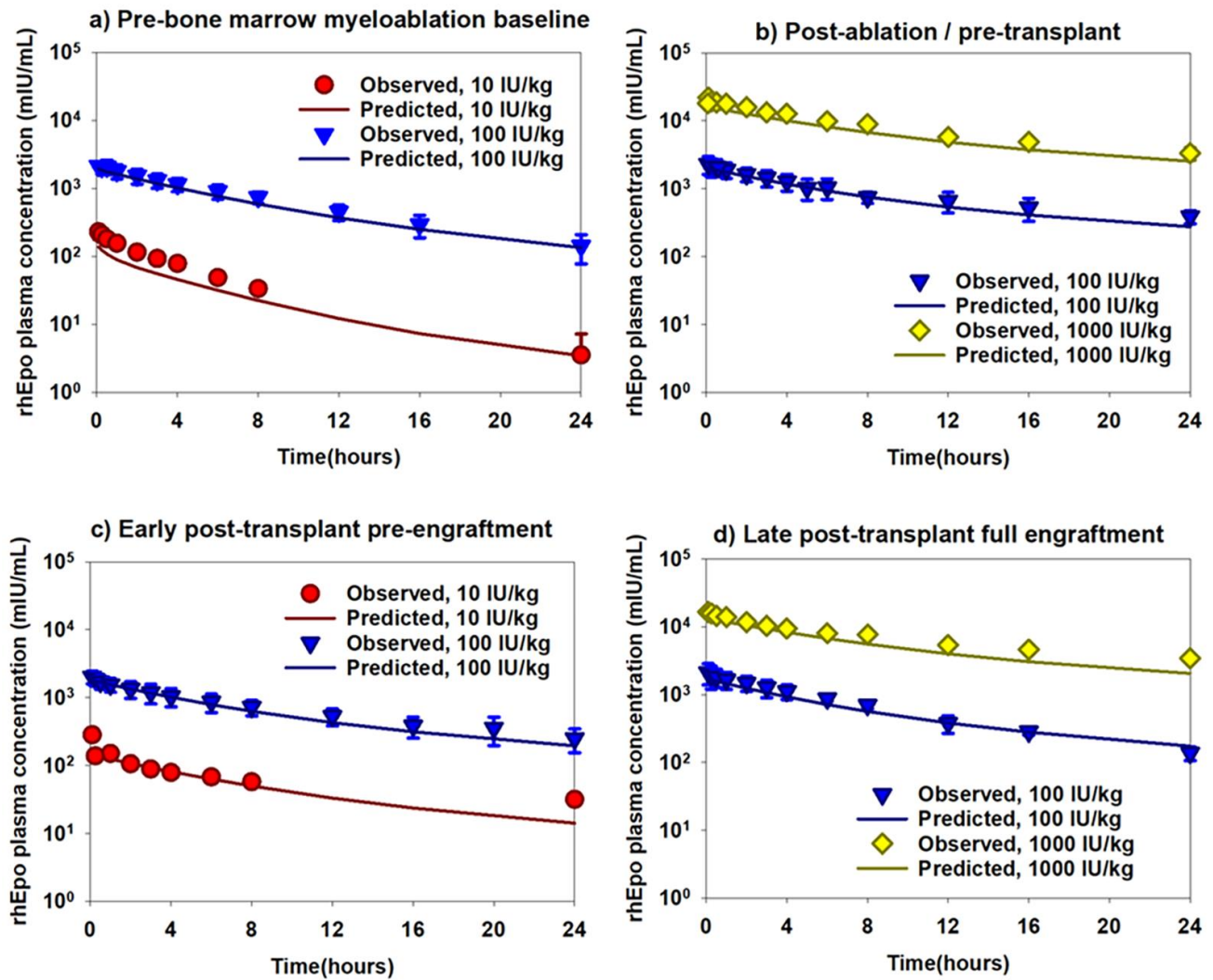


Figure 6-6. Time courses of mean \pm SD observed (symbols) and model predicted (lines) rhEpo plasma concentrations following 10, 100 and 1000 IU/kg doses in patients undergoing four periods of hematopoietic transplantation.

a) pre-bone marrow myeloablation baseline; b) post-ablation/pre-transplant; c) early post-transplant pre-engraftment; and d) late post-transplant full engraftment recovery.

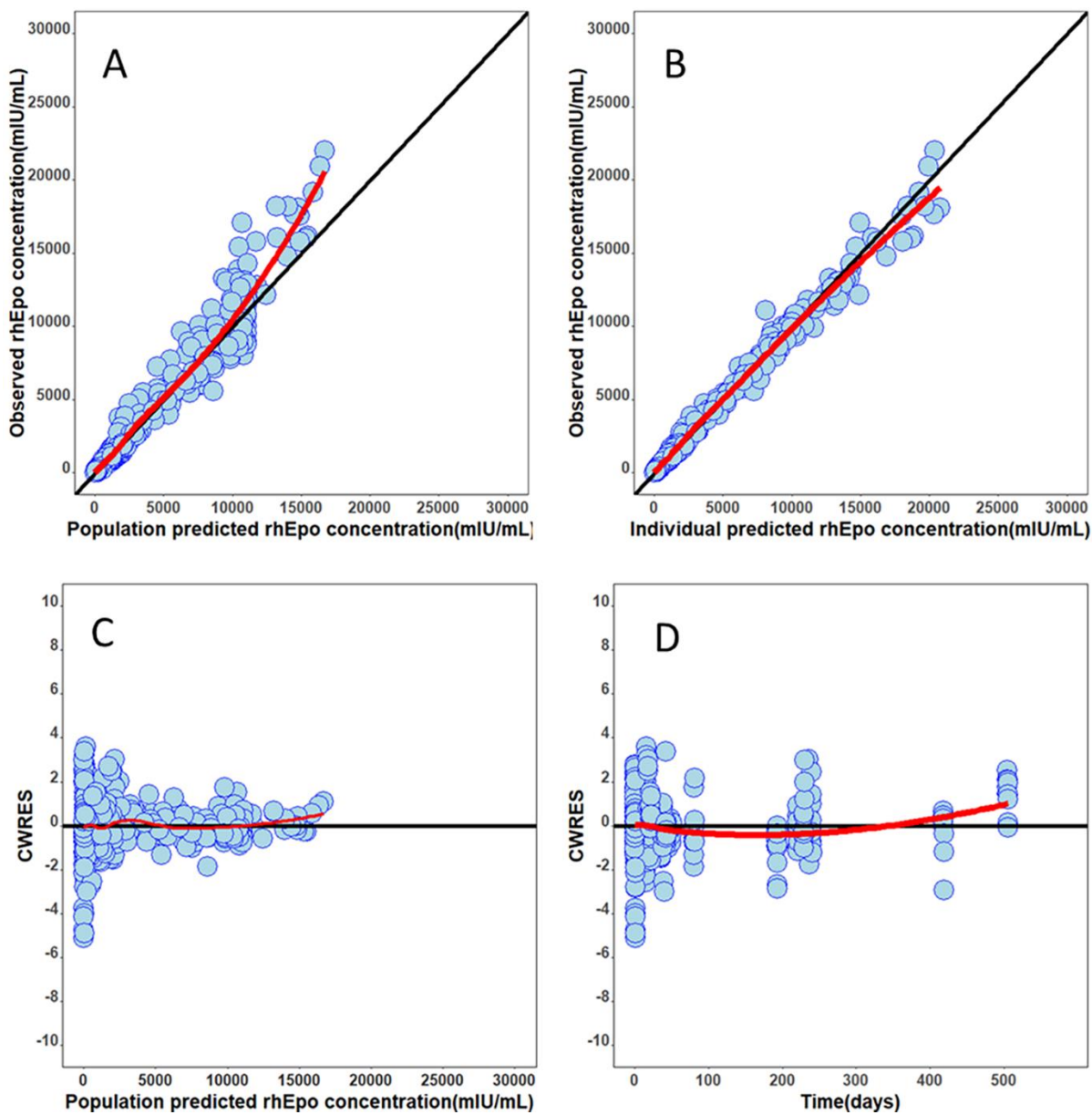


Figure 6-7. Goodness fit plots for the final population pharmacokinetics modeling.

a) rhEpo observed concentrations versus population-predicted concentrations b) rhEpo observed concentrations versus individual-predicted concentrations; c) rhEpo conditional weighted residual (CWRES) versus population-predicted concentrations, and d) rhEpo conditional weighted residual (CWRES) versus time. Solid black lines represent the lines of identity or lines of zero. Red solid lines represent the locally weighted scatterplot smoothing (lowess) lines.

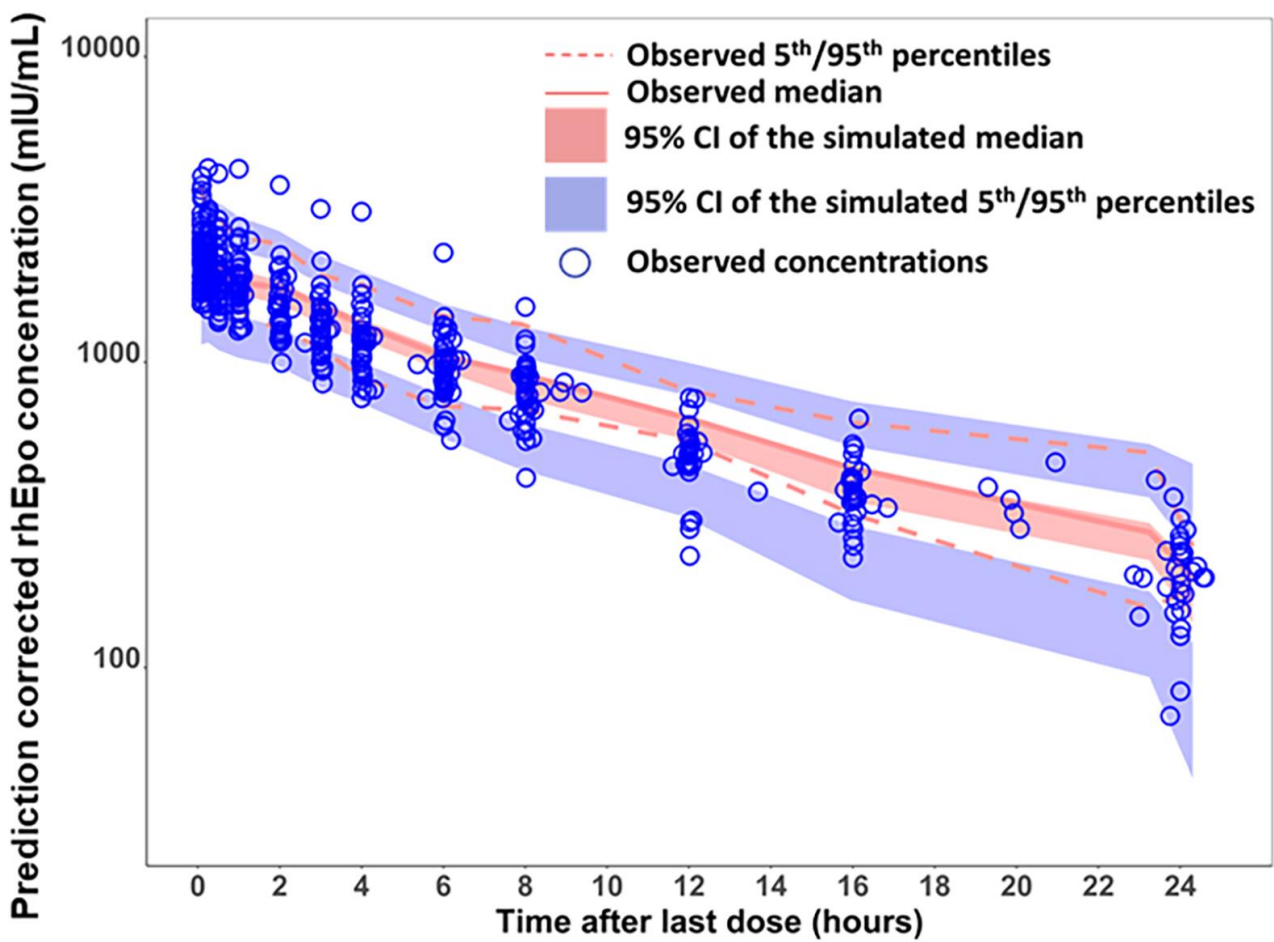


Figure 6-8. Prediction corrected visual predicted check (pcVPC) of plasma rhEpo data.

The solid red line represents the median prediction-corrected plasma concentration, and the semitransparent red field represents a simulation-based 95% confidence interval for the median. The observed 5% and 95% percentiles are presented with dashed red lines, and the 95% confidence intervals for the corresponding model predicted percentiles are shown as semitransparent blue fields. The observed plasma concentrations (prediction corrected) are represented by blue circles.

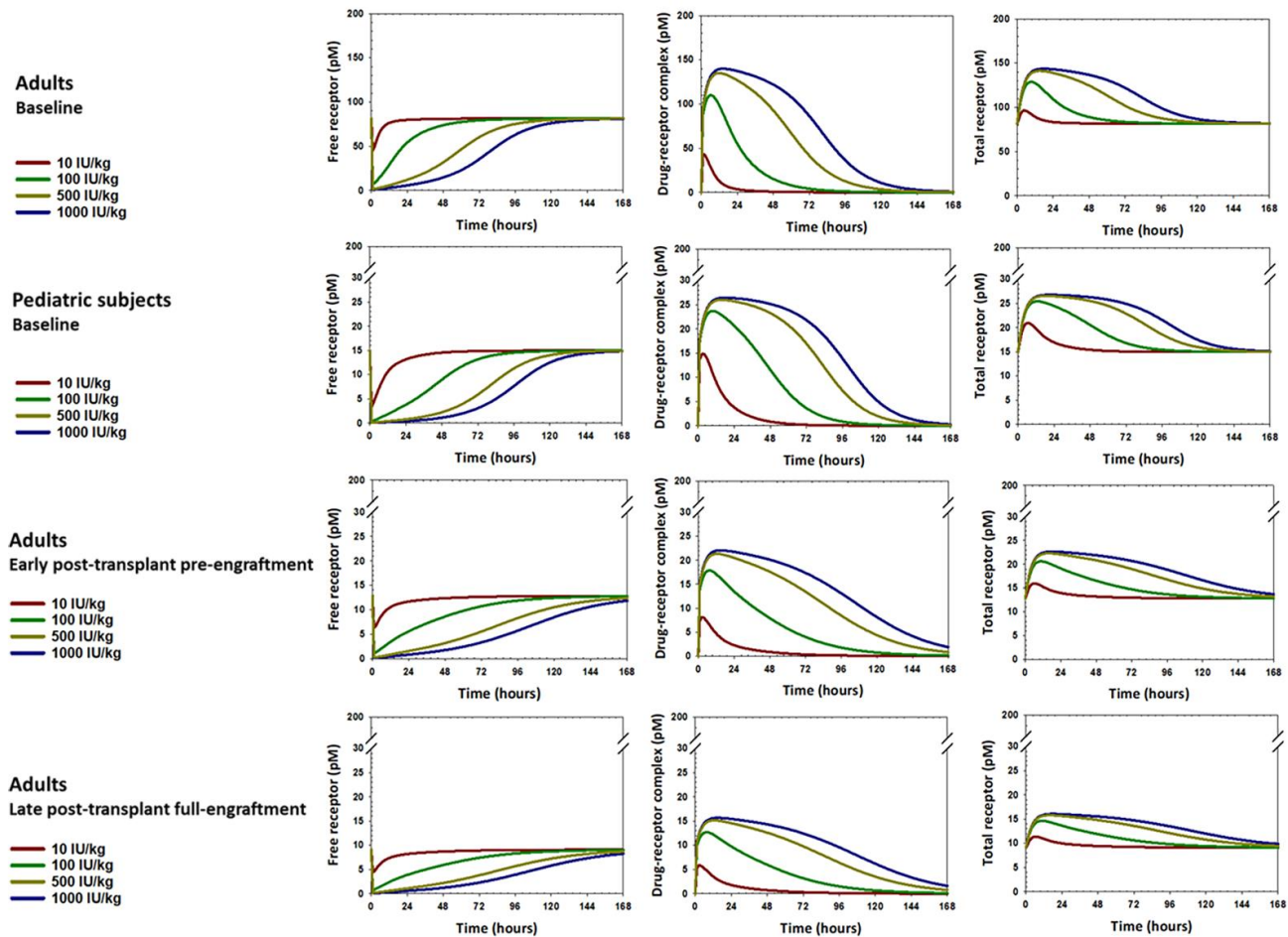


Figure 6-9. Graphs of simulated concentrations of free receptor (left), drug-receptor complex (middle) and total receptor (right) vs. time profiles.

Doses of rhEpo were administered intravenously (i.v.) at 10 IU/kg (depicted by red solid lines), 100 IU/kg (depicted by green solid lines), 500 IU/kg (depicted by yellow solid lines), and 1000 IU/kg (depicted by blue solid lines).

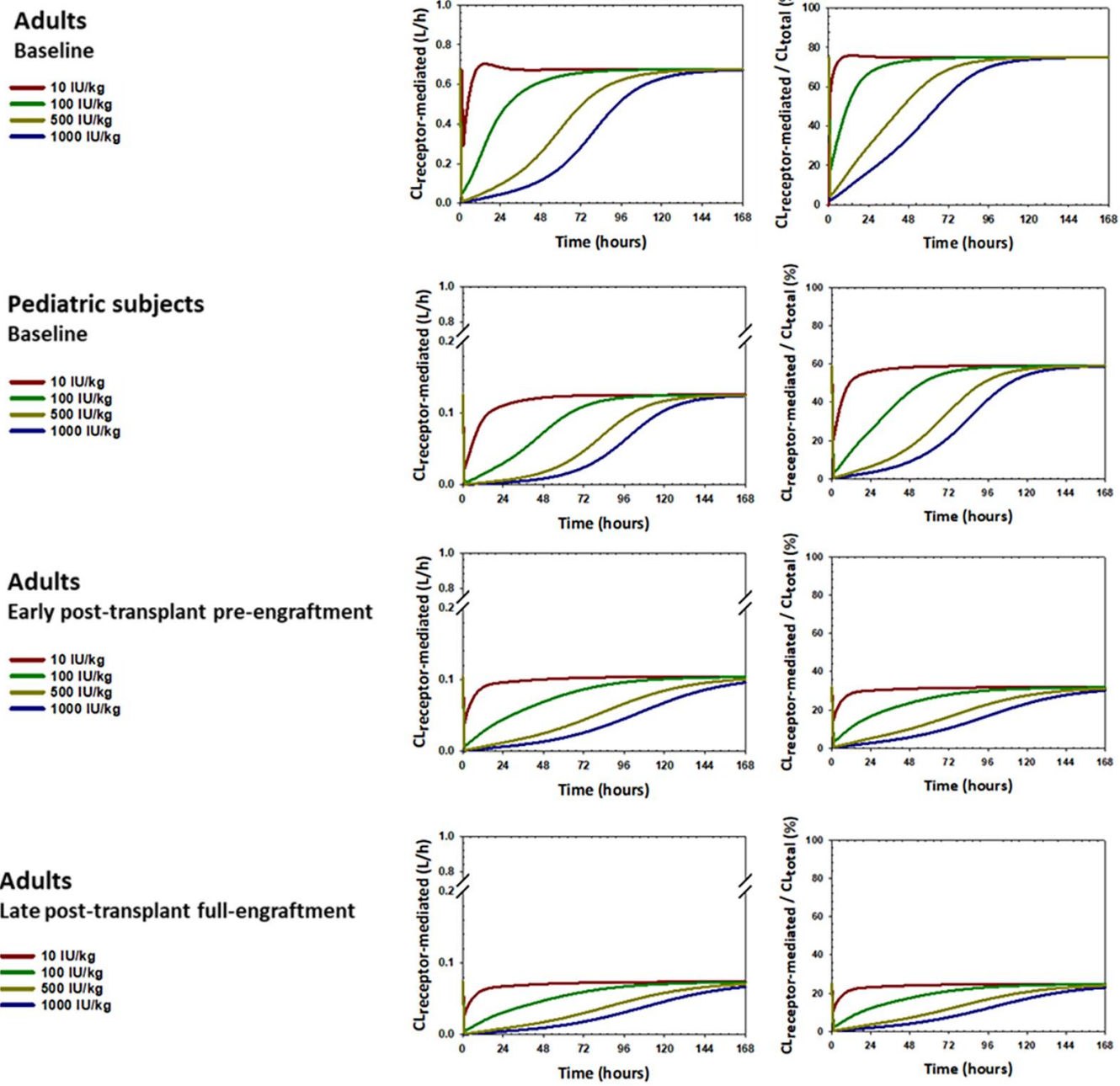


Figure 6-10. Graphs of simulated time course of receptor-mediated clearance and the ratio of receptor-mediated clearance to the total clearance in subjects.

Doses of rhEpo were administered intravenously (i.v.) at 10 IU/kg (depicted by red solid lines), 100 IU/kg (depicted by green solid lines), 500 IU/kg (depicted by yellow solid lines), and 1000 IU/kg (depicted by blue solid lines).

CHAPTER 7: SUMMARY AND CONCLUSIONS

The primary aim of this thesis is to employ a quantitative pharmacometrics modeling approach to investigate the influence of TMDD on both the PK and PD of both large-molecule and small-molecule compounds. This investigation is intended to contribute to the improvement of dose selection strategies at various stages of the drug development process.

To achieve this objective, the research presented in this dissertation is structured into three main modules: (1) Assessing quantitatively the impact of TMDD on PK of small molecules with pharmacological target in tissues (covered in Chapter 2 and 3) and (2) small molecules with pharmacological target in plasma (covered in Chapter 4 and 5) and (3) large molecule using erythropoietin as an example (covered in Chapter 6).

To fulfill the primary objective, Chapter 2 outlines the development of a TMDD model to elucidate the nonlinear PK and PD observed in a potent small-molecule HSD-1 inhibitor, SPI-62, administered to healthy adults. Given the intricate nonlinear PK profile and the apparent disconnect between plasma drug concentrations and PD effects (as evidenced by significant HSD-1 inhibition despite extremely low or undetectable plasma drug levels), pharmacometrics modeling becomes imperative to assess the dose-exposure-response relationship. In this analysis, we successfully constructed a TMDD-PD model for SPI-62, effectively capturing its complex nonlinear PK behavior and substantial, long-lasting hepatic HSD-1 inhibition in humans. Of utmost significance, we conducted simulations that lay the groundwork for dose selection in the upcoming phases of clinical trials. Chapter 3 focuses on the development of a TMDD model to characterize the PK interactions between two sEH inhibitors, both targeting the same pharmacological site, in a mouse model. While TMDD models have been extensively documented, most have been established within a single compound context. Our innovative model represents the first TMDD interaction model for two small-molecule compounds competing for the same

pharmacological target. The PK data for TPPU and TCPU in all mice were effectively described by our TMDD model. Our simulation results target occupancy levels which can facilitate dose selection in the future clinical trials.

To address the second objective, Chapters 4 and 5 detail the development of a WB-PBPK model for characterizing the PK of linagliptin in rats, with subsequent scaling to humans. Additionally, a QSP model is presented for comprehensively characterizing linagliptin's PK, its effect on DPP-4 inhibition, and its therapeutic modulation of crucial incretins, glucose, insulin, and glucagon dynamics in glycemic control. In Chapter 4, the developed WB-PBPK-TMDD model effectively characterized the concentration-time profiles of linagliptin in both plasma and various tissues, including wildtype rats and DPP4-deficient rats. Furthermore, our model accurately predicted the intricate nonlinear pharmacokinetic behavior of linagliptin in human adults. This modeling effort is not only pioneering but also of paramount importance, as the WB-PBPK-TMDD model platform, established using linagliptin as a model compound, can be applied to other small-molecule compounds exhibiting TMDD, thereby facilitating optimal dose selection for such compounds. Moving on to Chapter 5, the developed QSP model incorporated a dual TMDD model structure for linagliptin and intricate feedback loops governing the glucose regulation system. This approach effectively characterizes the nonlinear PK of linagliptin, the time course of DPP-4 inhibition, and the kinetics of GIP, GLP-1, glucagon, and glucose simultaneously in humans. Our model yields valuable insights into linagliptin's PK/PD profile and the complex dynamics of glucose homeostasis. It has the potential to be adopted by other researchers to assess the antidiabetic effects of different DPP-4 inhibitors or to evaluate combination antidiabetic therapies targeting various components of the glucose control system.

In Chapter 6, we delve into the development of a TMDD model aimed at characterizing the PK of rhEpo in patients with varying bone ablation conditions. In summary, we have successfully crafted a comprehensive mechanistic TMDD model that effectively delineates the PK of rhEpo in both healthy adults and patients with diverse bone marrow conditions. This chapter sheds light on the dynamics of free EpoR, total EpoR, and the interaction between recombinant human Epo (rhEpo) and EpoR. Notably, our model demonstrates greater robustness and yields more physiologically relevant binding parameters compared to previous TMDD models. The knowledge gained from this study holds significant importance in guiding and predicting future Epo dosing strategies for both pediatric and adult populations.

REFERENCES

1. Levy, G., *Pharmacologic target-mediated drug disposition*. Clin Pharmacol Ther, 1994. **56**(3): p. 248-52.
2. An, G., *Concept of Pharmacologic Target-Mediated Drug Disposition in Large-Molecule and Small-Molecule Compounds*. J Clin Pharmacol, 2020. **60**(2): p. 149-163.
3. Yan, X., et al., *Population pharmacokinetic and pharmacodynamic model-based comparability assessment of a recombinant human epoetin alfa and the biosimilar HX575*. The Journal of Clinical Pharmacology, 2012. **52**(11): p. 1624-1644.
4. Schropp, J., et al., *Target-mediated drug disposition model for bispecific antibodies: properties, approximation, and optimal dosing strategy*. CPT: pharmacometrics & systems pharmacology, 2019. **8**(3): p. 177-187.
5. Meijer, R., et al., *Pharmacokinetics of murine anti-human CD3 antibodies in man are determined by the disappearance of target antigen*. Journal of Pharmacology and Experimental Therapeutics, 2002. **300**(1): p. 346-353.
6. Kakkar, T., et al., *Population PK and IgE pharmacodynamic analysis of a fully human monoclonal antibody against IL4 receptor*. Pharmaceutical research, 2011. **28**: p. 2530-2542.
7. Jin, F. and W. Krzyzanski, *Pharmacokinetic model of target-mediated disposition of thrombopoietin*. AAPS PharmSci, 2004. **6**: p. 86-93.
8. El-Komy, M.H., J.A. Widness, and P. Veng-Pedersen, *Pharmacokinetic analysis of continuous erythropoietin receptor activator disposition in adult sheep using a target-mediated, physiologic recirculation model and a tracer interaction methodology*. Drug metabolism and disposition, 2011. **39**(4): p. 603-609.
9. Buchwalder, P.-A., et al., *Pharmacokinetics and pharmacodynamics of IFN- β 1a in healthy volunteers*. Journal of Interferon & Cytokine Research, 2000. **20**(10): p. 857-866.
10. Bauer, R.J., et al., *Nonlinear pharmacokinetics of recombinant human macrophage colony-stimulating factor (M-CSF) in rats*. Journal of Pharmacology and Experimental Therapeutics, 1994. **268**(1): p. 152-158.
11. Abraham, A.K., et al., *Type I interferon receptor is a primary regulator of target-mediated drug disposition of interferon- β in mice*. Journal of Pharmacology and Experimental Therapeutics, 2010. **334**(1): p. 327-332.
12. An, G. and D.A. Katz, *Importance of Target-Mediated Drug Disposition (TMDD) of Small-Molecule Compounds and Its Impact on Drug Development-Example of the Class Effect of HSD-1 Inhibitors*. J Clin Pharmacol, 2022.
13. An, G., *Small-Molecule Compounds Exhibiting Target-Mediated Drug Disposition (TMDD): A Minireview*. J Clin Pharmacol, 2017. **57**(2): p. 137-150.
14. Retlich, S., et al., *Binding to dipeptidyl peptidase-4 determines the disposition of linagliptin (BI 1356)-investigations in DPP-4 deficient and wildtype rats*. Biopharmaceutics & drug disposition, 2009. **30**(8): p. 422-436.
15. An, G., et al., *Population pharmacokinetics of the 11beta-hydroxysteroid dehydrogenase type 1 inhibitor ABT-384 in healthy volunteers following single and multiple dose regimens*. Biopharm Drug Dispos, 2014. **35**(7): p. 417-29.
16. Yamazaki, S., et al., *Application of target-mediated drug disposition model to small molecule heat shock protein 90 inhibitors*. Drug Metabolism and Disposition, 2013. **41**(6): p. 1285-1294.

17. van Waterschoot, R.A., et al., *Impact of target interactions on small-molecule drug disposition: an overlooked area*. Nature reviews Drug discovery, 2018. **17**(4): p. 299-299.
18. Smith, D.A., et al., *Importance of target-mediated drug disposition for small molecules*. Drug discovery today, 2018. **23**(12): p. 2023-2030.
19. Lee, K.S.S., et al., *Drug-Target Residence Time Affects in Vivo Target Occupancy through Multiple Pathways*. ACS central science, 2019.
20. Bach, T., et al., *General Pharmacokinetic Features of Small-Molecule Compounds Exhibiting Target-Mediated Drug Disposition (TMDD): A Simulation-Based Study*. J Clin Pharmacol, 2019. **59**(3): p. 394-405.
21. Levy, G., et al., *Comparative pharmacokinetics of coumarin anticoagulants L: Physiologic modeling of S-warfarin in rats and pharmacologic target-mediated warfarin disposition in man*. Journal of pharmaceutical sciences, 2003. **92**(5): p. 985-994.
22. Brazzell, R.K., et al., *Dose-dependent pharmacokinetics of the aldose reductase inhibitor imirestat in man*. Pharmaceutical research, 1991. **8**: p. 112-118.
23. Till, A.E., et al., *Pharmacokinetics of repeated single oral doses of enalapril maleate (MK-421) in normal volunteers*. Biopharmaceutics & drug disposition, 1984. **5**(3): p. 273-280.
24. Laine, K., et al., *Multiple-dose pharmacokinetics of selegiline and desmethylselegiline suggest saturable tissue binding*. Clinical neuropharmacology, 2000. **23**(1): p. 22-27.
25. Weber, C., et al., *Pharmacokinetics and pharmacodynamics of the endothelin-receptor antagonist bosentan in healthy human subjects*. Clinical Pharmacology & Therapeutics, 1996. **60**(2): p. 124-137.
26. Bellaire, S., et al., *Safety, Pharmacokinetics, and Pharmacodynamics of ASP3662, a Novel 11beta-Hydroxysteroid Dehydrogenase Type 1 Inhibitor, in Healthy Young and Elderly Subjects*. Clin Transl Sci, 2019. **12**(3): p. 291-301.
27. Wright, D.H., et al., *Pharmacokinetic-pharmacodynamic studies of the 11beta-hydroxysteroid dehydrogenase type 1 inhibitor MK-0916 in healthy subjects*. Br J Clin Pharmacol, 2013. **76**(6): p. 917-31.
28. Gong, J., L. Hansen, and L. Iacono, *Clinical Pharmacokinetics and the Impact of Genetic Polymorphism on a CYP2C19 Substrate, BMS-823778, in Healthy Subjects*. Drug Metab Dispos, 2018. **46**(3): p. 316-325.
29. Tu, R., et al., *Soluble epoxide hydrolase inhibition decreases reperfusion injury after focal cerebral ischemia*. Scientific reports, 2018. **8**(1): p. 5279.
30. Lee, K.S.S., et al., *Optimized inhibitors of soluble epoxide hydrolase improve in vitro target residence time and in vivo efficacy*. Journal of medicinal chemistry, 2014. **57**(16): p. 7016-7030.
31. Ostermann, A.I., et al., *Oral treatment of rodents with soluble epoxide hydrolase inhibitor 1-(1-propanoylpiperidin-4-yl)-3-[4-(trifluoromethoxy) phenyl] urea (TPPU): Resulting drug levels and modulation of oxylipin pattern*. Prostaglandins & other lipid mediators, 2015. **121**: p. 131-137.
32. An, G., et al., *Target-Mediated Drug Disposition—A Class Effect of Soluble Epoxide Hydrolase Inhibitors*. The Journal of Clinical Pharmacology, 2021. **61**(4): p. 531-537.
33. Wan, D., et al., *In vitro and in vivo metabolism of a potent inhibitor of soluble epoxide hydrolase, 1-(1-propionylpiperidin-4-yl)-3-(4-(trifluoromethoxy) phenyl) urea*. Frontiers in Pharmacology, 2019. **10**: p. 464.

34. Retlich, S., et al., *Pharmacokinetics and pharmacodynamics of single rising intravenous doses (0.5 mg–10mg) and determination of absolute bioavailability of the dipeptidyl peptidase-4 inhibitor linagliptin (BI 1356) in healthy male subjects*. Clinical pharmacokinetics, 2010. **49**(12): p. 829-840.
35. Fuchs, H., et al., *Concentration-dependent plasma protein binding of the novel dipeptidyl peptidase 4 inhibitor BI 1356 due to saturable binding to its target in plasma of mice, rats and humans*. Journal of Pharmacy and Pharmacology, 2009. **61**(1): p. 55-62.
36. Graefe-Mody, U., S. Retlich, and C. Friedrich, *Clinical pharmacokinetics and pharmacodynamics of linagliptin*. Clinical pharmacokinetics, 2012. **51**(7): p. 411-427.
37. Landersdorfer, C.B., Y.L. He, and W.J. Jusko, *Mechanism-based population pharmacokinetic modelling in diabetes: vildagliptin as a tight binding inhibitor and substrate of dipeptidyl peptidase IV*. British journal of clinical pharmacology, 2012. **73**(3): p. 391-401.
38. Thomas, L., et al., *(R)-8-(3-amino-piperidin-1-yl)-7-but-2-ynyl-3-methyl-1-(4-methyl-quinazolin-2-ylmethyl)-3, 7-dihydro-purine-2, 6-dione (BI 1356), a novel xanthine-based dipeptidyl peptidase 4 inhibitor, has a superior potency and longer duration of action compared with other dipeptidyl peptidase-4 inhibitors*. Journal of pharmacology and experimental therapeutics, 2008. **325**(1): p. 175-182.
39. Horie, Y., et al., *Pharmacokinetic, pharmacodynamic, and tolerability profiles of the dipeptidyl peptidase-4 inhibitor linagliptin: a 4-week multicenter, randomized, double-blind, placebo-controlled phase IIa study in Japanese type 2 diabetes patients*. Clinical therapeutics, 2011. **33**(7): p. 973-989.
40. Kotto-Kome, A.C., et al., *Evidence that the granulocyte colony-stimulating factor (G-CSF) receptor plays a role in the pharmacokinetics of G-CSF and PegG-CSF using a G-CSF-R KO model*. Pharmacological research, 2004. **50**(1): p. 55-58.
41. Yang, B.B., *Integration of pharmacokinetics and pharmacodynamics into the drug development of pegfilgrastim, a pegylated protein*. Pharmacokinetics and pharmacodynamics of biotech drugs: principles and case studies in drug development, 2006: p. 373-393.
42. Terashi, K., et al., *Close association between clearance of recombinant human granulocyte colony-stimulating factor (G-CSF) and G-CSF receptor on neutrophils in cancer patients*. Antimicrobial agents and chemotherapy, 1999. **43**(1): p. 21-24.
43. Johnston, E., et al., *Randomized, dose-escalation study of SD/01 compared with daily filgrastim in patients receiving chemotherapy*. Journal of Clinical Oncology, 2000. **18**(13): p. 2522-2528.
44. Chapel, S., et al., *Changes in erythropoietin pharmacokinetics following busulfan-induced bone marrow ablation in sheep: evidence for bone marrow as a major erythropoietin elimination pathway*. Journal of Pharmacology and Experimental Therapeutics, 2001. **298**(2): p. 820-824.
45. Widness, J., et al., *Change in erythropoietin pharmacokinetics following hematopoietic transplantation*. Clinical Pharmacology & Therapeutics, 2007. **81**(6): p. 873-879.
46. Chapel, S.H., et al., *Receptor-based model accounts for phlebotomy-induced changes in erythropoietin pharmacokinetics*. Experimental hematology, 2001. **29**(4): p. 425-431.
47. Espié, P., et al., *First-in-human clinical trial to assess pharmacokinetics, pharmacodynamics, safety, and tolerability of iscalimab, an anti-CD40 monoclonal antibody*. American Journal of Transplantation, 2020. **20**(2): p. 463-473.

48. Grimm, H.P., *Gaining insights into the consequences of target-mediated drug disposition of monoclonal antibodies using quasi-steady-state approximations*. Journal of pharmacokinetics and pharmacodynamics, 2009. **36**(5): p. 407.
49. Luu, K.T., et al., *A model-based approach to predicting the human pharmacokinetics of a monoclonal antibody exhibiting target-mediated drug disposition*. Journal of Pharmacology and Experimental Therapeutics, 2012. **341**(3): p. 702-708.
50. Gibbs, J.P., et al., *Impact of target-mediated elimination on the dose and regimen of evolocumab, a human monoclonal antibody against proprotein convertase subtilisin/kexin type 9 (PCSK9)*. The Journal of Clinical Pharmacology, 2017. **57**(5): p. 616-626.
51. Gibiansky, L. and E. Gibiansky, *Target-mediated drug disposition model and its approximations for antibody-drug conjugates*. Journal of pharmacokinetics and pharmacodynamics, 2014. **41**: p. 35-47.
52. Hedrich, W.D., et al., *Antibody-drug conjugates: pharmacokinetic/Pharmacodynamic modeling, preclinical characterization, clinical studies, and lessons learned*. Clinical pharmacokinetics, 2018. **57**: p. 687-703.
53. Singh, A.P. and D.K. Shah, *Application of a PK-PD modeling and simulation-based strategy for clinical translation of antibody-drug conjugates: a case study with trastuzumab emtansine (T-DM1)*. The AAPS journal, 2017. **19**: p. 1054-1070.
54. Yadav, R., et al., *Nonclinical pharmacokinetics and pharmacodynamics characterization of anti-CD79b/CD3 T Cell-Dependent bispecific antibody using a surrogate molecule: a potential therapeutic agent for B cell malignancies*. Pharmaceutics, 2022. **14**(5): p. 970.
55. Cai, H., et al., *Nonclinical Pharmacokinetics, Pharmacodynamics, and Translational Model of RO7297089, A Novel Anti-BCMA/CD16A Bispecific Tetraivalent Antibody for the Treatment of Multiple Myeloma*. The AAPS Journal, 2022. **24**(6): p. 100.
56. D'Cunha, R., et al., *A Mechanism-Based Population Pharmacokinetics Model of Erythropoietin in Premature Infants and Healthy Adults Following Multiple Intravenous Doses*. The Journal of Clinical Pharmacology, 2019. **59**(6): p. 835-846.
57. D'Cunha, R., et al., *Target-mediated disposition population pharmacokinetics model of erythropoietin in premature neonates following multiple intravenous and subcutaneous dosing regimens*. European Journal of Pharmaceutical Sciences, 2019: p. 105013.
58. Arantes Jr, L.H., et al., *A quick scoping review of efficacy, safety, economic, and health-related quality-of-life outcomes of short-and long-acting erythropoiesis-stimulating agents in the treatment of chemotherapy-induced anemia and chronic kidney disease anemia*. Critical reviews in oncology/hematology, 2018. **129**: p. 79-90.
59. Kimel, M., et al., *Does epoetin alfa improve health-related quality of life in chronically ill patients with anemia? Summary of trials of cancer, HIV/AIDS, and chronic kidney disease*. Value in Health, 2008. **11**(1): p. 57-75.
60. Bohlius, J., et al., *Recombinant human erythropoietin and overall survival in cancer patients: results of a comprehensive meta-analysis*. Journal of the National Cancer Institute, 2005. **97**(7): p. 489-498.
61. Bohlius, J., T. Tonia, and G. Schwarzer, *Twist and shout: one decade of meta-analyses of erythropoiesis-stimulating agents in cancer patients*. Acta haematologica, 2011. **125**(1-2): p. 55-67.
62. Kato, M., et al., *Pharmacokinetics of erythropoietin in genetically anemic mice*. Drug metabolism and disposition, 1998. **26**(2): p. 126-131.

63. Kato, M., et al., *Mechanism for the nonlinear pharmacokinetics of erythropoietin in rats*. Journal of Pharmacology and Experimental Therapeutics, 1997. **283**(2): p. 520-527.
64. Yoon, W.H., et al., *Pharmacokinetics of recombinant human erythropoietin in rabbits and 3/4 nephrectomized rats*. Research communications in molecular pathology and pharmacology, 1997. **96**(2): p. 227-240.
65. Veng-Pedersen, P., et al., *A comparison of nonlinear pharmacokinetics of erythropoietin in sheep and humans*. Biopharmaceutics & drug disposition, 1999. **20**(4): p. 217-223.
66. Veng-Pedersen, P., et al., *Kinetic evaluation of nonlinear drug elimination by a disposition decomposition analysis. Application to the analysis of the nonlinear elimination kinetics of erythropoietin in adult humans*. Journal of pharmaceutical sciences, 1995. **84**(6): p. 760-767.
67. Flaharty, K.K., et al., *Pharmacokinetics and erythropoietic response to human recombinant erythropoietin in healthy men*. Clinical Pharmacology & Therapeutics, 1990. **47**(5): p. 557-564.
68. Nalbant, D., et al., *Evidence of receptor-mediated elimination of erythropoietin by analysis of erythropoietin receptor mRNA expression in bone marrow and erythropoietin clearance during anemia*. Journal of Pharmacology and Experimental Therapeutics, 2010. **333**(2): p. 528-532.
69. Mager, D.E. and W.J. Jusko, *General pharmacokinetic model for drugs exhibiting target-mediated drug disposition*. J Pharmacokinet Pharmacodyn, 2001. **28**(6): p. 507-32.
70. Mould, D.R. and R.N. Upton, *Basic concepts in population modeling, simulation, and model-based drug development—part 2: introduction to pharmacokinetic modeling methods*. CPT: pharmacometrics & systems pharmacology, 2013. **2**(4): p. 1-14.
71. Holford, N., *Pharmacodynamic principles and the time course of immediate drug effects*. Translational and clinical pharmacology, 2017. **25**(4): p. 157-161.
72. Jusko, W.J. and H.C. Ko, *Physiologic indirect response models characterize diverse types of pharmacodynamic effects*. Clinical Pharmacology & Therapeutics, 1994. **56**(4): p. 406-419.
73. Gerlowski, L.E. and R.K. Jain, *Physiologically based pharmacokinetic modeling: principles and applications*. J Pharm Sci, 1983. **72**(10): p. 1103-27.
74. Sorger, P.K., et al. *Quantitative and systems pharmacology in the post-genomic era: new approaches to discovering drugs and understanding therapeutic mechanisms*. in An NIH white paper by the QSP workshop group. 2011. NIH Bethesda, MD.
75. Tomlinson, J.W., et al., *11beta-hydroxysteroid dehydrogenase type 1: a tissue-specific regulator of glucocorticoid response*. Endocr Rev, 2004. **25**(5): p. 831-66.
76. Diederich, S., et al., *11beta-hydroxysteroid dehydrogenase types 1 and 2: an important pharmacokinetic determinant for the activity of synthetic mineralo- and glucocorticoids*. J Clin Endocrinol Metab, 2002. **87**(12): p. 5695-701.
77. Newell-Price, J., et al., *Cushing's syndrome*. Lancet, 2006. **367**(9522): p. 1605-17.
78. Wang, M., *The role of glucocorticoid action in the pathophysiology of the Metabolic Syndrome*. Nutr Metab (Lond), 2005. **2**(1): p. 3.
79. Sandeep, T.C. and B.R. Walker, *Pathophysiology of modulation of local glucocorticoid levels by 11beta-hydroxysteroid dehydrogenases*. Trends Endocrinol Metab, 2001. **12**(10): p. 446-53.

80. Weiss, A.E., A; Bae, J; Encinosa, W, *Origin of Adverse Drug Events in U.S. Hospitals, 2011*. Healthcare Cost and Utilization Project (HCUP) Statistical Briefs [Internet]. 2013(<https://www.ncbi.nlm.nih.gov/books/NBK169247>).
81. Wamil, M. and J.R. Seckl, *Inhibition of 11beta-hydroxysteroid dehydrogenase type 1 as a promising therapeutic target*. Drug Discov Today, 2007. **12**(13-14): p. 504-20.
82. Sandeep, T.C., et al., *11Beta-hydroxysteroid dehydrogenase inhibition improves cognitive function in healthy elderly men and type 2 diabetics*. Proc Natl Acad Sci U S A, 2004. **101**(17): p. 6734-9.
83. Wu, N., D.A. Katz, and G. An, *A Target-Mediated Drug Disposition Model to Explain Nonlinear Pharmacokinetics of the 11beta-Hydroxysteroid Dehydrogenase Type 1 Inhibitor SPI-62 in Healthy Adults*. J Clin Pharmacol, 2021. **61**(11): p. 1442-1453.
84. Choi, K.B., *Hypertensive hypokalemic disorders*. Electrolyte Blood Press, 2007. **5**(1): p. 34-41.
85. Finken, M.J., et al., *Cortisol metabolism in healthy young adults: sexual dimorphism in activities of A-ring reductases, but not 11beta-hydroxysteroid dehydrogenases*. J Clin Endocrinol Metab, 1999. **84**(9): p. 3316-21.
86. Liu, W., et al., *Clinical Safety, Pharmacokinetics, and Pharmacodynamics of the 11beta-Hydroxysteroid Dehydrogenase Type 1 Inhibitor ABT-384 in Healthy Volunteers and Elderly Adults*. Clin Pharmacol Drug Dev, 2013. **2**(2): p. 133-51.
87. Wu, N., et al., *Simultaneous Target-Mediated Drug Disposition Model for Two Small-Molecule Compounds Competing for Their Pharmacological Target: Soluble Epoxide Hydrolase*. J Pharmacol Exp Ther, 2020. **374**(1): p. 223-232.
88. van Waterschoot, R.A.B., et al., *Impact of target interactions on small-molecule drug disposition: an overlooked area*. Nat Rev Drug Discov, 2018. **17**(4): p. 299.
89. Sura, P., et al., *Distribution and expression of soluble epoxide hydrolase in human brain*. Journal of Histochemistry & Cytochemistry, 2008. **56**(6): p. 551-559.
90. Marowsky, A., et al., *Distribution of soluble and microsomal epoxide hydrolase in the mouse brain and its contribution to cerebral epoxyeicosatrienoic acid metabolism*. Neuroscience, 2009. **163**(2): p. 646-661.
91. Wagner, K.M., et al., *Soluble epoxide hydrolase as a therapeutic target for pain, inflammatory and neurodegenerative diseases*. Pharmacology & therapeutics, 2017. **180**: p. 62-76.
92. Lee, K.S.S., et al., *Förster resonance energy transfer competitive displacement assay for human soluble epoxide hydrolase*. Analytical biochemistry, 2013. **434**(2): p. 259-268.
93. Goswami, S.K., et al., *Anti-ulcer efficacy of soluble epoxide hydrolase inhibitor TPPU on diclofenac-induced intestinal ulcers*. Journal of Pharmacology and Experimental Therapeutics, 2016. **357**(3): p. 529-536.
94. Yao, E.-s., et al., *TPPU protects tau from H₂O₂-induced hyperphosphorylation in HEK293/tau cells by regulating PI3K/AKT/GSK-3β pathway*. Journal of Huazhong University of Science and Technology [Medical Sciences], 2016. **36**(6): p. 785-790.
95. Guo, Y., et al., *TPPU enhanced exercise-induced epoxyeicosatrienoic acid concentrations to exert cardioprotection in mice after myocardial infarction*. Journal of cellular and molecular medicine, 2018. **22**(3): p. 1489-1500.
96. Liu, J., et al., *Substituted phenyl groups improve the pharmacokinetic profile of urea-based soluble epoxide hydrolase inhibitors*. 2012, Federation of American Societies for Experimental Biology.

97. Dua, P., E. Hawkins, and P. Van der Graaf, *A tutorial on target-mediated drug disposition (TMDD) models*. CPT: pharmacometrics & systems pharmacology, 2015. **4**(6): p. 324-337.
98. Gibiansky, L. and E. Gibiansky, *Target-mediated drug disposition model for drugs that bind to more than one target*. Journal of pharmacokinetics and pharmacodynamics, 2010. **37**(4): p. 323-346.
99. Yan, X., Y. Chen, and W. Krzyzanski, *Methods of solving rapid binding target-mediated drug disposition model for two drugs competing for the same receptor*. Journal of pharmacokinetics and pharmacodynamics, 2012. **39**(5): p. 543-560.
100. Ait-Oudhia, S., J.-M. Scherrmann, and W. Krzyzanski, *Simultaneous pharmacokinetics/pharmacodynamics modeling of recombinant human erythropoietin upon multiple intravenous dosing in rats*. Journal of Pharmacology and Experimental Therapeutics, 2010. **334**(3): p. 897-910.
101. de Witte, W.E., et al., *In vivo target residence time and kinetic selectivity: the association rate constant as determinant*. Trends in pharmacological sciences, 2016. **37**(10): p. 831-842.
102. Veng-Pedersen, P., et al., *A tracer interaction method for nonlinear pharmacokinetics analysis: application to evaluation of nonlinear elimination*. Journal of pharmacokinetics and biopharmaceutics, 1997. **25**(5): p. 569-593.
103. Copeland, R.A., *Drug-target interaction kinetics: underutilized in drug optimization?* Future Med Chem, 2016. **8**(18): p. 2173-2175.
104. Decker, M., M. Arand, and A. Cronin, *Mammalian epoxide hydrolases in xenobiotic metabolism and signalling*. Archives of toxicology, 2009. **83**(4): p. 297-318.
105. Zhao, P., et al., *Applications of physiologically based pharmacokinetic (PBPK) modeling and simulation during regulatory review*. Clinical Pharmacology & Therapeutics, 2011. **89**(2): p. 259-267.
106. Hartel, S., et al., *Dipeptidyl peptidase (DPP) IV in rat organs*. Histochemistry, 1988. **89**(2): p. 151-161.
107. Lankas, G.R., et al., *Dipeptidyl peptidase IV inhibition for the treatment of type 2 diabetes: potential importance of selectivity over dipeptidyl peptidases 8 and 9*. Diabetes, 2005. **54**(10): p. 2988-2994.
108. Elliott, R., et al., *Glucagon-like peptide-1 (7–36) amide and glucose-dependent insulinotropic polypeptide secretion in response to nutrient ingestion in man: acute post-prandial and 24-h secretion patterns*. Journal of Endocrinology, 1993. **138**(1): p. 159-166.
109. Nauck, M., et al., *Additive insulinotropic effects of exogenous synthetic human gastric inhibitory polypeptide and glucagon-like peptide-1-(7-36) amide infused at near-physiological insulinotropic hormone and glucose concentrations*. The Journal of Clinical Endocrinology & Metabolism, 1993. **76**(4): p. 912-917.
110. Schwartz, S.L., *Treatment of elderly patients with type 2 diabetes mellitus: a systematic review of the benefits and risks of dipeptidyl peptidase-4 inhibitors*. The American journal of geriatric pharmacotherapy, 2010. **8**(5): p. 405-418.
111. Heise, T., et al., *Pharmacokinetics, pharmacodynamics and tolerability of multiple oral doses of linagliptin, a dipeptidyl peptidase-4 inhibitor in male type 2 diabetes patients*. Diabetes, Obesity and Metabolism, 2009. **11**(8): p. 786-794.

112. Hüttner, S., et al., *Safety, tolerability, pharmacokinetics, and pharmacodynamics of single oral doses of BI 1356, an inhibitor of dipeptidyl peptidase 4, in healthy male volunteers*. The Journal of Clinical Pharmacology, 2008. **48**(10): p. 1171-1178.
113. Fuchs, H., R. Binder, and A. Greischel, *Tissue distribution of the novel DPP-4 inhibitor BI 1356 is dominated by saturable binding to its target in rats*. Biopharmaceutics & drug disposition, 2009. **30**(5): p. 229-240.
114. Volz, A.-K., et al., *Target-Mediated Drug Disposition Pharmacokinetic–Pharmacodynamic Model of Bosentan and Endothelin-1*. Clinical pharmacokinetics, 2017. **56**(12): p. 1499-1511.
115. Tadayasu, Y., et al., *Population pharmacokinetic/pharmacodynamic analysis of the DPP-4 inhibitor linagliptin in Japanese patients with type 2 diabetes mellitus*. Journal of Pharmacy & Pharmaceutical Sciences, 2013. **16**(5): p. 708-721.
116. Bi, Y., et al., *A Whole-Body Physiologically Based Pharmacokinetic Model of Gefitinib in Mice and Scale-Up to Humans*. AAPS J, 2016. **18**(1): p. 228-38.
117. Fuchs, H., F. Runge, and H.-D. Held, *Excretion of the dipeptidyl peptidase-4 inhibitor linagliptin in rats is primarily by biliary excretion and P-gp-mediated efflux*. European journal of pharmaceutical sciences, 2012. **45**(5): p. 533-538.
118. Sarashina, A., et al., *Linagliptin, a dipeptidyl peptidase-4 inhibitor in development for the treatment of type 2 diabetes mellitus: a phase I, randomized, double-blind, placebo-controlled trial of single and multiple escalating doses in healthy adult male Japanese subjects*. Clinical therapeutics, 2010. **32**(6): p. 1188-1204.
119. Blech, S., et al., *The metabolism and disposition of the oral dipeptidyl peptidase-4 inhibitor, linagliptin, in humans*. Drug Metabolism and Disposition, 2010. **38**(4): p. 667-678.
120. Delp, M.D., M.V. Evans, and C. Duan, *Effects of aging on cardiac output, regional blood flow, and body composition in Fischer-344 rats*. Journal of Applied Physiology, 1998. **85**(5): p. 1813-1822.
121. Nagler, R.M., B.J. Baum, and P.C. Fox, *Effects of X irradiation on the function of rat salivary glands at 3 and 40 days*. Radiation research, 1993. **136**(3): p. 392-396.
122. Mobarak, N. and Y. Alice, *Lead distribution in the saliva and blood fractions of rats after intraperitoneal injections*. Toxicology, 1984. **32**(1): p. 67-74.
123. Davies, B. and T. Morris, *Physiological parameters in laboratory animals and humans*. Pharmaceutical research, 1993. **10**(7): p. 1093-1095.
124. Jansky, L. and J. Hart, *Cardiac output and organ blood flow in warm-and cold-acclimated rats exposed to cold*. Canadian journal of physiology and pharmacology, 1968. **46**(4): p. 653-659.
125. Lee, H. and M. Blaufox, *Blood volume in the rat*. Journal of Nuclear Medicine, 1985. **26**(1): p. 72-76.
126. Valentin, J., *Basic anatomical and physiological data for use in radiological protection: reference values: ICRP Publication 89*. Annals of the ICRP, 2002. **32**(3-4): p. 1-277.
127. Feher, J.J., *Quantitative human physiology: an introduction*. 2017: Academic press.
128. Tarhan, S., et al., *Effect of varicocele on testicular artery blood flow in men color doppler investigation*. Scandinavian journal of urology and nephrology, 2003. **37**(1): p. 38-42.
129. Hurley, P.J., *Red cell and plasma volumes in normal adults*. Journal of nuclear medicine: official publication, Society of Nuclear Medicine, 1975. **16**(1): p. 46-52.

130. Choi, G.-W., Y.-B. Lee, and H.-Y. Cho, *Interpretation of Non-Clinical Data for Prediction of Human Pharmacokinetic Parameters: In Vitro-In Vivo Extrapolation and Allometric Scaling*. *Pharmaceutics*, 2019. **11**(4): p. 168.
131. Kenyon, E.M., *Interspecies extrapolation*, in *Computational Toxicology*. 2012, Springer. p. 501-520.
132. Yu, Y., et al., *A rat RNA-Seq transcriptomic BodyMap across 11 organs and 4 developmental stages*. *Nature communications*, 2014. **5**(1): p. 1-11.
133. An, G., W. Liu, and S. Dutta, *Small-molecule compounds exhibiting target-mediated drug disposition—A case example of ABT-384*. *The Journal of Clinical Pharmacology*, 2015. **55**(10): p. 1079-1085.
134. Deshpande, A.D., M. Harris-Hayes, and M. Shootman, *Epidemiology of diabetes and diabetes-related complications*. *Physical therapy*, 2008. **88**(11): p. 1254-1264.
135. Shah, N., et al., *Therapeutics for type-2 diabetes mellitus: a glance at the recent inclusions and novel agents under development for use in clinical practice*. *Therapeutic Advances in Endocrinology and Metabolism*, 2021. **12**: p. 20420188211042145.
136. DeMarsilis, A., et al., *Pharmacotherapy of type 2 diabetes: An update and future directions*. *Metabolism*, 2022: p. 155332.
137. Godinho, R., et al., *The place of dipeptidyl peptidase-4 inhibitors in type 2 diabetes therapeutics: a “me too” or “the special one” antidiabetic class?* *Journal of diabetes research*, 2015. **2015**.
138. Hartel, S., et al., *Dipeptidyl peptidase (DPP) IV in rat organs: comparison of immunohistochemistry and activity histochemistry*. *Histochemistry*, 1988. **89**(2): p. 151-161.
139. Wu, N. and G. An, *Incorporating Pharmacological Target-Mediated Drug Disposition (TMDD) in a Whole-Body Physiologically Based Pharmacokinetic (PBPK) Model of Linagliptin in Rat and Scale-up to Human*. *The AAPS journal*, 2020. **22**: p. 1-17.
140. Retlich, S., et al., *Impact of target-mediated drug disposition on linagliptin pharmacokinetics and DPP-4 inhibition in type 2 diabetic patients*. *The Journal of Clinical Pharmacology*, 2010. **50**(8): p. 873-885.
141. Vilsbøll, T., et al., *Both GLP-1 and GIP are insulinotropic at basal and postprandial glucose levels and contribute nearly equally to the incretin effect of a meal in healthy subjects*. *Regulatory peptides*, 2003. **114**(2-3): p. 115-121.
142. Nadkarni, P., O.G. Chepurny, and G.G. Holz, *Regulation of glucose homeostasis by GLP-1*. *Progress in molecular biology and translational science*, 2014. **121**: p. 23-65.
143. Mathiesen, D.S., et al., *The effects of dual GLP-1/GIP receptor agonism on glucagon secretion—a review*. *International Journal of Molecular Sciences*, 2019. **20**(17): p. 4092.
144. Meier, J.J., et al., *Reduced insulinotropic effect of gastric inhibitory polypeptide in first-degree relatives of patients with type 2 diabetes*. *Diabetes*, 2001. **50**(11): p. 2497-2504.
145. Bergman, R.N., et al., *Quantitative estimation of insulin sensitivity*. *American Journal of Physiology-Endocrinology And Metabolism*, 1979. **236**(6): p. E667.
146. Jauslin, P.M., N. Frey, and M.O. Karlsson, *Modeling of 24-hour glucose and insulin profiles of patients with type 2 diabetes*. *The Journal of Clinical Pharmacology*, 2011. **51**(2): p. 153-164.
147. Palumbo, P., et al., *Mathematical modeling of the glucose–insulin system: A review*. *Mathematical biosciences*, 2013. **244**(2): p. 69-81.

148. Mari, A., et al., *A model for glucose control of insulin secretion during 24 h of free living*. Diabetes, 2001. **50**(suppl_1): p. S164.
149. Bergman, R.N., *Toward physiological understanding of glucose tolerance: minimal-model approach*. Diabetes, 1989. **38**(12): p. 1512-1527.
150. Liu, W. and F. Tang, *Modeling a simplified regulatory system of blood glucose at molecular levels*. Journal of Theoretical Biology, 2008. **252**(4): p. 608-620.
151. Masroor, S., et al., *Mathematical modeling of the glucagon challenge test*. Journal of pharmacokinetics and pharmacodynamics, 2019. **46**(6): p. 553-564.
152. Schaller, S., et al., *A generic integrated physiologically based whole-body model of the glucose-insulin-glucagon regulatory system*. CPT: pharmacometrics & systems pharmacology, 2013. **2**(8): p. 1-10.
153. Schnell, K.B., et al., *Assessment of glycemic response to an oral glucokinase activator in a proof of concept study: application of a semi-mechanistic, integrated glucose-insulin-glucagon model*. Journal of pharmacokinetics and pharmacodynamics, 2013. **40**(1): p. 67-80.
154. Peng, J.Z., et al., *A semi-mechanistic model for the effects of a novel glucagon receptor antagonist on glucagon and the interaction between glucose, glucagon, and insulin applied to adaptive phase II design*. The AAPS journal, 2014. **16**(6): p. 1259-1270.
155. Balazki, P., et al., *A Physiologically-Based Quantitative Systems Pharmacology Model of the Incretin Hormones GLP-1 and GIP and the DPP4 Inhibitor Sitagliptin*. CPT: pharmacometrics & systems pharmacology, 2020. **9**(6): p. 353-362.
156. Landersdorfer, C.B., Y.L. He, and W.J. Jusko, *Mechanism-based population modelling of the effects of vildagliptin on GLP-1, glucose and insulin in patients with type 2 diabetes*. British journal of clinical pharmacology, 2012. **73**(3): p. 373-390.
157. Røge, R.M., et al., *Mathematical Modelling of Glucose-Dependent Insulinotropic Polypeptide and Glucagon-like Peptide-1 following Ingestion of Glucose*. Basic & Clinical Pharmacology & Toxicology, 2017. **121**(4): p. 290-297.
158. Rauch, T., et al., *Linagliptin increases incretin levels, lowers glucagon, and improves glycemic control in type 2 diabetes mellitus*. Diabetes Therapy, 2012. **3**(1): p. 10.
159. Golightly, L.K., C.C. Drayna, and M.T. McDermott, *Comparative clinical pharmacokinetics of dipeptidyl peptidase-4 inhibitors*. Clinical pharmacokinetics, 2012. **51**: p. 501-514.
160. Mentlein, R., *Mechanisms underlying the rapid degradation and elimination of the incretin hormones GLP-1 and GIP*. Best Practice & Research Clinical Endocrinology & Metabolism, 2009. **23**(4): p. 443-452.
161. Liu, W., *Control of blood glucose*, in *Introduction to Modeling Biological Cellular Control Systems*. 2012, Springer. p. 69-93.
162. Gromada, J., A. Duttaroy, and P. Rorsman, *The insulin receptor talks to glucagon?* Cell metabolism, 2009. **9**(4): p. 303-305.
163. Kaneko, K., et al., *Insulin inhibits glucagon secretion by the activation of PI3-kinase in In-R1-G9 cells*. Diabetes research and clinical practice, 1999. **44**(2): p. 83-92.
164. Holst, J.J., et al., *Glucagon and amino acids are linked in a mutual feedback cycle: the liver- α -cell axis*. Diabetes, 2017. **66**(2): p. 235-240.
165. Forst, T., et al., *The oral DPP-4 inhibitor linagliptin significantly lowers HbA1c after 4 weeks of treatment in patients with type 2 diabetes mellitus*. Diabetes, Obesity and Metabolism, 2011. **13**(6): p. 542-550.

166. Graefe-Mody, U., S. Retlich, and C. Friedrich, *Clinical pharmacokinetics and pharmacodynamics of linagliptin*. Clinical pharmacokinetics, 2012. **51**: p. 411-427.
167. Møller, J.B., et al., *Mechanism-based population modelling for assessment of L-cell function based on total GLP-1 response following an oral glucose tolerance test*. Journal of pharmacokinetics and pharmacodynamics, 2011. **38**: p. 713-725.
168. Widness, J.A., et al., *In vivo ^{125}I -erythropoietin pharmacokinetics are unchanged after anesthesia, nephrectomy and hepatectomy in sheep*. Journal of Pharmacology and Experimental Therapeutics, 1996. **279**(3): p. 1205-1210.
169. Walrafen, P., et al., *Both proteasomes and lysosomes degrade the activated erythropoietin receptor*. Blood, 2005. **105**(2): p. 600-608.
170. Betts, A.M., et al., *The application of target information and preclinical pharmacokinetic/pharmacodynamic modeling in predicting clinical doses of a Dickkopf-1 antibody for osteoporosis*. Journal of Pharmacology and Experimental Therapeutics, 2010. **333**(1): p. 2-13.
171. Olsson-Gisleskog, P., P. Jacqmin, and J.J. Perez-Ruixo, *Population pharmacokinetics meta-analysis of recombinant human erythropoietin in healthy subjects*. Clinical pharmacokinetics, 2007. **46**(2): p. 159-173.
172. Knebel, W., et al., *Population pharmacokinetic modeling of epoetin delta in pediatric patients with chronic kidney disease*. The Journal of Clinical Pharmacology, 2008. **48**(7): p. 837-848.
173. Krzyzanski, W., et al., *Pharmacokinetic and pharmacodynamic modeling of recombinant human erythropoietin after multiple subcutaneous doses in healthy subjects*. European journal of pharmaceutical sciences, 2005. **26**(3-4): p. 295-306.
174. Chakraborty, A., et al., *Population pharmacokinetics of erythropoietin in critically ill subjects*. The Journal of Clinical Pharmacology, 2005. **45**(2): p. 193-202.
175. Frymoyer, A., et al., *High-dose erythropoietin population pharmacokinetics in neonates with hypoxic-ischemic encephalopathy receiving hypothermia*. Pediatric research, 2017. **81**(6): p. 865-872.
176. Widness, J.A., et al., *Erythropoietin pharmacokinetics in premature infants: developmental, nonlinearity, and treatment effects*. Journal of applied physiology, 1996. **80**(1): p. 140-148.
177. Georgieff, M.K., et al., *Abnormal iron distribution in infants of diabetic mothers: spectrum and maternal antecedents*. The Journal of pediatrics, 1990. **117**(3): p. 455-461.
178. Woo, S., W. Krzyzanski, and W.J. Jusko, *Target-mediated pharmacokinetic and pharmacodynamic model of recombinant human erythropoietin (rHuEPO)*. Journal of pharmacokinetics and pharmacodynamics, 2007. **34**(6): p. 849-868.
179. Cooling, L., *The RBC as a Physiological Object*. 2014.
180. Adamson, J.W. *The relationship of erythropoietin and iron metabolism to red blood cell production in humans*. in *Seminars in oncology*. 1994.
181. Brody, V.C., et al., *Erythropoietin receptor characteristics on primary human erythroid cells*. 1991.
182. Gross, A.W. and H.F. Lodish, *Cellular trafficking and degradation of erythropoietin and novel erythropoiesis stimulating protein (NESP)*. Journal of Biological Chemistry, 2006. **281**(4): p. 2024-2032.